Ph. D. Thesis
NIRANJAN SURYAKANT RAMGIR
Feb 2006

SYNTHESIS AND CHARACTERIZATION OF TIN OXIDE AND ZINC OXIDE NANOSTRUCTURED MATERIALS FOR GAS SENSORS

NIRANJAN SURYAKANT RAMGIR

PHYSICAL AND MATERIALS CHEMISTRY DIVISION
NATIONAL CHEMICAL LABORATORY
PUNE – 411 008
INDIA

February 2006

SYNTHESIS AND CHARACTERIZATION OF TIN OXIDE AND ZINC OXIDE NANOSTRUCTURED MATERIALS FOR GAS SENSORS

A THESIS
SUBMITTED TO THE
UNIVERSITY OF PUNE
FOR THE DEGREE OF
DOCTOR OF PHILOSOPHY
IN
PHYSICS

BY
NIRANJAN SURYAKANT RAMGIR

PHYSICAL AND MATERIALS CHEMISTRY DIVISION
NATIONAL CHEMICAL LABORATORY
PUNE – 411 008
INDIA

February 2006

Dedicated to
My Parents
Kaku and Kaka

DECLARATION

I hereby declare that all the experiments embodied in this thesis entitled "**SYNTHESIS AND CHARACTERIZATION OF TIN OXIDE AND ZINC OXIDE NANOSTRUCTURED MATERIALS FOR GAS SENSORS**", submitted for the degree of Doctor of Philosophy in Physics, to the University of Pune has been carried out by me at the Physical and Materials Chemistry Division, National Chemical Laboratory, Pune, 411008, India, under the supervision of Dr. K. Vijayamohanan. The work is original and has not been submitted in part or full by me, for any degree or diploma to this or to any other University.

Date: **NIRANJAN SURYAKANT RAMGIR**
Physical and Materials Chemistry Division
National Chemical Laboratory
Pune – 411 008

Dr. K. Vijayamohanan
Scientist

Physical and Materials
Chemistry Division
National Chemical Laboratory
Pune – 411008
INDIA

Tel: 91-020-2590 2588
Res: 91-020-2589 3307
Fax: 91-020-2589 3044
Email: vk.pillai@ncl.res.in

CERTIFICATE

This is to certify that the work incorporated in the thesis entitled "**SYNTHESIS AND CHARACTERIZATION OF TIN OXIDE AND ZINC OXIDE NANOSTRUCTURED MATERIALS FOR GAS SENSORS**" submitted by **Mr. NIRANJAN SURYAKANT RAMGIR,** was carried out by him under our supervision at the Physical and Materials Chemistry Division, National Chemical Laboratory, Pune, 411008, India. All the materials from other sources have been duly acknowledged in the thesis.

Research Guide	Research Co-Guide
(Vijayamohanan)	**(Mulla)**

Date : 16th February, 2006
Place : Pune

Acknowledgements

There are so many people, whose support, encouragement and inspiration are very much obligatory to accomplish major achievements in life, especially, if it involves the elements of fulfilling one's cherish dreams. For me, this thesis is such an important destiny and I am indeed indebted to lot of people for their well wishes and blessings for completing this journey. A sense of appreciation automatically comes into mind at this stage to show my sincere gratitude to all of them, who played a pivotal role and without whom this thesis would not have been possible.

I would like to take this opportunity first, to pay my sincere approbation to Dr. K. Vijayamohanan, whose motivation, inspiration, advice, encouragement, timely criticism and continual guidance have lead me to bring my dream to reality. He has not only introduced me to my research problem, but also taught too many other exciting areas and subjects, sometimes more than science. His knowledge is like an ever-expanding encyclopedia, which has all possible answers to help me out of any problem. In this respect, I must mention that he is also a very good teacher and a wonderful research guide, which is often quite rare. I am very much honored to work under his esteemed guidance. He is very patient, understanding and above all a very good human being, whose life's sole motto is to help others; this automatically makes him as my Idol.

I would also like to offer my sincere admiration to my co-guide Dr. I. S. Mulla for all his help, support, suggestion and advice during the course of this study. He is very kind and considerate and has vast knowledge and expertise. I feel very fortunate to be able to learn few things from him.

I also extend my sincere appreciation to both Mrs Vijayamohanan and Mrs. Mulla for their motherly care, blessing and constant support.

It gives me great pleasure to thank Prof. D. S. Joag, HOD and Dr. M. A. More, both from the Department of Physics, University of Pune for their invaluable suggestions, encouragements and making all the laboratory facilities available to perform certain crucial experiments. Special thanks are due to both Mr. Dattatray Late and Mr. Ashok Bhise for their help in accomplishing such difficult experiments.

I wish to thank Dr. S. Sivaram, the Director, NCL for providing me all infrastructural facilities. I am also grateful to Dr. P. Ganguly, Dr. S. K. Date and Dr. S. Pal, former and present heads of Physical and Materials Chemistry Division, and Dr. S. P. Vernekar, former head of Polymer Engineering, for allowing me to use all the available facilities in these divisions and for their constant encouragement. I am also thankful to Prof. Jin Soo Yoo, Dr. Jong-San Chang and Dr. Young Kyu Hwang, KRICT, Korea for their help and support.

My heartfelt gratitude to Drs. S. D. Sathaye, C. S. Gopinath, Prakash Ghosh, Anil Kumar, P. A. Joy, Murali Sastry, B. L. V. Prasad, Pankaj Poddar, V. Ravi and K. Shreedhar for their advice and help. I am highly indebted to Dr. S. R. Sainkar, and Mr. A. Gaikwad for teaching me the SEM instrument, which helped me a lot in characterising my sample. I am also extremely grateful to Drs Mandale, Patil, Pawaskar, Mitra, Bhadbhade, and Mrs Renu Pasricha who were very helpful for characterizing my samples. Timely help from Mr. Dipak and Mr. Punekar and the entire library staff for excellent facilities is gratefully acknowledged. I wish to extend my sincere gratitude to Drs. B. B. Kale (C-MET), Chikate (Garware College), Deshpande (NCL) for their love, constant encouragement and timely help. I also take this opportunity to thank glass blowing, stores, purchase, workshop and administrative groups for their support during my study. Further, CSIR is gratefully acknowledged for the financial support.

I can never forget the help from my seniors, Drs. Varsha, Sudrik, Sushama, Aslam, Nirmalya and Trupti for their mentoring during my initial research days. A special thanks to all my labmates, Jadabji, Bhalu, Mahima (Chechi), Mrudula, Deepali, Girish, Kannan, Meera, Vivek and Bhaskar, and to Nabonita 'Bhabhi' who created a pleasant atmosphere to work truly in a group. I thank again Dr. Vijayamohanan for his constant efforts to imbue us with several, most essential habits, like weekly seminars and group meetings, monthly reports and daily planning, which make me now confident to start an independent scientific carrier.

I wish to thank all my fellow colleagues in my division, Rohini, Suvarna, Shraedha, Diganta, Joly, Shankar, Shekhar, Deka, Sanjay, Anita, Sumant, Debu are few among them. I also extend my thanks to several other friends in NCL, Sandeep, Mahesh, Ravindra Subramaniyam.

I find no words to express my feelings for my parents, whose moral support, love and constant encouragements have helped me to complete this journey. Their patience and sacrifice are always a main source of my inspiration and will remain throughout my life, motivating me to pursue still higher goals. This thesis is also a culmination of a dream for my elder brother 'Kiran Bhau', bhabhi 'Anuradha', my elder sisters 'Deepali and Aarti' and the brothers-in-law, Mr. Gunesh and Mr. Harish, who always encouraged me during my doctoral course. The presence of the little angels 'Vaishnavi' (Chimni) and Rohan 'Pillu' was always refreshing, making me feel relax and comfortable. I wish to extend my sincere gratitude to my grand mother and all other relatives for their blessings.

Finally, heartfelt thanks to my friends Onkar and Komal (Vaini), Vishal, Sagar, Kaustubh, Sachin, Rupesh, Rupali and Meghana without whose constant support and inspiration this would never have been possible.

The thesis would be useful, if my efforts are ever to be of any use for the welfare of mankind and the advancement of science.

Niranjan Suryakant Ramgir

Table of Contents

Chapter 1

1-66

Synthesis and Characterization of High Aspect Ratio Nanostructures of Semiconducting Oxides

Chapter 2

A Novel Route Towards Shape Selective Synthesis of SnO_2 Sub-Micron Structures: Bipyramids, Cubes and Wires

Chapter 3

Gas Sensing Properties of SnO_2: from Thin Films to Nanostructures

Chapter 4

Synthesis and Characterization of ZnO Microstructures

Chapter 5

Enhanced Field Emission Properties of ZnO Microstructures

Chapter 1

Synthesis and Characterization of High Aspect Ratio Nanostructures of Semiconducting Oxides

This chapter presents a critical summary of the semiconducting oxide nanostructures. The scope for these structures in nanotechnology along with several fundamental issues related to their origin and the evolution of size and shape dependent properties at nano scale and their potential applications are discussed. Particular emphasis has been placed on the synthesis, characterization, properties and diverse applications of tin oxide and zinc oxide nanostructures. The objectives of the present study and abstract of the overall investigation are also mentioned at the end of this chapter.

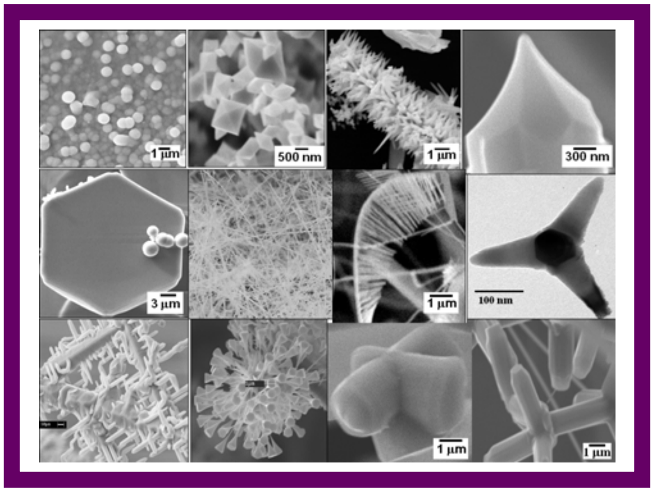

1.1. Introduction

A general concern about the future of industrial societies has stimulated intense discussions around the world, which has consequently led to a number of recommendations by world panels.[1] For example, United Nations has recommended eight prime millennium development goals, which range from halving extreme poverty to halting the spread of HIV/AIDS and providing universal primary education, all by the target date of 2015.[2] Leading the list is the necessity for a speedy and permanent turn towards resource-sparing and environmentally compatible technologies and innovations. However, consequences of this development will also include the exponential growth of the world's population, acceleration of environmental burdens and depletion of our primary resources. A solution to these problems presupposes the ongoing improvements in our technical competence and its optimum utilization. A major driving force in the research and development of new materials for the future technologies is to match in future devices the different performances that are currently achieved separately in biological and in technical systems. An often-considered example is the human brain as compared with the man-made computer. Technologically unmatched performance of the brain includes high information density, low power consumption, high flexibility, associated memory, etc. While in comparison, biologically unmatched performance of the computer includes quantitative information processing, high reproducibility, etc. With increasing complexity and demands for the future information technologies, a trend is to be seen towards the design of 'smart' nanostructures that will be interfaced to silicon or other substrates.[3] These structures consist either of physically or chemically synthesized units such as molecules, supramolecules, and biologically active recognition centers, or of natural and hence very complex biomolecular functional units with high molecular weight extracted from biological systems.

Accordingly, today, nanoscience and nanotechnology has become one of the hottest fields in social implications, business, investments, and finally capturing the media attention. Nanotechnology comprises the fabrication and understanding of matter at the ultimate scale at which nature designs: the molecular scale.[4] The famous quotes "*There is plenty of room at the bottom*" by Prof. Richard Feynman, and "*Nanotechnology* *holds the answers to the extend there are answers, to most of our pressing materials needs in energy, health, communication, transportation, food, water, etc*" by the famous Nobel laureate, late. Prof. Richard Smalley explain the vision behind this new idea. In particular, nanoscience comprises of manipulating and developing materials at nanoscale level (0.1 to 100 nm) to endow them with fascinating size and shape dependent properties for diverse set of applications in various fields of science and engineering. Nanotechnology on the other hand encompasses, how we harness our knowledge of nanoscience to create materials, machines, and devices that will fundamentally change the way we live and work. Often, it is defined as the technology to generate structures or devices less than 100 nanometers in size for performing complex and multiple functionalities using the knowledge of nanoscience and is expected to make a significant impact on the society.

The immediate objectives of the nanoscience and nanotechnology are (1) to fully master the synthesis of isolated nanostructures (building blocks) and their assemblies with consistent and desired properties, (2) to explore and establish nanodevice concepts and system architectures, (3) to generate new class of high performance materials like nanocomposites for structural and space applications, (4) to connect fundamental advances in nanoscience to molecular electronics and biology, and (5) to improve known tools like STM and AFM capable of atomic manipulation while discovering better tools for investing nanostructures. Although many visionaries tout it as the panacea for all our woes, it is important to be pragmatic keeping also in mind, both the exaggerated claims of proponents as well as the fears (antinanotechnology) of opponents.[4]

In an attempt to take part in the enthralling nanoworld, and to contribute to its striving challenges, the present thesis will expose recent developments in the field of semiconducting oxide nanostructures. The primary objective of this chapter is to summarize basic aspects of nanostructures of semiconducting oxides with their relevant characterization data, properties and applications with special emphasis on novel nanostructures of SnO_2 and ZnO. An exhaustive description, however, is difficult since innumerable reports do appear regularly about novel nanostructures with promising applications. Nevertheless, major developments of SnO_2 and ZnO nanostructures are mentioned in the text, while few other important contributions are cited in references.

Nanotechnology is such a *hot topic* that in each week at least 10-15 papers are added, which report various fascinating properties exhibited by these materials and hence it is quite natural to miss some of the recent work. Nevertheless, I believe that this brief summary will be helpful to understand the importance of semiconducting oxide nanostructures for developing next generation devices.

1.2. World of Nanostructured Semiconducting Oxides

It is easy to distinguish nanostructures of semiconducting oxides in terms of the dimensionality of a system, which can be envisaged, depending on the behavior of interest. Dimensionality often has a profound effect on the behavior of materials, for example changing the functional form of the dependence of one quantity on another. The classification scheme for defining the dimensionality of a system is a more macroscopic approach, based on the size dependence of some physical behavior of the system.[5] This could involve, for example, transport, usually of electrons, in which case an important length scale is the mean free path, Λ. Thus, a system is said to be of reduced dimensionality if the size, L_i, of a macroscopic sample of material is reduced sufficiently in one or more orthogonal directions, {x, y, or z}, so that in those directions the mean free path is determined by the boundary scattering and not by some other intrinsic mechanisms for electrons. Thus reduced dimensionality occurs in this picture if $\Lambda_{int} > L_i$, so that $\Lambda_{tot} \simeq L_i$ for transport in the ith direction, since the total mean free path is given by a reciprocal sum of intrinsic and extrinsic mechanisms. $\Lambda^{-1}_{tot} = \Lambda^{-1}_{int} + \Lambda^{-1}_{ext}$. Alternatively, the important length scale can be correlated to the size ‘L_o’ of electron wave function, such as the Fermi wavelength, $\lambda_F = 2\pi/k$, the effective Bohr radius, a^*_o, of the exciton or the electron phase coherence length L_φ given as, $L_\varphi = (D\tau_\varphi)^{1/2}$, where D is the diffusion coefficient of electron and τ_φ is the time between elastic collisions. In this case, size quantization sets in if $L_i < L_o$. Hence, a zero dimensional system (strictly speaking quasi-zero dimensional) is one in which all three orthogonal lengths of a sample are less than Λ_{int} and a quantum dot results when the length is such that $L_{x,y,z} < L_o$. Similarly, one-dimensional system is one in which two spatial dimensions are smaller than Λ_{int}; transport is then allowed along the remaining one dimension unencumbered by boundary scattering. For example, a quantum wire is a 1D sample with size quantization in two dimensions ($L_{y,z} < L_o$). Finally a two-dimensional system is that in which only one spatial dimension is less than Λ_{int} and hence transport is allowed in two dimensions limited only by intrinsic scattering mechanisms. A quantum well is a 2D sample with size quantization in the third dimension ($L_z < L_o$).

An alternate simple way of visualizing nanomaterials is by looking at their sizes. They are characterized by at least one dimension in the nanometer range, (1-100 nm) and can be considered to constitute a bridge between single molecules and infinite, bulk systems. Besides individual nanostructures involving clusters, nanoparticles, quantum dots, nanowires and nanotubes, collection of these structures in the form of arrays and superlattices (thin films) are of vital interest in nanotechnology.[6] The structure and properties of nanomaterials differ significantly from those of atoms and molecules as well as those of bulk materials. More specifically, synthesis, structure, energetics, response, dynamics and variety of other properties are related to the applications of the emerging area of nanotechnology. Chemistry plays a vital role in the synthesis and characterization of nanobuilding units while assembling these units into arrays involves physics, taking significant contributions from various branches of engineering. A better insight and synergy in the world of nanoscience and nanotechnology is indispensable for progressing with these nanobuilding blocks.

Nanotechnology in the broadest sense has immediate implications, since one can design a whole range of machines from nanoscale objects, but not necessarily by breaking up matter into individual atoms. Rather, it may be carried out using bits of crystals. The scientific rewards for building nanomachines atom-by-atom, should be greater than the shaping from top down approach, as researchers are likely to achieve an ultimate level of control in assembling matter one at a time.

1.3. Salient Features of Functional Nanostructured Oxides

Semiconducting oxides are the fundamentals of smart devices as both the structure and morphology of these materials can be controlled precisely and accordingly, are referred as functional oxides. They have two structural characteristics: cations with mixed valence states, and anions with deficiencies. By varying either one or both of these characteristics, the electrical, optical, magnetic, and chemical properties can be tuned, giving the possibility of fabricating smart devices. The structures of functional oxides are very diverse and varied, and there are endless new phenomena and applications. Such unique characteristics make oxides one of the most diverse classes of materials, with properties covering almost all aspects of materials science and physics in areas such as semiconductors, superconductivity, ferroelectricity, and magnetism. However, prior to looking for various applications it is worthwhile to consider the general features exhibited by some of these novel functional oxides.

1.4. Why and How Properties Change in Reduced Dimensions?

Before answering this particularly important question lets look at the bulk semiconductors:

1.4.1. Bulk Semiconductors. Structurally an ideal semiconductor, (free of defects), consists of a three-dimensional network of ordered atoms. The translational periodicity of the crystal imposes a special form on the electronic wave functions. An electron in the periodic potential field of a crystal can be described using a Bloch type wave function (equation 1), where *u(r)* represents a Bloch function modulating the plane wave $\phi(kr)$ of wave vector k.[7]

$$\psi(r) = \phi(kr)\, u(r) \qquad -(1)$$

$$u(r + na) = u(r) \text{ where, a is periodicity and n is an integer} \qquad -(2)$$

In a bulk semiconductor the large number of atoms leads to the generation of sets of molecular orbitals with very similar energies, which effectively form a continuum. At 0 K the lower energy levels, or valence band, are filled with electrons, while the conduction band consisting of the higher energy levels is unoccupied. These two bands are separated by an energy gap (E_g), the magnitude of which is a characteristic property of the bulk macrocrystalline material (at a specific temperature). Thermodynamically, the forbidden band gap E_g of a semiconductor is the standard chemical potential (O) for electron-hole pairs created or anhiliated in the reaction[8]

$$O = e + h,\ \Delta E_{cv} \qquad -(3)$$

where, e and h denote a free electron and a free hole belonging to the thermal distribution at the VB edge and the CB edge, respectively.

As a chemical potential, ΔE_{cv} is equal both to the increase in internal energy upon increasing the number of such pairs n_p by one, at constant entropy and volume, and to the increase in Gibbs free energy upon increasing n_p by one, at constant temperature and pressure.[9-10]

$$E_g = (\partial U/\partial n_p)_{S,V} = (\partial G/\partial n_p)_{T,P} \qquad -(4)$$

where U, G, S, V, T, and P denote the total internal energy, Gibbs free energy, entropy, volume, temperature and pressure of the sample, respectively. Materials normally considered as semiconductors typically exhibit band gaps in the range 0.3-3.8 eV.

At temperatures above 0 K, electrons in the VB may receive enough thermal energy to be excited across the band gap into the CB. An excited electron in the CB together with the resulting hole in the VB forms an "electron-hole pair"(exciton). The conductivity (σ) of the semiconductor is governed by the number of electron-hole pairs, the charge carrier concentration (*n*, normally expressed in terms of the number of particles per cubic centimeter), and their mobility (μ). Thus, conductivity can be expressed as the sum of the electrical conductivities of electrons and holes, equation 5 (*q* is the charge of the carrier). In conventional semiconductors electrons and holes are the charge carriers. They exist in small numbers (10^{12} per cm^3 of an intrinsic semiconductor) as compared to that in conductors. However, the carrier mobilities in semiconductors are substantially larger than that in many conductors.

$$\sigma = qn_e\mu_e + qn_h\mu_h \qquad -(5)$$

where, μ_e and μ_h are the mobility of electron and hole, respectively. The charge carriers in a semiconductor can form a bound state when they approach each other in space. This bound electron-hole pair, known as a Wannier exciton (larger and weakly bound compared to smaller and tightly bound Frankel exciton), is delocalized within the crystal lattice, which experiences a screened coulombic interaction. The Bohr radius of the bulk exciton is given by equation (6) ($\in$ represents the bulk optical dielectric coefficient, *e* the elementary charge, and m_e^* and m_h^* the effective masses of the electron and the hole, respectively).

$$a_B = (\hbar^2 \in / e^2)\,[1/m_e^* + 1/m_h^*] \qquad \text{-(6)}$$

This equation forms the basis of explaining many profound effects due to size confinement in semiconducting materials.

1.4.2. Semiconductors in reduced dimensions

Now, in the reduced dimensions, the main reason for the evolution of novel properties could be understood by considering the electronic energy levels. In the reduced dimensions the electron energy levels cannot exist in any form. A quantum dot is by defination a system where the motion of electron is confined in all three spatial dimentions. Consequently, in a quantum dot crystal, the band gap is size dependent and can be altered to produce a range of energies between the VB and CB (also known as band gap engineering). Quantum mechanics dictates that the band gap of a structures in reduced dimensions will always be larger in magnitude. More specifically, confining electrons to small structures causes the continuous bulk bands to split up into discrete levels, for example quantum well states in a slab. Unlike quantum wells and quantum wires, quantum dots have only a finite number of atoms. The overall DOS in different system is depicted in Figure 1.1.

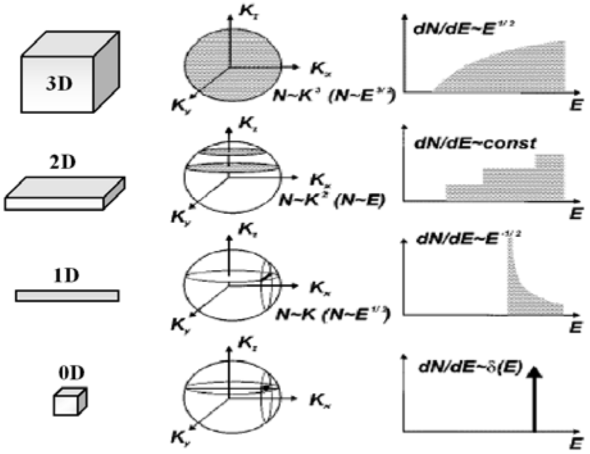

Figure 1. 1. DOS for charge carriers in structures with different dimensionalities calculated on the assumption that the carrier energy E in the band is a quadratic function of wave vector k[12]. The DOS of an ideal quantum dot is discrete, like in an atom.

Two fundamental factors, both related to the size of the individual nanostructures, distinguish their behavior from the corresponding bulk material[13]. The first is the high dispersity (large surface to volume ratio) associated with the particles, with both the physical and chemical properties of the semiconductor being particularly sensitive to the surface structure. The second factor is the actual size of the particle, which can determine the electronic and physical properties of the material. The absorption and scattering of incident light in larger colloidal particles is described classically by Mie's theory. However the optical spectra of nanocrystalline semiconductor[14, 15] that show blue shifts in their absorption edge with decrease in particle size cannot be explained by classical theory[16-17]. Such size dependent optical properties are examples of the size quantization effect which occurs[12] when the size of the nanoparticle is smaller than the bulk-exciton Bohr radius, a_B (equation 6), of the semiconductor. Equation 7 defines, for a spherical crystallite of radius R, the region of intermediate character between that of a "*molecule*" and that of the bulk material (l is the lattice spacing)

$$l << R \leq a_B \qquad \text{-(7)}$$

Charge carriers in semiconductor nanocrystallites are confined within three dimensions by the crystallite. In the case of ideal quantum confinement (Q-dot) the wave function in equation (1) has to satisfy the boundary conditions of

$$\psi(r \geq R) = 0 \qquad \text{-(8)}$$

For nanoparticles, if the electron and hole are closer together than in the macrocrystalline material, the Coulombic interaction between them cannot be neglected as they have much higher kinetic energy than in the macrocrystalline material. On the basis of the effective mass approximation, Brus showed [14, 18, 19] for Cd chalcogenide (especially sulphides and selenides) nanocrystallites that, the size dependence on the energy of the first electronic transition of the exciton (or the band gap shift with respect to the typical bulk value) could be approximately calculated using

$$\Delta E \cong (\hbar^2\pi^2/2R^2)\,[1/m_e^* + 1/m_h^*] - 1.8\, e^2/\epsilon R \qquad \text{-(9)}$$

where m_e^* is the mass of an electron, m_h^* is the mass of the hole, e is the charge on an electron and $\in$ is the appropriate dielectric constant. Equation (9) is an analytical approximation for the first electronic transition of an exciton, which can be described by a hydrogenic Hamiltonian,

$$\hat{H} = (-\hbar^2/2m_e^*)\ \nabla_e^2 - (\hbar^2/2m_h^*)\ \nabla_h^2 - e^2/\in|r_e - r_h| \qquad -(10)$$

In equation (9) the Coulomb term shifts the first excited electronic state to lower energy, R^{-1}, while the quantum localization terms shift the state to higher energy, R^{-2}. Consequently, the first excitonic transition (or band gap) increases in energy with decreasing particle diameter. This prediction has been confirmed experimentally for a wide range of semiconductor nanocrystallites, (Figure 1.2) with a blue shift in the onset of the absorption of light being observed with decreasing particle diameter[20-22]. Moreover, the VB and CB in nanocrystalline materials consist of discrete sets of electronic levels and can be viewed as a state of matter between that of molecular and the bulk material.

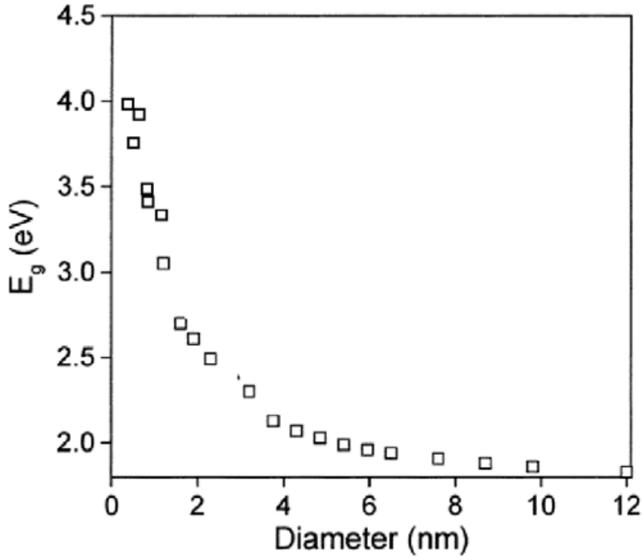

Figure 1. 2. Size dependence of the band gap for CdSe from the molecular regime to the bulk[15].

Another aspect of quantum confinement effect is the effect of crystal structure on the exciton energies (obtained by adding electron-hole Coulomb and correlation energy to the band gap). Friesner et al. have revealed that the exciton energies of zinc-blende and hexagonal clusters are nearly the same for large clusters, but significantly different for small clusters[9]. Exciton energies are also sensitive to the physical shape and the lattice constant of the clusters. The spherical shape gave the best agreement with experiment, indicative that even small clusters are approximately spherical. An anomalous redshift of the exciton energies in small GaP and GaAs clusters have been predicted, which still needs explanation.

Besides this, there are numerous reasons why size reduction can, in principle, affect behavior of materials, including catalytic, thermal, mechanical, optical, electronic, magnetic and electrochemical properties. The increment of catalytic activity with size can be rationalized on the basis of the increase in the surface to volume ratio with decrease in particle size, since the surface atoms are more active due to the presence of unsaturated co-ordinations or dangling bonds. Further, due to higher surface to volume ratio, considerable lattice contraction is observed in nanostructures, which increases with the decrease of particle size. The lattice contraction or lattice strain is generated due to the hydrostatic pressure on the surface induced by the intrinsic surface stress. As most of the atoms are situated on the surface and they have an excess free energy due to the large number of unsaturated bonds, the melting point also decreases with decreasing particle size.

Many semiconducting oxides such as ZnO, SnO_2, In_2O_3, Ga_2O_3, CdO, and PbO_2 have been demonstrated to be highly useful for the fabrication of nanodevices such as field-effect transistors and gas sensors[23-25]. Of these, SnO_2 and ZnO are widely exploited because of their unique conductance properties and process flexibility. The characteristics of SnO_2 containing cations with mixed valencies and the adjustable oxygen deficiency enable tuning of their structure and properties. The wide direct band gap (3.37 eV), large exciton binding energy (60 meV), negative electron affinity, and high mechanical strength makes ZnO one of the promising photonic materials in the ultraviolet region and a good candidate for field emitter arrays of flat panel display devices. Therefore, it is of particular importance to understand the structure of both bulk SnO_2 and ZnO before discussing their properties in reduced dimensions.

1.5. Band Structure and Properties of SnO_2 and ZnO

1.5.1. Band structure of SnO_2

SnO_2 is a wide band-gap semiconducting oxide (E_g = 3.57 eV at 300 K) crystallizing in a tetragonal rutile structure as shown below in Figure 1.2. [26] It belongs to the $P4_2/mnm$ space group and has a ditetragonal bipyramid type of symmetry. The number of macrocrystal habits observed is approximately 10. Its unit cell consists of two Sn and four O atoms. Each Sn atom is surrounded by a distorted octahedron of six O atoms while O atom has three nearest Sn neighbors at the corners of an almost equilateral triangle. Its composition is also represented as $SnO_{2-\delta}$, where $10^{-5} < \delta < 10^{-3}$ indicating deviation in stoichiometry.[27]

The schematic representation of VB and CB of SnO_2 is shown in Figure 1.3. The band located at -17 eV originates essentially from oxygen s states with a very small fraction of Sn s and Sn p admixture. Since it is effectively separated by a 7 eV wide gap from upper VB, these states are only weakly coupled to the higher bands. The main VB is 9 eV and is divided into three parts of different orbital compositions. The region between –9 and –5 eV results from the coupling of Sn s-orbitals to O p-orbitals. The latter have essentially a 'bonding p' character, i.e., they are directed along the nearest neighbor Sn-O axis, which appreciably contribute to the chemical bonding. The bands in the region between -5 and -2 eV consist of oxygen bonding of p orbitals mixed with smaller fraction of Sn p orbitals. The region between -2 eV and the VB edge (0 eV) consist mainly of O 2p lone pair orbitals, directed perpendicular to the Sn-O axis contributing little to the chemical bonding. The band gap has a width of 3.6 eV. The Fermi level (E_f) lies near the middle of the band gap. The bottom of the CB from 3.6 to 8 eV is made up of 90% of the Sn s states and the top of the conduction band has a dominant Sn p character.[28] All states in the CB also contain a small admixture of O 2p bonding states. The wide band gap of tin oxide offers possibilities of n type or p type conduction depending upon impurities. The type of doping leads to the formation of energy levels in the band gap.

In addition to these characteristic bulk energy levels, there are also surface states in which electrons are localized and cannot move into the bulk without exchanging energy with the outer medium. The changed structure at the surface can also give rise to electronic states with corresponding energy values in the forbidden gap. Since the electrical conductivity of SnO_2 is related to the DOS as well as the energy levels in the mid-gap region caused by doping, it is easy to tailor its conductivity by appropriate doping or controlling surface states (functionalization).

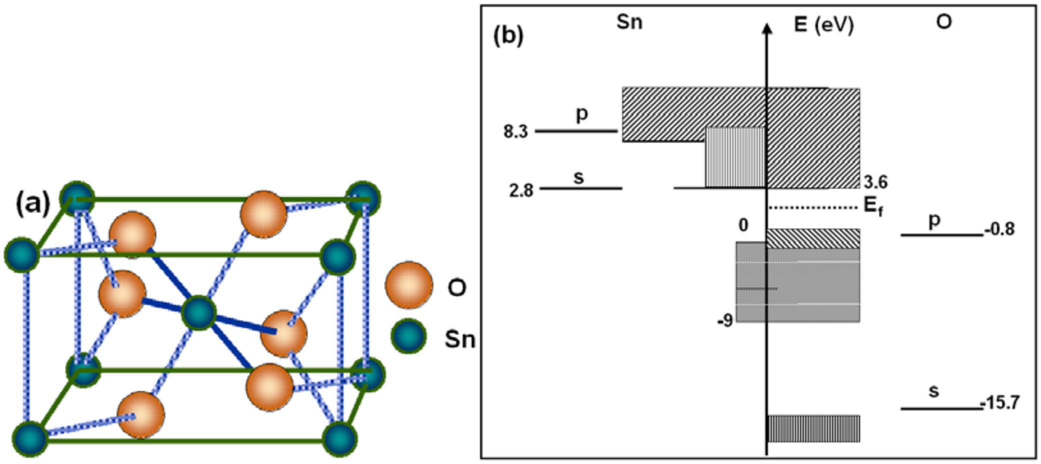

Figure 1.3. (a) Tetragonal structure of SnO_2 (b) Electronic Structure of SnO_2: Schematic draft of valence and conduction bands. The top of the valence band is at 0 eV and the bottom of the conduction band is 3.6 eV[21].

Recently, bulk orthorhombic SnO_2 has also been synthesized at a high pressure of 158 kbar[29]. Although, its lattice parameters have been determined, the atomic positions in the crystal have not been reported. To understand the structural relationship between the orthorhombic and normal rutile SnO_2, a schematic diagram of the crystal structure is presented in Figure 1.4. This Figure is constructed on the basis of the orientational relationships between the two structures. The rectangular parallelopiped BOAC-$B_1D_1A_1C_1$ represents a unit cell for the rutile structured SnO_2 crystal. Here, the large spheres denote O atoms and small spheres Sn atoms. Six unit cells of rutile SnO_2 are drawn in the diagram, as indicated by the dotted lines. The rectangular parallelopiped A_1OBC_1-$E_1O_1G_1F_1$ is a unit cell for the orthorhombic SnO_2. This unit cell of the orthorhombic SnO_2 results from the parallelopiped A_1OBC_1-EDGF in the rutile structured SnO_2 by shearing along the [101] crystal direction, followed by a slight compression along the *c*-axis of orthorhombic SnO_2. The shearing angle is 20.2^0, and the compression in length is 1.6%. The dimensions of the *a*-axis and *b*-axis of the orthorhombic SnO_2 are also adjusted very slightly (0.5% compression in the *a*-axis and 0.3% expansion in the *b*-axis) relative to the corresponding spacing in the rutile SnO_2 structure. Approximate volume decrease is 1.8%.

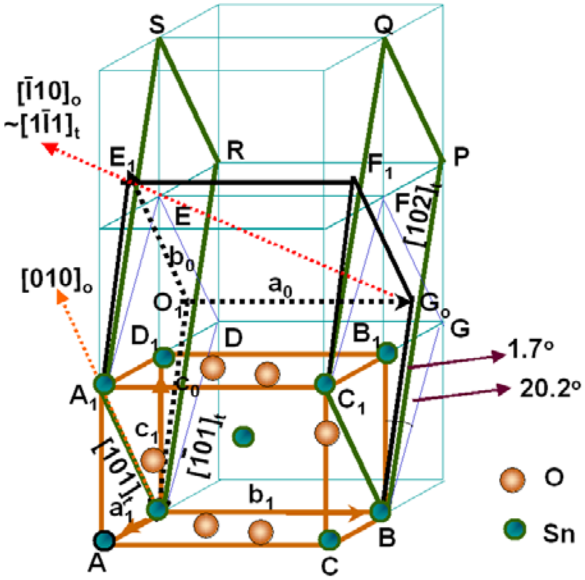

Figure 1.4. Schematic diagram of the crystal structures of rutile SnO_2 and orthorhombic SnO_2, where the a_t, b_t, and c_t represent the base vectors of the rutile structured SnO_2, and the a_o, b_o, and c_o denote the base vectors for the orthorhombic SnO_2[24].

1.5.2. Band structure of ZnO

Zinc oxide, for example, is a unique material that exhibits semiconducting, piezoelectric and pyroelectric properties. It is commonly referred to as photoelectrical information material because of its UV self-luminescence and excited-luminescence, photoelectrical conversion and a particular characteristic of photoelectrical coupling. ZnO wurtzite structure (Figure 1.5) has being defined by Rossler, using the Korringa-Kohn-Rostoker (KKR) method.[27] This method is basically a variation iteration method to solve the Schrodinger equation in a periodic lattice yielding a compact scheme if the potential is spherically symmetric with in the inscribed spheres of the atomic polyhedra and constant in the space between them. The band structure of the lattice is calculated by (1) geometrical structure constants characteristic of the type of lattice and (2) the logarithmic derivatives, at the surface of the inscribed sphere of the s, p, d, … functions corresponding to V(r). The band structure of ZnO thus calculated exhibits a broad free-electron-like lowest CB, relatively wide (1.6 eV) Zn 3d levels lying closely below the upper VB states and p-antibonding CB states 17 eV above the valence band maxima. Experimentally determined maxima in the VB and CB are sketched in the Figure 1.6.

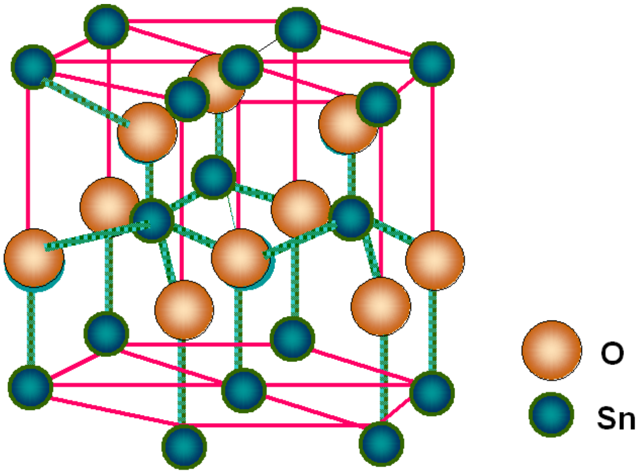

Figure 1.5. Wurtzite Structure of ZnO

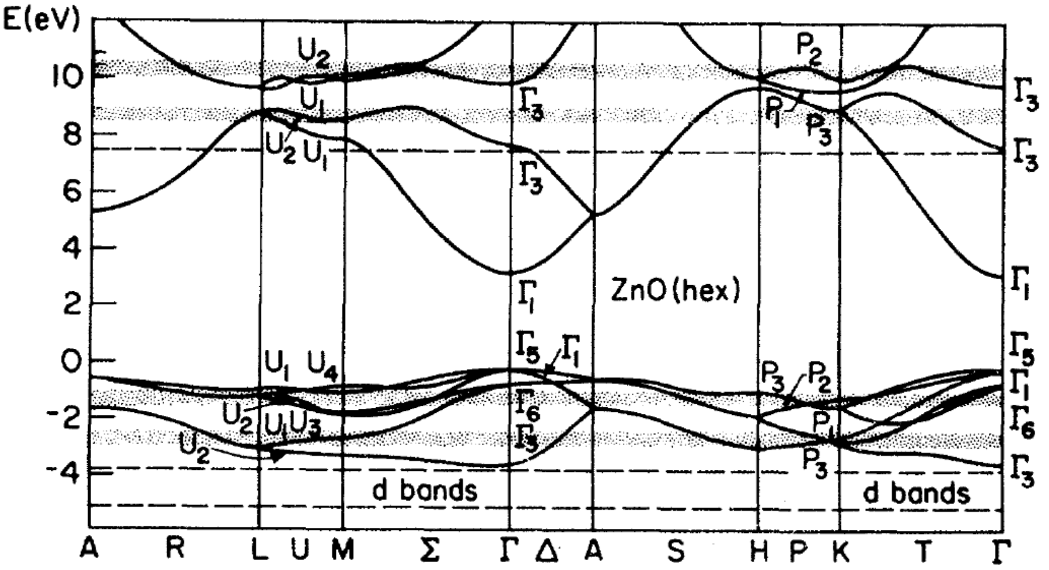

Figure 1.6. KKR band structure for wurtzite ZnO. The shaded sections represents maxima in the VB and CB density of states (DOS) as determined from the photoemission experiment. The vacuum level is indicated by the dashed line at 7.8 eV[27].

Table 1 shows some of the important parameters and properties of bulk SnO_2 and ZnO, for comparison.

Table 1. compares the different properties of bulk ZnO and SnO_2

Sr. No	Properties	ZnO	SnO_2
1.	Molecular mass	81.389	150.710
2.	Specific gravity at 300 K (g/cm^3)	5.642	6.95
3.	Point group	6mm (Wurtzite)	$P4_2$/mnm (tetragonal)
4.	Lattice constants (nm) at 300 K	a = 0.32495 c = 0.52069 c/a = 1.602	a = 0.4737 c = 0.3186 c/a = 0.673
5.	Melting point (^{0}C)	1975	1630
6.	Linear Expansion Coefficient ($^o C^{-1}$)	a_0: $6.5x10^{-6}$ c_0: $3.0x10^{-6}$ Wurtzite structure	
7.	Electron mass	0.28	
8.	Hole mass	1.8	
9.	Bandgap energy at 300 K, E_g (eV)	3.2, direct	3.6, direct
10.	Exciton binding energy (meV)	60	
11.	Specific heat (cal/gm)	0.125	
12.	Thermal conductivity (W/cm/^{o}C)	0.6	0.98
13.	Dielectric constant $\in(o)$	8.75	9.58
14.	Dielectric constant $\in(\infty)$	3.75	4.175

The above band structure discussed for bulk ZnO can have very interesting changes due to size quantization. Recently, Li et al. determined the loss function [Im(–1/ε)] of the ZnO nanowires with selected diameters (~20, ~40, and ~60 nm) by removing the plural scattering from the corresponding electron energy-loss spectra (EELS) using a conventional Fourier-log deconvolution method.[28] They have identified several size-related features: a surface-plasmon oscillation at about 11.5 eV, whose oscillator strength increases as the nanowire diameter decreases, a broadening of the bulk-plasmon peak with decrease in wire diameter, and a splitting of the O 2*s* state together with the red shift of the bulk plasmon in small-diameter ZnO nanowires with circular cross sections. These were attributed to the increased scattering of the oscillating electrons by the wire surface when the surface to volume ratio increases, a decrease in the relaxation time of the oscillating electrons leading to broadening of the bulk-plasmon peak. Similar features have also been observed in nanocombs, nanorings, nanohelixes/nanosprings, nanobows, nanobelts, nanowires and nanocages of ZnO grown under specific growth conditions using a solid-vapor phase thermal sublimation technique.[30-31]

Thus, several experimental results strongly suggest that careful control of the growth conditions can result in nanostructures of SnO_2 and ZnO possessing high electronic quality, which can serve as effective building blocks for optoelectronic nanodevices and other applications. A great potential to serve as a functional building blocks also signifies the tremendous importance necessary in controlling the synthetic parameters to obtain these nanostructures with desired size, shape and morphology.

1.6. Preparation of Semiconducting Oxide Nanostructures

The synthetic approaches for preparing semiconducting oxide nanostructures can be generally classified into several categories: solution-phase growth, template-based methods, non-template-based methods, carbothermal reactions, solid liquid solid processes, solvothermal processes and vapor phase growth (including thermal evaporation, chemical vapor-phase deposition, metal-organic chemical vapor phase deposition, arc discharge and laser ablation).

1.6.1. Solution Phase Growth

This method makes use of anisotropic growth dictated by crystallographic structure of a solid material. Moreover, the structures can be kinetically controlled by supersaturation or by the use of appropriate capping agents. For example, Peng and coworkers demonstrated that the growth of CdSe nanorods is a diffusion controlled process and have shown further that a strong cadmium ligand was required to maintain a relatively high precursor concentration in the solution.[33, 34] Similarly, using an aqueous solution growth, Yang et al. and Zhu et al. have successfully demonstrated the growth of well-aligned ZnO nanorods and nanowires at a relatively low temperature of 65-75 ^{0}C[35-36]. They have demonstrated the growth of large-scale arrays of highly oriented ZnO nanorods on ZnO-film-coated substrates of any kind (glass, silicon, poly(ethylene terephthalate), etc.). Further, the approach was also used to produce nanorod arrays on other substrates coated with indium tin oxide (ITO), Al-doped ZnO, etc. This selectively patterned growth of ZnO nanorod arrays on patterned substrates is crucial to the design of electronic and optoelectronic devices.

1.6.2. Template Based Synthesis

Template directed approach represents a convenient and versatile method for generating nanostructures.[37] In this technique, the template simply serves as a scaffold against which other kinds of materials with similar morphologies are synthesized. In other words, the *in situ* generated material is shaped into a nanostructure with its morphology complementary to that of the template.[38] These templates could be nanoscale channels within mesoporous materials or porous alumina and polycarbonate materials. They can be filled using a (i) solution route or (ii) a sol-gel technique or (iii) an electrochemical route to generate nanowires. These nanowires can be released from the templates by selectively removing the host matrix. Porous anodic aluminium oxides (AAO) containing hexagonally packed 2D arrays of cylindrical pores with a uniform size are prepared using anodization of aluminium foils in acidic medium. These are used as templates for the synthesis of nanowires of various inorganic materials such as Au, Ag, Pt, TiO_2, MnO_2, SnO_2, ZnO, electronically conducting polymers: polypyrrole, polyaniline, and carbon nanotubules. Mesophase structures self-assembled from surfactants themselves can also act as useful and versatile templates for generating nanostructures in relatively larger quantities.

1.6.3. Non-Template Methods

Many solid materials such as polysulphur nitride grow into nanostructures and this habit is determined by the highly anisotropic bonding in the crystallographic structure.[39] Other materials such as selenium, tellurium and molybdenum chalcogenides are also easily obtained as nanowires due to the anisotropic bonding which makes the crystallization along the c-axis, favoring the stronger covalent bonds over the relatively weak van der Waals forces between the chains[40]. These non-template directed methods are readily extended to a range of other solid materials whose crystallographic structures are characterized by chain like building blocks.

1.6.4. Carbothermal Reactions

A variety of oxides, nitrides and elemental nanowires can also be synthesized by carbothermal reactions[41]. For example carbon mixed with an oxide produces oxide or sub oxide vapor species, which react with other reactants (O_2, N_2 or NH_3) to produce the desired nanowires. Yang et al. reported the synthesis of MgO, Al_2O_3, ZnO, and SnO_2 nanowires via a carbothermal reduction process[42].

1.6.5. Solution-Liquid-Solid (SLS) Process

Buhro et al. have developed a low temperature ($\leq 203^0$C) SLS method for the synthesis of highly crystalline nanowires of III-V semiconductors[43]. In a typical procedure, a metal (e.g., In, Sn, Bi) with a low melting point was used as a catalyst, and the desired material was generated through the decomposition of organometallic precursors. The product formed are usually single crystalline with a controlled aspect ratio. Using this technique it is also possible to reduce the operation temperature to a value below the boiling points of commonly used aromatic solvents.

In addition to these solution routes to elemental and III-V semiconductor nanowires, it has been recently reported that, by exploring the selective capping capabilities of mixed surfactants, it is possible to extend the well-established II-IV semiconductor nanocrystal synthesis to the synthesis of semiconductor nanorods, a unique version of nanowires with relatively shorter aspect ratio[44].

1.6.6. Solvothermal Synthesis

Solvothermal method has been extensively examined as a possible solution route to prepare semiconductor nanowires and nanorods[45]. In this process, a solvent is mixed with certain metal precursors and possibly crystal growth regulating and templating agents such as amines. This solution mixture is then placed in an autoclave kept at relatively high temperature and pressure above the critical point to carry out the crystal growth and assembly process. The methodology seems to be quite versatile and has been demonstrated to produce many different crystalline semicondutor nanorods and nanowires[46].

1.6.7. Thermal Evaporation

Among various approaches, thermal evaporation is one of the most commonly employed method for the investigation of oxide nanostructures.[47-48] In principle, the thermal evaporation technique is a simple process in which condensed or powder source material(s) is/are vaporized at an elevated temperature (600-1400^{0}C) and the resultant vapor phase(s) condense(s) under well-defined certain conditions (temperature, pressure, reaction atmosphere, type of substrate, etc.) to form the desired product(s). The process is usually conducted in a tubular furnace.

One of the main features of nanostructures related to their crystallization is the evolution of solid from a vapor, a liquid, or a solid phase involving critical nucleation and growth conditions. As concentration of the building units (atoms, ions or molecules) of a solid becomes sufficiently high, they aggregate into small nuclei or clusters through homogeneous nucleation. These clusters serve as seeds for further growth to form larger structures.

1.6.8. Growth Models

Several strategies have been developed for growth of nanostructures like nanowires, nanobelts, nanorods etc, with different levels of control over the growth parameters. These include: (1) the use of anisotropic crystallographic structure of the substrate to facilitate nanostructure growth (2) the introduction of solid-liquid interface to reduce the symmetry of a seed, (3) employing templates to direct the formation (1D morphologies) of nanowires, (4) control of supersaturation to modify the growth habit of seed; (5) the use of capping agents to kinetically control the growth rates of various facets of a seed and finally (6) self assembly of Q-dots to form extended structures. All the growth models, however, can be classified into different forms as discussed below:

1.6.8.1. Vapor Phase Growth

This is commonly used to produce metallic as well as semiconducting nanowires. Starting with the simple evaporation technique in an appropriate atmosphere to produce elemental or binary nanostructures, this includes vapor-liquid-solid (VLS), vapor-solid

(VS) and other processes as predicted by appropriate phase diagrams as a function of temperature and pressure.

1.6.8.1.1. Vapor-Liquid-Solid Growth

The growth of nanostructures via a gas phase reaction involving a VLS process has been extensively studied. Wagner, during his studies on the growth of large single-crystalline whiskers, proposed in the 1960s, a mechanism for the growth via a gas phase reaction involving the so-called VLS process.[49] According to this mechanism, the anisotropic crystal growth is essentially promoted by the presence of a liquid alloy-solid interface. This mechanism is widely accepted and applied to understand the growth of many nanowires of Si, Ge and others as shown sequentially in Figure 1.7.

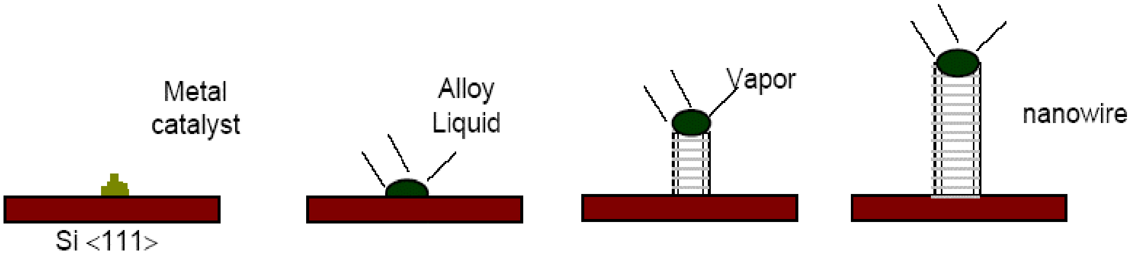

Figure 1.7. Different stages involved during the vapor-liquid-solid (VLS) growth[49].

In particular, when a substrate with a metal source is placed in a tubular furnace, the metal particles act as catalysts for the growth of the semiconductor nanowires. Interestingly, the diameter of the wires is set by the catalyst dimension (typically 1-100 nm) and the nanowire length (typically 1-100 micron) is proportional to the growth time. During growth, the semiconductor material is provided by thermal evaporation of a powder target. The resulting vapor is transported to the substrate by the Ar flow, which also ensures the partial pressure of species, involved in the reaction. The vapor dissolves in the metal particles and forms a eutectic. When the liquid particle becomes supersaturated, the crystalline nanowire starts to grow (tip growth). The liquid surface has a large accommodation coefficient and is therefore a preferred deposition site for incoming vapor. Because new vapor is continuously supplied, the nanowires will keep on growing in order to reach lengths exceeding even 100 μm.

By controlling the nucleation and growth, it is possible to produce semiconductor nanowhiskers (e.g. InAs, GaAs) using organometallic vapor phase epitaxy[50]. By knowing the equilibrium phase diagram one can predict the catalyst materials and the growth condition for VLS approach. One of the advantages of the conventional metal-catalytic VLS growth is that the diameter and growth alignment of the nanowires can be readily controlled by using uniformly distributed metal seeds with well-designed sizes on the substrate. An important disadvantage is the use of flammable or toxic precursor gases such as SiH_4 or $SiCl_4$ and there are also environmental impacts for large-scale manufacturing.

1.6.8.1.2. Oxide Assisted Growth

In contrast to the well-established VLS mechanism, Lee et al. have recently proposed a new nanowire growth route called oxide-assisted nanowire growth (OAG).[51] They report the synthesis of GaAs nanowires by the oxide-assisted laser ablation of a mixture of GaAs and Ga_2O_3. The nanowires have a thin oxide layer covering and a crystalline GaAs core with a [111] growth direction. In this oxide-assisted growth method, oxides, instead of metals play an important role in inducing the nucleation and growth of nanowires (Figure 1.8). The OAG technique not only allows a large-quantity production of nanowires with controllability, but also yields high-purity nanowires, free of metal impurities. The oxide-assisted 1D nanomaterials synthesis is complementary to and coexistent with the conventional-catalyst VLS approach.

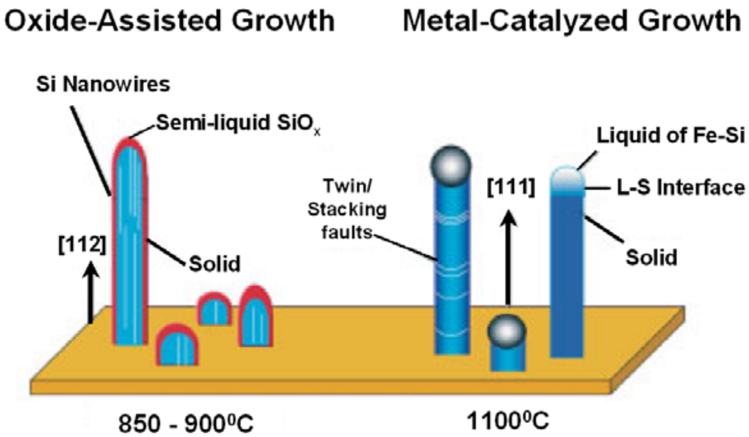

Figure 1.8. Schematic comparison of the laser ablation of SiNWs via a metal catalyst (VLS method) and the oxide assisted growth of SiNWs by thermal evaporation.[51]

The OAG approach can be a generic method capable of bulk production of nanostructures from a host of materials other than Si including Ge nanowires, carbon nanotubes, silicon and SnO_2 nanoribbons, as well as Group III-V and II-VI compound semiconductor nanowires[52]. Interestingly, the OAG and metal catalytic VLS process can be co-existent, a fact that could be exploited for optimization of the nanowire growth by combining the complementary advantages of the two distinct methods.

However, both these processes vary in their growth mechanism, growth conditions, yield of the nanowires, abundant growth direction, diameters and finally in the chemical purity. Understandably, in the metal catalyst growth, the characteristics of the grown nanowires critically depend on the nature and size of metal catalyst used.

1.6.8.1.3. Vapor-Solid (VS) Method

In this process, vapors are first generated by evaporation, chemical reduction or gaseous reaction, which are subsequently transported and condensed onto a substrate. The VS method has been used to prepare oxide, metal whiskers with micrometer diameters. Using the VS method, synthesis of nanowires for oxides of Zn, Sn, In, Cd, Mg and Ga have been attempted.[53, 54] Although, the VS growth process has demonstrated considerable flexibility in fabricating a wide range of nanosystems, it is difficult to control the nucleation i.e., the size control of the products. On the other hand, for growth of nanostructures by the VLS process, the key advantage is to generate nanosized catalyst clusters that define their size and direction of the growth.

1.7. Growth control of semiconducting oxide nanostructures

A significant challenge for the chemical synthesis is how to rationally control the nanostructure assembly so that the size, dimensionality, interface and ultimately the 2D and 3D superstructures can be tailor made to a desired functionality. Many physical and thermodynamic properties are size and shape dependent and hence controlling the growth orientation is important for the applications of nanowires. It is clear from the VLS nanowire growth mechanism that the positions of the nanowires can be controlled by the initial positions of the catalyst clusters or catalyst (seed) thin films. By creating desired patterns of catalyst using lithography, it is possible to grow ZnO nanowires of the same designed pattern since they grow vertically only from the region that is coated with the catalyst and form the designed patterns of ZnO nanowires arrays. The integration of nanowire building blocks into a complex functional network in a predictable and controlled way is a major challenge, which is expected to be accomplished soon.

1.8. Characterization of Nanostructures of Semiconducting Oxides

As briefly outlined in the introduction, nanostructured semiconducting oxides are nowadays generated by a series of different physical and chemical methods. Although such synthetic methods have reached significant maturity in terms of homogeneity in the structural/electronic properties of the particles forming the solid, as well as in the size distribution, still much work is needed to obtain full control over the synthesis variables and their influence in the final semiconducting oxide material prepared especially in large scale. Problems related to oxide stoichiometry or the presence of impurities and amorphous phases coexisting with the crystalline one are often encountered. A glimpse into these problems indicate that structural and electronic properties as well as the primary particle size distribution are strongly dependent on the preparation method at the state of the art; a first goal is to perform a detailed and full characterization of the particular solid yielded by the specific preparation method. To do this in a systematic way, one needs a diverse array of characterization techniques. An important issue is the correct interpretation of the experimental results obtained by characterization tools. To help in reaching this goal, in this section we will describe the most often used techniques and the specific consequences that nanostructure induces in their corresponding physicochemical observables. This part of the chapter is devoted in explaining the basic principles on which different techniques are based and their application to understanding various aspects of formation of nanomaterials. In general, the individual characterization technique should not be invasive, but should be able to provide all quantitative details of the structure or composition. Few of such techniques are discussed below:

1.8.1. X-Ray Diffraction

X-rays are electromagnetic radiations with typical photon energies in the range of 100 eV-100 keV. These energetic X-rays can penetrate deep into the material and provide information about the structural arrangement of atoms and molecules.[55] X-rays are generated when a focused electron beam accelerated across a high voltage field bombards a stationary or rotating solid target. As electrons collide with atoms in the target and slow down, a continuous spectrum of X-rays are emitted, which are termed Bremsstrahlung radiation. The high-energy electrons also eject inner shell electrons in atoms through the ionization process. When a free electron fills the shell, an X-ray photon with energy characteristic of the target material is emitted. Common targets used in X-ray tubes include Cu and Mo, which emit 8 keV and 14 keV X-rays with corresponding wavelengths of 1.54 Å and 0.8 Å, respectively.

X-rays primarily interact with electrons in atoms, and during the coarse of interaction some photons from the incident beam will be deflected away from the direction where they originally travel, much like billiard balls bouncing off one anther. If the wavelength of these scattered X-rays does not change, the process is called elastic scattering (Thompson Scattering: only momentum has been transferred in the scattering process). The scattered X-rays carry information about the electron distribution in materials. However, in the inelastic scattering process (Compton Scattering), energy is transferred to the electrons and the scattered X-rays will have different wavelength than the incident X-rays. Diffracted waves from different atoms can interfere with each other and the resultant intensity distribution is strongly modulated by this interaction. If the atoms are arranged in a periodic fashion, as in crystals, the diffracted waves will consist of sharp interference maxima (peaks) with the same symmetry as in the distribution of atoms. Measuring the diffraction pattern therefore allows one to deduce the distribution of atoms in a material. The peaks in an X-ray diffraction pattern are directly related to the atomic distances. Figure 1.9 shows incident X-ray beam interacting with the atoms in the two different planes.

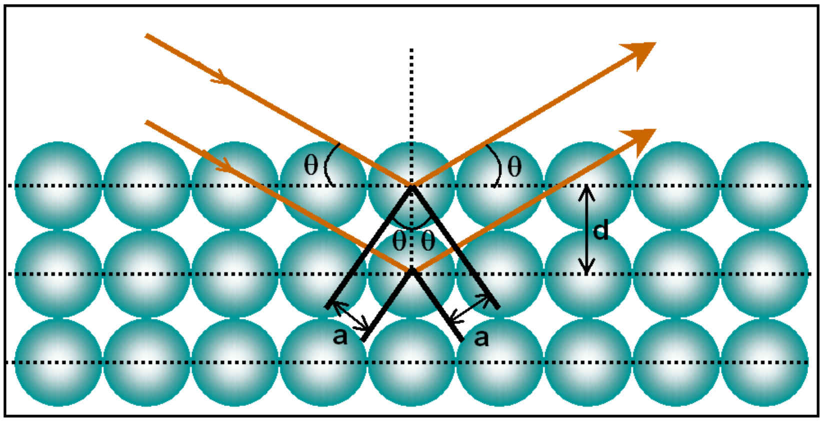

Figure 1.9. X-ray reflections from a crystal. Consider parallel lattice planes spaced d apart. The radiation is incident in the plane of the paper. The path difference for rays reflected from adjacent planes is 2a = 2dsinθ. Constructive interference of the radiation from successive planes occurs when 2dsinθ = nλ, where 2πn is the difference in phase between reflections from successive planes.

For a given set of lattice plane with an inter-plane distance of d, the condition for a diffraction (peak) to occur can be simply written as the Bragg's law:

$$2d \sin\theta = n \lambda \qquad -(11)$$

where, λ is the wavelength of the X-ray, θ the scattering angle, and n an integer representing the order of the diffraction peak.

Conventionally, XRD has several limitations. A key disadvantage of XRD is that it is highly applicable to crystalline materials. Moreover, it is time-consuming and requires a large quantity of sample. Fortunately, synchrotron-based XRD is useful to circumvent these limitations. They offer exceptional resolution, even on very small samples containing only a few grains of a particular mineral.

The structure, crystallinity and the particle size are often measured using XRD.[55] For example, XRD studies of SnO_2 nanostructures have shown that it mainly occurs in a tetragonal/rutile phase (space group: $P4_2/mnm$, with crystal constant a = b = 0.4738 nm and c = 0.3187 nm).[56] While, ZnO occurs mainly into a hexagonal wurtzite structure (space group: P63mc with crystal constant a = b = 0.3249 nm and c = 0.5206 nm).[57] Further, the technique can be effectively used in determining the strain and stress induced in the nanostructures, in addition to the calculation of the grain size using the Scherrer equation.[55]

1.8.2. Transmission Electron Microscopy

In transmission electron microscopy (TEM), a thin specimen is illuminated with electrons in which the electron intensity is uniform over the illuminated area.[58] As electrons travel through the specimen, they are either scattered by a variety of processes or they may remain unaffected by the specimen. The net result is that a non-uniform distribution of electrons emerges from the exit surface of the specimen that contains all the structural and chemical information about the specimen. Electron microscope is constructed to display this non-uniform distribution of electrons in two different ways.

Angular distribution of scattering can be viewed in the form of scattering patterns, usually called diffraction patterns, commonly referred to as selected area electron diffraction (SAED). Spatial distribution of scattering can be observed as contrast in images of the specimen. The advantage of this arrangement is the possibility of directly viewing the area from which the diffraction pattern arises. Further, Kikuchi patterns obtained by inelastic scattering of electrons is also very useful for understanding the crystallographic orientation as these are rigidly attached to a crystal plane and therefore move in the diffraction pattern when the crystal is tilted.

Many materials require extensive sample preparation and thinning procedures to produce a sample thin enough to be electron transparent, and changes in the structure may be caused during this process. Also the field of view is relatively small, raising the possibility that the region analysed may not be characteristic of the whole sample. Also there is potential that the sample may be damaged by the electron beam, particularly in the case of biological materials. Despite these limitations, TEM has been the technique of choice due to atomic-level resolution leading direct visual information of size, shape, dispersion and structure. Further, when coupled with SAED, the technique can provide important information on the crystallographic directions in the structures, helpful to understand the growth kinetics.[59]

1.8.3. Scanning Electron Microscopy

In a typical scanning electron microscope (SEM), electrons are thermionically emitted from a tungsten or lanthanum hexaboride (LaB_6) cathode, which fly towards an anode; alternatively electrons can be emitted via field emission (FE).[60] Tungsten is used because it has the highest melting point and lowest vapour pressure of all metals, thereby allowing it to be heated for electron emission. The electron beam, which typically has an energy ranging from a few hundred eV to 50 keV, is focused by one or two condenser lenses into a beam with a very fine focal spot sized 1 nm to 5 nm. The beam passes through pairs of scanning coils in the objective lens, which deflect the beam in a raster fashion over a rectangular area of the sample surface. As the primary electrons strike the surface they are inelastically scattered by atoms in the sample. Through these scattering events, the primary electron beam effectively spreads and fills a teardrop-shaped volume, known as the interaction volume, extending about less than 100 nm to 5 µm depths into the surface. Interactions in this region lead to the subsequent emission of electrons which are then detected to produce an image. The most common imaging mode monitors low energy (<50 eV) secondary electrons. Due to their low energy, these electrons originate within a few nanometer from the surface. The electrons are detected by a scintillator-photomultiplier device and the resulting signal is rendered into a two-dimensional intensity distribution that can be viewed and saved as a Digital image. X-rays, which are also produced by the interaction of electrons with the sample, may also be detected in an SEM equipped for energy dispersive X-ray spectroscopy (EDX) or wavelength dispersive X-ray spectroscopy (EDS). EDX or EDS is a method used to determine the energy spectrum of X-ray radiation using a semiconductor silicon drift or a silicon crystal doped with lithium (Si-Li) detector. The semiconductor is polarised with a high voltage; when an X-ray photon hits the detector, it creates electron-hole pairs that drift due to the high voltage. The electric charge is collected in a way similar to charging of a condenser; the increment of voltage of the condenser is proportional to the energy of the photon, it is thus possible to determine the energy spectrum. The condenser voltage is reset regularly to avoid saturation. However, SEM coupled with EDX suffers from various drawbacks namely, elements below C in the periodic table cannot be detected also it cannot be used precisely for element below Na. Moreover, X-ray detection limit is ~ 0.1% depending on the element and samples must be compatible with vacuum (no fluids).

1.8.4. X-Ray Photoelectron Spectroscopy

X-ray photoelectron spectroscopy (XPS) is based on the well-known photoelectric effect (a single photon in/electron out process) first explained by Einstein in 1905.[61] Photoelectron spectroscopy uses monochromatic sources of radiation (i.e. photons of fixed energy given by the relation, $E = h\nu$).[62] In XPS the photon is absorbed by an atom in a molecule or solid, leading to ionization and the emission of a core (inner shell) electron. The kinetic energy distribution of the emitted photoelectrons (i.e. the number of emitted photoelectrons as a function of their kinetic energy) can be measured using any appropriate electron energy analyzer and a photoelectron spectrum can thus be recorded. The one way to look at the overall process of photoionization is as follows:

$$A + h\nu = A^{+} + e- \qquad -(12)$$

Conservation of energy then requires:

$$E(A) + h\nu = E(A^{+}) + E(e-) \qquad -(13)$$

Since the energy of electron is present solely as kinetic energy (KE) this can be rearranged to give the following expression for the KE of the photoelectron:

$$KE = h\nu - (E(A^{+}) - E(A)) \qquad -(14)$$

The final term in brackets, representing the difference in energy between the ionized and neutral atoms, is generally called the *binding energy* (BE) of the electron - this then leads to the following commonly quoted equation:

$$KE = h\nu - BE \qquad -(15)$$

The binding energies (BE) of energy levels in solids are conventionally measured with respect to the Fermi-level of the solid, rather than the vacuum level. This involves a small correction to the equation given above in order to account for the *work function* (ϕ) of the solid,

$$KE = h\nu - BE - \phi \qquad \text{-(16)}$$

Employing photons with fixed energy $h\nu$, it is obvious that if kinetic energy KE and work function ϕ of the sample are measured, it is possible to measure binding energy of electron in a solid. Binding energies being characteristic of atoms, different elements present in the sample under investigation can be easily identified. Electrons traveling through a material have a relatively high probability of experiencing inelastic collisions with locally bound electrons as a result of which, they suffer energy loss contributing to the background of the spectrum rather than a specific peak. Due to this inelastic scattering process, the flux of photoelectrons emerging from the sample is much attenuated. Consequently, in some cases the satellite peaks emerge on both the high and low BE side of the main peaks. These peaks give valuable information about the defect complex or the different charge states present, if any. Moreover, the higher binding energy satellite peak could also arise from an inelastic electron scattering process.

Sometimes a closely placed doublet instead of single peak is observed and could be attributed to the spin-orbit coupling effects in the final state. Spin-orbit coupling is generally treated using one of two models which correspond to the two limiting ways in which the coupling can occur - these being the LS (or Russell-Saunders) coupling approximation and the j-j coupling approximation. This spin-orbit splitting of course is not evident with s-levels ($l = 0$), but is seen with p, d and f core-levels which all show characteristic spin-orbit doublets.

There are many limitations associated with this technique since this detects the kinetic energy of electrons. First, since electrons do not pass through air, these experiments must be run in vacuum. This also means that samples must be dried and this drying may impact few subtle systems resulting in many chemical transformations. Also, since this technique is highly surface sensitive, it is less useful to analyze bulk properties; in fact, it may make it impossible to identify anything but interferences on a dirty surface. Consequently, XPS is often done with clean, freshly cleaved single crystals.

Significant qualitative and quantitative information about the chemical state of elements present in nanostructures can be obtained from XPS analysis. When performed intermittently by quenching the process or *in situ* is useful for understanding the growth kinetics. For SnO_2, two prominent peaks with a symmetric Voigt profile (the convolution of a Lorentzian profile and a Doppler profile) corresponding to the binding energies of $Sn3d_{5/2}$ (486.5 eV) and $Sn3d_{3/2}$ (495.1 eV), respectively[63]. However, the presence of Sn^{2+} cannot be ruled out in SnO_2 because the energy of $Sn3d_{5/2}$ for SnO is very close to that for SnO_2 (0.7 eV). The peak-to-peak separation of Sn 3d peaks for commercial SnO_2 is 8.48 eV. In case of ZnO, two peaks at B.E. of 1021.7 and 1044.8 eV attributed to the signal from Zn $2p_{3/2}$ and Zn $2p_{1/2}$ signals are observed, respectively[64].

1.8.5. Raman Spectroscopy

When light encounters molecules in air, the predominant mode of scattering is elastic scattering, called Rayleigh scattering[65]. This scattering is responsible for the blue color of the sky; it increases with the fourth power of the frequency and is consequently more effective at short wavelengths. It is also possible for the incident photons to interact with the molecules in such a way that energy is either gained or lost so that the scattered photons are shifted in frequency. Such inelastic scattering is called Raman scattering.

Like Rayleigh scattering, the Raman scattering depends upon the polarizability of the molecules. For polarizable molecules, the incident photon energy can excite vibrational modes of the molecules, yielding scattered photons, which are diminished in energy by the amount of the vibrational transition energies. A spectral analysis of the scattered light under these circumstances will reveal spectral satellite lines below the Rayleigh scattering peak at the incident frequency. Such lines are called "Stokes lines". If there is significant excitation of vibrational excited states of the scattering molecules, then it is also possible to observe scattering at frequencies above the incident frequency. These lines, generally weaker, are called anti-Stokes lines. (Figure 1.10)

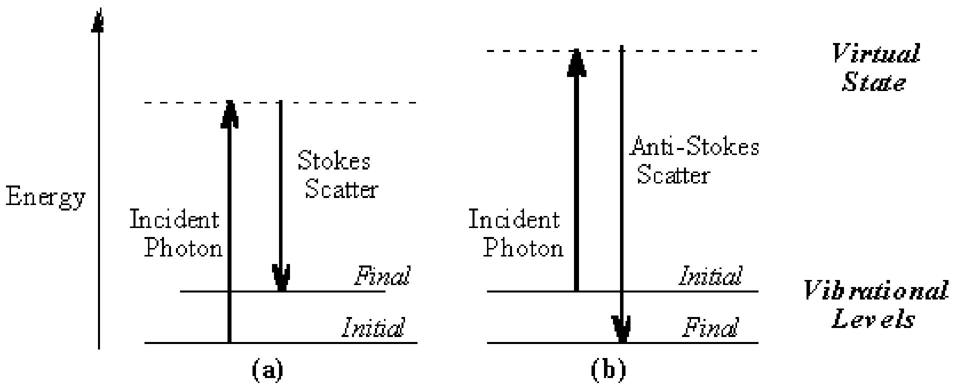

Figure 1.10. Energy level diagram for Raman scattering; (a) Stokes Raman scattering (b) anti-Stokes Raman scattering[65].

Raman scattering can also involve rotational transitions of the molecules from which the scattering occurs. Thornton and Rex picture a photon of energy slightly more than the energy separation of two levels being scattered, with the excess energy released in the form of a photon of lower energy. Since this is a two-photon process, the selection rule is ΔJ = 0, ±2 for rotational Raman transitions, where ΔJ = 0 corresponds to Rayleigh scattering, ΔJ = +2 and -2 corresponds to a Stokes transition and anti-Stokes transition, respectively. The sketch below (Figure 1.11) is an idealized depiction of a Raman line produced by interaction of a photon with a diatomic molecule for which the rotational energy levels depends upon moment of inertia. The upper electronic state of such a molecule can have different levels of rotational and vibrational energy. In this case the upper state is shown as being in rotational state J, scattering associated with an incoming photon at energy matching the J+2 state.

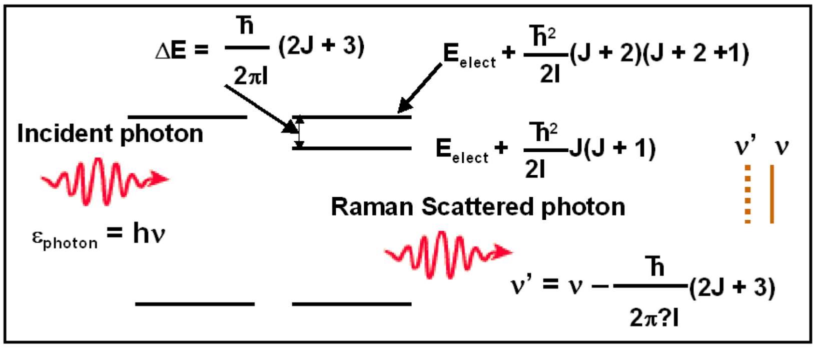

Figure 1.11. An idealized depiction of a Raman line produced by interaction of a photon with a diatomic molecule for which the rotational energy levels depend upon one moment of inertia.

Since the Raman effect depends upon the polarizability of the molecule, it can be observed for molecules, which have no net dipole moment and therefore produce no pure rotational spectrum. This process can yield information about the moment of inertia and hence the structure of the molecule.

In Raman scattering, an intense monochromatic light source (laser) can give scattered light, which includes one or more "sidebands" that are offset by rotational and/or vibrational energy differences. This is potentially very useful for remote sensing, since the sideband frequencies contain information about the scattering medium, which could be useful for identification. The Raman bands are the characteristics of the structure and gives valuable information about the structure, size and crystal surface area[66].

The main limitations of Raman spectroscopy are its inherently low intensity compared to that of the elastically scattered laser intensity and interference from fluorescence due to the electronic excitation of the molecule by the laser.

1.8.6. Thermogravimetry/Differential Thermal Analysis (TG-DTA)

Thermogravimetric analysis (TGA) involves monitoring the weight of the sample while varying temperature at a controlled rate. Differential thermal analysis (DTA) involves comparing the precise temperature difference between a sample and an inert reference material, while heating both.[67] Thermogravimetric curves (thermograms) provide information regarding the efficiencies of activators and stabilizers through mass changes and hence the thermal stability of many materials like moisture, solvent, additives, polymer, filler etc., can be studied along with the kinetics. On the other hand, varied information can be gleaned from the DTA namely glass transitions/melting temperatures, phase formations/transitions and reaction kinetics. Interestingly, thermal events under both reactive (e.g. air) and inert conditions (e.g. nitrogen, helium and argon) can be investigated. Thus, valuable information about the growth mechanism of the nanomaterials could be obtained from the TG-DTA when coupled with evolved gas analysis - mass spectrometry (EGA-MS) and other imaging tools like SEM and TEM. However, the accuracy, precision and overall quality of thermal analysis data depends critically on the ability of the operator to optimize instrument performance and the selection of appropriate conditions for the experiment.

1.8.7. Conductivity Measurements

There are various methods for electrical (I-V) characterization, which are applicable to single crystalline as well as polycrystalline materials. However, following points needs to be understood prior to the measurement: Grain boundaries behave differently from individual crystallites and it is not possible to tell *a priori* whether the apparent resistivity will be greater or less than that of a single crystal of the same material. Further, it is important to note that the surface penetration can affect apparent resistivity. An inversion layer may form which the probes may or may not punch through. Sometimes the sample may get damaged in the process and such damage-induced defects give rise to additional charge carriers. Thus, it is expected that resistivity drops significantly for highly resistive materials. Resistivity measurements are geometry dependent and sensitive to boundary conditions and hence correction factor needs to be considered[68].

Two basic methods have been adopted for I-V characterization namely, 2-point probe and 4-point probe methods (Figure 1.12), respectively. Schematic representation of 2-point probe is shown in Figure 1.12(a). Resistivity, thus obtained also includes contact resistance, which is appreciable in case of semiconductors. Using 2-point probe, if the specimen cross-section is uniform, it can eliminate the effect of contact resistance. However, one needs to keep current low enough to prevent heating of the sample. Also, the voltmeter must have a high input impedances (above 10^{13} ohms) and measurements must be made far enough away from the contacts so that any minority carriers injected will have already recombined.

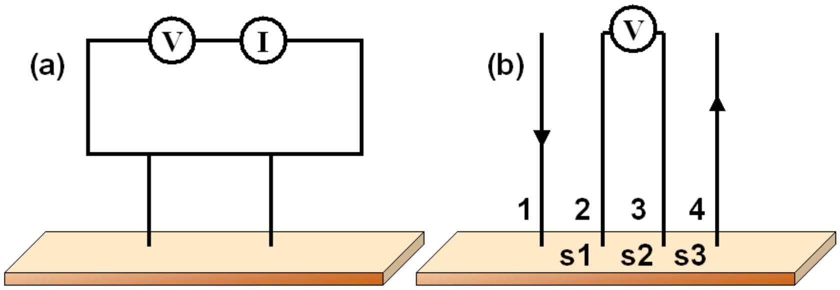

Figure 1.12. Schematic representation of (a) 2-point probe method and (b) 4-point probe method.

The 4-point probe is preferable over a 2-point probe because the contact and the spreading resistance associated with the 2-point probe cannot be measured. This means that the true sheet resistance cannot be accurately separated from the measured resistance. The 4-point probe consists of two current carrying probes (1 and 4), and two voltage-measuring probes (2 and 3). Since very little contact and spreading resistance is associated with the voltage probes, one can obtain a fairly accurate calculation of the sheet resistance, which is then used to calculate the resistivity. The resistivity (p) of a semi-infinite wafer with equal probe spacing (s) is given by:

$$p=2*\pi*s*V/I\ ,\ \text{where } s = s_1 = s_2 = s_3 \qquad -(17)$$

Since wafers are not semi-infinite in extent, a combination of correction factors must be multiplied by the right hand side of this equation.

It is known that the ‘as-synthesized’ and undoped ZnO NWs are n-type semiconductor due to a high density of oxygen vacancies.[69] Typical *I-V* curve of a single undoped NW as measured by Wang et al. is given in Figure 1.13. The current changes linearly from about -3 to 3 nA as *V* is varied from -1 to 1 V with a resistivity (ρ) of 390 Ωcm. High electrical resistivity in a single undoped NW indicates its high quality of crystalline structure with low oxygen deficiencies. However, after doping with Ni the conductivity increases by 30 times to give a final value of ρ = 12 Ωcm.

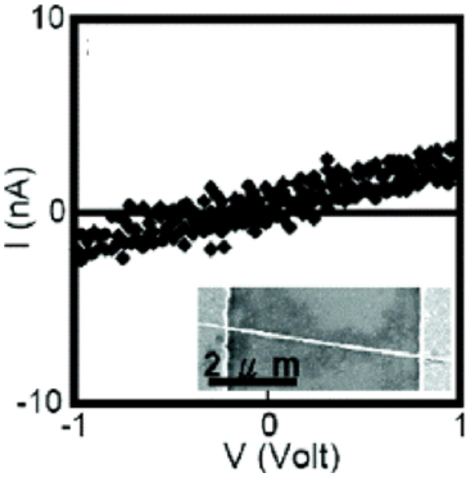

Figure 1.13. *I-V* characteristics of undoped ZnO NW with an inset showing the device to perform electrical measurements fabricated by electron beam lithography with lift-off technique.[69]

1.8.8. Other Characterization Techniques

Apart from these techniques, several other special characterization techniques, such as, electron and neutron diffraction, photoluminescence (PL), optical absorption, electron energy loss spectroscopy (EELS), surface plasmon spectroscopy (SPS), scanning tunneling microscopy (STM), and atomic force microscopy (AFM) have been applied for investigations of nanostructures[70-72]. The complimentary aspect of these techniques suggests clearly that one or two techniques cannot provide reliable information. However a judicious application of a variety of techniques can provide all molecular level information like precise composition, consistence and purity. It will now be interesting to take into note the various fascinating properties exhibited by nanostructures of semiconducting oxides.

1.9. Properties of Nanostructured Semiconducting Oxides

Compared with bulk materials, low dimensional nanoscale materials, with their large surface area and possible quantum confinement effect, exhibit distinct electrical, optical, chemical and thermal properties, which are explained in detail in the following subsections:

1.9.1. Thermal Properties

The thermal stability of low dimensional nanostructures is of critical importance for their implementation as building blocks in nanoscale electronic and photonic devices. It is well documented that the melting point of a solid material will be greatly reduced when it is processed as nanostructures. Yang and co-workers observed two distinct features in the melting recrystallization cycle of Ge nanowires.[73] One was the significant lowering of the melting point, which was found to be inversely proportional to the diameter of the nanowire. The other was the large hysteresis loop associated with the melting-recrystallization cycle. Further, using the advantage of the relatively low melting points, they have also demonstrated the capability to manipulate individual nanowires using techniques like cutting, interconnecting, and welding. Also, Wang, Lee and coworkers have demonstrated that the design and the controlled synthesis of nanostructures could be achieved using the knowledge of their thermal stability.[74] As driven by the Rayleigh instability, nanowires may spontaneously undergo a spheroidization process to break up into shorter segments at room temperature to reduce the relatively high free energy associated with them, when their diameters are sufficiently thin or the bonding between atoms are too weak.

1.9.2. Mechanical Properties

Understanding the mechanical properties of nanostructures is essential for the atomic-scale manipulation and modification of these materials, which have been known to behave differently when the dimensions are reduced from micro- to nanoscale.[75] For example, the hardness and yield stress of a polycrystalline material typically increases with decreasing the grain size on the micrometer scale, a phenomenon known as the Hall-Petch effect.[75] It can be explained in terms of the pilling up of dislocations at the grain boundaries when the crystal planes in individual grains are sheared. As the grains are downsized, the area of their boundaries increases and thereby makes the material tougher by blocking dislocations more effectively. On the nanometer scale, however, Schatcz and Co-workers discovered an opposite behavior in their computational simulations, samples of nanocrystalline copper and palladium become softer with decreasing the grain size.[76] This abnormal behavior was believed to be mainly arising from sliding motions at grain boundaries. As a result the strength of a polycrystalline material first increases and then decreases with decreasing grain size, and there exists a characteristic length for each solid material to achieve the toughest strength. Nanowires also provide the direct evidence of the mechanism responsible for the plastic deformation when it undergoes mechanical stretching or compression. Further, it was found that the bond strength of the nanowire is approximately twice of a bulk metallic bond. Computational studies indicate that the total effective stiffness of the nanowires had a strong dependence on the local arrangement of atoms.[77]

1.9.3. Electrical Transport

The answer to the question ‘How electrons respond to an applied electric field?’ in different nanostructured systems is of crucial importance, before applying these materials for any practical application. As explained earlier, size can have dramatic effects on the electronic properties of samples in nanoscale range. Electron confined within a small radius spherical potential well will occupy discrete energy levels given by the particle in a box solution.[78] Single electron tunneling is one of the most remarkable effects exhibited by quantum dots. The capacitance of a dot can be changed drastically simply by the addition of a single extra electron as a result of one electron tunneling.

In case of 1D nanomaterials (nanowires) two limiting types of behavior can be envisaged. The first is the diffusive-transport regime for which Λ<< w, L with the (elastic) electron mean-free path (resulting from elastic scattering from impurities) given by $\Lambda = v_F\tau$, where v_F is the Fermi velocity and τ is the scattering relaxation time, and w and L are the width and the length of the wire, respectively. The opposite limiting behavior is the ballistic-transport regime, in which Λ >> w, L, in this case elastic boundary scattering is dominant. Although it might be thought that ballistic transport would be resistance free, in fact a non-zero electrical resistance can result from back scattering of electrons at the connection between the nanowire and the electrical reservoirs connected to it. An intermediate regime can also be distinguished, the quasi-ballistic regime, in which w< Λ >L and impurity scattering and boundary scattering are of comparable importance. The study of electron transport in low-dimensional semiconductor is one of the exciting and active fields in condensed matter research today. Of the many aspects of it, universal conductance fluctuations, weak localization in the diffusive transport regime and quantized point-contact conductance in the ballistic-transport regime are the more significant ones.[79]

Two-dimensional system is of much interest from a scientific point of view, and many of the results are of great technological importance. For example, the entire microelectronics industry is based on the behavior of electrons moving at interfaces between a semiconductor-semiconductor, semiconductor-insulator or a semiconductor-metal. 2D systems can occur naturally as layered crystals (like graphite) or as artificial structures involving one or more interfaces. Size quantization, resulting in 2D transport behavior occurs when the spacing d between two heterojunctions is very small ($d<\lambda_F$): commonly referred to as quantum well.[79]

1.9.4. Non-linear optical properties

Size confinement plays a crucial role in determining the energy levels of the nanostructures when one of the dimensions is reduced below a critical value (the Bohr radius)[11]. The optical absorption spectrum of a semiconducting nanostructure provides an accessible and straightforward method for the evaluation of quantum size effects. The absorption of a photon, leading to excitation of an electron from the VB to the CB, is associated with the band gap energy (E_g). The absorption of photons with energy similar to that of the band gap, $h\nu \geq E_g$, leads to an optical transition, producing an electron in the CB of the semiconductor along with a hole in the VB. Absorption of photons with energy much greater than E_g leads to excitations above the CB edge; these electrons can lose the excess energy by radiationless processes.

The absorption (A) of light by a semiconductor material with thickness l can be expressed by an expression analogous to the Beer-Lambert's law (equation 18), where α represents the absorption coefficient of the solid and is a function of frequency.

$$A = \alpha\, l \qquad -(18)$$

All electronic transitions are subject to selection rules; for semiconductors the requirement (besides $h\nu \geq E_g$) is that the wave vector, k, should be conserved.

$$k_e + k_{photon} = k'_e \qquad -(19)$$

$$k_e = k'_e \qquad -(20)$$

when, k_{photon} is small when compared with the wave vectors of the electron before (k_e) and after excitation (k'_e). The absorption coefficient for a photon of a given energy is proportional to the probability (P_{if}), of the density of states in the initial state (n_i), and the density of available final states (n_f). This process must be summed for all possible transitions between states separated by an energy difference equal to the energy of the incident photon

$$\alpha(h\nu) \propto \sum P_{if} n_i n_f \qquad -(21)$$

Semiconductors in which the wave vector for optical transitions is conserved, are referred to as direct band gap semiconductors (Figure 1.14) and these generally have large absorption coefficients. A useful expression relating the absorption coefficient and the photon energy of a direct transition near the threshold is given by equation (22)[80]. Semiconductors where the lowest electronic transition, between the VB and the CB, is formally forbidden are referred to as indirect band gap (Figure 1.10) and normally have small absorption coefficients.

$$\alpha(h\nu) \propto (E_g - h\nu)^n \qquad -(22)$$

where, n equals $^1/_2$ or 2 for direct and indirect semiconductors, respectively. The "band gap" energy of a nanostructured semiconductor can be experimentally estimated from its optical spectrum by using the above equation. Experimentally, quantum size effects are observed as a shift toward higher energy values for the band edge (a blue shift), as compared to the typical value for the corresponding macrocrystalline (bulk) material. The onset of the optical absorption spectrum occurs at the so-called first exciton (electron-hole pair created after light absorption) or optical band gap energy. The most widespread, simple theoretical framework to study the influence of confinement effects and, particularly, the primary particle size influence in exciton energy, is the so-called effective-mass approximation (EMA)[81]. This assumes parabolic energy bands, infinite confining potential at the interface of the spherical semiconductor particle, and limits main energy terms to electron-hole interaction energy (Coulomb term) and the confinement energy of electron and hole (kinetic term). From experimental work, it is customary to identify three different energy regions as a function of the average crystalline radius (R) of the semiconductor particle:

(i) $R > a_B$, where a_B is the exciton Bohr radius of the extended/bulk semiconductor, defined as $a_B = a_e + a_h$ where a_e and a_h are the electron and hole Bohr radii, respectively. This is the regime of weak confinement and the dominant energy is the Coulomb term and there occurs a size quantization of the motion of the exciton (electron-hole pair is treated as a quasi- particle). The energy of the lowest excited state is a function of R as

$$E(R) = E_g + \hbar^2\pi^2/2MR^2 \qquad -(23)$$

where, E_g is the band gap energy of the bulk semiconductor, and M is the mass of the exciton ($M = m^*_e + m^*_h$; m^* being the effective mass of electron and hole). This indicates a blue shift of $E(R)$ as a function of R^{-2}.

(ii) $R < a_B$ or strong confinement region, where the Coulomb term can be treated as a perturbation, and electron and holes are treated as confined independent particle, so the exciton is not formed and separate size quantization of electron and hole is the dominant factor. In this case $E(R)$ for the lowest excited state of a spherical cluster is given by

$$E(R) = E_g + \hbar^2\pi^2/2MR^2\ (1/m^*_e + 1/m^*_h) - 1.786e^2/\in_2 R + 0.248\ E_R \qquad -(24)$$

where, the first corrective term to E_g is the confinement term, the second is the Coulomb correction with $\in_2$ the dielectric constant of the bulk semiconductor, and the third is the spatial correlation energy correction, being E_R the exciton Rydberg energy[82]. As is well-known, these formulae overestimate the $E(R)$ energy and are being corrected by using an effective bond-order model (EBOM) to construct the hole Hamiltonian, include spin-orbit coupling, and finite confining potential[83], or by introducing the effect of shape distortion from a spherical particle model[84]. Alternative methods including these novel points in the framework of the tight-binding[85] or pseudopotential[86-87] theories have been also published. An important additional challenge to all theories is to develop consistent theoretical estimates of the $\in_2$ dependence with R.[81]

(iii) The region between weak and strong confinement has not been thoroughly investigated but has deserved some attempts for specific semiconductors[88]. In this case, the large difference between the effective mass of the electron and the much heavier hole gives the quantization of the electron motion and its interaction with the hole by a Coulomb potential[82].

As a first rough approximation, metal oxide semiconductors would present an optical band gap with an inverse square dependence of the primary particle size if quantum confinement dominates the energy behavior of the band gap e.g., for (direct band gap) Fe_2O_3[89] or (indirect band gap) CdO[89], but not for Cu_2O,[90] CeO_2,[90] and TiO_2[92-93]. Limited deviations from the R^{-2} behavior, as observed for ZnO,[94] can be based on the known fact that the theory (equations 23 and 24) overestimates the blue shift, while marked deviations are usually based on several chemical/physical phenomena like the presence of ions at the surface of the nanostructured materials (Cu_2O or CeO_2,[90, 95]), since such ions induce strain effects and concomitant structural differences in atomic positions with respect to bulk positions (ZnO, [96] SnO_2[97], ZrO_2[98], TiO_2[98], NiO[99]). For small primary particle sizes, below 3-4 nm, small variations has been claimed to be based on a fortuitous cancellation effect between the kinetic/confinement and Coulomb terms in equation 24, but electronic grounds for this phenomenon still need to be understood. For indirect band gap semiconductors, recent theoretical results[86] suggest the presence of a red shift instead of a blue one with a primary particle size decrease, but recent careful experimental data (in case of nanocrystalline-Si) corroborate the existence of the blue shift qualitatively described by equation 24[100].

Different from their 0D counterparts, the 1D nanostructures exhibit two surface plasmon resonance modes, corresponding to the transverse and longitudinal excitations. Further, the light emitted from the nanowires is highly polarized along their longitudinal axes. For instance, in case of Si nanowires the absorption edge is significantly blue-shifted as compared with the indirect band gap of bulk Si. In addition, the variation in growth direction also leads to different optical signatures. Coherent non-linear optical (NLO) phenomenon observed for semiconductor nanostructures, such as second- and third-harmonic generations, depends explicitly on the crystallographic structure of the medium, as well as the polarization scheme. NLO measurements of ZnO nanowires are potentially useful as an effective frequency converter in the UV region. This might also find application as logic components in nanoscale optoelectronics.

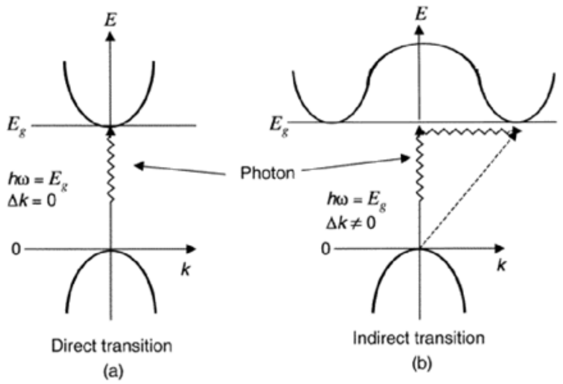

Direct transition
(a)

Indirect transition
(b)

Figure 1.14. Excitation across the band gap of a semiconductor by photon absorption: (a) direct process; (b) indirect process[101]. The threshold frequency ω_g for absorption by the direct transition

determines the energy gap $E_g = \hbar\omega_g$. The indirect transition in (b) involves both a photon and a phonon because the band edges of the conduction and valence bands are widely separated in k-space. The absorption threshold for the indirect transition between the band edges is at $\hbar\omega = E_g \pm \hbar\Omega$, Ω is the frequency of emitted/absorbed phonon.

Thus, from the above discussion it is clear that nanostructures exhibit a wide range of fascinating properties that vary with size, shape and morphology, and have consequently led to a tremendous upsurge in designing next generation devices.

1.10. Applications of Semiconducting Oxide Nanostructures

From the above discussion it is clear that properties of these nanomaterials are determined by the elementary composition and the morphology. In the nano to micro domain, the material properties in structures (crystallites and grains, phase and grain boundaries) become discrete that do not act in an integral manner on the function of the device, but influence as individual structures, the individual function of an individual element. Accordingly, several novel properties of nanostructures have been successfully employed towards fabrication of next generation devices. Some of these are described below:

1.10.1. Miniaturized Electronic Devices

Semiconductor nanostructures have recently been used as building blocks for assembling a range of nanodevices including FETs, p-n diodes, bipolar junction transistors, and complementary inverters[102-104]. For example, previously unknown zinc oxide nanostructures like nanobelts, nanohelixes and nanorings, could provide engineers with new building blocks for creating nanometer-scale sensors, transducers, resonators and other devices that rely on electromechanical coupling. Recently, Wang et al. have demonstrated the successful fabrication of field effect transistors based on single SnO_2 and ZnO nanobelts of thickness between 10 and 30 nm[105]. They have switching ratios as large as 6 orders of magnitude, conductivity as high as 15 $(\Omega cm)^{-1}$, and electron mobility as large as 125 cm^2/Vs. (Figure 1.15) Furthermore, SnO_2 nanobelts can be doped with surface oxygen vacancies by annealing them in reducing environment. This process increases the conductivity and decreases the gate threshold voltage drastically, indicating the feasibility of tuning the device characteristics, by controlling adsorbed oxygen species. Short channel effects have been observed in SnO_2 nanobelts showing the inability of the gate electrode to modulate source-drain channel conductivity in nanobelts shorter than about 500 nm.

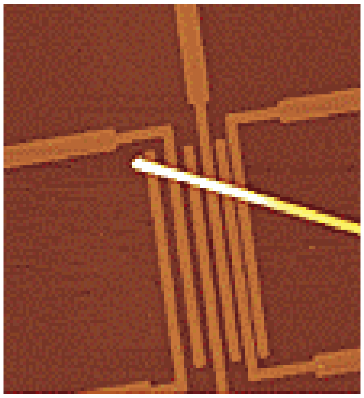

Figure 1.15. An AFM image (10 x 10 μm^2) non-contact mode of ZnO FET across gold electrodes[106]. The field-effect transistors were fabricated by depositing dispersed ZnO nanobelts on predefined gold electrode arrays. Further, the SiO_2 gate dielectric thickness was 120 nm, and the back gate electrode was fabricated by evaporation of gold on the Si (p^+) side of the substrate.

1.10.2. Photoconductivity and Optical Switching

Korgel et al. have shown that the absorption edge of Si nanowires was strongly blue shifted from the bulk indirect band gap of 1.1 eV[106]. They also observed sharp discrete absorbance features and relatively strong ‘band edge’ photoluminescence. This can be attributed to a quantum confinement effect as well as to the lattice orientation effect of the nanowires. Lieber et al. studied the fundamental PL properties of individual isolated InP nanowires[107]. These polarization sensitive measurements revealed a striking anisotropy in the PL intensity recorded parallel and perpendicular to the long axis of the nanowire. This intrinsic anisotropy was used to create polarization sensitive nanoscale photodetectors, which may be useful in optical switches, high-resolution detectors and integrated photonic circuits.

Recently Xie et al. using a ZnO/SnO_2 core-shell heterostructure as an example, demonstrated the possibility of establishing a 3D epitaxial interface between two materials with different crystal systems along with the possibility of tailoring optical properties by building the heteroepitaxial crystal interface[108]. The as-prepared ZnO/SnO_2 heterostructure has a tetrapod-like (T) ZnO core and a SnO_2 shell with 15-30 nm, and their special epitaxial relation is $(010)_{SnO_2}||(0\bar{1}10)_{ZnO}$ and $[100]_{SnO_2}||\ [0001]_{ZnO}$. Such a 3D epitaxy between ZnO core and SnO_2 shell is quite different from the usual planar epitaxy or 3D epitaxy between materials having the same crystal structure. The as-prepared T-ZnO/SnO_2 epitaxial heterostructure exhibits unique luminescence in contrast with that of individual tetrapod ZnO and SnO_2 nanostructures, in which the epitaxial interface induces new luminescent properties. This result may inspire great interest in exploring other complicated epitaxy systems and their potential applications in lasers, gas sensors, solar energy conversion, photo catalysis, and nanodevices in the near future[109].

1.10.3. Lasing

Nanostructures with flat ends can be exploited as optical resonant cavities to generate coherent light on the nanoscale. Huang et al. have demonstrated the room temperature UV lasing of ZnO nanowires[110]. The observed lasing action in these nanowire arrays without any fabricated mirror indicates that these single-crystalline faceted nanowires can, indeed, function as natural resonant cavities. This nanowire lasing has been further confirmed with the optical characterization of single ZnO nanowire by near-field scanning optical microscopy (NSOM).

1.10.4. Sensors

Chemical sensors and microanalytical systems constitute a paradigm for relevant, interdisciplinary endeavor in which some of the key limiting problems are remarkably fundamental in nature. A successful sensor-based system must respond with application-dependent sensitivity, selectivity, reversibility, speed, and longevity to a desired analyte, while consuming minimal power and volume, not to mention being manufacturable from inexpensive materials using economical batch methods. This overconstrained problem can be solved only by an ingenious combination of the most fundamental interfacial chemistry, the basic physics of device platforms, clever engineering of the package and overall system, and an optimal use of mathematical techniques to produce from raw data, a meaningful response.

Among solid-state devices, semiconducting oxide sensors are one of the most promising conductometric chemical sensors, due to their smaller size, low price, compatibility with signal processing, minimum power consumption and modularity[111]. The sensing properties of these materials are based on reactions between semiconductor surfaces and the analyte gas and these reactions produce changes in the semiconductor electrical properties. Although there are many possible kinds of surface fragmentation reactions, the more common interaction that leads to changes in the conductivity is the adsorption of analyte gases on its surface. The resistance of semiconducting thin films is strongly influenced by the presence of oxidizing or reducing gases. The molecules of the analyte gas can indeed interact with the surface of the semiconductor, which already has many oxygen species (O_2, O_2^- and O^-) due to chemisorption. The charge exchange between adsorbed molecules and the analyte gas modifies the energy barrier, eV_s, for grain-to-grain current percolation and in turn, the electrical conductance of the layers. Accordingly, the conductance of the layer can be expressed by $G = G_o\exp(-eV_s/kT)$ where G_o is a constant. The interaction of an oxidizing (reducing) gas occurs with either the film surface or the oxygen coverage. It results in donating (capturing) electrons at the semiconductor surface, which leads to a positive (negative) conductance variation for an n-type semiconductor. In other words, for an n-type material like SnO_2, reducing gases (such as hydrogen, hydrocarbon, ammonia) will cause a significant increase in conductivity. The opposite behavior occurs for a p-type semiconductor. In both cases, the variation of conductance, ΔG, depends on gas concentration [*gas*], according to the empirical formula $|\Delta G|/G = A[gas]^B$ where, A and B are constants determined by temperature, grain size, porosity and specifically on gas adsorption.

The effects of microstructure (which includes ratio of surface area to volume, grain size and pore size) have a strong influence on the sensing properties. Further, It has been established that with the decrease in the particle size down to nano regime, the sensitivity of the sensor material towards a particular gas gets enhanced[112]. The extremely high surface-to-volume ratio associated with these nanostructures makes their electrical properties significantly sensitive to the specific moieties adsorbed selectively on the surface. Further, they also offer the advantage of potentially drift free operation combined with smaller size, fast response and enhanced sensitivity. In addition a shorter response time (75 ms), low detection limit (2 ppm) and above all, room temperature detection is possible using these low dimensional structures.

As compared to other gas sensing semiconducting oxides such as WO_3, TiO_2, ZnO, In_2O_3, Fe_2O_3, and other mixed oxides, it is found that SnO_2 sensors are highly sensitive to reducing gases even at trace amounts. More significantly, the composition of SnO_2 can be tailored easily using different approaches for achieving high selectivity[112]. It is interesting to note here that the mobility of conduction electrons in SnO_2 and ZnO are quite high (160 and 200 $cm^2/V.s$ respectively) compared to that of other semiconducting oxides like In_2O_3 (100) and WO_3 (10 $cm^2/V.s$). Further, hole mobility as low as 0.2 $cm^2/V.s$ has been reported in p-type oxide such as NiO, which is one of the reasons for its less utility as a p-type oxide. The same is also true for some of the other n-type semiconducting oxides such as TiO_2, which has only 0.4 $cm^2/V.s$ mobility of conduction electrons. Amongst ZnO and SnO_2 as gas sensing materials, both have their own merits and demerits. SnO_2 has proved, as a unique oxide sensor material due to its inherent physical and chemical properties. In this n-type material, the conductivity is very sensitive to the surface states in a temperature range between 300 and 700 K. At this temperature range, the redox reaction takes place on the surface of oxides. Besides, SnO_2 surface exhibits good adsorption/desorption phenomenon and surface reactivity, mainly due to the availability of free electrons in its CB and the presence of surface and bulk oxygen vacancies and active chemisorbed oxygen species. Further, it can be more easily processed in the bulk, thin film, and dispersed state of crystallite sizes of 5-20 nm. Nanosized powder has shown promising properties in sensor applications especially at low operating temperatures with enhanced sensitivity[113]. Different forms of nanostructured SnO_2 have been prepared in thin film, belts/ribbons, wires, tubes, diskettes and network forms with higher thermal stability[114-115]. The availability of high surface area and stability of such structures demonstrates their usefulness to make improved and reliable gas sensors. The relationship between the synthetic conditions, microstructure, electric and sensing properties of undoped SnO_2 has also been widely investigated[116-117]. By carefully controlling the preparation parameters and incorporation of additives, catalysts, promoters or by surface functionalization, SnO_2 can be tailor made to highly sensitive and selective sensors for a particular gas. The use of catalytic additives such as Ru, Cu, Pd, Pt, Ag and Au in SnO_2 plays an important role in increasing the reaction rate of the gas molecule. In general, SnO_2 can be sensitized to different gases by a judicious choice of operating temperature, microstructure modification, and selection of desired dopant and catalysts.

1.10.5. Field Emission

The usual theoretical treatment of electron emission from metal into vacuum on the application of high electrostatic field is based on the Fowler-Nordheim (F-N) model, which assumes-[118] (i) the temperature of the metal is 0 K, (ii) inside the metal, the free electron model is valid, (iii) the surface is a smooth plane, and (iv) the potential barrier close to the surface in the vacuum region consists of an image force potential and a potential due to the applied electric field. According to the Sommerfield free electron model, the potential energy of electrons inside the metal V_p, is constant[119]. Thus,

$$V(x) = V_p \quad x < 0 \qquad -(25)$$

Outside the metal,

$$V(x) = -e^2/4x - eF_x \quad x > 0 \qquad -(26)$$

where, e is the charge of the electron and F the electric field strength. The first term on the R.H.S. in equation (26) is potential energy due to the image force on electron due to the induced charge in the metal, and the second term is the contribution due to the presence of external electric field. The F-N model of electron emission is based upon tunneling of electron through 1D barrier. If E is the total energy and W the part of this energy, then,

$$W = p_x^2/2m + V\,(x) \qquad -(27)$$

where, p_x is the momentum of the electron in the x-direction and m is its mass. It is assumed that only the kinetic energy normal to the surface determines the penetration probability of the potential barrier by the electron. The probability of barrier potential D(W) is found by solving the time independent Schrodinger equation. Application of the WKB (Wentzel, Kramers, Brillouin) approximation[120] demonstrate the wave function as a oscillatory wave depending on a phase integral helps to solve problems by a mere quadrature valid for $W \ll V_{max}(x)$ where $V_{max}(x)$ is the maximum potential at the Schottkey hump. Considering that the electrons penetrate the barrier originating in the neighborhood of the Fermi level, one obtains:

$$D(W) = \exp [-c + (W + \phi)/d] \qquad -(28)$$

$$\text{where } c = 4(2m\phi^3)^{1/2}/3\hbar e.f(y) \qquad -(29)$$

$$d = \hbar eF/2(2m\phi)^{1/2}t(y) \qquad -(30)$$

$$\text{and } t(y) = f(y) - 2/3\ y\ df(y)/dy \qquad -(31)$$

$$\text{where } y = (e^3F)^{1/2}/\phi \qquad -(32)$$

f(y) and t(y) are the functions of y, tabulated by Burgess, Kroemer and Houston[121].

Now P(W)dW, the number of electrons in the range of x component of energy between W and W + dW tunneling through the barrier, can be calculated by multiplying D(W) by the supply function N(W) dW, the number of electrons with the x component of the energy in the range W to W+dW incident normal to the surface per unit area per unit time. Thus, the normal energy distribution is given by

$$P(W)dW = N(W)\, D(W)\, dW \qquad -(33)$$

The current density, J is found by multiplying P(W)dW by e, the electronic charge and integrating over all values of W,

$$J = e \int_{Vp}^{\infty} P(W)dW \qquad -(34)$$

The supply function N(W)dW is obtained from the Fermi-Dirac energy distribution. Equilibrium distribution of electrons inside the metal is assumed, although electrons do escape from the metal,

$$N(W)dW = 4\pi mk_BT/h^3 \ \ln [1+ \exp (-W-\phi/k_BT)]dW \qquad -(35)$$

where k_B is the Boltzmann constant, T the absolute temperature and h is the Plank's constant. For low temperatures,

$$\left|(W-\phi)/k_BT\right| >> 1 \text{ and if } W \leq \phi, \qquad -(36)$$

$$k_BT \ln [1+ \exp (-W-\phi/k_BT)] = \phi - W \qquad -(37)$$

combining (37), (36) and (34), and substituting in (35), integrating over all W, yields

$$J = e^3F^2/8\pi\phi\hbar t^2(y) \exp [-4(2m)^{1/2}/3\hbar e \quad \phi^{3/2}/F\ f(y)] \qquad -(38)$$

Expressing J in A/cm^2, F in V/cm, ϕ in eV and substituting the numerical values of other constants, the F-N equation is obtained as,

$$J = 1.54 \times 10^{-6}\ F^2/\phi t^2(y) \exp [-6.83 \times 10^7\ \phi^{3/2}/F\ f(y)] \qquad -(39)$$

The F-N equation has been found to be adequate for describing field emission from metals and to some extent also for emission from semiconductors.

With the advent of various nanostructures, a variety of field emission (cold) cathode materials have been developed to date[121]. These include materials for microfabricated field emitter arrays, diamond and related films, carbon nanotubes, other quasi 1D nanomaterials and printable composite materials. Important parameters include electron affinity, dielectric constant, thermal conductivity, chemical and physical robustness. In addition, cold cathode materials have a wide range of applications such as in flat panel displays, high-power vacuum electronic devices, microwave-generation devices, vacuum microelectronic devices and vacuum nanoelectronic devices. Recently, recognizing the strong possibility that vacuum nanoelectronic devices using quasi 1D nanomaterials, such as carbon nanotubes may emit electrons with driving voltages comparable to that of a solid-state device, there is a growing interest in novel applications of such devices. With such exciting opportunities, there is now a flurry of activities to explore applications far beyond those considered for the conventional hot cathodes that operate on thermionic emission. In particular, nanotubes and nanowires with sharp tips are promising materials for applications as cold cathode field emission devices. Field emission characterization has been carried out on a host of wide band-gap semiconductor nanomaterials. They include nanomaterials of SiC, SiCN, BCN, ZnO, GaN, MoO_3 and WO_3. Typical linearity of F–N plot is obtained from wide band-gap semiconductor nanowires. The Si and SiC exhibit robust field emission with turn-on fields of 15 and 20 V/μm, respectively with current densities of 0.01 mA/cm^2, which are comparable with those of other field emitters like diamond and carbon nanotubes.

1.10.6. Other Applications

Apart from the above-mentioned specific applications, the semiconductor nanostructures have wide range of utility in other fields. For example, quasi-1D ZnO nanobelts have been used for the fabrication of FETs, gas sensors, resonators, and nanocantilevers[122]. These applications mainly utilize the semiconducting properties and geometrical shape and size offered by nanostructures. Further, individual ZnO nanobelt is a promising piezoelectric material for nanosensor and nanoactuator applications due to its perfect single crystalline structure and its dislocation free nature[123].

Wurtzite-structured cadmium selenide (CdSe) is an important II-VI semiconducting compound for optoelectronics. CdSe quantum dots are the most extensively studied quantum nanostructures due to their size-tunable properties. CdSe was also the first example of self-assembled semiconductor nanocrystal superlattices. With a direct band gap of 1.8 eV, CdSe quantum dots have been used for laser diodes, nanosensing, and biomedical imaging[124].

Gamelin et al, have reported a method for the preparation of colloidal ZnO-diluted magnetic semiconductor quantum dots (DMS-QDs) by alkaline-activated hydrolysis and condensation of zinc acetate solutions in dimethyl sulfoxide (DMSO)[125]. Diluted magnetic semiconductors (DMSs) are currently attracting immense interest in the emerging field of spin-based electronics, or "spintronics." The broad objective of this field is to control electron spins, in addition to charges, so as to transmit information and provide new functionality to semiconductor devices. Operational spin-dependent light-emitting diodes (spin LEDs) have been demonstrated to use II-VI and III-V DMSs as the key spin-polarization materials. The mechanistic studies reveal that Co^{2+} and Ni^{2+}

dopants inhibit nucleation and growth of ZnO nanocrystals. A "giant Zeeman effect" is observed in the band gap transition of Co^{2+}: ZnO DMS-QDs. MCD and Zeeman spectroscopies are used to quantify the magnitude of the p-d exchange interaction (N_0^{β}) that gives rise to this effect. N_0^{β} values of -2.3 ± 0.3 eV (-18 500 cm^{-1}) for Co^{2+}:ZnO and -4.5 ± 0.6 eV (-36 300 cm^{-1}) for Ni^{2+}:ZnO have been determined. Ligand-to-metal charge-transfer transitions are observed in the MCD spectra of both Co^{2+}:ZnO and Ni^{2+}:ZnO DMS-QDs and are analyzed in the context of an optical electronegativity model. Ferromagnetism with $T_C > 350$ K is observed in aggregated nanocrystals of Co^{2+}:ZnO that unambiguously demonstrates the existence of intrinsic high-T_C ferromagnetism in this class of DMSs.

1.11. Conclusions and Perspectives

Thus some of the most recent developments of semiconducting oxide nanostructures have been presented in this chapter with particular emphasis on their preparation, characterization, size-dependent properties and various applications. Semiconducting oxide nanostructures are elegant examples of inorganic nanomaterials, having vast tunabilty with respect to their structure, property and application and are expected to lead the prospect of this field for continuing decades with more tangible applications. More specifically, these nanostructures act as indispensable building blocks for creating designer materials, devices and systems. Although there are many well-established methods to synthesize and understand the properties, several daunting challenges of these materials such as control of shape and aspect ratio, electron and phonon transport properties, difficulties of scale-up, require immediate attention to fructify their technological benefits.

1.12. Motivation, Scope and Organization of the Thesis

Because of their unique conductance properties, SnO_2 nanostructures are promising candidates towards fabricating miniaturized, ultra sensitive and remarkably efficient chemical sensors. It has been shown that the reduction in the grain size of SnO_2 leads to an increase in its sensitivity, owing to the high surface to volume ratio. Accordingly, SnO_2 has been synthesized in various forms like whiskers, nanorods, nanotubes, nanodiskettes, nanobelts and nanowires using techniques like laser ablation, thermal evaporation etc with controlled dimensions. More specifically, the method based on the vaporization of oxide materials at high temperature requires a complex apparatus and precise control of temperature and gas flow. Besides, size and shape dependent behavior, the doping of nanostructured materials preserving the structural integrity, can provide a far more favorable means of tailoring their properties due to their aspect ratio induced changes in electronic structure.

Pristine SnO_2 based nanostructures have been reported to act as room temperature sensors for NO_x, CO, O_2, H_2 and C_2H_5OH depending on parameters such as operating temperature, analyte concentration and UV illumination. However, high sensitivity and reversibility is achieved only at an elevated temperature or by exposure to UV light of energy near the SnO_2 band gap, as the surface areas of these nanostructures are limited. Interestingly all these work on nanowire sensors to date is based on pure SnO_2 and there has been no attempt to explore the sensing applications of doped nanowires, although doping is one of the important strategies for controlling both sensitivity and selectivity. The doping or compositional changes in nanowires can be controlled by pre-evaporation in a way similar to that in metal-organic chemical vapor deposition (MOCVD). Although several other procedures for synthesizing pristine nanowires have been recently demonstrated, the preparation of doped SnO_2 has not been reported so far, despite its significance in nanotechnology. Hence it is particularly significant to explore simpler methods of synthesis of SnO_2 nanostructures, simultaneously modulating its electronic properties by means of doping for particular applications like gas sensing.

ZnO is yet another semiconducting oxide material like SnO_2, which is acquiring a great deal of interest. The wide direct band gap (3.37 eV), large exciton binding energy (60 meV), negative electron affinity, and high mechanical strength makes it one of the promising photonic materials in the ultraviolet region and a good candidate for field emitter arrays of flat panel display devices. This wurtzite structured ionic crystal with noncentral symmetry, is described schematically as a number of alternating planes composed of fourfold tetrahedral-coordinated O^{2-} and Zn^{2+} ions, stacked alternatively along the *c* axis. The oppositely charged ions produce positively charged $(000\bar{1})$-Zn and negatively charged (0001)-O polar surfaces. It has been found that the (0001)-Zn surface is chemically active in growing nanostructures, while the $(000\bar{1})$-O surface is smooth and inert. Accordingly, the nanostructures of ZnO have been synthesized by different means and been employed successfully in fabricating nanolaser, field effect transistors, and gas sensors. However, most of the available reports deal with the field emission studies that are carried out in a narrow voltage range as these are measured in an assembly having the samples in close proximity with screen.[95] Such type of experimental arrangement limits the measurement at higher values of field that can be applied as it can lead to the arc formation. The study of the field emission characteristics over a wide spectrum is critical to understand the physics at low dimensions. Hence, in order to understand the reason for the higher field enhancement and the proper relation of the geometry with the field emission characteristics, it is important and desirable to study and understand the field emission from the single nanostructures over a wide range of applied field.

The thesis addresses some of the major issues of semiconducting oxide nanostructures with special emphasis on SnO_2 and ZnO, the motivation being both fundamental and technological applications in nanotechnology. This includes synthesis, characterization, gas sensing and field emission studies of these nanostructures to address the size and shape dependent issues on their electron transport properties. Spray pyrolysis and vapor deposition methods have been explored to develop novel nanostructures of SnO_2 and ZnO. The unique conductance property exhibited by SnO_2 nanostructures has been exploited by employing it for designing materials for gas sensing applications. Monolayer protected copper nanoclusters along with other doping elements like Ru, Cu and Th have been effectively used for tailoring the sensitivity of SnO_2 towards gases like H_2S, LPG and TMA. The use of nanostructures, remarkably, has made possible the room temperature detection of NO_2. Further, novel nanostructures of ZnO have been synthesized and investigated for their possible application towards field emission devices.

1.13. Objectives of the Present Study

The foregoing critical review of semiconducting oxide nanostructures shows several methods for their synthesis, characterization, property and application; although several lacunae are still present for their wide utilization for various electronic applications. For example, most of the nanostructures synthesized by vapor deposition contain other unwanted structures along with the desired materials or structures, whose removal is very troublesome. Accordingly, the size and shape selectivity is a daunting task, involving several complex procedures; thus, a simple preparation of size and shape selective nanostructures is important for any practical application. Since the nanostructures of SnO_2 is important for gas sensing applications, it is necessary to understand the effect of morphology, size and doping element. Further, various structures of ZnO exhibit the sharp tip or needle like morphology. Hence, it will be interesting to explore the field emission features for designing next generation field emission devices and current sources. The specific objectives of the work embodied in this thesis are set out in this perspective as follows:

a) To accomplish selective synthesis and characterization of SnO_2 structures in the form of nanostructures and thin films;

b) To explore the effect of doping element, temperature, substrate, carrier gas and heating duration on the yield and growth of nanostructures of SnO_2

c) To demonstrate the dual role of dopants as sensitizer and promoter for low temperature crystallization of SnO_2 thin films;

d) To elucidate the effect of surface functionalization on gas sensing properties of SnO_2 thin films;

e) To demonstrate the room temperature detection of H_2S and NO_2 using MPC's and nanostructures of SnO_2, respectively;

f) To synthesize and characterize shape controlled ZnO nanostructures;

g) To understand the effect of morphology on the field emission behavior of ZnO nanostructures.

The present thesis addresses few important questions related to the synthesis and characterization of high aspect ratio structures of SnO_2 and ZnO and more specifically to their applications in gas sensing and field emission. These have been discussed in detail spread in **five separate chapters**. The **first chapter** represents a critical review of the synthesis, characterization, properties and various strategies for the synthesis of functional oxide nanostructures. The electron transfer features of these nanostructures have been elaborately discussed to harness their potential applications in nanoelectronics, nanosensors and field emission. The impact of these materials on nanotechnology for diverse applications such as catalysis, optical, electronic and magnetic device construction, medical diagnostics and therapeutics, environmental and pollution control has been briefly discussed. The chapter concludes by providing specific objectives for the present study, future prospects, and finally mentioning some of the existing limitations of these novel high aspect ratio materials.

The **second chapter** primarily deals with a novel route towards shape selective synthesis of SnO_2 nanostructures: Bipyramids, Cubes and Wires and their detailed characterization using XRD, SEM, TEM (SAED), TGA, Uv-vis and XPS. The incorporation of Ru in SnO_2 thin films results in the low temperature crystallization implying the role of Ru as a promoter/nucleating aid besides sensitizer. This has been further extended to other nanostructures of SnO_2 wherein we have observed that when Ru is mixed with oxide of Sn, it act as nucleating agents promoting the 1D growth and the formation of other high aspect ratio nanostructures. The effect of various parameters like temperature, heating duration, nature of carrier gas, flow rate is investigated with the help of SEM, TEM and XRD in conjunction with TG-DSC and XPS analysis. A plausible growth mechanism is proposed using the results of these studies. The texture coefficient values of all the nanostructures, indexed to a tetragonal lattice, exhibit an amazing variation in the preferred orientation with respect to their shapes. Although, XPS data indicates that nanowires and cubes have a strong SnO_2 type signal, nanobipyramids interestingly exhibit both SnO and SnO_2 signals and a correlation of the binding energy helps in understanding the growth kinetics of such nanostructures. The results suggest that the nanobipyramids are formed due to the vapor-solid process (VS) while nanowires and cubes are formed by the vapor-liquid solid (VLS) progression.

The **third chapter** starts with the discussion of the SnO_2 as a gas sensor material, explaining briefly the advantages and limitations of the sensors based on it. Different means of controlling the cross selectivity and enhancing the sensitivity have been discussed and demonstrated using surface functionalisation with monolayer protected Cu-nanoclusters, RuO_2 in SnO_2 nanostructures and doping of SnO_2 thin films with Ru, Cu and Th. Our result suggests the feasibility of room temperature detection of H_2S and NO_2 using Cu nanoclusters and RuO_2 doped SnO_2 nanowires. Further, the doping elements act as a promoter for low temperature crystallization of SnO_2 as demonstrated for thin films besides acting as a sensitizer. Our result opens up the possibility of synthesizing doped SnO_2 nanowires that can be used as extremely sensitive, drift free and robust sensors towards NO_2 and LPG. The response towards different gases can be controlled by varying the dopant and its concentration and distribution. The low temperature four probe conductivity measurements of SnO_2 nanowires suggest these to be behaving as a luttinger liquid i.e. a system with highly co-related electrons.

Using the simple method of growth of SnO_2 nanostructures, a wealth of interesting novel high aspect ratio nanostructures of ZnO have been synthesized successfully which are discussed in detail in the **fourth chapter.** Besides temperature, nature of carrier gas and flow rate, the substrate template is found to play a crucial role in governing the shape and size of the nanostructures. The effect of different templates like Si-wafer, alumina and refractory bricks has been explored and a plausible growth mechanism has been proposed using the results of the XRD, SEM, TEM (SAED), XPS, and TGA studies.

In the **fifth chapter**, field emission properties of the high aspect ratio nanostructures of ZnO have been demonstrated. A single multipod structure and a single arm of the larger multipod structure have been isolated and skillfully mounted on W-tips, which exhibit an ultralow onset voltage of 40 V to draw a current of 1 nA. Further, the current density of 2.8×10^4 A/cm^2 could be achieved with a field of 1.26×10^5 V/μm. A common feature in all multipod structures is the non-linearity and the appearance of the break in the FN plot, which is expected for a semiconductor material. All the other structures show good field emission properties suggesting that ZnO nanostructures are promising for applications in field emission devices.

Finally, **chapter six** outlines a summary of all the major conclusions of the present study with respect to the synthesis, characterization, gas sensing and field emission properties of high aspect ratio nanostructures of SnO_2 and ZnO. One major advantage is the simple synthesis of these nanostructures by thermal evaporation without using any catalyst or sophisticated instrumentation and the gas sensing and the field emission properties further support the utility. Room temperature detection of H_2S and NO_2 has been demonstrated successfully using monolayer protected Cu nanoclusters and the nanostructures of SnO_2. The amount of ruthenium is found to be the deciding factor for the sensitivity and the operating temperature. Further increase in sensitivity is possible by using thinner nanowires, utilizing a single nanowire with proper SnO_2-metal ohmic contacts. This chapter also outlines some of the limitations of these materials along with probable hazardous effects on the environment and necessary precautions. Finally, the future prospects of these materials are outlined for next 10-20 years within the broad perspective of both fundamental and technological interests in diverse fields such as chemistry, physics, biology and engineering.

The results presented in the thesis clearly suggest, that high aspect nanostructures of SnO_2 and ZnO can act as promising building blocks for nanoelectronic circuit components. Thus, this simple method of preparation and results related to gas sensing, field emission and the electron transfer properties of such high aspect ratio materials embodied in this thesis will be useful hopefully to resolve several important issues related to their possible future device applications.

1.13. References

1. (a) *Societal Implications of Nanoscience and Nanotechnology*; Roco, M. C.; Bainbridge, W. S., Eds. National Science Foundation Report: Arlington, VA, **2001** and also published by Kluwer Academic Publishers: Boston, MA, **2001**. (b) http://www.nano.gov.
2. www.un.org/millenniumgoals/
3. Kohler, M.; Fritzsche, W. Nanotechnology, An Introduction to Nanostructuring Techniques, Wiley-VCH Verlag GmbH & Co. KgaA, **2004**.
4. Ratner, M.; Ratner, D. Nanotechnology: A Gentle Introduction to the Next Big Idea, **2003**.
5. Elliot, S. R. The Physics and Chemistry of solids, Wiley-VCH Verlag GmbH & Co. KgaA, **2003**.
6. Zhang, W.-X.; Karn, B. *Environ. Sci. Technol. A-Pages;* **2005**, *39*(5), 94A-95A.
7. Kittle, C. Introduction to Solid state Physics, John Wiley and Sons, Inc., Singapore New York, 2000.
8. Brus, L. E. *J. Chem. Phys.* **1984**, 80, 4403.
9. (a) Rama Krishna, M. V.; Friesner, R. A. *Phys. Rev. Lett.* **1991**, 67, 629. (b) Bylander, D. M.; Kleinman, L.; Lee, S. *Phys. Rev. B* **1990**, 42, 1394.
10. (a) Van Vechten, J. A.; Thurmond, C. D. *Phys. Rev. B* **1976,** 14, 3539. (b) Wang, Y.; Herron, N. *Phys. Rev. B* **1990**, 42, 7253. (c) Lippens, P. E.; Lannoo, M. *Phys. Rev. B* **1990**, 41, 6079.
11. Trindade, T.; O'Brien, P.; Pickett, N. L. *Chem. Mater.* **2001**; *13*(11), 3843.
12. (a) Rego, L. C. G.; Kirczenow, G. *Phys. Rev. B* **1999**, *59*, 13080. (b) Yu, C.; Shi, L.; Yao, Z.; Li, D.; Majumdar, A. *Nano Lett.* **2005**, *5*(9), 1842.
13. (a) Henglein, A. *Chem Rev*. **1989**, *89*, 1861. (b) Steigerwald, M. L.; Brus, L. E. *Acc. Chem. Res*. **1990**, *23*, 183. (c) Bawendi, M. G.; Steigerwald, M. L.; Brus, L. E. *Annu. Rev. Phys. Chem.* **1990**, *41*, 477. (d) Weller, H. *Angew. Chem., Int. Ed. Engl*. **1993**, *32*, 41. (e) Weller, H. *Adv. Mater.* **1993**, *5*, 88.
14. (a) Hagfeldt, A.; Grätzel, M. *Chem. Rev*. **1995**, *95*, 49. (b) Fendler, J. H.; Meldrum, F. C. *Adv. Mater.* **1995**, *7*, 607. (c) Alivisatos, A. P. *J. Phys. Chem.* **1996**, *100*, 13226.

15. Haug, H.; Koch, S. W. *Quantum theory of the optical and electronic properties of semiconductors*; World Scientific Publishing Co. Pte. Ltd.: London, 1990; p 333.
16. Brus, L. E. *J. Chem. Phys.* **1983**, *79*, 5566.
17. Brus, L. E. *J. Chem. Phys.* **1984**, *80*, 4403.
18. Brus, L. *J. Phys. Chem.* **1986**, *90*, 2555.
19. Soloviev, V. N.; Eichhofer, A.; Fenske, D.; Banin, U., *J. Am. Chem. Soc.;* **2000**; *122*(11); 2673.
20. (a) El-Sayed, M. A. *Acc. Chem. Res.* **2001**, *34*, 257. (b) El-Sayed, M. A. *Acc. Chem. Res.* **2004**, *37*, 326. (c) Ghosh, S. K.; Nath, S.; Kundu, S.; Esumi, K.; Pal, T. *J. Phys. Chem. B* **2004**, *108*, 13963.
21. *Nanoparticles: From Theory to Application*; Schmid, G.; Eds. Wiley-VCH: Weinheim, **2004**.
22. (a) Wang, Z. L.; Kang, Z. C. Functional and smart materials- structural evolution and structure analysis, Plenum Press, New York, **1998**. (b) A special issue on nanoscale materials, *Acc. Chem. Res.* **1999**, 32. (c) Wang, X. D.; Summers, C. J.; Wang, Z. L. *Nano Lett.* **2004**, *4*, 423.
23. (a) Xia, Y.; Yang, P.; Sun, Y.; Wu, Y.; Mayers, B.; Gates, B.; Yin, Y.; Kim, F.; Yan, H. *Adv. Mater.* **2003**, 15, 5, 353. (b) Wang, J.-G.; Tian, M.-L.; Mallouk, T. E.; Chan, M. H. W. *Nano Lett.* **2004**, 4(7), 1313.
24. (a) Cui, Y.; Duan, X.; Hu, J.; Lieber, C. M. *J. Phys. Chem. B* **2000**, 104, 5213. (b) Gudiksen, M. S.; Lauhon, L. J.; Wang, J.; Smith, D. C.; Lieber, C. M. *Nature* **2002,** *415,* 617. (c) Wang, Z. L. *Materials Today,* **2004**, 7(6), 26.
25. Munnix, S.; Schmeits, M. *Phys. Rev. B*, **1983**, 27, 7624.
26. Mizusaki, J.; Koinuma, H.; Shimoyama J. I.; Kawasaki, M. *J. Solid State Chem.* **1990**, 8, 443.
27. Sherwood, P. M. A. *Phys. Rev. B* **1990**, 41, 10151.
28. Dai, Z. R.; Gole, J. L.; Stout, J. D.; Wang, Z. L., *J. Phys. Chem. B,* **106** (6), 1274 - 1279, 2002.
29. Hughes, W. L.; Wang, Z. L. *J. Am. Chem. Soc.* **2004**, *126*(21), 6703.
30. Yang, R.; Ding, Y.; Wang, Z. L. *Nano Lett.* **2004**, *4*(7), 1309.
31. Dong, C. L.; Persson, C.; Vayssieres, L.; Augustsson, A.; Schmitt, T.; Mattesini, M.; Ahuja, R.; Chang, C. L.; Guo1, J.-H., Physical Review B **2004,** 70, 195325.

32. Wang, J.; An, X.; Li, Q.; Egerton, R. F. *Appl. Phys. Lett.* **2005***,* 86, 201911.
33. (a) Golden, J.H.; DiSalvo, F.J.; Fréchet, J.M.J.; Silcox, J.; Thomas, M.; Elman, J. *Science* **1996**, 273, 782. (b) Peng, Z. A.; Peng, X. A. *J. Am. Chem. Soc.* **2001,** 123, 1389.
34. (a) Golden, J.H.; Deng, H.; DiSalvo, F.J.; Fréchet, J.M.J.; Thompson, P.M. *Science* **1995**, 268, 1463. (b) B. Gates, B. Mayers, B. Cattle, Y. Xia, *Adv. Funct. Mater.* 2002, **12**, 219.
35. Greene, L. E.; Law, M.; Goldberger, J.; Kim, F.; Johson, J. C.; Zhang, Y.; Saykally, R. J.; Yang, P. *Angew. Chem., Int. Ed.* **2003**, *42*, 3031.
36. Yu, H.; Zhang, Z.; Han, M.; Hao, X.; Zhu, F. *J. Am. Chem. Soc.* **2005,** *127*(8), 2378.
37. Madou, M. *Fundamentals of Microfabrication*, CRC Press, Boca Raton, FL **1997**.
38. (a) Jones, E.T.T.; Chyan, O.M., Wrighton, M.S. *J. Am. Chem. Soc.* **1987,** 109, 5526. (b) Fasol, G. *Science* **1998**, 280, 545.
39. Dai, H.; Wong, E.W.; Lu, Y.Z.; Fan, S.; Lieber, C.M. *Nature* **1995**, 375, 769.
40. Liu, H.; Biegelsen, D.K.; Johnson, N.M.; Pnoce, F.A.; Pease, R.F.W. *J. Vac. Sci. Technol. B* **1993**, 11, 2532.
41. Zhang, H.; Zuo, M.; Tan, S.; Li, G.; Zhang, S.; Hou, J. *J. Phys. Chem. B.;* **(Article); 2005**; *109*(21); 10653.
42. Zhao, H.; Lei, M.; Yang, X.; Jian, J.; Chen, X., *J. Am. Chem. Soc.* **2005**; *127*(45); 15722.
43. Trentler, T.J.; Hickman, K.M.; Geol, S.C.; Viano, A.M.; Gibbons, P.C.; Buhro, W.E. *Science* **1995,** 270, 1791.
44. (a) Markowitz, P.D.; Zach, M.P.; Gibbons, P.C.; Penner, R.M.; Buhro, W.E. *J. Am. Chem. Soc.* **2001**, 123, 4502. (b) Lourie, O.R.; Jones, C.R.; Bartlett, B.M.; Gibbons, P.C.; Ruoff, R.S.; Buhro, W.E. *Chem. Mater.* **2000**, 12, 1808.
45. Heath, J.R.; LeGoues, F.K. *Chem. Phys. Lett.* **1993**, 208, 263.
46. Li, Y.-D.; Duan, X.-F.; Qian, Y.-T.; Yang, L.; Ji, M.-R.; Li, C.-W. *J. Am. Chem. Soc.* **1997**, *119*(33), 7869.
47. Dai, Z.R.; Pan, Z.W.; Wang. Z.L. *Advan. Func. Mater.* **2003,**13, 9.

48. (a) Lao, J. Y.; Huang, J. Y.; Wang, D. Z.; Ren, Z. F. *Nano Lett.* **2003**, *3*(2), 235. (b) Burda, C.; Chen, X.; Narayanan, R.; El-Sayed, M. A. *Chem. Rev.* **2005,** *105*(4), 1025.
49. Wagner, R. S.; Ellis, W. C. *Appl. Phys. Lett.* **1964**, 4, 89.
50. (a) Madhukar, A.; Lu, S.; Konkar, A.; Zhang, Y.; Ho, M.; Hughes, S. M.; Alivisatos, A. P. *Nano Lett.* **2005**, *5*(3), 479. (b) Rajeshwar, K.; de Tacconi, N. R.; Chenthamarakshan, C. R. *Chem. Mater.* **2001**, *13*(9), 2765.
51. Lee, S.T.; Wang, N.; Zhang Y.F. et al., *MRS Bull.* **1999**, 24, 36.
52. Zhang, R.-Q.; Liftshtz, Y.; Lee, S. T. *Adv. Mat.* **2003**, 15, 635.
53. Zhang, Y.; Wang, L.; Liu, X.; Yan, Y.; Chen, C.; Zhu, J. *J. Phys. Chem. B.* **2005**, *109*(27), 13091.
54. Levitt, A. P., Ed.; *Whisker Technology*; Wiley-Interscience: New York, 1970.
55. Cullity, B. D.; Stock, S. R. Elements of X-ray Diffraction, 3rd Ed., Prentice Hall Pub. **2001**, New Jersey.
56. (a) Deng, H.; Hossenlopp, J. M. *J. Phys. Chem. B.* **2005**, *109*(1), 66. (b) Xu, G.; Zhang, Y.-W.; Sun, X.; Xu, C.-L.; Yan, C.-H. *J. Phys. Chem. B.* **2005**, *109*(8), 3269.
57. Bae, S. Y.; Na, C. W.; Kang, J. H.; Park, J. *J. Phys. Chem. B.* **2005**, *109*(7), 2526.
58. Williams, D. B.; Carter, C. B. Transmission Electron Microscopy, Vol I-III, Kluwer Academic, Plenum Publishers, **1996**.
59. (a) Duan, J.; Yang, S.; Liu, H.; Gong, J.; Huang, H.; Zhao, X.; Zhang, R.; Du, Y. *J. Am. Chem. Soc.* **2005**, *127*(17), 6180. (b) Ding, Y.; Wang, Z. L. *J. Phys. Chem. B.* **2004**, *108*(33), 12280.
60. Goldstein, J. I. et al., Scanning electron microscopy and X-ray microananalysis, Kluwer Academic/ Plenum Publishers, New York, 3rd ed., **2003**.
61. Arons, A. B.; Peppard, M. B.; Einstein's Proposal of the Photon Concept - a Translation of the Annalen der Physik Paper of 1905, American Journal of Physics, **1965**, 33(5), 367.
62. (a) Wagner, C. D.; Riggs, W. M.; Davis, L. E.; Moulder, J. E. *Handbook of X-ray Photoelectron Spectroscopy*; Perkin-Elmer Corp.: **1979**. (b) Sherwood, P. M. A. In *Surface Analysis by Auger and X-ray Photoelectron Spectroscopy*; Briggs, D., Grant, J. T., Eds. Surface Spectra Ltd. and IM Publications: Chichester, **2003**.

63. Mazher, J.; Shrivastav, A. K.; Nandedkar, R. V.; Pandey, R. K. *Nanotechnology* **2004,** *15*, 572.
64. Martin-Concepción, A. I.; Yubero, F.; Espinós, J. P.; González-Elipe, A. R.; Tougaard, S. *J. Vac. Sci. Technol.* A **2003,** 21, 1393**.**
65. Long, D. A. Raman Scattering, Mcgraw Hill Book Company, New York, 1977.
66. (a) Fernandez-Garcia, M.; Martinez-Arias, A.; Hanson, J. C.; Rodriguez, J. A. *Chem. Rev.* **2004**, *104*(9), 4063. (b) Anchell, J. L.; Hess, A. C. *J. Phys. Chem.* **1996**, *100*, 18317.
67. Dollimore, D. *Anal. Chem.* **1996**, *68*(12), 63.
68. (a) Sze, S. M. VLSI Technology, AT&T Bell Laboratories, Murray Hill, New Jersey. (b) Wieder, H.H."Four Terminal Nondestructive Electrical and Galvanomagnetic Measurements," in *Nondestructive Evaluation of Semiconductor Materials and Devices* (J.N. Zemel, ed.), Plenum Press, New York, NY, 1979, 67-104.
69. (a) Blaser, G.; Ruhl, Th.; Diehl, C.; Ulrich, M.; Kohl, D. *Phys. A* **1999**, *266*, 218. (b) He, J. H.; Lao, C. S.; Chen, L. J.; Davidovic, D.; Wang, Z. L. *J. Am. Chem. Soc.* 2005, 127(47), 16376.
70. Rubio-Bollinger, G.; Bahn, S.R.; Agraït, N.; Jacobsen, K.W.; Vieira, S. *Phys. Rev. Lett.* **2001**, 87, 026 101.
71. Wong, E.W.; Sheehan, P.E.; Lieber, C.M. *Science* **1997**, 277, 1971.
72. Chattopadhyay, S.; Shi, S. C.; Lan, Z. H.; Chen, C. F.; Chen, K.-H.; Chen, L.-C. *J. Am. Chem. Soc.* **2005**, *127*(9), 2820.
73. (a) Wu, Y.; Yang, P. *Adv. Mater.* **2001**, 13, 520. (b) Wu, Y.Y.; Yang, P.D. *Appl. Phys. Lett.* **2000**, 77, 43.
74. (a) Pan, Z.W.; Dai, Z.R; Xu, L.; Lee, S.T.; Wang, Z.L. *J. Phys. Chem. B* **2001**, 105, 2507. (b) Peng, H.Y.; Pan, Z.W.; Xu, L.; Fan, X.H.; Wang, N.; Lee, C.S.; Lee, S.T. *Adv. Mater.* **2001**, 13, 317.
75. (a) Hall, E.O. *Proc. Phys. Soc. London B* 1951, **64**, 747. (b) Petch, N.J. *J. Iron Steel Inst.* **1953**, 174, 25.
76. Schiøtz, J.; Di Tolla, F.D.; Jacobsen, K.W. *Nature* **1998**, 391, 561.
77. Poncharal, P.; Wang, Z.L.; Ugarte, D.; de Heer, W.A. *Science* **1999**, 283, 1513.
78. Nilius, N.; Wallis, T. M.; Ho, W. *J. Phys. Chem. B.* **2005**, *109*(44), 20657.

79. (a) Diol, S.; Poles, E.; Rosenwaks, Y.; Miller, R. J. D. *J. Phys. Chem. B* **1998**, *102*, 6193. (b) Braun, M.; Burda, C.; El-Sayed, M. A. *J. Phys. Chem. A.* **2001**, *105*(23), 5548.
80. Gu, F.; Wang, S. F.; Lu, M. K.; Zhou, G. J.; Xu, D.; Yuan, D. R. *J. Phys. Chem. B.* **2004**, *108*(24), 8119.
81. Yoffe, A. D. *Adv. Phys.* **2001**, *50*, 1.
82. Bawendi, M. G.; Wilson, W. L.; Rothberg, L.; Caroll, P. J.; Jedji, T. M.; Steigerward, M. L.; Brus, L. E. *Phys. Rev. Lett.* **1990**, *65*, 1623.
83. Laheld, V. E. H.; Einevoll, G. T. *Phys. Rev. B* **1997**, *55*, 5184.
84. Efros, A. L.; Rosen, M.; Kuno, M.; Normal, M.; Norris, D. J.; Bawendi, M. *Phys. Rev. B* **1996**, *54*, 4843.
85. Von Grumber, H. H. *Phys. Rev. B* **1997**, *55*, 2293.
86. Tomasulo, A.; Ramakrisna, M. V. *J. Chem. Phys.* **1996**, *105*, 3612.
87. Wang, L.-W.; Kim, J.; Zunger, A. *Phys. Rev. B* **1999**, *59*, 5678.
88. Uzomi, T.; Kayanuma, Y.; Yamanaka, K.; Edamatsu, K.; Itoh, T. *Phys. Rev. B* **1999**, *59*, 9826.
89. Iwamoto, M.; Abe, T.; Tachibana, Y. *J. Mol. Catal. A* **2000**, *55*, 143.
90. Vigil, O.; Cruz, F.; Morales-Acabedo, A.; Contreras-Puente, G.; Vaillant, L.; Santana, G. *Mater. Chem. Phys.* **2001**, *68*, 249.
91. Borgohain, K.; Morase, N.; Mahumani, S. *J. Appl. Phys.* **2002**, *92*, 1292.
92. Suzuki, T.; Kosacki, I.; Petrovsky, V.; Anderson, H. U. *J. Appl. Phys.* **2001**, *91*, 2308.
93. Serpone, N.; Lawless, D.; Khairutdinov, R. *J. Phys. Chem.* **1995**, *98*, 16646.
94. Monticone, S.; Tufeu, R.; Kanaev, A. V.; Scolan, E.; Sanchez, C. *Appl. Surf. Sci.* **2000**, *162-163*, 565.
95. Viswanaha, R.; Sapra, S.; Satyani, B.; Der, B. N.; Sarma, D. D. *J. Mater. Sci.* **2004**, *14*, 661.
96. Tsunekawa, S.; Fukuda, T.; Kasuya, A. *J. Appl. Phys.* **2000**, *87*, 1318.
97. Ong, H. C.; Zhu, A. X. E.; Du, G. T. *Appl. Phys. Lett.* **2002**, *80*, 941.
98. Kang, J.; Tsunekawa, S.; Kasuya, A. *Appl. Surf. Sci.* **2001**, *174*, 306.
99. Kosacki, I.; Petrovsky, V.; Anderson, H. U. *Appl. Phys. Lett.* **1999**, *74*, 341.

100. (a) Matsumoto, T.; Suzuki, J.-I.; Ohmura, M.; Kanemitsu, Y.; Masumoto, Y. *Phys. Rev. B* **2001**, *63*, 195322. (b) Mahmond, S. A.; Akl, A. A.; Kand, H.; Adbel-Had, K. *Phys. B* **2002**, *111*, 366.
101. Rosenberg, H. M. *The solid state*; Oxford University Press: Oxford, U.K.
102. Wan, Y.-M.; Lin, H.-T.; Sung, C.-L.; Hu S.-F.; *Appl. Phys. Lett.* **2005,** 87, 123506.
103. Chakraborty, A.; Emadi, A. Proc. SPIE **2005,** 5824, 260.
104. Balandin, A. A. Proc. SPIE **2005,** 5846, 82.
105. Arnold, M. S.; Avouris, P.; Pan, Z. W.; Wang, Z. L. *J. Phys. Chem. B.* **2003**, *107*(3), 659.
106. (a) Henrath, T.; Korgel, B. A. *Adv. Mat.* **2003**, 15, 437. (b) L. Brus, *J. Phys. Chem.,* **1994**, 98,3575.
107. Wang, J. F. et al *Science* **2001**, 293, 1455.
108. Kuang, Q.; Jiang, Z.-Y.; Xie, Z.-X.; Lin, S.-C.; Lin, Z.-W.; Xie, S.-Y.; Huang, R.-B.; Zheng, L.-S. *J. Am. Chem. Soc.,* **2005,** 127(33), 11777.
109. Bae, S. Y.; Na, C. W.; Kang, J. H.; Park, J.; *J. Phys. Chem. B.* **2005** 109(7), 2526.
110. (a) Huang, M. H.; Mao, S.; Feick, H.; Yan, H.; Wu, Y.; Kind, H.; Weber, E.; Russo, R.; Yang, P. *Science* **2001**, 292, 1897. (b) Johnson, J. C.; Yan, H.; Schaller, R. D.; Haber, L. H.; Saykally, R. J.; Yang, P. *J. Phys. Chem. B* **2001**, 105, 11387.
111. (a) Göpel, W.; Schierbaum, K. D. *Sens. Actuators.* B, **1995**, 26(1-3) 1. (b) Comini, E.; Ferroni, M.; Guidi, V.; Faglia, G.; Martinelli, G.; Sberveglieri, G. *Sens. Actuators.* B, **2002,** 84(1), 26.
112. Gopel, W.; Hesse, W. J.; Zemel, J. N. **1989**, *Sensors: A Comprehensive Survey*, Vol. I, Fundamental and General Aspect, Weinheim Verlagsgesellschaft mbH, 3-4.
113. (a) Shimizu, Y.; Maekawa, T.; Nakamura; Y. Egashira, M. *Sens. Actuators, B,* **1998,** 46(3) 163. (b) Semancik, S.; Cavicchi, R. *Acc. Chem. Res.* **1998,** *31*(5), 279. (c) Shenhar, R.; Rotello, V. M. *Acc. Chem. Res.* **2003**, *36*(7), 549.
114. (a) Raju, A.R.; Rao, C.N.R. *Sens. Actuators B*, **1991**, 3/4 365. (b) Ohgi, H.; Maeda, T.; Hosono, E.; Fujihara, S.; Imai, H. *Cryst. Growth Des.* **2005**, *5*(3), 1079.
115. (a) Wang, Z. L. *Adv. Mater.* **2003** 15(5) 432. (b) Toupance, T.; Babot, O.; Jousseaume, B.; Vilaca, G. *Chem. Mater.* **2003**, *15*(24), 4691.
116. (a) Sberveglieri, G. *Sens. Actuators B,* **1992**, 6, 239. (b) Kolmakov, A.; Klenov, D. O.; Lilach, Y.; Stemmer, S.; Moskovits, M. *Nano Lett.* **2005**, *5*(4), 667.

117. McAleer, J. F.; Maignan, A.; Moseley, P. T.; Williams, D. E. *J. Chem. Soc., Faraday Trans.* **1989,** 1(85) 783.
118. Modinos, A. Field emission, thermionic and secondary electron emission spectroscopy, *Plenum Press*, New York (1984).
119. Stratton, R. *Phys. Rev. Lett.* **1962**, 125, 61.
120. Wentzel, G. *Zeits. f. Phys.* **1926**, 38, 518. (d) Kramers, H. A. *Zeits. f. Phys.* **1926**, 39, 828. (e) Brillouin, L. *Comptes Rendus* **1926**, 83, 24.
121. Xu, N. S.; Huq, S. E. *Mater. Sci. & Eng.* R **48**, 47-189 (2005).
122. (a) Arnold, M.; Avouris, Ph.; Pan, Z. W.; Wang, Z. L. *J. Phys. Chem. B* **2003**, *107*, 659. (b) Comini, E.; Faglia, G.; Pan, Z. W.; Wang, Z. L. *Appl. Phys. Lett.* **2002**, *81*, 1869.
123. (a) Bai, X. D.; Wang, E. G.; Gao, P. X.; Wang, Z. L. *Appl. Phys. Lett.* **2003**, *82*, 4806. (b) Huges, W.; Wang, Z. L. *Appl. Phys. Lett*. **2003**, *82*, 288.
124. (a) Ma, C.; Ding, Y.; Moore, D.; Wang, X.; Wang, Z. L.; *J. Am. Chem. Soc.* **2004**, 126(3), 708. (b) Na, C. W.; Bae, S. Y.; Park, J.; *J. Phys. Chem. B.* **2005**, 109(26); 12785.
125. Schwartz, D. A.; Norberg, N. S.; Nguyen, Q. P.; Parker, J. M.; Gamelin, D. R.; *J. Am. Chem. Soc.* **2003**, 125(43), 13205.

Chapter 2

A Novel Route towards the Shape Selective Synthesis of SnO_2 Nanostructures: Bipyramids, Cubes and Wires *

This chapter primarily deals with a novel route for preparing shape selective SnO_2 nanostructures like bipyramids, cubes and wires from the same precursors. Detailed characterization using various analytical techniques elucidates the role of various interactions between the nuclei of the building blocks (RuO_2 and SnO liquid droplets at the prevailing temperatures). The presence of an inert (carrier) gas and the amount of RuO_2 in the initial reaction mixture helps in gaining adequate control over these interactions at well defined temperatures. The shape dependent preferential growth directions observed in SnO_2 structures indicates that a control over the growth position and shape could be achieved by changing the initial positions of Ru and its concentration.

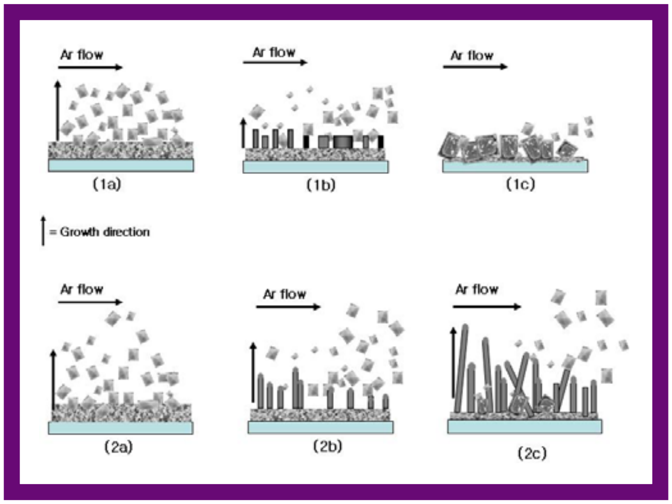

---

* A part of the work presented in this chapter has been published in “***J. Phys. Chem. B*** **2004**, *108***,** 14815, and another part in **J. Phys. Chem. B 2005***, 109*(25), 12297”.

2.1. Introduction

The shape and texture of semiconducting oxides has a substantial effect on their optical[1], electrical[2], and gas sensing[3] properties. For example, several anisotropic semiconducting nanostructures have been prepared in the form of nanowire superlattices (group III−V and group IV materials). Further, photoluminescence, electrical transport and electroluminescence measurements of single-nanowire show the unique photonic and electronic properties of these superlattices, suggesting potential applications ranging from nano-barcodes to polarized nanoscale LEDs.[4] These architectures display new properties and enrich the selection of nano–building blocks for electrical, optical, and sensing device construction.[5] Hence an accurate control over the particle size and shape offers new application possibilities facilitating to enmesh desired characteristics in next generation materials. Tin oxide, as a wide band gap semiconducting oxide attracts an awesome interest due to its distinctive electrical, optical and thermal properties. Two unique characteristics, i.e., the variation in valence state and oxygen vacancy make tin oxide indispensable for a variety of applications including many smart and functional devices. Consequently, in a short span of last few years, various forms of tin oxide namely microwires[6], nanowires[7], nanotubes[8], nanobelts[9], and nanodiskettes[10], have been synthesized using diverse techniques of thermal evaporation, laser ablation, carbothermal reduction, solution precursor route, etc. All these studies clearly show that reduced dimensionality causes a radical change in the density of states highlighting the prominence of surface effects. Besides size and shape dependent behavior, the doping of these materials preserving the structural integrity, can also provide a far more favorable means of tailoring their properties due to their aspect ratio induced changes in the electronic structure. Doping is particularly significant in the field of electronics as illustrated in examples, like the one for constructing the contacts whose conductivity can be tailored by controlling the level of doping. Moreover, new functionality, such as emissive or rectifying junctions, can also be introduced into the nanostructure by anisotropic growth with compositional variations.[5] Thus, specific shape of the particles and the asymmetric interaction patterns on their surface could induce orientation specific exchanges at lower dimensions.

Among the various methods adopted for the synthesis of SnO_2 nanostructures, thermal vapor method is the widely exploited as it offers various advantages like low reaction time below 1h and the precise control of geometry of the materials by a simple control over the reaction parameters viz. heating temperature and duration, nature of substrate, carrier gas and oxygen flow rate.[1, 7] Usually, nanostructured growth takes place via a self-catalytic process in which the precision, prediction and reproducibility all emerge from the nature of forces between the constituent elements. The method based on the vaporization of oxide materials at high temperature requires a complex apparatus with good vacuum, precise control of temperature and gas flow and the products are generally collected at the downstream end onto a substrate or at the inner wall of alumina or quartz tube.

Because of its unique change in conductance upon the adsorption of gases, tin oxide, a wide band gap semiconductor (3.6 eV) is a promising candidate towards miniaturized, ultrasensitive chemical sensors.[11-16] The characteristics of tin oxide like the presence of cations with mixed valences and adjustable oxygen deficiency enables tuning of their structure and properties. For example Meyyappan et al.[17] have shown the synthesis of In-doped tin oxide nanowires using a carbothermal reduction followed by a catalyst mediated heteroepitaxial growth. The doping or compositional changes in nanowires can be controlled by pre-evaporation in a way similar to that in metallorganic chemical vapor deposition (MOCVD). Although several other procedures for synthesizing pristine nanowires have been recently demonstrated, the preparation of doped SnO_2 has not been reported so far, despite its tremendous significance in nanotechnology

In this chapter, we describe a simple synthetic procedure for the shape selective preparation of several dissimilar types of tin oxide structures including bipyramids (a double tetrahedron with a common plane, which is a natural habitat of rutile RuO_2 and SnO_2), cubes and wires using chemical vapor deposition employing RuO_2 as a promoter/nucleating agent. In order to understand the growth kinetics and to explore intellectual terra incognita further, we had carried out X-ray diffraction (XRD), Thermogravimetric/differential thermometric analysis (TG-DTA) and x-ray photoelectron spectroscopy (XPS) of these low dimensional structures. The results of these investigations are presented below with the help of a plausible model describing the growth mechanism. In particular, the texture coefficient values of all the structures, indexed to a tetragonal lattice, exhibit amazing variation in the preferred orientation with respect to their shapes. Although, XPS data indicate that wires and cubes have a strong SnO_2 type signal, bipyramids interestingly exhibit both SnO and SnO_2 signals and a correlation of the binding energy helps in understanding the growth kinetics of such submicron structures. More significantly, the results suggest that the bipyramids are formed due to the vapor-solid process (VS) while wires and cubes are formed by the vapor-liquid-solid (VLS) progression. In addition, the present study indicates the key role of RuO_2 as an important nucleating agent in promoting the growth of low dimensional structures of SnO_2.

2.2. Experimental Section

2.2.1. Materials

Tin (II) oxide and Ruthenium oxide were used as received from the Aldrich (99.99%), while acetone and ethanol (AR grade from Merck) were used after further purification; deionised water (16 MΩ) from Milli-Q system was used for all experiments.

2.2.2. Experimental Set-Up

Scheme 2.1 shows the experimental set-up used for the synthesis of nanowires and nanobipyramids. It consists of a tubular furnace open at one end, in which the starting material, a mixture of SnO and RuO_2 in a weight ratio of 1:0.2 was kept in the middle of the furnace. Ar was passed continuously at a flow rate of 100 ± 5 sccm (standard cubic centimeter) through the furnace upto 950°C. The material was heated for two hours and the furnace was allowed to cool naturally with uninterrupted Ar flow. The cubes and nanowires were grown on an alumina boat kept in the middle of the furnace while a nanobipyramidal structure was collected on the alumina substrates kept near the end of tube where the temperature was between 200 °C and 500 °C.

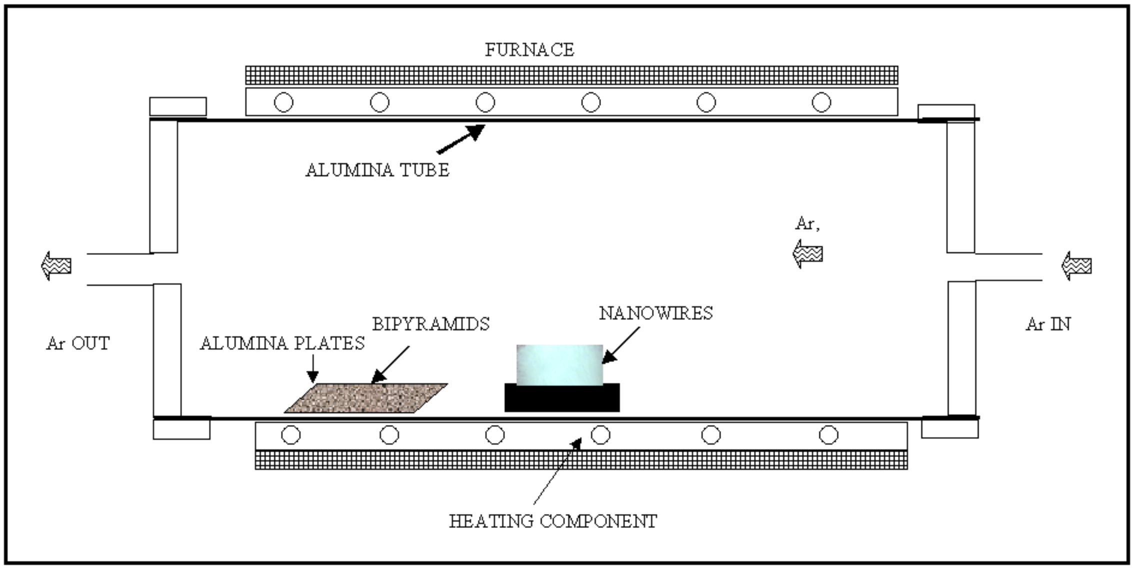

Scheme 2.1. Experimental set-up used for the synthesis of nanobipyramids, cubes and nanowires.

2.3. Structural and morphological characterization

2.3.1 X-ray diffraction

XRD was carried out on a Rigaku, D/MAX IIIB diffractometer using Cu-K_α radiation from a rotating anode x-ray generator operating at 30 kV and 15 mA at room temperature. Diffraction patterns were collected at a step of 0.02° (2θ) using a fixed Cu-Kα radiation. The background was subtracted with the linear interpolation method.

The preferred orientation of the crystallographic planes was estimated by performing the Harris analysis[18]. The texture coefficient $P(h_ik_il_i)$ and the preferred orientation of the $(h_ik_il_i)$ planes were conferred by the following relationship,

$$P(h_ik_il_i) = I\,(h_ik_il_i)/\,I_o(h_ik_il_i)\,\{(1/n)\sum I(h_ik_il_i)/\,I_o(h_ik_il_i)\}^{-1} \qquad (1)$$

for i = 1, 2, 3… n.

where, $I\,(h_ik_il_i)$ is the diffraction intensity of the $(h_ik_il_i)$ plane of the sample under investigation, $I_o\,(h_ik_il_i)$ is the intensity of the $(h_ik_il_i)$ plane of the standard sample and 'n' is the number of reflections present.

2.3.2. Scanning electron microscopy (SEM) and Energy dispersive X-ray analysis (EDAX)

The surface morphology was characterized by a Lieca Stereoscan 440 model SEM with a Kevex model EDAX system. For comparative studies, the energy of the electron beam was kept constant while analyzing all the samples. The micrographs of the samples were recorded with a 20 kV electrical high tension and 25 pA camera attached on the high-resolution recording unit.

2.3.3. High-resolution transmission electron microscopy (HRTEM)

TEM images were taken with a JEOL Model 1200 EX instrument equipped with a field emission gun at an accelerating voltage of 200 kV, magnification 389,000× and the coefficient of spherical aberration 1.35 mm. As the nanowires were large, they could be picked up on a Cu grid directly by sliding over the “as-deposited” wires. The images were digitized in the size of 256 × 256 pixels with a pixel size of 0.03994 nm and thus atomically resolved images were possible. Images were stored in the computer after digitization and power spectra were calculated so that structural analysis such as interplanar distances, angle between planes could be determined.

2.3.4. X-ray photoelectron spectroscopy (XPS)

XPS measurements were carried out on a VG MicroTech ESCA 3000 instrument at a pressure of $>1 \times 10^{-9}$ Torr (pass energy of 50 eV, electron takeoff angle 60^{o}, and overall resolution ~1 eV using monochromatic Mg Kα (source, $h\nu = 1253.6$ eV). The core level spectra of the C 1s and S 2p orbitals were recorded with an overall instrumental resolution of ~1 eV. The alignment of binding energy (BE) was carried out using Au 4f BE of 84 eV as the reference. The X-ray flux (power 70 W) was kept deliberately low to reduce the beam-induced damage. The Spectra were fitted using a combined polynomial and Shirley type background function.[19, 20]

2.3.5. Thermogravimetric and differential thermal analysis (TG-DTA)

TG-DTA was carried out in the temperature range 323-1173 K under N_2 flow at a heating rate of 5 K/min on a Perkin-Elmer thermal analyzer.

2.4. Results and Discussion

2.4.1. Shape Selective Synthesis: Bipyramids, Cubes and Wires

2.4.1. Bipyramids

SnO_2 in the cassiterite phase belongs to the $P4_2/mnm$ space group and has a ditetragonal bipyramid type of symmetry. The number of macrocrystal habits observed is approximately 10[14]. Figure 2.1 shows typical micrographs of RuO_2 doped SnO_2 nanobipyramidal structures, which also reveal their natural habitat. Upon heating the reaction mixture (RuO_2: SnO) containing 0.1 wt. fraction of RuO_2 at 950^0C for 2h, nanobipyramids are deposited on the alumina substrates that are kept in the temperature range of 200-500°C (Figure 2.1 a-g). No other structure is interestingly found in this region implying high shape selectivity of the process. Interestingly, two types of bipyramids are observed, one where the pyramid ends with a tip and the other where a small separation is present between the two opposite triangular planes, suggesting a deviation from the perfect square geometry to be a nearly rectangular one. The bipyramids are polydispersed with size varying between 100 and 800 nm. Although most of them are located flat with another end at the backside, base of the bipyramid is thin with varied dimensions suggesting the growth process to be initiated from the base, from both sides and growing further, leading to a pyramid like geometry at the end. Some of them lie in different orientations as shown in Figure 2.1f, confirming the bipyramidal nature of the structures. The TEM analysis further confirms that the bipyramids are not monodispersed in nature. Steps at the edge of the structure suggest the growth mechanism to be starting from the edge of cubical structure that is formed prior to the bipyramidal structure. Selected area electron diffraction (SAED) exhibits a kikuchi pattern that can be attributed to the uneven thickness of the structure and the orientation being not parallel to the incident beam. This is, perhaps, due to the electrons that are first scattered inelastically and then elastically from a thick crystalline sample, forming a system of kikuchi lines.

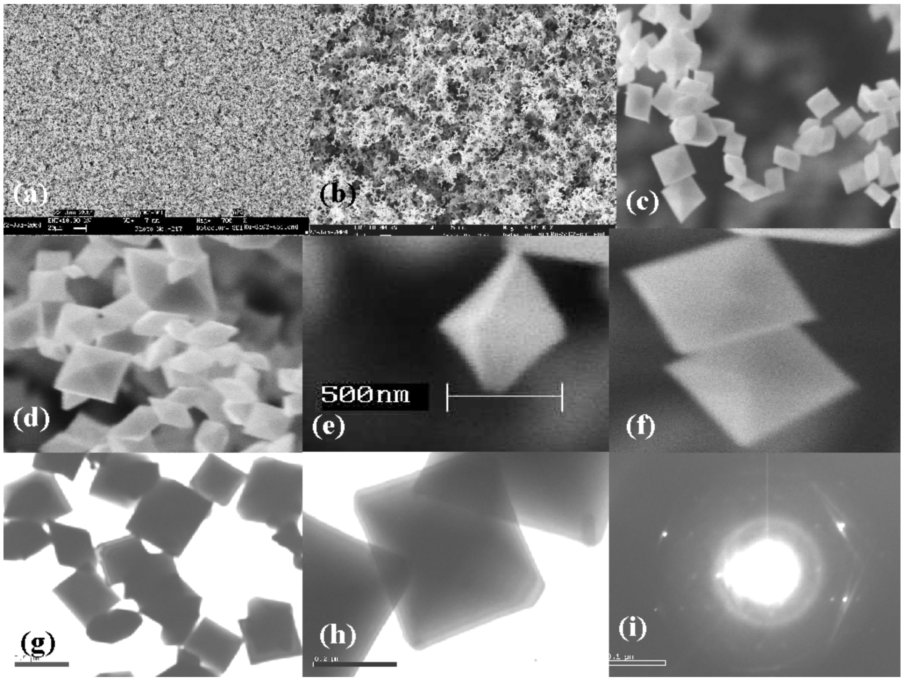

Figure 2.1. SEM images of "as-synthesized" nanobipyramids collected on alumina substrates kept downstream where the temperature is between 200 and 500°C, upon heating the reaction mixture containing 0.1 weight fraction of RuO_2; (a) to (f) shows SEM images of nanobipyramids; (g and h) reveal TEM images while (i) shows SAED of single smaller nanobipyramid

As explained in section 1.5.1, the rutile structure of pure SnO_2 is 6:3 coordinated and the bonding between atoms has a relatively strong ionic character. The tetragonal unit cell contains two Sn and four O atoms. Perpendicular to the surface in the [110] direction, the rutile structure is built up from neutral stacked layers of three alternating planes (O), (2Sn+2O), and (O) with nominal ionic charges of 2-, 4+ and 2- respectively in the surface unit cell. The termination of the SnO_2 (110) called a stoichiometric surface with these three planes is possible. Removal of the topmost bridging-oxygen atom results in the reduced (110) surface, which is the case in the nanobipyramidal structure.

2.4.2. Cubes

In case of samples with a low wt. % of RuO_2 in the starting material, non-uniform cubical structures are grown on the substrate containing the reaction mixture (Figure 2.2). However, with an increase in the RuO_2 percentage in the starting material, the cubes get slowly transformed into nanowires implying Ru playing a crucial role as a promoter for 1D growth of SnO_2 nanowires. Two types of cubes are observed (RuO_2 - 1wt %), one with similar upper and lower surface having dimensions of a = b = 10-20 μm and c = 1-3 μm and detailed analysis suggests that the cubes are porous in nature with a diffused boundary. Moreover, the extent of porosity varies from cube to cube that can be attributed to the non-homogeneity of RuO_2 in the starting material. Further, the cubical edges are likely to be formed first, followed by there filling to give a complete cubical morphology. The other cubical structure has one surface slightly shorter than the opposite surface, called a biscuit shape, which in the present case accounts nearly 10% of total structures. Interestingly, no such structure formation is observed when experiments are carried out under similar conditions with pure SnO and RuO_2 alone, which further confirms the role of RuO_2 as a nucleating aid.

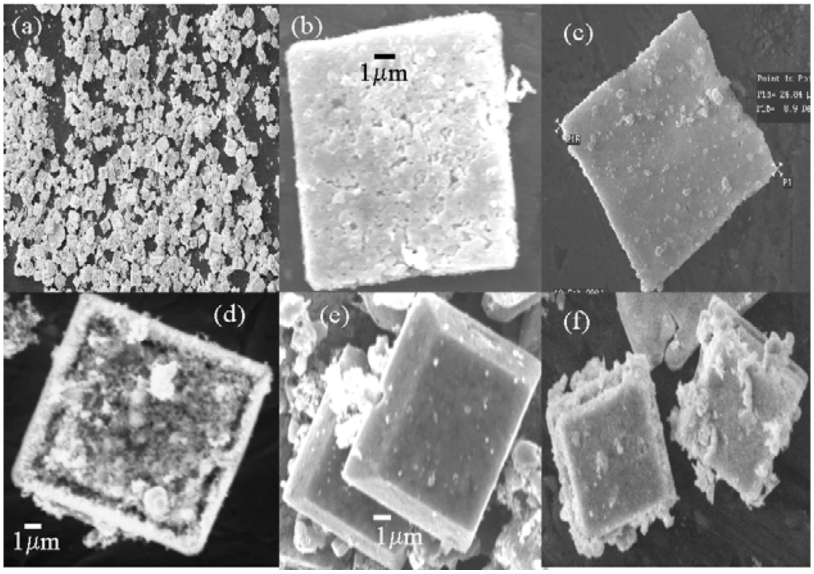

Figure 2.2. SEM images of SnO_2 cubes synthesized at 950°C with 1 wt.% of RuO_2 in the reaction mixture; (a-d) show general images while (e and f) reveal biscuit shape.

2.4.3. Wires

Figure 2.3 shows typical images of the “as-synthesized nanowires” formed by heating the reaction mixture containing 20 wt. % RuO_2. Most of the wires appear rather straight, exhibiting smooth sidewalls and detailed examination shows that the wires have diameter between 100-900 nm and length of the order of <1 mm, indicating an aspect ratio of ~1000 (Figure 2.3b). This large length of the wire is particularly significant in the field of electronics for making the contacts whose conductivity can be tailored by controlling the level of doping. It is also seen that some of the wires are transformed to a highly porous structure consisting of interconnected nanocrystallites (~5 nm diameter) due to the incomplete 1D growth, further supporting the role of Ru as a nucleating agent (Figure 2.3c). As these nanowires are large, they can be easily picked up on a Cu grid directly by sliding over the ‘as-synthesized’ wires on alumina substrates. Figure 2.3d shows the TEM image of RuO_2 doped SnO_2 nanowires. The wires are not, however, monodispersed in nature with diameter varying between 100-900 nm. A liquid droplet equilibrated with the RuO_2 and SnO vapors is likely to form first under the reaction conditions directing the growth of SnO_2 into nanowires. Figure 2.3f shows the SAED and most of the wires exhibit a kikuchi pattern like that of the nanobipyramid structure implying the higher crystallinity.

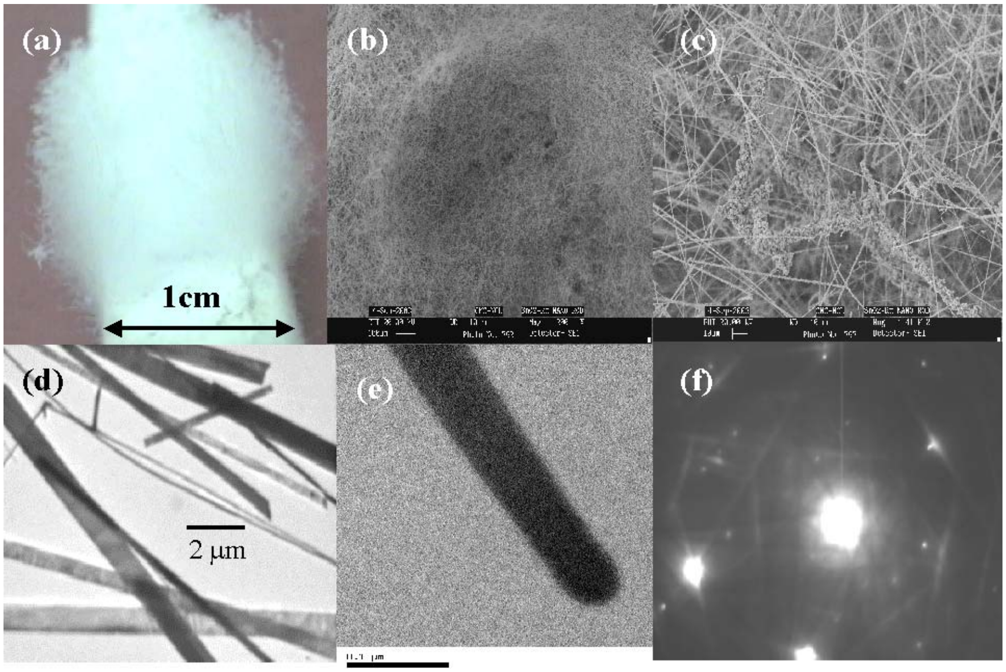

Figure 2.3. Morphology of as-synthesized nanowires; formed by heating the reaction mixture containing 20 wt. % RuO_2 (a) photograph, (b and c) SEM images and (d) TEM images of nanowires; (e) the rounded tip is clearly seen in the TEM image of a single wire; (f) SAED pattern of a single wire of diameter 300 nm.

2.5. Structural and morphological characterization

Figure 2.4 depicts the XRD patterns of different forms of SnO_2 nanostructures along with the commercial SnO_2 (Aldrich 99.99%) powder. The presence of characteristic SnO_2 peaks, indexed to a tetragonal lattice, without any RuO_2 or mixed oxide, indicates single-phase formation. One peak corresponding to Al (200) can also be identified which is attributed to the aluminium sample holder used in XRD system. A comparison of the relative intensities of samples with their standard values indicates the existence of a shape dependent preferential growth in different planes. Interestingly, in bipyramids, cubes and wires, the preferential growths are in (101), (110) and (211) crystal directions respectively. (Table 2.1) We propose that such different shapes are triggered by the presence of RuO_2 along with metallic tin droplets acting together as nucleating aids. When all the SnO grains initially are embedded in RuO_2, the growth is supposed to trigger through a liquid droplet at those prevailing temperature (>500 °C). This liquid droplet is composed of higher RuO_2 and lower SnO concentrations, and is likely to generate the reaction conditions directing the growth of SnO into wires, cubes and bipyramids.

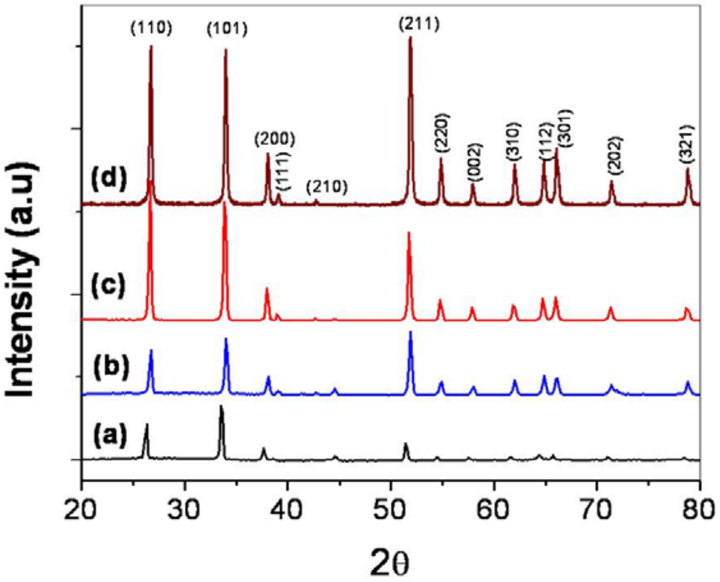

Figure 2.4. XRD patterns of different forms of SnO_2 (a) bipyramids, (b) wires, (c) cubes and (d) commercial SnO_2 (Aldrich 99.99%) powder exhibiting single-phase formation.

Table 2.1. The texture coefficient values for the different structures calculated using Harris analysis (equation 1) [18].

Sr. No	Planes	Texture Coefficient value		
		Wires	**Bipyramids**	**Cubes**
1	(110)	1.807	2.814	3.144
2	(101)	2.305	4.264	2.672
3	(200)	0.681	0.895	0.691
4	(211)	2.619	1.279	1.980

The lattice constants (Table 2.2) of all these interesting structures are further determined to understand the strain dependent properties. As depicted in Table 2.2, larger lattice parameters are observed for bipyramids (a = 4.750(3) Å and c = 3.199(3) Å) as compared to that of commercial SnO_2 powder (a = 4.730(1) Å, c = 3.183(1) Å) although, no marked variation in the lattice parameters, interestingly, is observed for cubes and wires. The unit cell volume for the structures as revealed in Table 2.2 shows that for wires and cubes there is no dramatic variation while for bipyramids an increase in the cell volume by 1.3 % is observed. The a/c ratio, which is a measure of lattice distortion, does not show any effective variation implying the stability of the structures.

Table 2.2. Values of lattice constant, a (Å) and c (Å), a/c ratio, crystallite size (nm) calculated using the Scherer equation; the cell volume ($Å^3$) is also indicated in the last column.

Sr. No	Lattice Parameters	Bipyramids	Wires	Cubes	SnO_2-aldrich
1	a (Å)	4.750(3)	4.728(3)	4.733(1)	4.730(1)
2	c (Å)	3.199(3)	3.183(3)	3.181(1)	3.183(1)
3	V ($Å^3$)	72.2(1)	71.1(1)	71.29(4)	71.23(3)
4	a/c ratio	1.484	1.485	1.487	1.486
5	Crystallite size (nm)	50.26	46.94	62.80	57.1
6	Uniform strain (110)	6.08×10^{-3}	-7.75×10^{-3}	3.08×10^{-3}	-

Analysis of the effect of dopant molecule on the electronic state of host material is of particular importance to understand the growth kinetics and hence XPS studies were carried out on all these structures. Accordingly, Figure 2.5 shows the deconvoluted

C1s peaks for all the structures of SnO_2. In all the cases representing XP spectra, the hollow circles denote the original data and solid lines represent the fitted curves and the deconvoluted individual peaks of different species present in the sample. All the binding energy positions of the elements are listed in Table 2.3. For commercial SnO_2, the spectrum can be deconvoluted into three peaks at 285, 286.9 and 289.1 eV corresponding to C1s, and adsorbed carbon species respectively. No signal corresponding to Ru is observed for commercial SnO_2 and cube samples, while for wires and bipyramids the peaks at 282.0 and 282.8 eV respectively confirm the presence of Ru in the submicron structures. These peaks can be attributed to the thermodynamically stable oxide i.e., RuO_2, signifying the binding energy of Ru $3d_{5/2}$ corresponding to Ru^{4+}.[21]

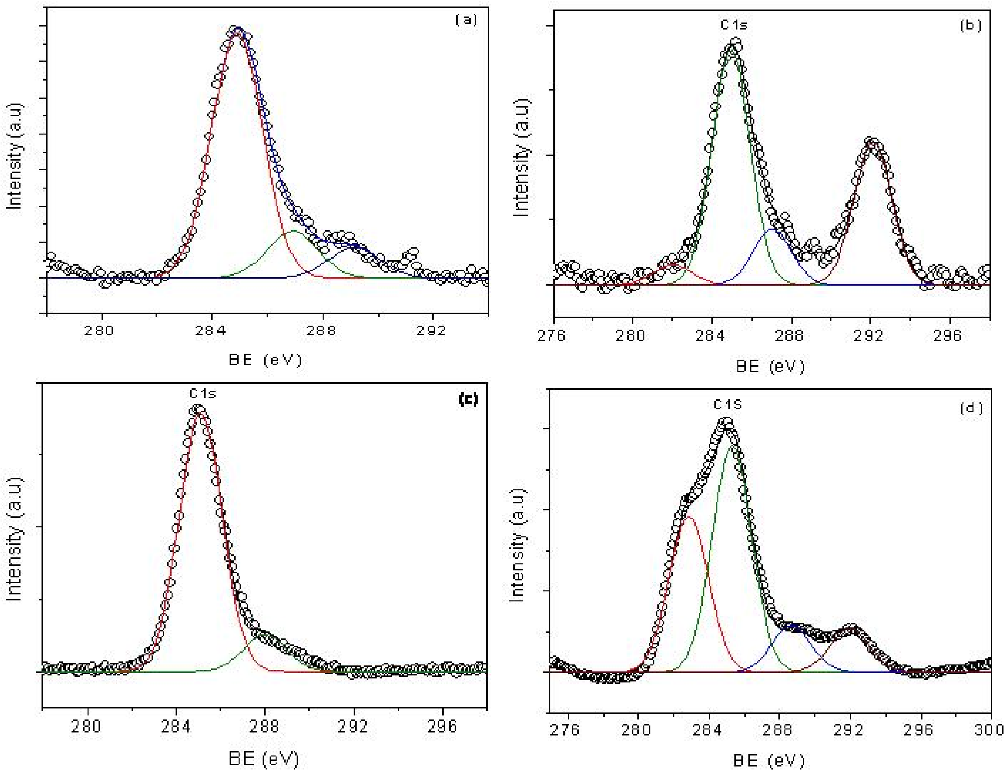

Figure 2.5. The deconvoluted C1s peaks for all the structures of tin oxide (a) commercial SnO_2 (Aldrich 99.99%) powder, (b) wires, (c) cubes and (d) bipyramids.

Table 2.3. All the binding energy positions of the element present in different submicron structures of tin oxide.

Species	**BE (eV)**			
	SnO_2-Aldrich	**Bipyramids**	**Cubes**	**Wires**
C1s	285 286.9 289.1	285.2 288.6 291.9	285 287.9	285 287 292.1
Ru 3d	-	282.8	-	282
Sn 3d	486.6 495.1	484.5 487.3 493.5 496.6	486.4 494.9	486.1 494.6
O 1s	530.7 532.5 (minor)	529.6 532.1 534.1	530.5 532.5 (minor)	530.3 532 (minor)

Figure 2.6 shows separate $Sn3d_{5/2}$ and $Sn3d_{3/2}$ signals for the Sn present in these structures. Commercial SnO_2, freshly prepared wires and cubes all exhibit two prominent peaks with a symmetric Voigt profile corresponding to the binding energies of $Sn3d_{5/2}$ and $Sn3d_{3/2}$ respectively. However, the presence of Sn^{2+} cannot be ruled out because the energy of $Sn3d_{5/2}$ for SnO is very close to that for SnO_2 (0.7 eV). The peak to peak separation of Sn 3d peaks for commercial SnO_2 is 8.48 eV while for wires and cubes, this amount to 8.48 and 8.79 eV respectively. For the bipyramids, four peaks at the BE of 484.5, 487.3, 493.5 and 496.6 eV are observed corresponding to metallic Sn and SnO_2 3d levels respectively. The binding energy difference between the Sn^{4+} and Sn^o is 2.2 eV as in accordance with the literature values.[18] The broadening on the higher binding energy side of the peak can be attributed to the doping effect.

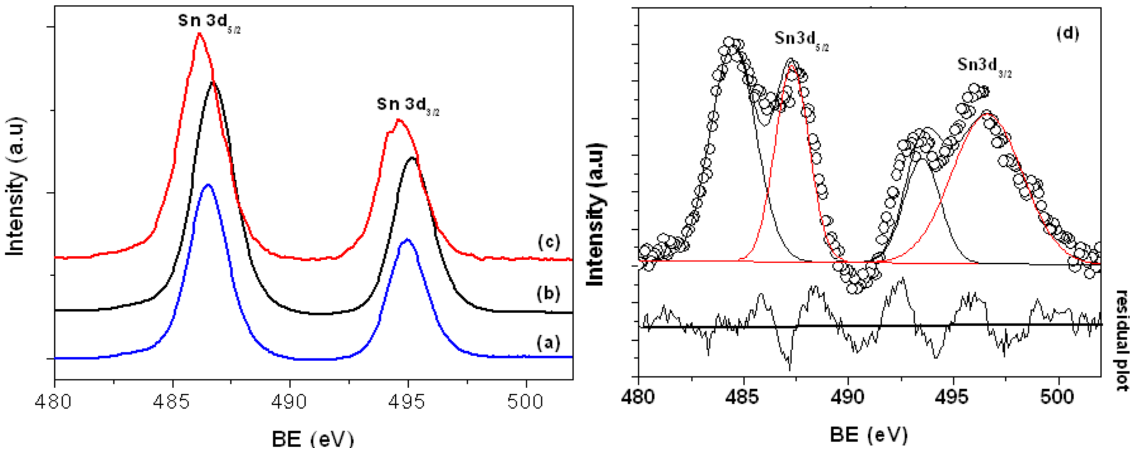

Figure 2.6. The separate $Sn3d_{5/2}$ and $Sn3d_{3/2}$ signals for Sn in (a) cubes, (b) commercial SnO_2 (Aldrich 99.99%) powder (c) wires and (d) bipyramids.

Figure 2.7 depicts the spectra for O1s signal. For the commercial SnO_2, freshly prepared wires and cubes, the O1s major peak maxima occurs at BE of 530.7, 530.3 and 530.5 eV respectively and are attributed to the lattice oxygen in the SnO_2 crystal structure.[23] The existence of other minor peaks can be attributed to the adsorbed oxygen species. In case of bipyramids, the broad peak can be deconvoluted into three peaks at BE of 529.6, 532.1 and 534.0 eV corresponding to the oxygen of RuO_2, SnO_2 lattice and the adsorbed oxygen respectively. Analysis of the difference between the energies of the $Sn3d_{5/2}$ (E_1) and O1s (E_2) electronic levels characterizing the Sn-O bond energy suggests that the incorporation of Ru in the SnO_2 matrix does not cause any noticeable change in the ΔE value for wires and cubes. In contrast, for bipyramids the change in the ΔE value is 0.9 eV as compared to that of commercial SnO_2, suggesting that Ru species in the bipyramidal structures alter the Sn-O bond energy. This is in accordance with the results of Rumyantseva et al., where they have observed a shift in ΔE when Ru is present in 1.1-1.2 at. %, thus further confirming the incorporation of Ru^{4+} into the Sn^{4+} positions changing the Sn-O bond energy.[22] Moreover, RuO_2 evaporates at low temperature compared with the SnO and hence during the synthesis of bipyramids, vapors are likely to have excess of RuO_2 which are relocated through the carrier gas to the substrates kept downwards. Consequently, the substrate is left with lower concentration of Ru on its surface that acts as nucleating centers for the growth of wires and cubes. Thus, RuO_2 in its initial position acts as nucleating centers for the anisotropic growth that continues due to the self-catalyzed growth process in Sn-O system.

Moreover, the values of the relative intensity of adsorbed oxygen are dependent on the grain size - smaller the grain size is, higher is the intensity of the adsorbed oxygen peak. Thus a comparison of the relative adsorbed oxygen peak intensities of all the structures suggests that the grain size decreases from cubes to bipyramids to wires further supporting the conclusions derived from the XRD results.

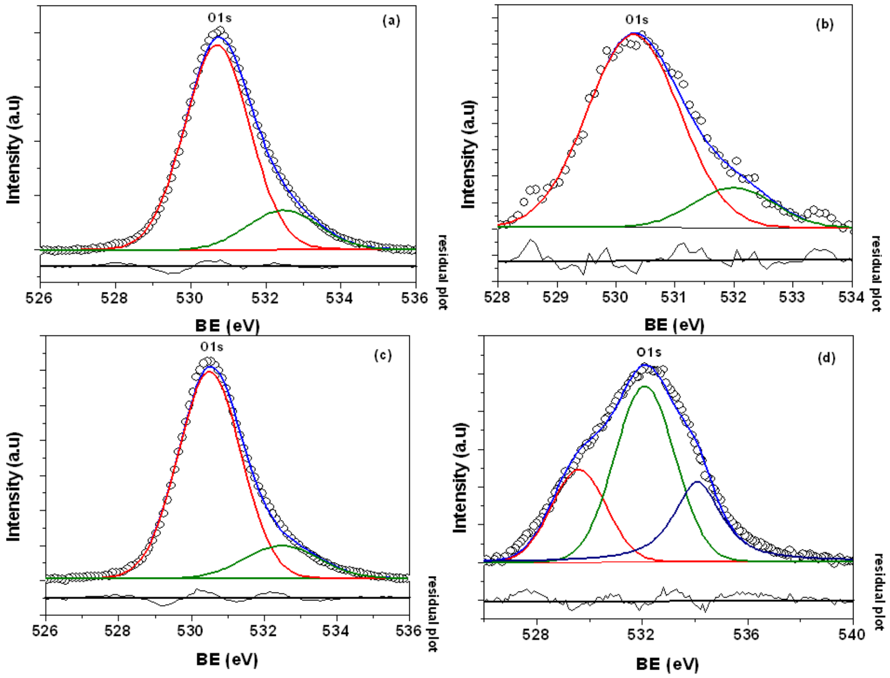

Figure 2.7. The spectra for O1s for different forms of SnO_2 (a) commercial SnO_2 (Aldrich 99.99%) powder, (b) wires, (c) cubes and (d) bipyramids.

2.6. Effect of reaction composition, temperature, time and carrier gas

In order to understand the role of RuO_2, further experiments were carried out with and without different weight percentage of RuO_2 in the starting material. The presence of RuO_2 in the reaction mixture leads to the transformation of cubical structure into deformed porous structure. With increase in RuO_2 percentage, there is an increase in the number of nucleating sites leading to the formation of small nanobelts or nanowires with smaller aspect ratios. The deformity in cubical structure, nanowire percentage and their aspect ratio, all are found to increase with the amount of Ru content. At higher weight percentage (2 wt%), nearly 80% of material contains nanowire with few cubes and small irregular shaped granules. With further increase upto 2.2 wt% the total yield of nanowires is increased to 90%.

Further, to understand the effect of temperature on nanowire growth kinetics, several experiments were designed and performed with the optimized reaction mixture (2.2 wt%, RuO_2). Accordingly, Figure 2.8 shows the SEM images of these samples prepared at different temperatures from 800-950^{0}C for 2 h. Remarkably, only cubes are observed for temperatures as low as 800^{0}C, identical to the products obtained when pure SnO is heated at 1150^{0}C, thus supporting our assertion of the role of RuO_2 as a promoter for growth. As the temperature increases from 800^{0}C, some nanowires with no smooth sidewalls along with cubes are formed indicating incomplete oxidation. With a further increase in temperature, both yield of nanowires and their aspect ratio are found to improve. For example, at a temperature of 950^{0}C, nearly 90% of all the samples are in the form of nanowires, implying this temperature to be optimum for nanowire formation. It is interesting to note that the results obtained both by increasing the amount of RuO_2 and the temperature variation are identical pointing out to the optimum temperature of 950^{0}C and with 2.2 wt% RuO_2. These results clearly demonstrate the importance of temperature and the amount of RuO_2 in the reaction mixture, as crucial factors, which govern the final shape, aspect ratio and yield.

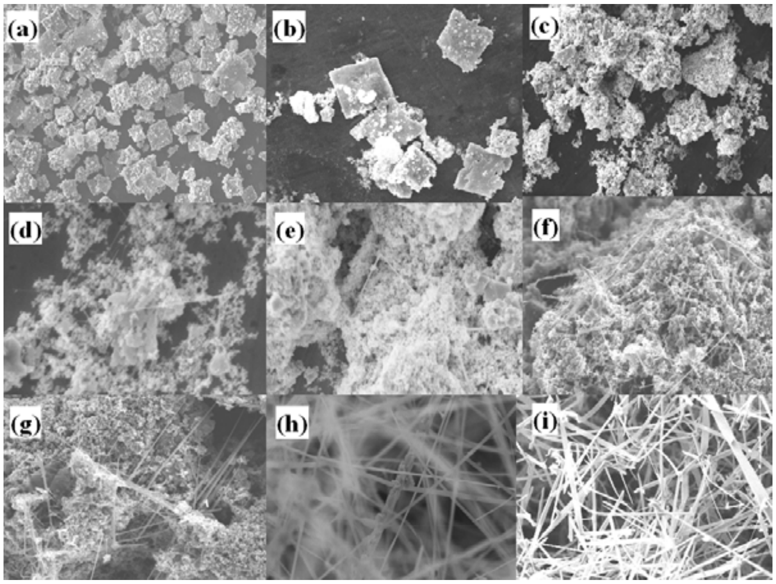

Figure 2.8. SEM images of sample prepared with 2.2 wt% RuO_2 in SnO heated at different temperature (a, b) 800 (c, d) 850 (e-g) 900 and (h) 950^{0}C.

Additional experiments carried out for different time intervals with the above reaction mixture provide further insight into the growth mechanism and these results are in accordance with the results obtained by varying the temperature and RuO_2 content. For example, when the reaction is deliberately stopped after five minutes, only the deformed cube like geometry is observed as shown in figure 2.9 while an increase in the duration enhances the amount of nanowires**.** In addition, the quality as well as the aspect ratio increases leading to a complete nanowire growth by the end of 2 h. During the initial growth, grains of about 100-250 nm are first formed, which attach to themselves forming a long chain of interconnected structure. Subsequently, more number of grains coalesces with time to form a nanowire with a higher aspect ratio and the number of grains taking part in the nanowire formation decides the final shape and the aspect ratio.

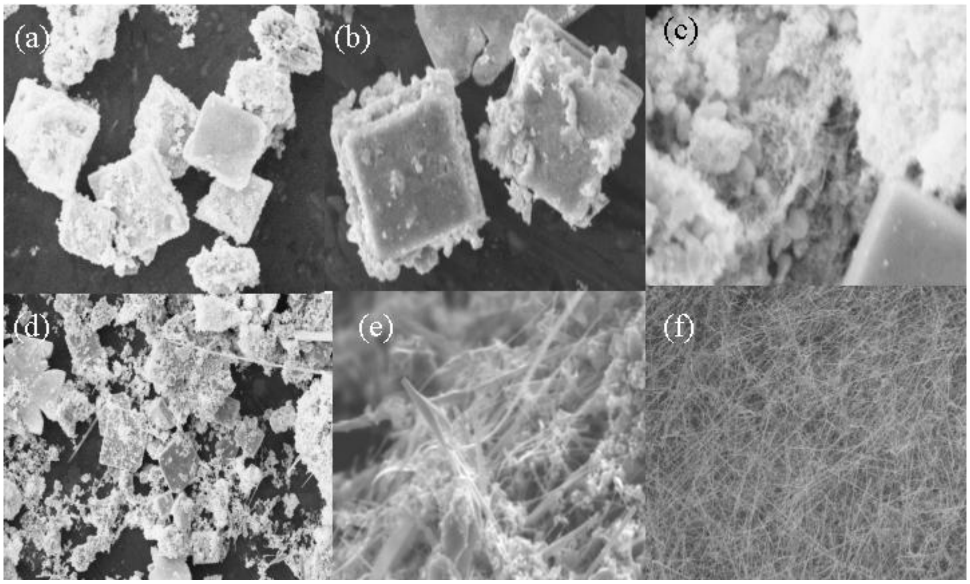

Figure 2.9. SEM images of samples prepared with 2.2 wt% RuO_2 in SnO heated at 950^{0}C for different time interval (a) 5 min, (b) 30 min, (c) 60 min, (d, e) 90 min and (f) 120 min.

After optimizing the reaction composition, temperature and time, we proceeded further to study the effect of carrier gas. Figure 2.10 shows the SEM images of samples heated in different environments of N_2 and O_2 by keeping all the other process parameters identical. Interestingly, only cubical structures are formed in O_2 environment although structures are somewhat distorted with plenty of non-uniformity in shapes implying the importance of Ar environment during the nanowire formation. However for the case of N_2 as a carrier gas, nanowires are formed along with distorted cubes, although the yield of total nanowire is 10%, which is still small compared to the case of synthesis under Ar. This shows that removal of O_2 by Ar to cause negligible oxygen partial pressure plays a very crucial role in deciding the yield and quality of the nanowires.

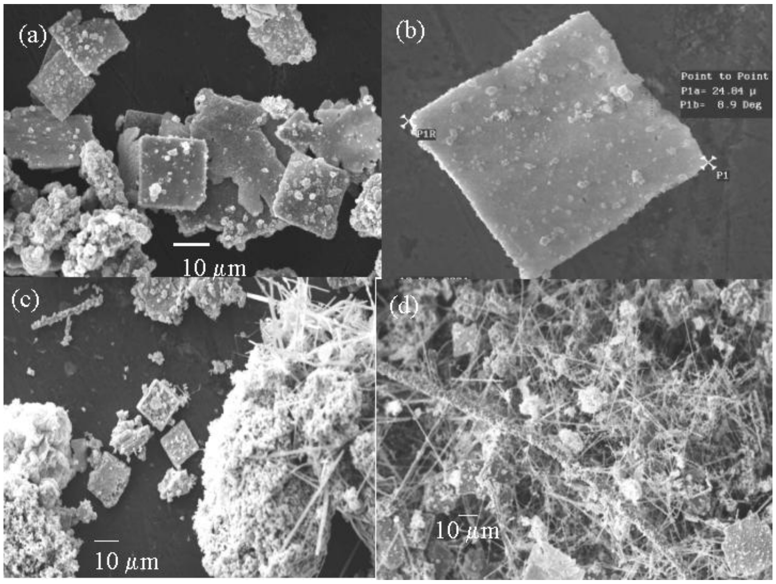

Figure 2.10. SEM images of sample prepared with 2.2 wt% RuO_2 in SnO heated in different environment of (a-b) O_2 and (c-d) N_2. From the images it is clear that the yield of wires using both O_2 and N_2 is less as compared with Ar.

2.7. A Plausible Growth mechanism

In order to understand the growth kinetics, SEM images (figure 2.11(a-d)) were taken at different areas on the surface of the "as-synthesized" nanowires. At the edge of the substrate as shown in Figure b, c and d, a large number of nanowires are found to grow on a single wire resembling a fractal growth common in nature. Initially all the SnO grains are assumed to be covered from all sides by RuO_2 and the growth is supposed to take place through a liquid droplet composed of more of RuO_2 and less of SnO vapors, which is likely to form first under the reaction conditions directing the growth of SnO into nanowires. The oxygen partial pressure is sufficient for the formation of SnO_2. When the length of the wire grown is sufficiently high, it breaks off from the central main wire, which is supported by figures c and d (taken from different distances from the periphery, approaching towards the center). In the central region, no branched network is observed and interestingly all the nanowires exhibit smooth edge and appear rather straight. Thus the growth process is assumed to be initiated at all points as indicated by the traces of branched network appearing at the end. This signifies the important role of Ru as a nucleating aid during the formation of nanostructures.

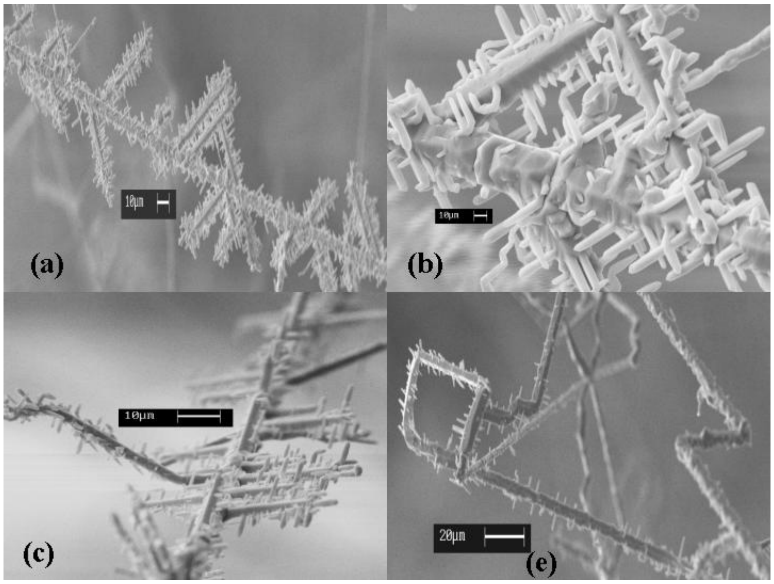

Figure 2.11. SEM images of SnO_2 nanowires (a-d) taken at different distances from the periphery approaching the center of alumina substrate

In order to further understand the role of RuO_2, we have carried out TG-DTA of these structures. Figure 2.12 depicts the thermal profiles of reaction mixtures, pure SnO and RuO_2 under Ar environment. Their SEM images taken immediately after TGA are also shown in order to correlate the morphology with weight loss. A gradual weight loss of 2.7 % upto 510 ^oC is observed for pure SnO, which could be attributed to the formation of metallic tin droplets by the disproportion reaction,

$$\mathbf{2SnO \rightarrow 2Sn + O_2} \qquad \text{-(2)}$$

This is followed by a 7% increase in the mass upto 900 ^oC, owing to oxygen uptake and the formation of SnO_2 as per the equation:

$$\mathbf{Sn + O_2 \rightarrow SnO_2} \qquad \text{-(3)}$$

In comparison, a total weight loss of 10% is seen for pure RuO_2, which could be attributed to the following reaction,

$$3RuO_2 \rightarrow Ru_3O_4 + O_2 \qquad \text{-(4)}$$

For the reaction mixture containing SnO and RuO_2, however, a weight loss of 1.4 % upto 520 °C (equation (2) and (4)) is observed followed by an increase in weight of about 2 % upto 800 °C. Thus the overall reaction could be expressed as

$$Sn + 3RuO_2 \rightarrow Ru_3O_4 + SnO_2 \qquad \text{-(5)}$$

The appearance of maximum at 800°C suggests the predominance of equation (4) as compared with equation (2). Thus it can be considered that metallic tin droplets are formed along with Ru_3O_4 inside the reaction chamber and at high temperature (900 °C) and low oxygen partial pressure, which serve as both catalyst and active sites for SnO_2 vapor adsorption and subsequent SnO_2 deposition with a concomitant Ru incorporation into the structure. The DTG analysis as depicted in Figure 2.12 (b) shows two peaks for pure SnO at 435 °C and 487 °C respectively, which correspond to the points of maximum slope on TG curves upto 561 °C, where the rate of weight change is minimum. The RuO_2 sample shows a peak around 210 °C while the reaction mixture exhibits two peaks centered at 302 °C and 465°C respectively. The SEM images taken after the TG-DTG studies for pure RuO_2 do not show any distinct morphological features except a large number of irregular shaped particles (Figure 2.12 (c)), although in the case of pure SnO only cubical structures are observed (Figure 12 (d, e)). In contrast, cubes with bipyramid like (Figure 2.12 (f, g)) feature and rod like geometry within (Figure 2.12 (h, i)), are observed for the reaction mixture further indicating that the bipyramid and rod structures are likely to be formed from the onset. However, being a static system, these structures grow further to attain cubical morphology along with traces of persisting bipyramids and wires. Our studies further demonstrate the significance of the amount and distribution of RuO_2 in the reaction mixture governing the shape selectivity during the growth process.

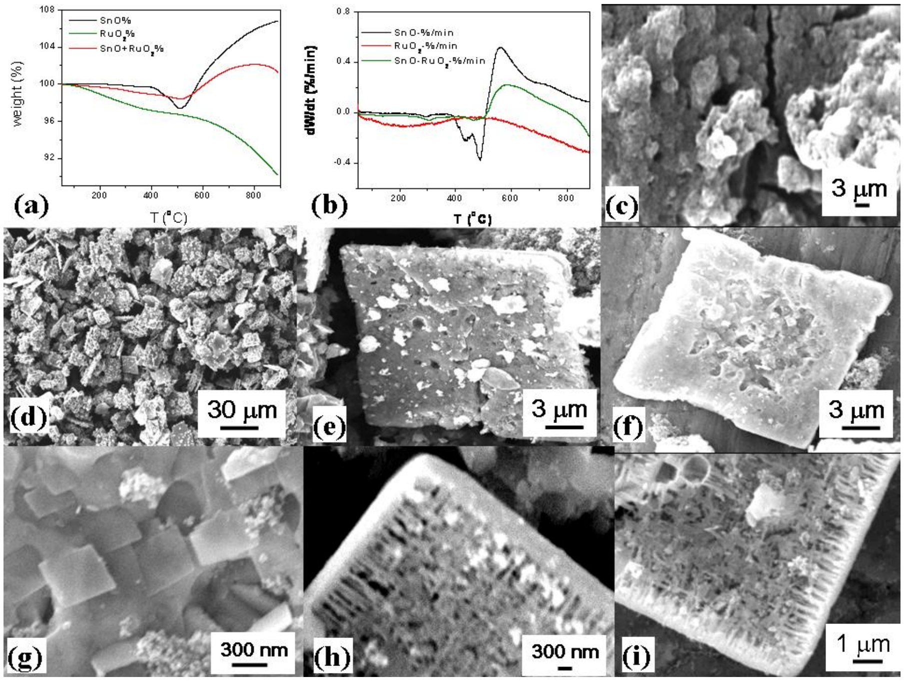

Figure 2.12. (a) TGA- (b) DTA curves for the reaction mixture of SnO and RuO_2, pure SnO and RuO_2 under Ar environment. The SEM images of (c) Pure RuO_2, (d-e) pure SnO and the reaction mixture, showing (f-g) pyramid like and (h-i) wire like geometry taken immediately after TGA-DTG studies.

Based on the above experimental results we suggest a possible model for the growth, where atomic clusters i.e. aggregates of atoms and/or molecules are in the size range from a few to thousands of the components. Their structural and electronic properties bear no resemblance either to the atoms they are composed of, or to solids or structures they can eventually grow.[23] The growth mechanism of 1D SnO_2 structures prepared by thermal evaporation is very well described by the vapor-liquid-solid (VLS) model.[24.25] It is assumed that metallic tin droplets act as catalysts as well as active sites for SnO_2 vapor adsorption and subsequent growth-deposition as confirmed by the presence of spherical particles at the tip of these structures (Figure 2.13). Initially all the SnO grains are assumed to be embedded in the RuO_2 and the growth process gets initiated via the evaporation of a liquid droplet comprising higher concentration of RuO_2 and lower SnO. SnO_2 and RuO_2 both have natural habitats of octahedral and bitetragonal symmetries, and hence the vapors are most likely to be condensed in the bipyramidal form. In addition, the fraction of RuO_2 still residing on the substrate, acts as a structure-directing agent, initiating the wire growth, which is sustained by the self-catalyzed growth process. (Scheme 2.2, Figure 2.14.) The carrier gas, Ar, carries the bipyramids to the substrates kept downward stream, where the temperature varies between 200 - 500 °C. With a negligible amount of RuO_2 (6 wt. %) in the reaction mixture, the appearance of biscuit shaped cube suggests that the growth is initiated by the slow evaporation, perhaps directed upwards. As RuO_2 has higher vapor pressure[26] the lower concentration residing on the surface is insufficient for wire formation and hence gives favorable conditions for cubical form. The sharp edge to the cubical structure is given by the wires. Thus the results propose that the bipyramids are formed due to the vapor-solid process (VS) while wires and cubes are formed due to the vapor-liquid-solid (VLS) process. The change in the flow rate does not have a noticeable effect on the morphology of cubes or wires. On the other hand, experiments carried out with different amount of RuO_2 in the reaction mixture clearly indicate that the yield of wire increases with RuO_2 content along with a decrease in the extent of cubical structures.

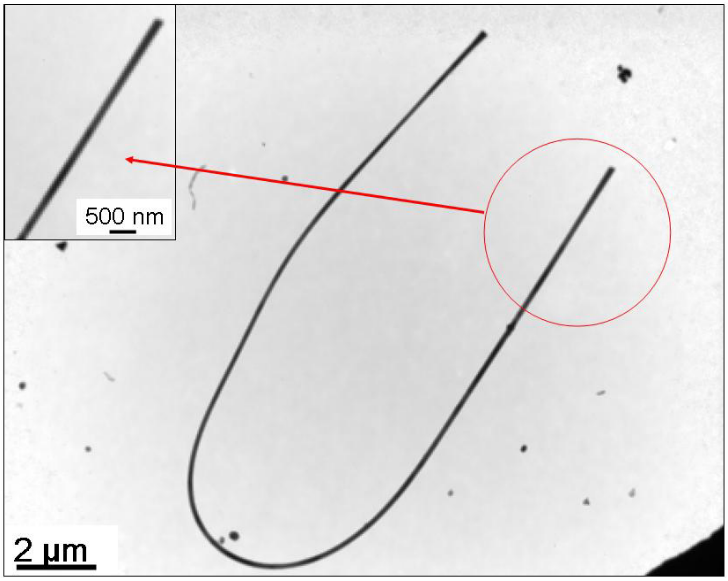

Figure 2.13. TEM image of a single wire, the spherical tip of which confirms the growth mode belonging to vapor-liquid-solid process.

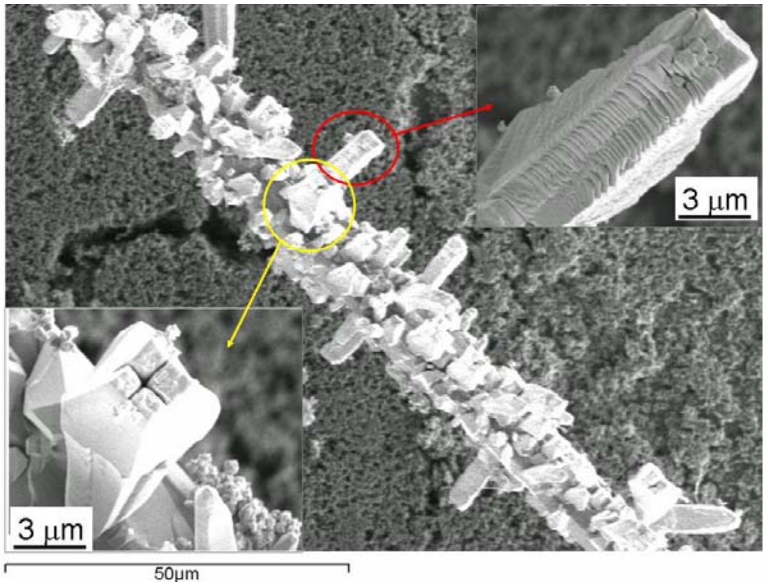

Figure 2.14. SEM images of sample prepared with 2.2 wt% RuO_2 in SnO, illustrating the steps involved in the growth processes. A single wire, on which different wires protrude out confirming the initiation of growth in all possible directions, is clearly indicated. Black circle: Stacking of cubical structures to give wires; white circle: simultaneous growth of four wires with traces of octahedral crystals.

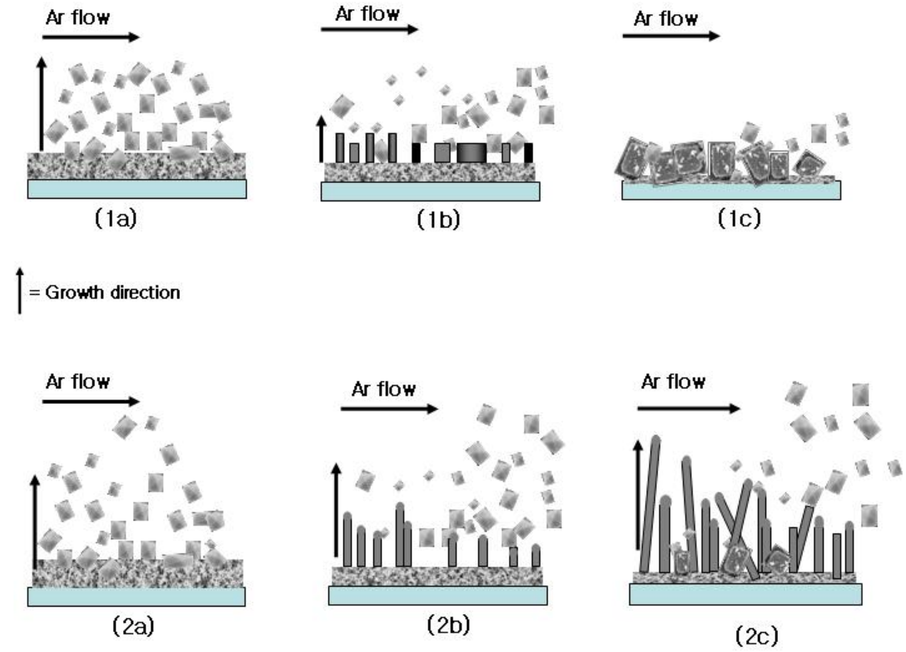

Scheme 2.2. Schematic illustration of the growth of bipyramids along with cubes (1 (a-c)) and wires (2 (a-c)). (1a) Evaporation of the SnO and RuO_2 atoms at high temperature and the formation of bipyramids, (1b) Scarcity of RuO_2 lead to the insufficient growth of wires with low

ambient pressure, and the main mechanism of cube growth is absorption. (1c) Formation of cubes whose envelop is given by the wires that are formed.

(2a) Evaporation of the SnO and RuO_2 atoms at high temperature and the formation of bipyramids. (2b) Bipyramids are taken away by the carrier gas to the substrates kept downwards and the initial growth of wires. (2c) When the ambient pressure is high, wires grow up mainly by the coalescence mechanism due to the high probability of collisions among droplet, growth process is continued further by the self catalyzed mechanism, bipyramids percentage on the surface decreases as mostly they are carried away to the substrates kept downstream.

The growth mechanism of 1D SnO_2 nanostructures prepared by thermal evaporation is very well described by the vapor-liquid-solid model.[7] It is assumed that the tiny liquid metallic tin droplet acts as a catalyst as well as the active site for the SnO_2 vapor adsorption and subsequent deposition. The presence of spherical particles at the tip of nanostructures [tip growth mechanism] confirms the process and RuO_2 is assumed to play a crucial role for nucleating the nanostructure formation. With a negligible amount of RuO_2 in the reaction mixture, the appearance of biscuit shaped cube suggests that the growth is initiated by slow evaporation directed upwards. However, with the increase in RuO_2 percentage the cubes appear to be more porous and deformed further supporting the process. Initially all the SnO grains are assumed to be covered from all side by the RuO_2 and the growth is supposed to take place through a liquid droplet composed of more RuO_2 and less of SnO vapors, which is likely to form first under the reaction conditions directing the growth of SnO into nanowires. The oxygen partial pressure is sufficient for the formation of SnO_2. While in case of nanobipyramids the evaporation of RuO_2 leads to the lifting of smaller cubical structures although growth process is still in progress, leading to the formation of tip on either side resulting in a pyramid like appearance. These structures are carried by the Ar present in the system to the substrates. The randomness in the size and the orientation suggests that each nanobipyramids is isolated, formed separately and is carried away by the carrier gas. Experiments carried out with different composition of RuO_2 in the reaction mixture indicate that the nanowire percentage increases with increase in RuO_2. Moreover, it is possible to control the diameter and length of nanowires by varying the RuO_2 weight percentage and the duration of heating. The nature of carrier gas also has a strong influence on the yield and aspect ratio of these nanowires.

2.8. Conclusions

In this chapter, we have clearly demonstrated the shape selective synthesis of different forms of submicron sized SnO_2 bipyramids, cubes and wires using RuO_2 as a unique catalyst during chemical vapor deposition. These forms represent promising candidates for both fundamental studies of low dimensional physics and the applications in various fields like nanoelectronics, nanosensors etc. In addition, the present study indicates the key role of RuO_2 as an important nucleating agent in promoting the growth of low dimensional structures of SnO_2. Further, the XRD, TGA-DTA and XPS studies elucidate the interactions between the nuclei of the building blocks (RuO_2 and SnO liquid droplets). The presence of carrier gas and the amount of RuO_2 in the initial reaction mixture help in gaining control over these interactions. Such interactions are extremely helpful in understanding, how specific types of reactions are responsible for specific target structures, as demonstrated. Our results further signify that the growth process is governed by the kinetics. Moreover, the shape dependent preferential growth directions observed in SnO_2 nanostructures indicates that the control over growth position and shape could be achieved by controlling the initial positions of Ru and its concentration.

The importance of the present synthetic method for nanostructures lies in its selectivity and simplicity, as it neither requires a sophisticated technique nor a rigorous air-sensitive atmosphere. We believe that the present work demonstrates an ability to exert a simple control over the shape of the nanostructures. An understanding of the growth mechanism of these structures is important for both the creation of new materials as well as the fabrication of devices using these structures. Furthermore, the preparation process is easy and cost effective, as the synthesis is carried out in a tubular furnace open at one end, which does not require any controlled atmosphere and instrumentation. Consequently, we believe that this type of study concerning the shape evolution of nanocrystals will be valuable to design and develop advanced nanoscale building-block architectures for valuable applications like chemical sensors, ultracapacitors, nanoelectronic circuits, batteries and fuel cells.

2.9. References

1. (a) Wang, Z. L.; Kang, Z. C. Functional and smart materials- structural evolution and structure analysis, Plenum Press, New York, **1998**. (b) A special issue on nanoscale materials, *Acc. Chem. Res.* **1999**, 32. (c) Wang, X. D.; Summers, C. J.; Wang, Z. L. *Nano Lett.* **2004**, *4*, 423.
2. (a) Xia, Y.; Yang, P.; Sun, Y.; Wu, Y.; Mayers, B.; Gates, B.; Yin, Y.; Kim, F.; Yan, H. *Adv. Mater.* **2003**, 15, 5, 353. (b) Wang, J.-G.; Tian, M.-L.; Mallouk, T. E.; Chan, M. H. W. *Nano Lett.* **2004**, 4(7), 1313.
3. Cui, Y.; Duan, X.; Hu, J.; Lieber, C. M. *J. Phys. Chem. B* **2000**, 104, 5213.
4. Gudiksen, M. S.; Lauhon, L. J.; Wang, J.; Smith, D. C.; Lieber, C. M. *Nature* **2002,** *415,* 617.
5. Mokari, T.; Rothenberg, E.; Popov, I.; Costi, R.; Banin U. *Science* **2004,** *304,* 1787.
6. (a) Scott, R. W. J.; Yang, S. M.; Chabanis, G.; Coombs, N.; Williams, D. E.; Ozin, G. A. *Adv. Mater.* , **2001** 13, 19, 1468. (b) Srivastava, D. N.; Chappel, S.; Palchik, O.; Zaban, A.; Gedanken, A. *Langmuir* **2002**, 1*8*(10), 4160.
7. (a) Wang, Z. L. *Adv. Mater.* **2003**, 15, 5 432. (b) Dai, Z. R.; Gole, J. L.; Stout, J. D.; Wang, Z. L. *J. Phys. Chem. B* **2002**, 106, 1274. (c) Dai, Z. R.; Pan, Z. W.; Wang, Z. L. *Solid State Comm.*, **2001,** 118, 351. (d) Z. R. Dai, Z. W. Pan. Z. L. Wang, *J. Am. Chem. Soc.* **2002**, 124, 8637.
8. Law, M.; Kind, H.; Messer, B.; Kim, F.; Yang, P. Angew*. Chem. Inter. Ed.* **2002**, 41, 13, 2405.
9. Wang, Y.; Jiang, X.' Xia, Y. *J. Am. Chem. Soc.* **2003.** 125 (52) 16176.
10. Maiti, A.; Rodriguez, J. A.; Law, M.; Kung, P.; Mckinney, J. R.; Yang, P. *Nano Lett.* **2003**, 3 (8) 1025**.**
11. Kolkamov, A.; Zhang, Y.; Cheng, G.; Moskovits, M. *Adv. Mater.* **2003**, 15, 12, 997.
12. (a) Zheng, M.; Li, G.; Zhang, X.; Huang, S.; Lei, Y.; Zhang, L. *Chem. Mater.* **2001**, 13, 3859. (b) Sun, S. H.; Meng, G.; Zhang, M. G.; An, X. H.; Wu, G. S.; Zhang, L. D. *J. Phys. D: Appl. Phys.* **2004,** 37, 409.
13. Hu, J. Q.; Ma, X. L.; Shang, N. G.; Xie, Z. Y.; Wong, N. B.; Lee, C. S.; Lee, S. T. *J. Phys. Chem. B* **2002**, 106, 3823.
14. Xu, C.; Zhao, X.; Liu, S.; Wang, G. *Solid State Comm.* **2003,** 125, 301.
15. Lui, Y.; Dong, J.; Liu, M. *Adv. Mater.* **2004,** 16, 4, 353.

16. Hurlburt, C. S.; Klien, C. D. *Manual of Mineralogy*, J. Wiley & Sons, New York, **1985**.
17. Nguyen, P.; Ng, H. T.; Kong, J.; Cassell, A. M.; Quinn, R.; Li, J.; Han, J.; Mcneil, M.; Meyappan, M. *Nanolett.* **2003**, 3, 7, 925.
18. Mazher, J.; Shrivastav, A. K.; Nandedkar, R. V.; Pandey, R. K. *Nanotechnology* **2004,** *15*, 572.
19. H. Borchert, D. V. Talapin, N. Goponik, C. McGinley, S. Adam, A. Lobo, T. Moller and H. Weller, *J. Phys. Chem. B* **2003**, *107*, 9662.
20. The spectras were fitted using the software XPSPEAK4.1 which is available free on website www.uksaf.org/software.html#7.
21. Rumyantseva, M. N.; Safanova, O. V.; Boulova, M. N.; Ryabova L. I.; Gaskov, A. M. *Russ. Chem. Bull. Int. Ed.* **2003**, *52,* 1217.
22. Egdell, R. G.; Rebane, J.; Walker T. J.; Law, D. S. L. *Phys. Rev. B* **1999**, *59*, 1792.
23. Wang, Z. L.; Liu, Y.; Zhang, Z. Handbook of nanophase and nanostructured materials, Kluwer academic/plenum publishers, (**2003**), volume *3*, pg 1.
24. Ding, Y.; Gao, P. X.; Wang, Z. L. *J. Am. Chem. Soc.* **2004**, *126(7)*, 2066.
25. Gao, P. X.; Wang, Z. L. *J. Phys. Chem. B* **2004**, *108*(23), 7534.
26. Lee, D.-J.; Kang, S.-W.; Rhee, S.-W. *Thin Solid Films* **2002**, *413*, 237.

Chapter 3

Gas Sensing Properties of SnO_2: from Thin Films to Nanostructures *

This chapter primarily deals with the gas sensing properties of SnO_2 thin films and nanostructures. Chemical functionalization of SnO_2 surface with Ru species is found to improve the sensitivity and selectivity as compared to that of pure SnO_2 thin films towards LPG. A room temperature sensor for H_2S is also demonstrated in this chapter, using surface functionalized SnO_2 with CuMPC's. Further, doping of SnO_2 matrix with Ru, Cu and Th leads to an improvement in sensor performance towards LPG, H_2S and TMA gases. This chapter ends with a discussion about the remarkable shape dependent NO_2 sensing behavior at room temperature for SnO_2 nanostructures in the form of wires, bipyramids and cubes.

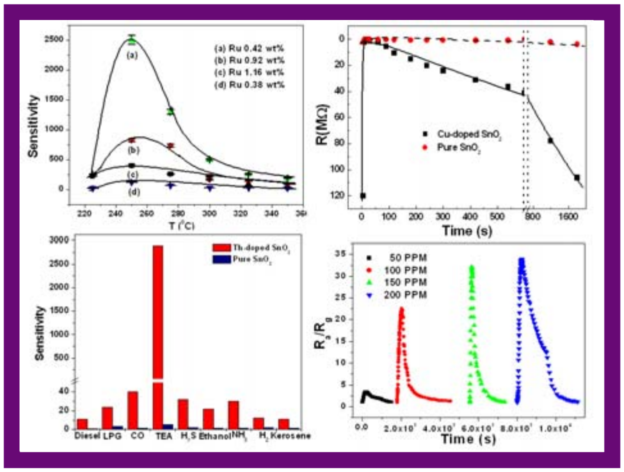

---

* Various parts of the work described in this chapter have been published in "**Sensors & Actuators B 2001**, *79*, 132; *85*, 26, **2002**, *82*, 82, *37*, 84 and **2005**, *107*, 708".

3.1. Introduction

Wide band-gap semiconducting oxide materials namely TiO_2, WO_3, ZnO and SnO_2, have been widely used for designing oxidative catalysts, optoelectronic devices and solid-state gas sensors, because of their unique properties namely high thermal and chemical stability, flexibility of processing and low cost fabrication[1-4]. More specifically, their range of conductance variation due to the chemical environment and their distinct response towards both the oxidizing and reducing gases have resulted in a remarkable upsurge in studying their gas sensing behavior. They are used in the form of bulk material, thick films as well as thin films[5]. Nevertheless, the sensing performance of these sensors are often modified by altering the operating temperature, irradiation, incorporation of specific additives as catalysts and promoters (such as noble metals like Pd, Pt, Ru, metal oxides like MoO_3, Al_2O_3, ThO_2, ZrO_2 etc) and using masks or filters in order to improve sensitivity, selectivity and response time[6]. These materials can be prepared with controlled properties either in nanocrystalline powders, thin films or as demonstrated more recently in different nanostructures[7].

Nanocrystalline powders are generally prepared by a well-known precipitation method using ammonium hydroxide[8]. This powder is often transformed into pellets or thick films using screen-printing before their utilization as gas sensors. However, a large quantity of material requirement and more significantly, a poor or weak coupling with the electronic circuitry impose major limitations on their wide usage[9]. Accordingly, thin film gas sensors are emerging in a large way due to the ease of flexibility for miniaturization without affecting the desired properties in the materials and good stability. Moreover, high surface area in thin films has high advantage in the device due to the quicker recovery, lower power consumption and cost effectiveness. A large number of thin film gas sensors based on different materials have been reported. For example, thin films of MoO_3 deposited by various techniques show selective response to CO[10]. Similarly, TiO_2 thin films with and without dopants are also used for sensing applications[11]. Further, thin films based on In_2O_3[12]; SnO_2[13] and ZnO[14] for sensing various gases are also reported. Other materials such as Ga_2O_3[15] (Ba, Sr) TiO_3[16] and titanyl pthalocyanine[17] films are also used as sensors. However, one of the major drawbacks of thin films sensors is their diminished sensitivity as compared to that of thick films and pellets. This results from the comparatively lower porosity of such films due to their uniform crystallanity that leads to the decrease in the surface area and eventually lowering the sensitivity. Other drawbacks are poor selectivity, ageing and humidity-induced effects involving grain growth and surface poisoning, all contributing collectively to the poor reliability. Widespread utility for industrial, commercial and domestic purpose makes it essential to have reliable commercial low cost gas detectors as early warning systems incorporated in the building[18].

Recently, it has been revealed that the reduction in grain size of the sensor material leads to an increase in the sensitivity due to high surface to volume ratio[19]. In particular the sensors resistance depends on the barrier height and the concentration of the target gas. This situation is essentially unchanged with the variation in the grain size (diameter, D) of the oxide unless D is kept above a critical value (D_c), which is just equal to twice the thickness (L_s) of surface space charge layer of the oxide commonly referred to as Yamazoe criterion[19]. For D smaller than D_c (6 nm for SnO_2), sensitivity increases sharply with decreasing D. Since usually L_s is a function of the concentration of electron donors in the bulk oxide, D_c can be changed by doping the base oxide with a foreign oxide. When the oxide is loaded with a foreign additive, the additive can modify L_s as well, if it interacts electronically with the oxide. The advent of different synthetic approaches, has lead to an upsurge in the interest towards uncovering novel nanostructures like nanowires, nanobelts and nanodiskettes of semiconducting oxides.[20, 21] In such nanostructures, their aspect ratio dependent electrical properties can be altered by the addition of small amounts of a second substance (dopant), which is well illustrated by the incorporation of boron or phosphorous in silicon nanowire for modulating the electron or hole concentration, respectively. Additionally, nanoparticles/nanoclusters of metals and semiconductors have found to exhibit single electron characteristics and can be organized through simple self-assembly methods into ordered hierarchal structures with the precise control of their location[22]. Accordingly, these structures have been demonstrated to exhibit a great potential in the development of smart functional materials, devices and systems[23]. Interestingly, the high surface to volume ratio resulting in the faster kinetics of these nanomaterials looks promising for making single molecule detection realistic.

In the earlier chapter, it has been elucidated that among various semiconducting oxides, SnO_2 is promising candidate towards miniaturized, ultrasensitive chemical sensors because of its unique conductance properties. In particular, it was emphasized that the characteristic of SnO_2 with mixed valencies of cations and variable oxygen deficiency enables tuning of their electronic structure and properties[24]. Accordingly, it has been synthesized in various forms like whiskers, nanorods, nanotubes, nanodiskettes, nanobelts and nanowires using techniques like laser ablation and thermal evaporation with controlled dimensions[24-26]. Pristine SnO_2 based nanostructures have been reported to act as a room temperature sensor for NO_x, CO, O_2, H_2 and C_2H_5OH[27, 28]. More recently, Yang et al. have reported photochemical gas sensing properties of single crystalline SnO_2 nanowires towards NO_2[29], where high sensitivity and reversibility was achieved only at elevated temperatures or by exposure to the UV light corresponding to energy near the SnO_2 band-gap. Similarly, Xia et al. have developed a solution route for the synthesis of SnO_2 nanowires that exhibit enhanced sensitivity towards CO, ethanol and H_2 at ambient temperature[30]. Moskovits et al. have also demonstrated that the SnO_2 nanowires can be successfully employed towards gas sensing of CO and O_2 at operating temperature of 200 °C and above[31]. Although, doping is one of the important strategies for controlling both sensitivity and selectivity, surprisingly, most of the work on the nanowire sensors to date has been based on pure SnO_2 without attempts to explore the sensing applications of doped nanowires.

In this chapter, we describe a simple approach for controlling the performance of sensors based on SnO_2 thin films and nanostructures. More specifically, SnO_2 is anchored with ruthenium to achieve a remarkable enhancement towards the hydrocarbon selectivity and sensitivity. The main aim is to control the amount and distribution of ruthenium in the SnO_2 matrix so that the misfit regions are distributed at the grain boundaries in such a way to obtain very high sensitivity with good selectivity. The misfits created alter the physical and chemical properties leading to unusual effects such as high sensitivity and selectivity. Additionally, we demonstrate for the first time a surface functionalized (with Cu nanoclusters) SnO_2 sensor for the detection of H_2S at room temperature. The dependence on the terminal functional group and the chain length of the outer organic thiol molecule towards the recognition of H_2S molecule has also been carried out to establish the importance of orientational flexibility in controlling the sensing behavior. Further, we also demonstrate the sensor performance towards LPG, H_2S and TMA by mixed metal oxide wherein the SnO_2 matrix is modified with the Ru, Cu and Th species. The effect of the amount of doping element, operation temperature and concentration of gas on sensitivity has been established to get the sensor with enhanced sensing properties. Finally, the unique gas sensing property of SnO_2 nanowires is demonstrated in this chapter, by studying their selective response towards NO_2 detection in air at room temperature.

3.2. Experimental Aspects

3.2.1. Materials

The following chemicals were used: octadecanethiol (ODT), pentanethiol (PT), dodecanethiol (DDT), lauric acid (LA), octadecylamine (ODA), octadecylcarboxylicacid, $CuCl_2{\cdot}2H_2O$, ethanol (A.R. grade) and $NaBH_4$ (99.99%) all Aldrich make; tin tetrachloride ($SnCl_4$) was of E. Merck make, while the remaining (A.R. grade) reagents were obtained from the standard indigenous sources.

3.2.2. Thin Film Deposition

SnO_2 films were prepared by using the conventional spray pyrolysis technique [12]. In brief, different molar solutions (0.001 – 1.0 M) of tin tetrachloride were prepared in a mixture of ethanol and deionised water in the volumetric ratio of 10:1. Commercial silicate glass slides were cleaned thoroughly by first washing in soap solution followed by boiling in concentrated HCl (12.3 M) for few hours. The slides were then rinsed in deionised water and subsequently subjected to ultrasonic treatment followed by drying before using as substrates. The substrate temperature to be deposited was controlled between 300 and 500 °C $\pm$ 1 °C. A typical volume of the solution used for a deposition was around 10 mL, with the total number of spray being 25. The spray time was maintained at 3 s with a waiting time of 3 min between successive spraying. The normalized distance between a substrate and a spray nozzle was kept constant to 25 cm and all parameters connected with the atomizer were kept constant during the deposition process. Compressed air with a flow rate of 70 mL min^{-1} was used as a carrier gas. The solution flux was kept at 8 mL min^{-1}. A batch of 10 substrates with an effective area of

1.0 cm × 2.5 cm was deposited at a time. Films were then subjected to the annealing at the deposition temperature for 12 h to obtain uniformity. The average film thickness determined by Fizeau fringes was in the range of 800 – 1500 Å. The estimated error for our experimental set-up did not exceed 2%.

3.2.3. Surface Functionalisation

3.2.3.1. Chemical Self Organization of Ru Species

Surface modification of spray pyrolysed films was carried out using Ru species via a self-organization route. Different solutions of $RuCl_3$ (0.001 to 0.1M) in a mixture of isopropanol and water (in the volumetric ratio of 10:1) were prepared. 10 μl of each solution was transferred on to the freshly prepared SnO_2 films and was allowed to evaporate at room temperature. These films were then heated at 350^{o}C for 2 h before testing.

3.2.3.2. Monolayer Protected Copper Nanoclusters (CuMPCs)

Copper (Cu) clusters capped with thiols having different chain lengths and functional groups were prepared as per the modified Brust synthesis[32]. The synthesis is a standard procedure within which two conditions were strictly followed: (i) the molar ratio of Cu: capping agent was kept constant (3:1); and (ii) the rate of addition of $NaBH_4$ was also kept constant.

For example, to 60 ml of 3 mM aqueous copper chloride solution, 200 ml of toluene with respective capping agent in 1 mM concentration was slowly added with vigorous stirring. To this solution 50 mL of 0.4 M $NaBH_4$ aqueous solution was added dropwise. A black color was appeared during the addition of reducing agent. The stirring was continued upto 8 h, finally the black aqueous solution became clear indicating the transfer of all Cu ions into the non-aqueous layer. This non-aqueous layer was separated by a separating funnel and the nanoparticles were precipitated by adding copious amount of acetone. The particles were allowed to settle and the excess acetone was decanted to remove the unbound thiol and other unwanted by-product. Finally, surface functionalization was carried out by keeping 10 µl of the cluster solution on the SnO_2 thin film surface followed by air-drying.

3.2.4. Preparation of thin film of Ru/Cu/Th -doped SnO_2

A 1 M solution of tin tetrachloride was prepared in a mixture of ethanol and deionised water in the volumetric ratio of 10:1. The solution for spray pyrolysis was prepared after adding different amount of doping elements namely ruthenium, copper, thorium (0.0 to 5.0 wt.%) in the tin chloride solution. The source of Ru, Cu, Th and Sn were ruthenium chloride, copper acetate, thorium nitrate and tin tetrachloride, respectively. The films were deposited in a way similar to the one described earlier in section 3.2.1.

3.2.5. Spectroscopic characterization

All the Uv–vis spectra were recorded on a Hewlett Packard 8452 diode array spectrophotometer with 2 nm spectral resolutions at room temperature. Other characterization details like XRD, SEM, HR-TEM, XPS and TG-DTA have been already described in chapter 2, section 2.2.

3.2.6 Gas sensing set-up

These modified SnO_2 films were tested for sensitivity to various gases in a dynamic (air as a carrier gas) as well as static set-up as shown in Scheme 3.1. Briefly, the sensor material was kept in a glass chamber, which was insulated properly to avoid significant heat losses. The test gases like LPG, H_2S and TMA were injected in the gas-mixing chamber using calibrated gas tight syringe so that the required ppm level was attained. The sensor was connected to a current measuring device through a power supply. Sensitivity s is defined as $s = R_a/R_g$ in case of reducing gas like LPG, H_2S and TMA and as $s = R_g/R_a$ for oxidizing gas like NO_2, Cl_2, ozone.

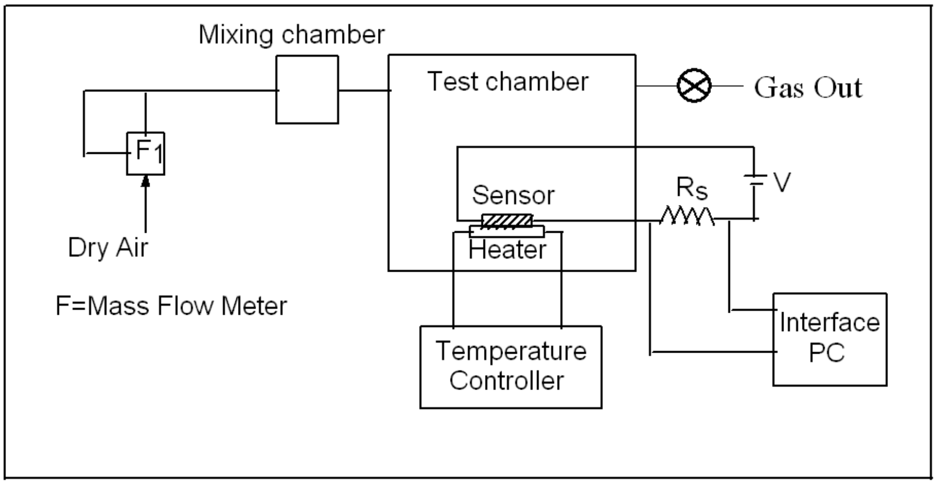

Scheme 3.1. Experimental set-up for gas sensing measurements.

3.3. Results and Discussion

3.3.1. Gas Sensing properties of surface functionalized SnO_2 thin films

When a reducing gas, such as LPG comes in contact with the SnO_2 surface, it undergoes oxidation by reacting with the oxygen species concomitantly donating electrons to the surface states during the process. In such processes RuO_2 species act as catalyst promoting the reaction more effectively. Thus, replacement of the few of the Sn–O linkages by grafting Ru–O linkages can cause a dramatic change in the adsorption–desorption kinetics depending upon the nature and concentration of the adsorbed oxygen species. Further, the high surface state density at the SnO_2–RuO_2 interface limits the modulation of carrier concentration by pinning the Fermi level and a strong dependence of the carrier energy on the spatial disorder due to RuO_2 regions, which may result in the enhanced sensitivity[34]. Accordingly, the surface of SnO_2 thin films modified with Ru species improves significantly the sensing performance towards LPG. Correspondingly, Figure 3.1 shows the variation of sensitivity with the amount of Ru to 1000 ppm of LPG at 250°C. Sensitivity increases with the amount of Ru and is highest for 1.65 wt.% Ru. This enhanced performance is to be compared with that of SnO_2 pellet modified with Ru, which show maximum sensitivity with 0.27 wt.% Ru species.[33] The difference in the amount may be attributed to the morphological changes of the film and pellet before and after modification. Further, the enhanced sensitivity could also be assigned to the amount and distribution of Ru species on the surface of SnO_2. The low Ru concentration has a discontinuous distribution on the surface causing an insufficient catalytic activity leading to a smaller sensitivity, while higher concentration gives a continuous distribution leading to a lower initial resistance and hence a lower sensitivity value.

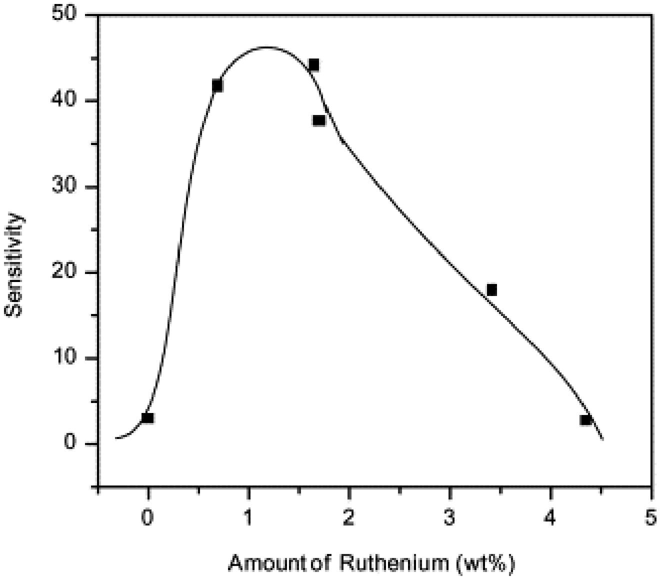

Figure 3.1. Variation of sensitivity with the amount of Ru species on the surface of SnO_2 towards 1000 ppm LPG at 250°C.

Figure 3.2 compares the sensitivity of (a) pure SnO_2 film and (b) surface ruthenated SnO_2 (1.65 wt.%) film towards 1000 ppm of LPG. As the operating temperature increases the sensitivity increases, attains a maximum at 250°C and again decreases with a further increase in temperature. However, at all temperatures the ruthenated sample exhibits higher sensitivity as compared to that for pure SnO_2. The improvement in the sensing could probably be assigned to the Ru (IV) oxide at the grain boundaries creating surface states in the SnO_2, which are in excess of electrons. At higher temperatures oxygen gets adsorbed on the SnO_2 surface and abstracts electrons from the surface states increasing the resistance of the film. Ru(IV) oxide acts as a catalyst for oxygenation and allows more oxygen species to be adsorbed on the surface as compared to pure SnO_2.

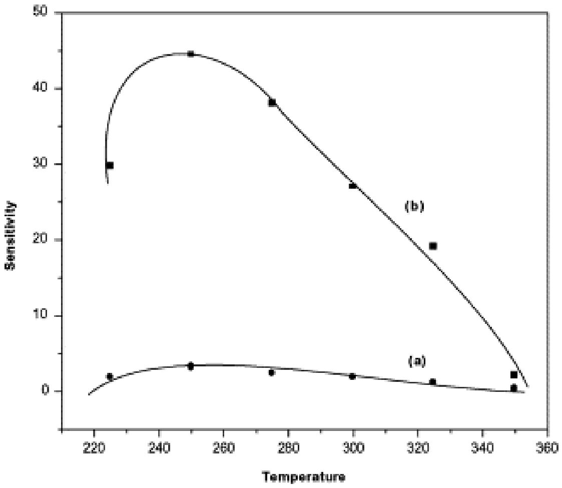

Figure 3.2. Variation of sensitivity with operating temperature of (a) pure SnO_2 and (b) ruthenated SnO_2 toward 1000 ppm of LPG.

Additionally, surface ruthenated sample (1.65 wt.%) also shows a superior response time (time required for a sensor output to change from its previous state to a final settled value within a tolerance band of the correct new value) (Figure 3.3) of only 5 s towards 1000 ppm of LPG as compared to that of pure SnO_2 film, which shows a negligible response. Moreover, the recovery of ruthenated sample is also faster (15 min) than that of pure SnO_2 film (25 min). This quicker response and recovery time could also be attributed to the catalytic activity of Ru species.

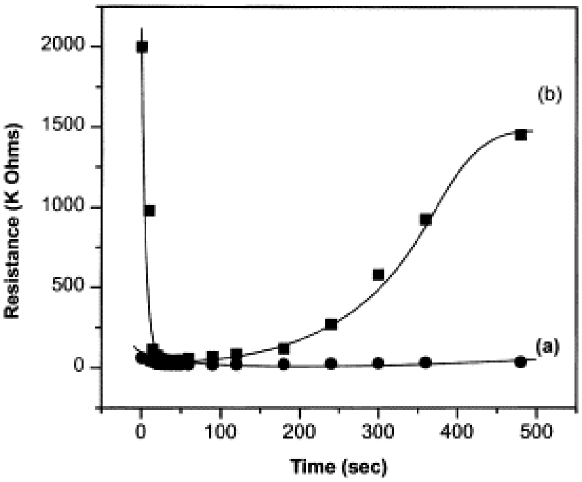

Figure 3.3. Response and recovery curves of (a) pure SnO_2 and (b) surface ruthenated SnO_2 after exposure to 1000 ppm LPG at 250°C.

It is well known that hydrocarbons and hydrogen can undergo surface reactions and Ru–O sites can act as active centers for abstraction of H atom, which is common for both LPG as well as H_2 fragmentation patterns. Accordingly, Figure 3.4 shows a histogram indicating the selectivity of pure SnO_2 and surface ruthenated SnO_2 films (1.65 wt.%) to 1000 ppm of various gases. Surface ruthenated SnO_2 is highly selective towards LPG, as the sensitivity is approximately 45 as compared to 3 for pure SnO_2 under similar conditions. It also has a reasonably good sensitivity towards hydrogen, which is expected due to the reducing behavior of both these gases. However, the sensitivity is apparently negligible for other gases, such as CO, NH_3 and H_2S. Different types of adsorption configurations of gas molecules and various surface fragmentation reactions on the Ru sites are probably responsible for this high selectivity.

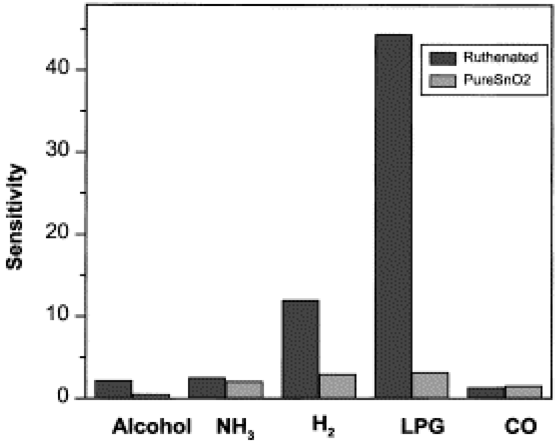

Figure 3.4. Sensitivity of (a) pure and (b) ruthenated SnO_2 films towards 1000 ppm of various gases at 250°C.

In order to confirm the oxidation state of Ru on the SnO_2 surface, XPS studies were carried out on both pure and ruthenated films. Figure 3.5 shows the spectra of Sn 3d, O 1 s and Ru $3d_{5/2}$ levels recorded after surface functionalisation. The spectrum of pure SnO_2 film shows two separate signals at the BE values of 486.8 and 495.2 eV corresponding to Sn $3d_{5/2}$ and Sn $3d_{3/2}$ levels, respectively. The asymmetry in the oxygen peak implies that it can be resolved into two components[35] corresponding to O1s (BE = 530.8 eV) and adsorbed oxygen (BE = 532.7 eV). The spectra of the ruthenated sample show no shift in the tin (a) and oxygen (b) peaks implying that the oxide–oxide interaction is negligible. The peak at 281.4 eV (Ru $3d_{5/2}$) (c) confirms the formation of

RuO_2 on the surface of SnO_2. The Ru $3d_{3/2}$ peak, however can not be resolved due to overlapping of the carbon (BE = 285 eV) and carbonate (BE = 288 eV) signals. For all the spectra, the peak after background subtraction is indicated by a Gaussian fit. In all these plots the scattered points indicates the actual spectra while the line indicates the fitted curves.

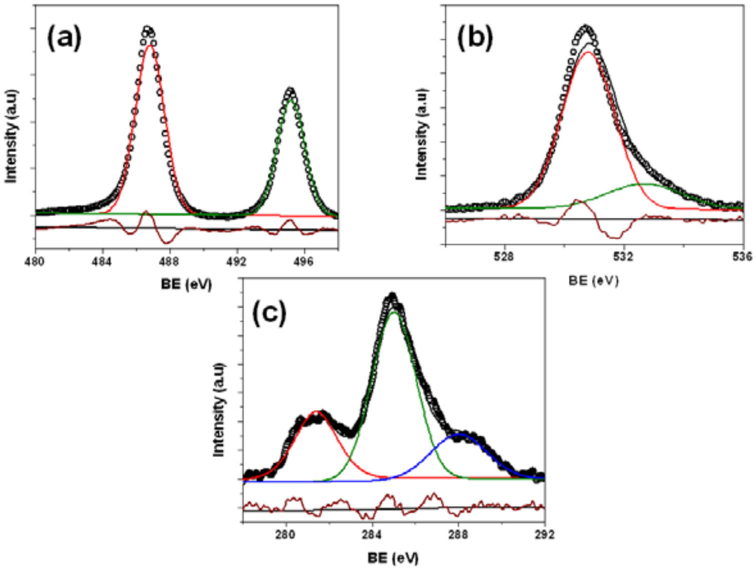

Figure 3.5. XPS spectra of (a) Sn $3d_{5/2}$ and Sn $3d_{3/2}$, (b) O 1 s and (c) Ru $3d_{5/2}$ levels confirming the presence of Ru species on the surface of SnO_2.

Further, surface functionalisation is expected to affect the morphology of SnO_2 thin films. Figure 3.6 compares the microstructure of the pure SnO_2 film to that of the surface ruthenated SnO_2. It is evident that there is a distinct morphological change on modification with Ru species. The pure SnO_2 film is smooth and does not seem to have a highly porous structure, which is probably one of the reasons for low sensitivity of the film. However, due to the presence of Ru species ruthenated film shows a large number of grains. It is evident that the surface area of the film has increased drastically which is one of the reasons for the enhanced sensitivity of the films. However, in comparison to the surface ruthenated SnO_2 pellets[34] the porosity of the films seems to be very low which leads to the lowering of the sensitivity of these films as compared to that of pellets.

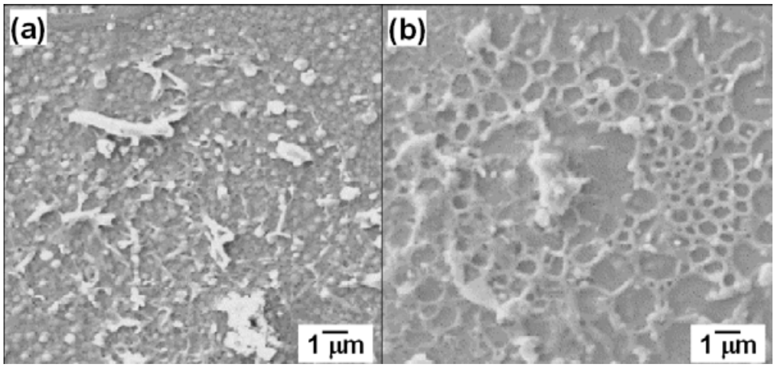

Figure 3.6. Micrographs of (a) pure and (b) ruthenated SnO_2 film (1.65 wt.% Ru) clearly revealing the network formation on the surface of SnO_2 after surface functionalisation.

Thus, surface functionalisation with Ru species results in the improvement in sensing performance towards LPG. In particular, both the sensitivity and selectivity are improved implying the utility of the modification method.

3.3.2. Room Temperature Gas Sensing Properties of SnO_2 Thin Films Modified by Monolayer Protected Cu Nanoclusters

The advantage of high surface to volume ratio has lead to an upsurge in the interest in nanoparticles as explained in detail in Chapter 1. Depending upon the preparative conditions, the particles have a tendency to agglomerate slowly and flocculate. A stable nanoparticle could be achieved by surface functionalisation using the so-called 'passivation' strategy of these clusters, and accordingly these surface capped nanoparticles are also called as monolayer protected clusters (MPCs). Since the kinetics of cluster growth is determined by the surface coverage, cluster size can be controlled by the reaction conditions. These hydrophobic clusters are of considerable interest since in some respect they behave like simple chemical compounds. For instance, they can be precipitated, redissolved and chromatographically saperated without any apparent change in properties. Accordingly, optical sensors could be designed using these materials and recently, the chain length dependent sensing capabilities of AgMPCs using surface plasmon resonance have been reported.[36] Thus, MPCs could be the new choice of materials to improve the sensing performance. Though there have been few reports of biosensors[44] and amperometric sensors[45] based on MPCs, a simple chemical sensor based on the conductivity characteristic has not been reported so far. Optical properties of Ag nanoparticles chemically modified with alkanethiol SAMs are especially useful for sensor studies by measuring the localized surface plasmon resonance (LSPR) spectrum. The LSPR shifts to red (5 nm) with the adsorption of the polypeptide poly-L-lysine (PL) to Ag nanoparticles modified with deprotonated carboxylate groups from 11-mercaptoundecanoic acid (11-MUA). Previously, Sarala Devi et al.[46], have demonstrated that SnO_2 doped with CuO senses H_2S in trace amounts (2 ppm) at high temperature (200 °C). The sensitivity obtained towards H_2S is normally high but requires higher temperatures; however, SnO_2 surface functionalized with Cu clusters can effectively detect H_2S at room temperature and before discussing the gas sensing properties, it is crucial and desirable to characterize these CuMPCs.

One of the commonly adopted characterization tools for determining the size and optical band gap of nanoparticle is the Uv-vis spectroscopy. Colloidal dispersions of metal exhibits absorption bands or broad regions of absorption in the Uv–vis range. These bands are due to the excitation of plasma resonance or interband transitions and are characteristic properties of the metallic nature of the particle[36]. According to Mie theory, the surface plasmon resonance for copper clusters is expected to have a strong broadening for the particles smaller than 100 Å. The UV–VIS spectrum of Cu clusters in toluene shows a strong absorption peak at 289 nm as shown in the inset of Figure 3.7 (b) indicating that the cluster size is smaller than 4 nm[37]. For clusters capped with different functional groups along with a strong absorption at 289 nm, a shoulder appears at higher wavelength for TDA and ODT while LA capped clusters do not show any shoulder. The Uv–vis spectrum (Figure 3.7 (a)) scanned for SnO_2 film with Cu clusters capped with ODT shows a broadening in the plasmon resonance. An absorption peak at 389 nm along with a shoulder at 544 nm confirms the agglomeration of smaller particles (≤4 nm) on the SnO_2 surface[38]. However, after exposure to H_2S gas the shoulder gets shifted to a higher wavelength side indicating deformation in the cluster environment.

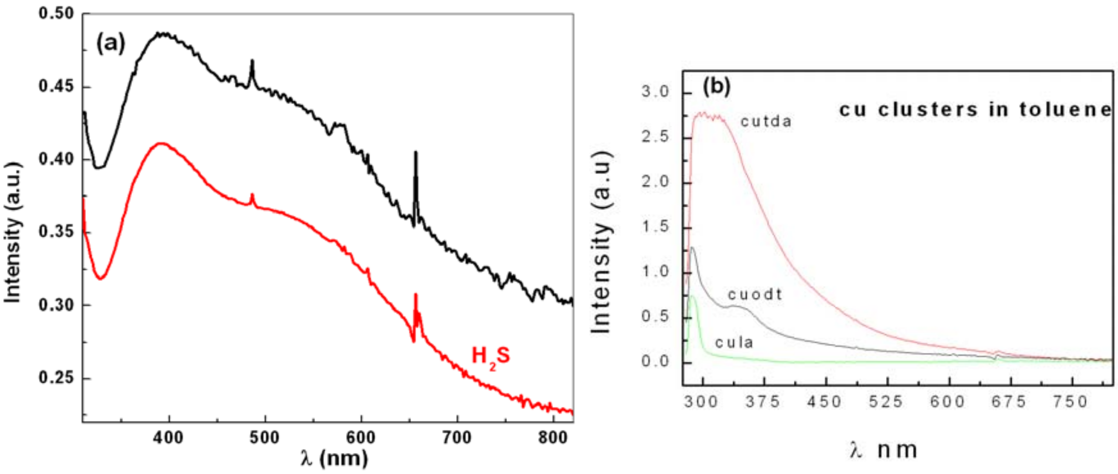

Figure 3.7. (a) Uv–vis spectrum for the SnO_2 film modified with ODT capped Cu clusters with and without exposure to H_2S. (b) The spectrum for Cu clusters capped with different capping agents in toluene.

It is well known, that CuMPCs tend to aggregate very quickly[39]. Figure 3.8 shows the corresponding TEM image of these nano-sized polydispersed particles. Average core diameter ranges from 10 to 42 nm with an average diameter of 24 nm with a significant amount of aggregation. This discrepancy may also be attributed to the aggregation of clusters on drying or by the electron beam effect. The distribution of CuMPCs on the SnO_2 surface is clearly the product of competing nanoparticle– SnO_2 and nanoparticle–nanoparticle interactions. Previous investigators have cited particle–particle and particle–substrate electrostatic interactions[40], Van der waal forces[41], hydrophobic interaction[42] and capillary force[43] as the driving force for the particle distribution or array formation. It has been reported that the array formation starts when the thickness of the liquid containing clusters becomes approximately equal to the particle diameter and the crystal growth takes place through a directional motion of particles towards the ordered regions. The rate of liquid evaporation and the shape of air liquid surface significantly affect the type and quality of the distribution on the surface of SnO_2.

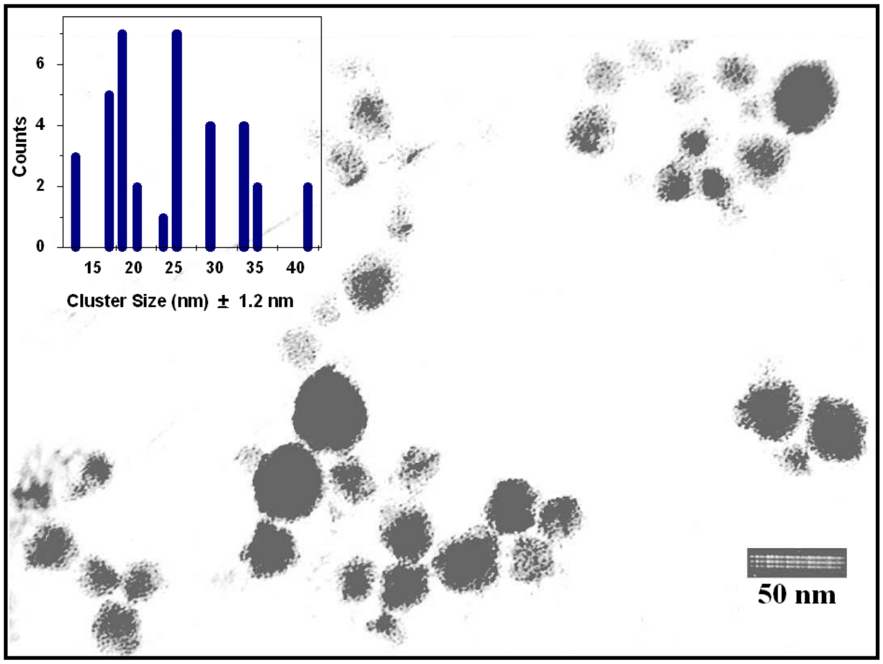

Figure 3.8. Transmission electron photograph of Cu clusters capped with ODT with an inset showing the size distribution histogram.

Thus, CuMPCs with the smaller size are expected to affect the sensing properties of SnO_2 thin films. Table 3.1 indicates the H_2S sensitivity of SnO_2 film when the surface modification is accomplished using Cu clusters capped with thiols having the same chain length (C_{18}) with different functional groups ($-NH_2$, -COOH, $-CH_3$) and same functional group with different chain lengths to 400 ppm of H_2S at room temperature. For the samples with different functional groups the response time is similar, i.e. 60 s. The films with Cu clusters capped with amino terminated thiol shows the best sensing characteristics. The differences in the sensitivity and the recovery can be attributed to the presence of different functional groups. Since the amino group has a tendency to adsorb water from the atmosphere there can be excess of hydroxyl groups on the SnO_2 film. Further, the attachment of these chains on the SnO_2 film is via the -OH groups that are present on the film. As a result, when the Cu clusters are protected by C_{18}–NH_2, the end groups of the thiols can attach themselves on the SnO_2 film more effectively. It is expected that after exposure to H_2S, the thiol chains get reorganized allowing the H_2S molecule to access the Cu clusters forming CuS.

Table 3.1. The sensitivity and response of SnO_2: When the surface modification is accomplished using Cu clusters capped with thiol having the same chain length (C_{18}) but different functional groups and with the same functional group but different chain lengths to 400 ppm of H_2S at room temperature.

Functional Group	Chain length	Sensitivity	Response (s)
$-NH_2$	C_{18}	200	60
-COOH	C_{18}	70	60
-SH	C_{18}	125	60
-SH	C_{12}	44	90
-SH	C_5	43	120

It can also be seen from the table that as the chain length decreases the sensitivity also decreases. The sensitivity is maximum when the chain length has eighteen carbon atoms (C_{18}). It has been reported that for chain length $\leq C_{16}$, exposure to H_2S gives a disordered liquid like state but maintains a well ordered but physisorbed monolayer for chain length $\geq C_{18}$[36]. Since a liquid like state may be obtained when the chain length $\leq C_{16}$, the access of the H_2S molecule to the Cu cluster may be restricted. Further, electron tunneling via the thiol chains is also dependent on the cluster–cluster spacing, which also plays a crucial role in determining the sensitivity. The long chains may also maintain the required distance as compared to that of the shorter chains, which could also be one of the reasons for decreased sensitivity to the films that are surface functionalized with Cu clusters capped with short chain thiols. Recently, the rate of electron self-exchange reactions between discretely charged metal-like cores of nanoparticles has been measured in multilayer films of nanoparticles by an electrochemical method[47]. All the samples required about 6 h for their recovery. The change in the carrier concentration as observed after exposure to H_2S gas is two orders for Cu clusters capped with $C_{18}SH$ on SnO_2 surface (4.34×10^{13} to 5.48×10^{15}); while for pure SnO_2 it is only three times ($(1.38–4.45)\times10^{13}$).

The above results are well supported by XPS studies of Cu clusters capped with ODT before and after the exposure to H_2S gas as shown in Figure 3.9. As seen in Figure 3.9a, the Cu spectra for Cu clusters capped with $C_{18}SH$ on SnO_2, show peaks at 933.3, 953.7 and 943.5 eV corresponding to Cu $2p_{3/2}$, Cu $2p_{1/2}$ and $Cu(OH)_2$, respectively. However, after exposure to H_2S, only two peaks at 932.6 and 940.6 eV corresponding to CuS and Cu^+ are seen[48]. The appearance of Cu–S peak strongly confirms the process, which is further, supported by the sulfur spectra. Figure 3.9b shows the sulfur spectra recorded for Cu clusters capped with ODT before and after the exposure to H_2S gas. For both cases only one sulfur species at an S $2p_{3/2}$ BE of 163.5 and 168.9 eV, respectively is observed. The sulfur species at 163.5 eV is in the BE range for neat thiol and disulfide thus can be assigned to unbound thiol molecules, which are observed between the BE 163 and 165 eV[49]. The shift in the sulfur peak from 163.5 (S $2p_{3/2}$) to 168.9 eV, after the exposure to H_2S, suggests the formation of sulfate or sulphonic acid moiety[50]. However, since the thiols are also attached to the SnO_2 films effectively via the -OH groups the transfer of the electrons to the SnO_2 bulk is much favored and as a result the sensitivity of this film is enhanced dramatically.

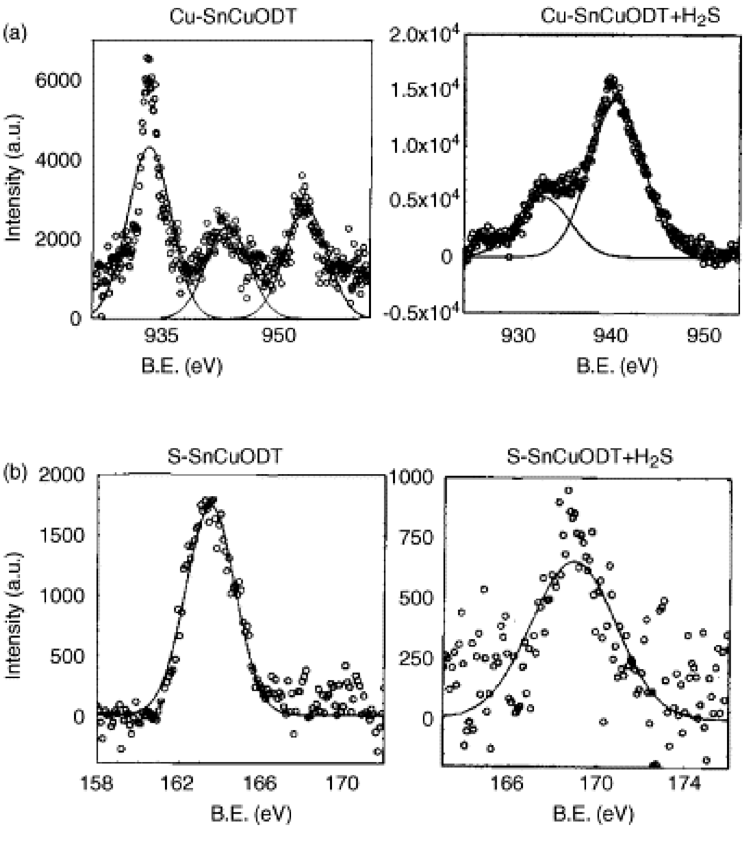

Figure 3.9. XPS plot for (a) copper and (b) sulfur before and after the exposure to H_2S gas.

Figure 3.10 shows the superimposed TG/DTA plot of freshly prepared Cu nanoclusters capped with ODT. A three step weight loss initiating at 206°C is observed. In the first step (206–245 °C), a sharp weight loss upto 13% attributed to the loss of adsorbed water and toluene molecules is observed. In the second step (245–300 °C), the 43% weight loss could be assigned to the thermal desorption of thiol molecules from the surface. In the third step from 300 to 375 °C, a sharp weight loss of (22%) could be attributed to the decomposition of remaining capped clusters. In the end, a very slow mass increase, possibly due to the oxygen pickup from the atmosphere is seen. The above results could be further illustrated by the DTA profiles of clusters. First, two endothermic peaks are observed around 55 and 135 °C, respectively, probably owing to the reorganization of the alkyl chains on the surface of the Cu clusters. Temperature driven phase transition of alkyl chains is common on both two and three-dimensional monolayers and the reversibility of this transition indicate such a possibility[51]. Second, two exothermic peaks at 215 and 300 °C support desorption of thiol molecules from the surface of the clusters. The additional broader exothermic peak at 480 °C may be due to the larger decomposition range of thiol molecule, forming cuprites. Elemental analyses of clusters also suggest identical C:H and C:S ratios, comparable to pure ODT, within the experimental uncertainties as shown in the Table 3.2.

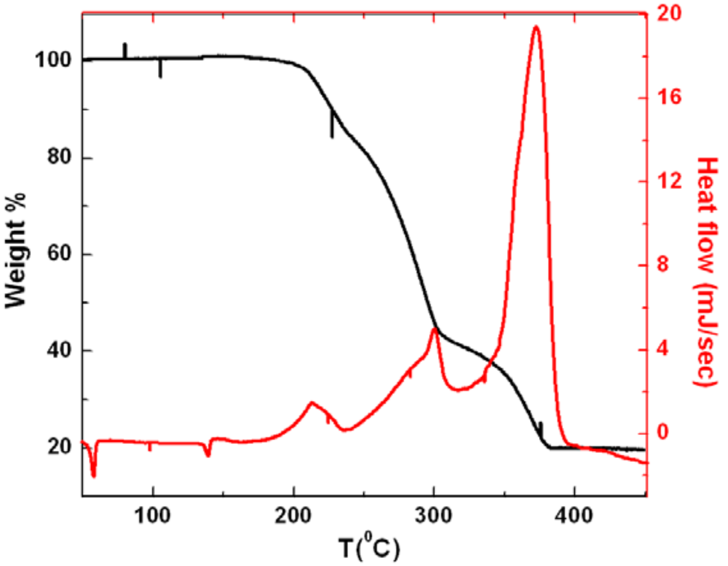

Figure 3.10. The superimposed TG/DTA plot of freshly prepared CuMPCs capped with ODT.

Table 3.2. Elemental analysis data

Molecular Formula	C: H ratio	C: S ratio
Calculated, $C_{18}H_{38}S$	1:5.7	1:6.7
Experimental, $C_{20}H_{42}S$	1:5.7	1:7.4

The experiments performed at different temperature reveals that although the thiols are stable upto 200 °C the sample does not show sensitivity to H_2S at these temperatures. This may be attributed to the absence of -OH groups.

Thus, extending the surface functionalisation of SnO_2 thin film with Cu MPCs allows the detection of H_2S gas at room temperature. However, both the response and recovery time are slow and need to be improved further prior to their utility as sensor material.

3.4. Gas Sensing Properties of Ru, Cu and Th Doped SnO_2 Thin Film

As stated earlier, (section 3.1) doping is also an important method to modify/improve the sensors performance. Consequently, in order to improve the sensing performance further, the SnO_2 matrix is doped with different doping elements namely Ru, Th and Cu in order to achieve selective detection of commercially important LPG, H_2S and TMA gases, respectively.

The structural properties of SnO_2 films have a significant effect on the electrical and gas-sensing property and hence structure and the grain size measurements of the crystallite are important. Figure 3.11 illustrates the XRDs for thin films of pure and Ru-doped SnO_2 deposited at the temperatures between 300 and 500 °C. Pure SnO_2 film deposited between 300 and 400 °C results in an amorphous structure, although, above 450 °C, the reflections from the tetragonal crystallographic pattern of SnO_2 become more defined. At 500 °C, the diffraction peaks become more intense and sharp. The XRD pattern could be indexed on the basis of tetragonal structure with lattice parameters a = 4.804 Å and c = 3.079 Å.

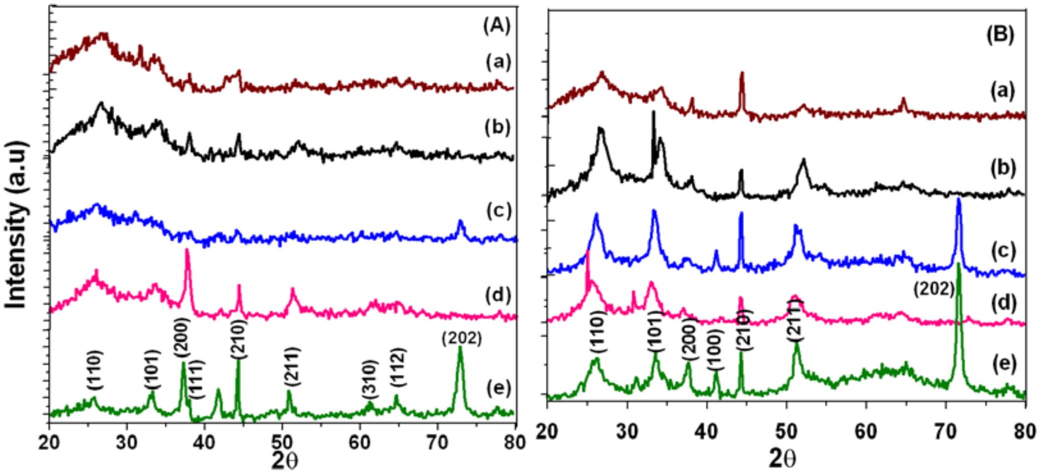

Figure 3.11. XRD of pure SnO_2 (A) and Ru-doped SnO_2 (B) deposited at various temperatures (a) 300, (b) 350, (c) 400, (d) 450 and (e) 500 °C.

The XRD (Figure 3. 11 B) of 0.42 wt.% Ru-doped SnO_2 films show a very interesting pattern. For example, at a deposition temperature as low as 300 °C it shows a polycrystalline pattern, which on the higher deposition temperature becomes more intense. Unlike pure SnO_2 the appearance of crystallization at such a low temperature in the Ru-doped SnO_2 film can be attributed to the probability of its role as a sintering aid. It is also significant to note that the ionic radius of Ru^{4+} is 0.76 Å and of Sn^{4+} is 0.83 Å, and hence, it can be assumed that ruthenium replaces tin without any significant change in the lattice parameters. These films exhibit a highly crystalline structure with average lattice parameters a = 4.736 Å and c = 3.069 Å (for films deposited at 500 °C) comparable to the reported values[52]. The crystallite size calculated from Scherrer formula for Ru-doped SnO_2 is between 200 and 250 Å while for pure SnO_2 it is above 330 Å[53]. These characteristics are expected to have a large impact on the gas sensing behavior.

Further, Figure 3.12 shows the XRD profile for Cu-doped SnO_2 thin films deposited at temperatures between 300 and 500 °C. From the XRD profile it is clear that SnO_2 exhibits a single-phase cassiterite structure without the formation of any ternary compound with Cu or any oxides of Cu. At 300 °C the pattern looks nearly amorphous, although, the adhesion of the film with glass substrate is also poor. However, unlike pure SnO_2, the Cu-doped SnO_2 film indicates the formation of crystalline SnO_2 phase at a deposition temperature as low as 350 °C. The crystallization of the film is almost complete at 400 °C with average lattice parameters a = 4.794 Å and c = 3.181 Å comparable to the reported values. The crystallite size that is calculated from the Scherrer formula for the Cu-doped SnO_2 film is between 60 and 170 Å while for pure SnO_2 it is above 330 Å. With increase in temperature the crystallite size decreases as expected. As ionic radii of Cu^{2+} and Sn^{4+} are 0.69 and 0.83 Å, respectively. With a small percentage of Cu in SnO_2 (1.19 wt.%) there is no marked variation in the lattice parameters.

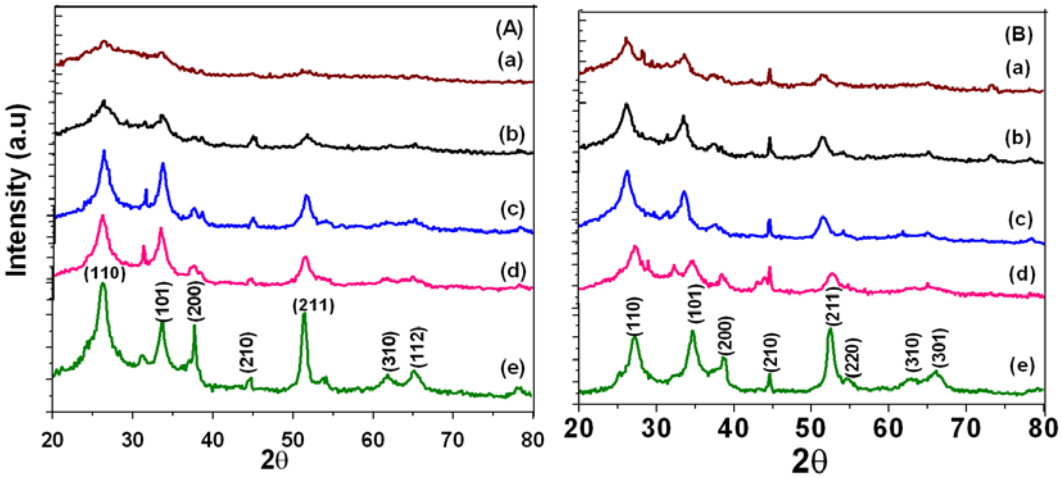

Figure 3.12. XRD profiles for (A) Cu-doped SnO_2 film and (B) Th-doped SnO_2 film deposited at different temperatures: (a) 300 °C, (b) 350 °C, (c) 400 °C, (d) 450 °C and (e) 500 °C.

Figure 3.12 B shows the XRD profile for Th-doped SnO_2 films deposited at temperatures between 300 and 500 °C. All the diffractograms contain the characteristic SnO_2 peaks. The addition of Th results in the preferred (110) orientational growth of the films. The most striking feature from the XRD results is that the films prepared with thorium incorporation starts exhibiting a polycrystalline behavior at a deposition temperature of as low as 300 °C, which on higher deposition temperature becomes more intense. Another significant difference is the intensity of these peaks. For example, thorium incorporation leads to an increase in the peak intensity as compared to that of pure SnO_2 thin films. Moreover, after incorporation of thorium, there is a slight shift towards a higher theta value of about 1.54° implying the decrease in the crystallite size. These films exhibit a crystalline structure with lattice parameters a = 5.154 Å and c = 2.975 Å for the films deposited at 500 °C. The difference in the lattice parameters could be assigned to the higher ionic size of Th (1.79 Å) in comparison with that of Sn (0.83 Å). The crystallite size calculated from the Scherrer formula for Th-doped SnO_2 thin film is between 30 and 80 Å. Thus, a common feature of low temperature crystallization in Ru/Cu/Th -doped SnO_2 is observed, which could be attributed to the role of these doping elements as a promoter for crystallization besides acting as sensitizer.

The observed features are also expected to affect the overall morphology of the sensor material. Thus, Figure 3.13 shows a comparative morphology of pure and doped SnO_2 thin films, deposited at temperatures between 300 and 500 °C. However, the SEM images of films deposited at 300 and 350 °C for pure (A) and Ru-doped SnO_2 (B) do not show any significant morphological differences, since both show only a smooth deposition without the formation of distinct grains. Uniformly distributed grains of less than 1 µm size are observed in Ru-doped SnO_2 at 400 °C, although such features are absent in pure SnO_2. At a higher deposition temperature (450 °C), this distinction becomes more pronounced where the Ru-doped SnO_2 shows nearly spherical grains of ≈1 µm size with a decrease in the grain size from surface to bulk. Pure SnO_2 at the same temperature, however, shows non-uniform grains of smaller dimensions along with the agglomerated grains of 1–2 µm. At higher deposition temperature, however, the grains of Ru-doped films look distorted with a marginal increase in the grain size while pure SnO_2 shows a further increase in the number and size of the grains.

Similar features are also observed for both Cu and Th-doped SnO_2 films. In particular, Cu-doped SnO_2 thin films (C) deposited at 300 exhibits a uniform deposition without the formation of distinct grains. However, for the sample deposited at 400 °C uniformly distributed grains of < 1 µm size are observed. At a higher deposition temperature (450 °C) this distinction becomes more pronounced showing uniformly distributed spherical grains of ~ 500 nm. At a deposition temperature of 500 °C the grains of the Cu-doped films look distorted, clearly depicting the agglomeration of grains of about 150 nm to form clusters of 700 nm grain sizes and more. In case of Th-doped SnO_2 film deposited at 350^0C a spherulite structure with a size varying between 400 and 700 Å are observed. At 400 °C (Figure 3.13 D3), the distinction with that of pure SnO_2 becomes more prominent with the grains increasing in numbers and more spherical, having a size between 200 and 500 Å, showing reduction in the grain size from the surface into the bulk. At higher deposition temperature of 450 °C, (Figure 3.13 D4) an increase in grain size (600 Å and above) and above 450 °C, the appearance of slightly distorted grains of bigger dimensions with few agglomerated grains, are in accordance with the doping effect of Ru and Cu.

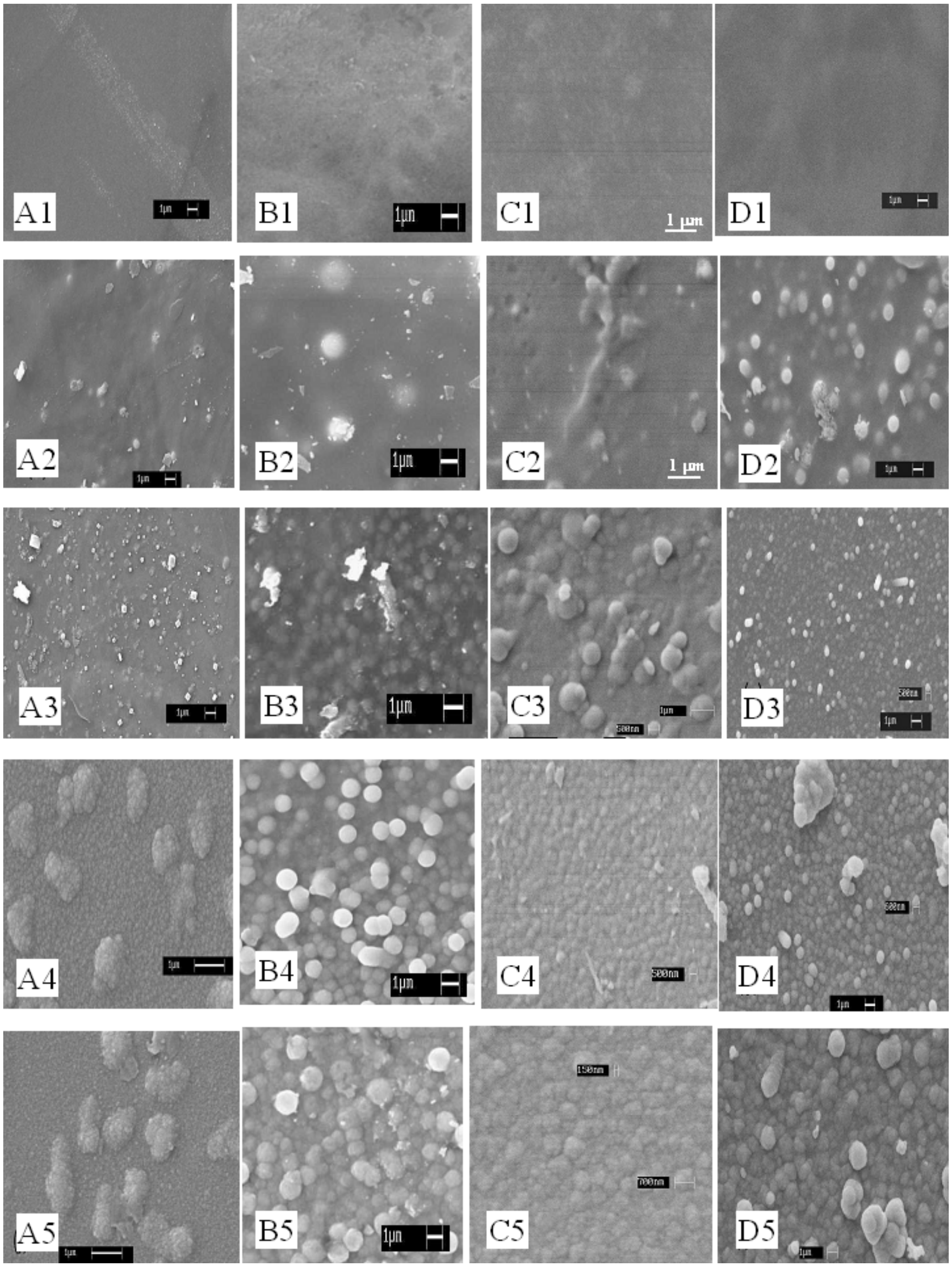

Figure 3.13. SEM micrographs of pure (A), Ru-doped (0.42 wt.%) (B), Cu-doped (1.19 wt.%) and Th-doped (1.18 wt.%) SnO_2 films at: (1) 300 °C, (2) 350 °C, (3) 400 °C, (4) 450 °C and (5) 500 °C.

Thus, the modification with above doping elements has resulted in a systematic transformation of morphology of SnO_2 thin films from smooth to spherical grains and then to agglomeration resulting in the larger grains with diffused grain boundaries. However, the temperature at which a prominent sphere like geometry is seen differs with the specific doping element.

The doping elements thus exhibit a strong influence on both the structure and morphology of SnO_2 and these are expected to have corresponding effects on the sensing performances. Accordingly, Figure 3.14 (a) shows the variation of sensitivity to 1000 ppm of LPG with the operating temperature for different wt.% of ruthenium in SnO_2. It is observed that sensitivity increases with temperature and attains a maximum at 250 °C and again decreases with further increase in the temperature. It is evident from the figure that the composition containing 0.42 wt.% Ru in SnO_2 exhibits highest sensitivity (s = 2500) to LPG at 250 °C. Such a high sensitivity can be attributed to the smaller grain size with uniform distribution. Figure 3.14 (b) indicates the dependence of sensitivity to the amount of ruthenium in the SnO_2 film. The sensitivity increases dramatically when the amount of Ru is 0.42 wt.% followed by a sharp decrease, as the amount of Ru is further increased. The large change in the conductivity in presence of reducing gases can be explained if we consider the changes in the potential barriers at grain boundaries[54]. SnO_2 is an n-type semiconductor in which adsorbed oxygen reacts with a reducing gas releasing electrons into the conduction band by which the conductivity increases. Ruthenium sites act as a catalyst for oxygenation generating many adsorb oxygen species. These adsorbed species can be represented by a surface density of states that are mainly acceptor type. The acceptor or donor like behavior depends on the kind of the adsorbent. The degree of this depletion or accumulation depends inversely on the grain size. The number of surface states is inversely proportional to r^2 where r is the radius of grain while the number of electrons inside the grain is proportional to r^3. Thus, stronger depletion or accumulation will occur in a smaller grain size than in a larger one.

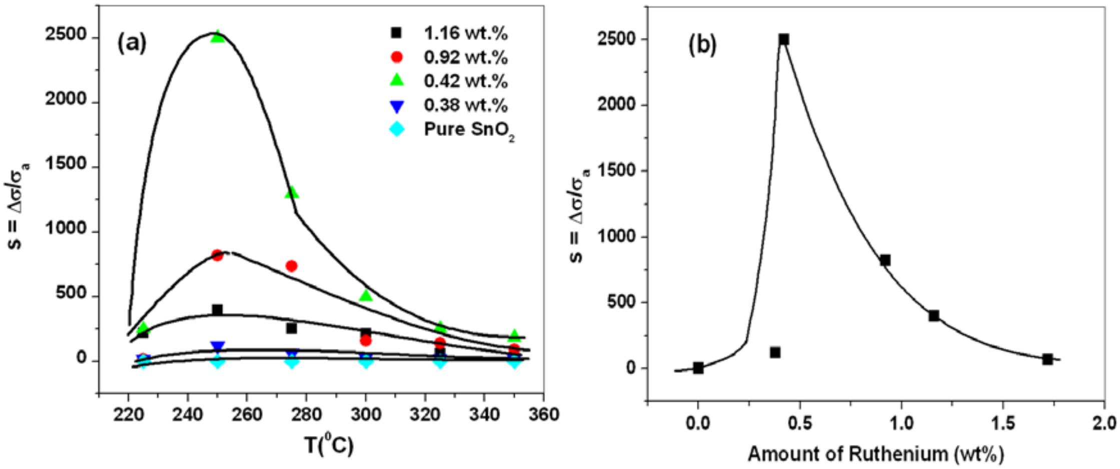

Figure 3.14. (a) Variation of sensitivity to 1000 ppm of LPG with the operating temperature for different wt.% of Ru in SnO_2, (b) dependence of sensitivity on the amount of ruthenium impregnated in the SnO_2 film.

Figure 3. 15 (a) shows the variation of gas sensitivity with concentration change for LPG in ppm. It is found that sensitivity increases linearly with the hydrocarbon gas concentration upto 1000 ppm and saturates for gas concentration of 1200 ppm and above. Figure 3. 15 (b) show the response and recovery behavior of pure and Ru incorporated SnO_2 for 1000 ppm of LPG at 250 °C. The response time for the gas sensing is observed between 30 and 50 s with a recovery time of about 25 min for testing temperature of 250 °C.

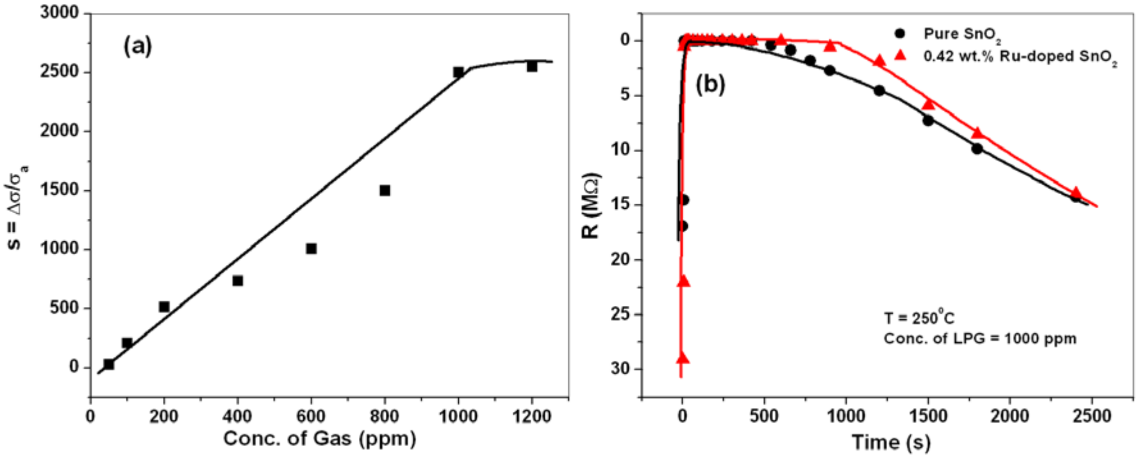

Figure 3.15. (a) Sensitivity variations with gas concentration for 0.42 wt.% ruthenium in SnO_2, (b) response and recovery behavior of pure and Ru incorporated SnO_2 for 1000 ppm of LPG at 250 °C.

Figure 3.16 shows a histogram indicating the selectivity of pure and Ru-doped SnO_2 film (0.42 wt.%) to 1000 ppm of various gases at 250 °C. Ru-doped SnO_2 is highly selective to LPG, the sensitivity (*s*) being 2500 as compared to 3 obtained for the pure SnO_2. It also shows some sensitivity towards higher hydrocarons and hydrogen. However, the sensitivity is negligible for other reducing gases such as CO, NH_3, H_2S, ethanol and kerosene vapors. The adsorption configurations of the gas molecules and the fragmentation reactions on the Ru sites are probably responsible for the high selectivity. Studies of CO oxidation on Ru(0001) reveal that the chemisorption energy of adsorbed O and CO on Ru(0001) are 5.67 and 1.97 eV, respectively[55]. This implies that the oxygen adsorbs more strongly on to Ru(0001) surface. Since CO molecule interacts with the adsorbed oxygen only if it is at the bridge site, the stronger bonding at the hollow site on the Ru surface implies that the adsorbed oxygen at this site is more stable and hence does not react with CO. Thus, this type of sensor element may not show sensitivity to CO. Further, HREELS and TPD studies of NO_2 adsorption on oxygen adsorbed Ru(0001) surface indicate that the presence of pre-adsorbed oxygen poisons the surface with respect to dissociative adsorption[56]. Thus, the sites of adsorbed oxygen and adsorption configuration of the gas molecules may play a significant role in determining the selectivity.

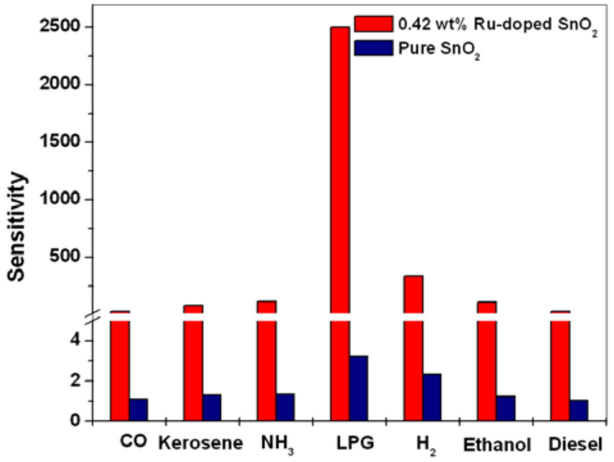

Figure 3.16. Histogram indicating the selectivity of pure and Ru-doped SnO_2 film (0.42 wt.%) to 1000 ppm of different gases at 250 °C.

In the case of Cu-doped SnO_2, the variation of the sensitivity to 1000 ppm of H_2S with the operating temperature for different weight percentages of Cu in the SnO_2 matrix is shown in Figure 3.17 (a). It is observed that the sensitivity towards H_2S increases with temperature and attains a maximum value at 200 °C, followed by a decrease with further increase in the operating temperature. It is observed from the figure that the films containing 1.19 wt.% Cu exhibits the highest sensitivity (910) to H_2S at 200 °C. Figure 3.17 (b) shows the dependence of the sensitivity to the amount of Cu in the SnO_2 film. The sensitivity increases dramatically when the amount of Cu on the surface as detected by EDX is 1.19 wt.%, followed by a sharp decrease with further increase in the amount of Cu.

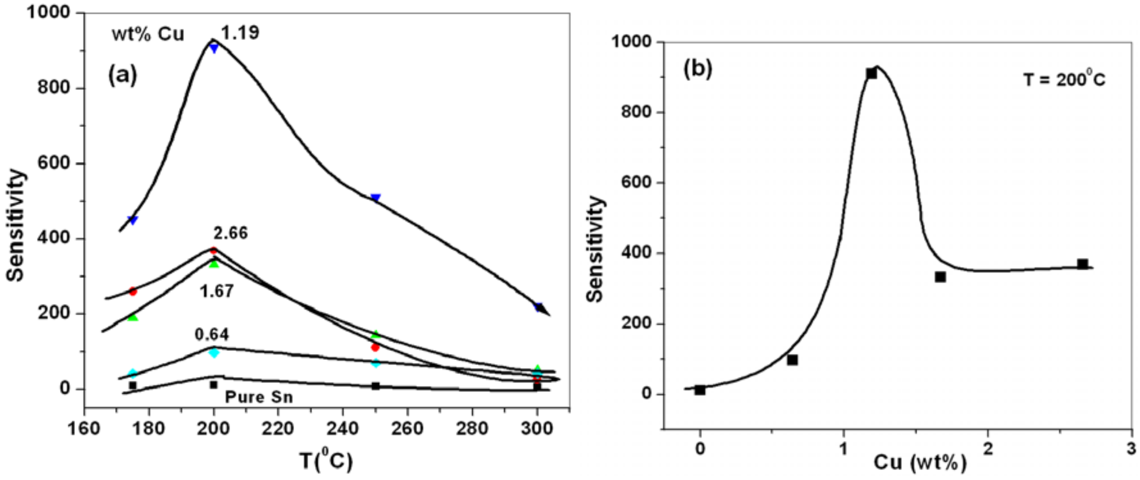

Figure 3.17. (a) Variation of the sensitivity to 1000 ppm of H_2S with the operating temperature for different weight percentages of Cu in the SnO_2 matrix, (b) The dependence of sensitivity to the amount of Cu in the SnO_2 film.

Figure 3.18 shows the response and recovery behavior of pure and Cu-doped SnO_2 for 1000 ppm of H_2S at 200 °C. The gas responds within 10 s with a recovery time of about 25 min wherein about 40% of the recovery takes place within 10 min. The kinetics of the desorption involve many stages and Cu doping obviously helps to rejuvenation.

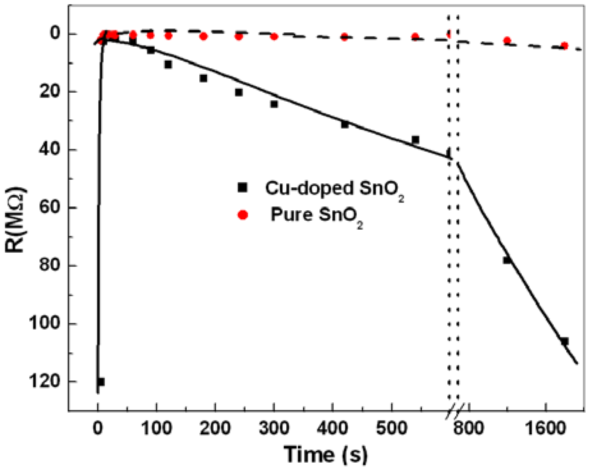

Figure 3.18. Response and recovery behavior of pure and Cu-doped SnO_2 for 1000 ppm of H_2S at 200 °C.

Figure 3.19 shows the variation in the gas sensitivity with its concentration. The sensitivity increases linearly with the H_2S gas up to a concentration of 1000 ppm and saturates at 1200 ppm.

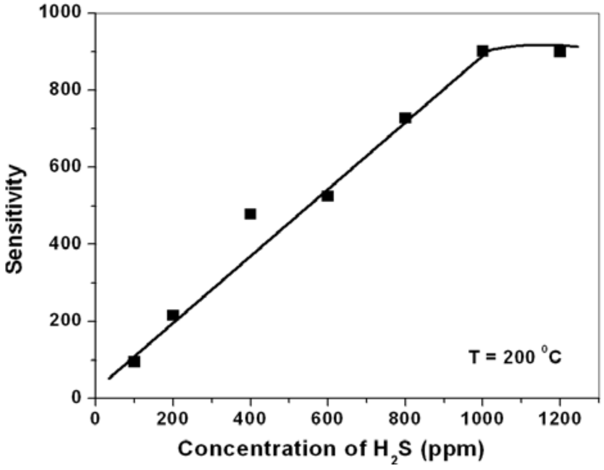

Figure 3.19. Variation of the gas sensitivity with its concentration in ppm range at an operating temperature of 200 °C.

Figure 3.20 shows a histogram indicating the selectivity of pure and Cu-doped SnO_2 films (1.19 wt.%) to 1000 ppm of various gases at 200 °C. Cu-doped SnO_2 is highly selective for H_2S with a sensitivity of 910 as compared to 12 obtained for pure SnO_2. It also shows some sensitivity towards diesel vapors (mixture of mainly benzene, ethylbenzene toluene and xylenes) and hydrogen. However, the sensitivity is negligible for other reducing gases such as CO, NH_3, ethanol and kerosene vapors (mixture of benzene, ethylbenzene toluene and xylenes, straight chain and branched higher (C4-C19) hydrocarbons).

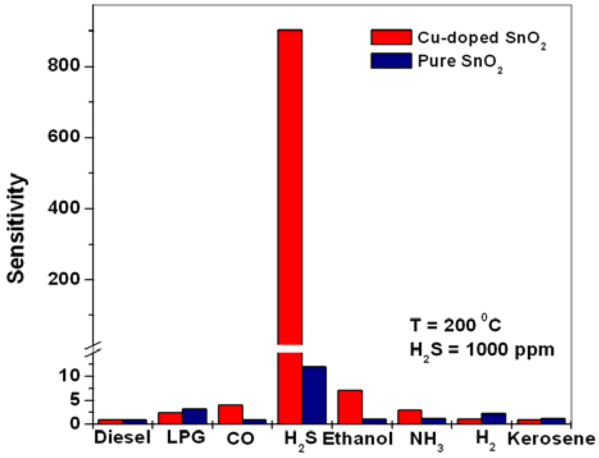

Figure 3.20. A histogram indicating the selectivity of pure and Cu-doped (1.19 wt.%) SnO_2 film to 1000 ppm of various gases at 200 °C.

Recently, conductimetric sensors have also been used in the food industry especially for finding out the freshness of many materials. For example, fish, despite of many precautions like chilling, fast transport etc easily get deteriorated after death[57] and it is important to determine the degree of freshness defined as the number of storage days at a certain temperature from time to time. Chemical investigations have shown that there are five sources of odors, which combine to give rise to the overall odor of fish. It is basically due to the long chain alcohol and carbonyls, bromophenols, and N-cyclic compounds. Opposite to the fresh fish odor is the microbial spoilage odor caused by compounds that are microbially formed during the degradation. These compounds are short chain alcohols and carbonyls, amines, sulfur compounds, aromatics, N-cyclic compounds and some acids. The concentrations of these volatile species increase with time as the fish spoils; some of these are often used as indicators of spoilage. It is also reported that gases like trimethylamine (TMA), dimethylamine (DMA), triethylamine (TEA) and NH_3 are liberated during the deterioration of fish and that the concentration of

TMA and TEA increases significantly after death[58]. Sintered titania with ruthenium is highly sensitive towards TMA but needs a high operating temperature[59].

Figure 3.21 shows the dependence of the sensitivity to the amount of thorium in SnO_2 for 800 ppm TMA at 250 °C. The sensitivity of the Th-doped SnO_2 increases dramatically when the amount of thorium is 1.18 wt.%, followed by a sharp decrease with further increase in the Th content. The enhanced sensitivity is attributed to the amount and distribution of thorium. The lower thorium concentrations have a discontinuous distribution, causing insufficient catalytic activity leading to the lower sensitivity, while a higher concentration leads to a continuous distribution, thereby resulting into a lower initial resistance and hence lower sensitivity values. The inset in Figure 3.21 shows the variation in the gas sensitivity with its concentration. It is found that the sensitivity increases linearly with TMA up to 800 ppm concentration, and saturates at around 1000 vol. ppm.

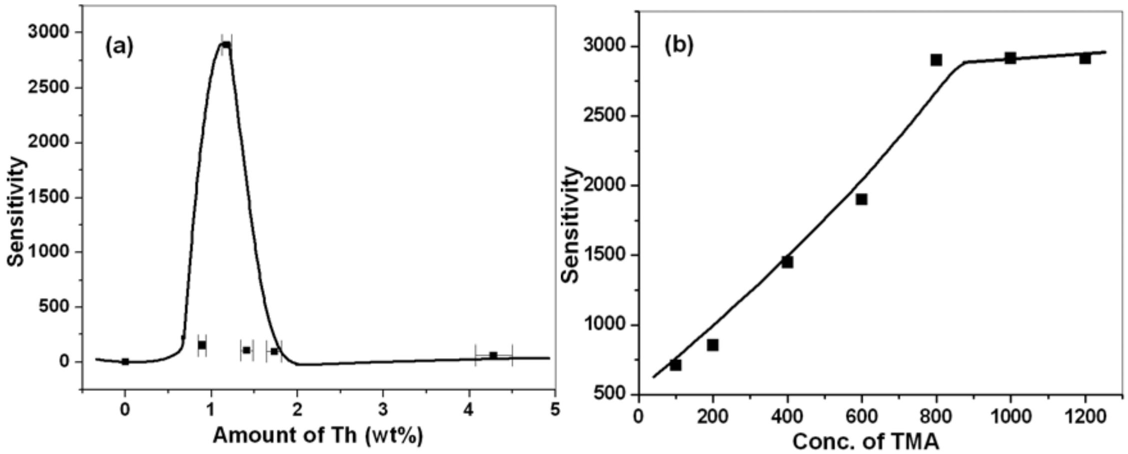

Figure 3. 21. Dependence of sensitivity to the amount of thorium in SnO_2 for 800 vol. ppm TMA at 250 °C with an inset showing variation in the gas sensitivity with its concentration in ppm.

Figure 3.22 shows the variation of sensitivity to 800 vol. ppm of TMA with the operating temperature for 1.18 wt.% of thorium in SnO_2 matrix deposited at different temperature. The sensitivity towards TMA increases with the operating temperature and attains a maximum value at 250 °C followed by the decreases with further increase in the operating temperatures. Sensitivity also increases with the deposition temperature and is highest for 350 °C although it reduces further for films prepared at higher deposition temperature. This is due to the fact that films deposited at 350 °C have a large surface area. At higher deposition temperature, the grain size also increases leading to a concomitant decrease in the number of adsorption sites hence the sensitivity.

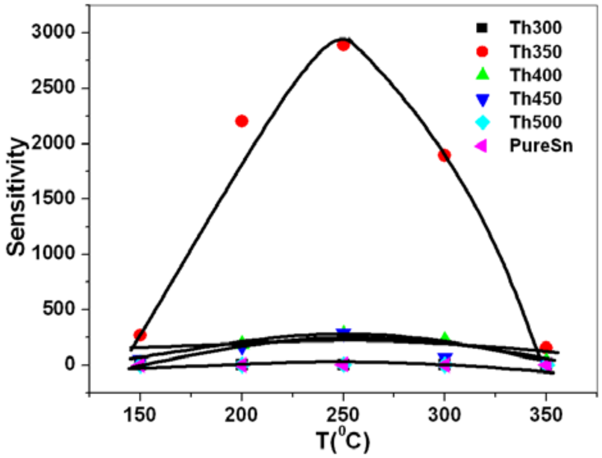

Figure 3.22. Variation of sensitivity to 800 ppm of TMA with operating temperature for 1.18 wt.% of thorium in the SnO_2 matrix deposited at different temperature.

Figure 3.23 shows a histogram indicating the selectivity of pure and thorium-doped SnO_2 film (1.18 wt.%) to 800 ppm of various gases at 250 °C. Thorium-doped SnO_2 is highly selective for TMA with the sensitivity of 2900 as compared to only 5 obtained for the pure SnO_2. As compared to TMA, a very small sensitivity ranging between 20 and 60 are observed for DMA, alcohol and hydrogen, while the sensitivity is negligible (<10) for other reducing gases such as CO, NH_3, H_2S and kerosene vapor.

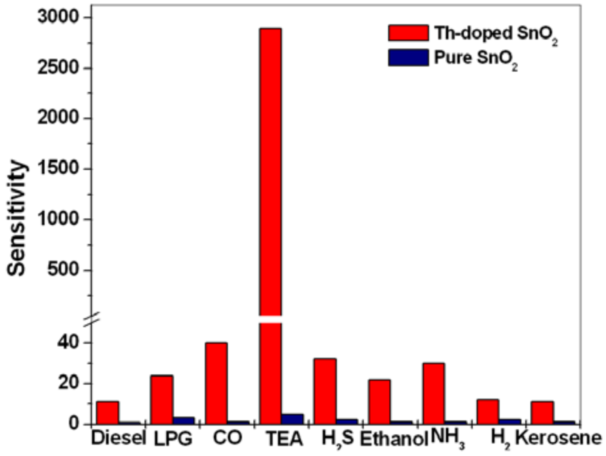

Figure 3. 23. Histogram indicating the selectivity of pure and Th-doped SnO_2 film to 800 vol. ppm of various gases at 250 °C.

In order to understand the gas sensing mechanism, XPS studies on the films with optimum doping element are very useful. It is well known that the BE values are sensitive to the covalent character of a metal–oxygen bond with larger covalency resulting in smaller binding values. Therefore, it follows that the Sn–O bond in SnO_2 is more covalent than the Sn–O bond in SnO. Figure 3.24 shows the XP spectra of Cu-doped SnO_2 film before and after the exposure to H_2S gas. Figure 3. 24a shows the XPS spectra corresponding to the Cu content in the doped SnO_2 film, with peaks at 933.3, 956.8 and 944.8 eV, indicating the presence of Cu($2P_{3/2}$), Cu ($2P_{1/2}$) and $Cu(OH)_2$ species, respectively. However, after the exposure to H_2S gas (Figure 3.26b) only two peaks at 932.6 and 952.4 eV with apparent shifts corresponding to the formation of CuS and Cu^+ are seen[60]. The appearance of the Cu-S peak strongly suggests the role of Cu in the detection of H_2S through the formation of a chemical bond, which is further supported by the emergence of the sulfur peak. Figure 3.25a shows the sulfur spectrum recorded for the Cu-doped SnO_2 film before and after the exposure to H_2S gas. After the exposure to H_2S, interestingly, three sulfur peaks at BE of 162, 164.2 and 169.4 eV are seen. The sulfur species at 162 and 164.2 eV are in the BE range for CuS and disulfide, which can be assigned to unbound thiol molecules. The sulfur peak at 169.4 eV suggests the formation of sulfate or sulphonic acid moiety[60]. It is also observed that the H_2S treatment results in a shift of the binding energies of Sn and oxygen, respectively (Figure 3.27b and c).

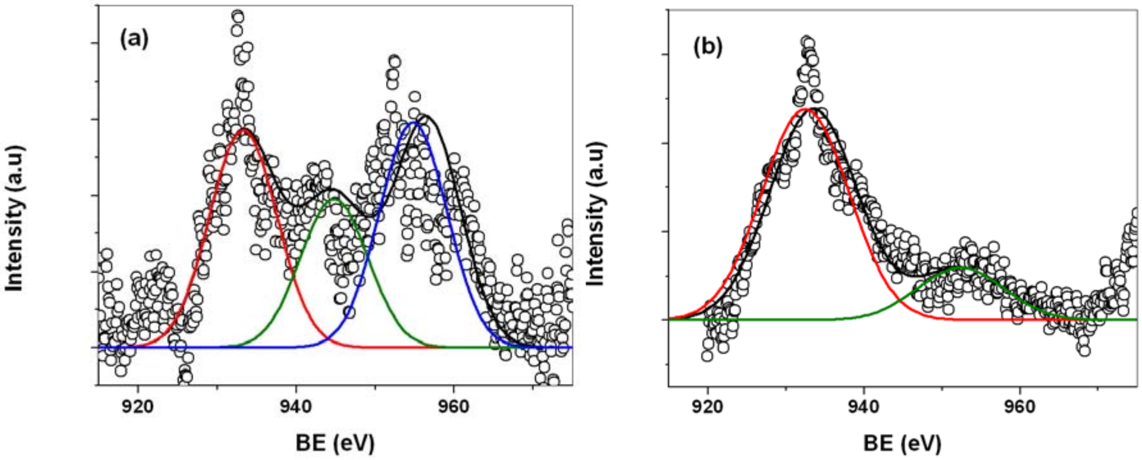

Figure 3.24. XP spectra of Cu in a Cu-doped SnO_2 thin film before (a) and after (b) the exposure to H_2S gas.

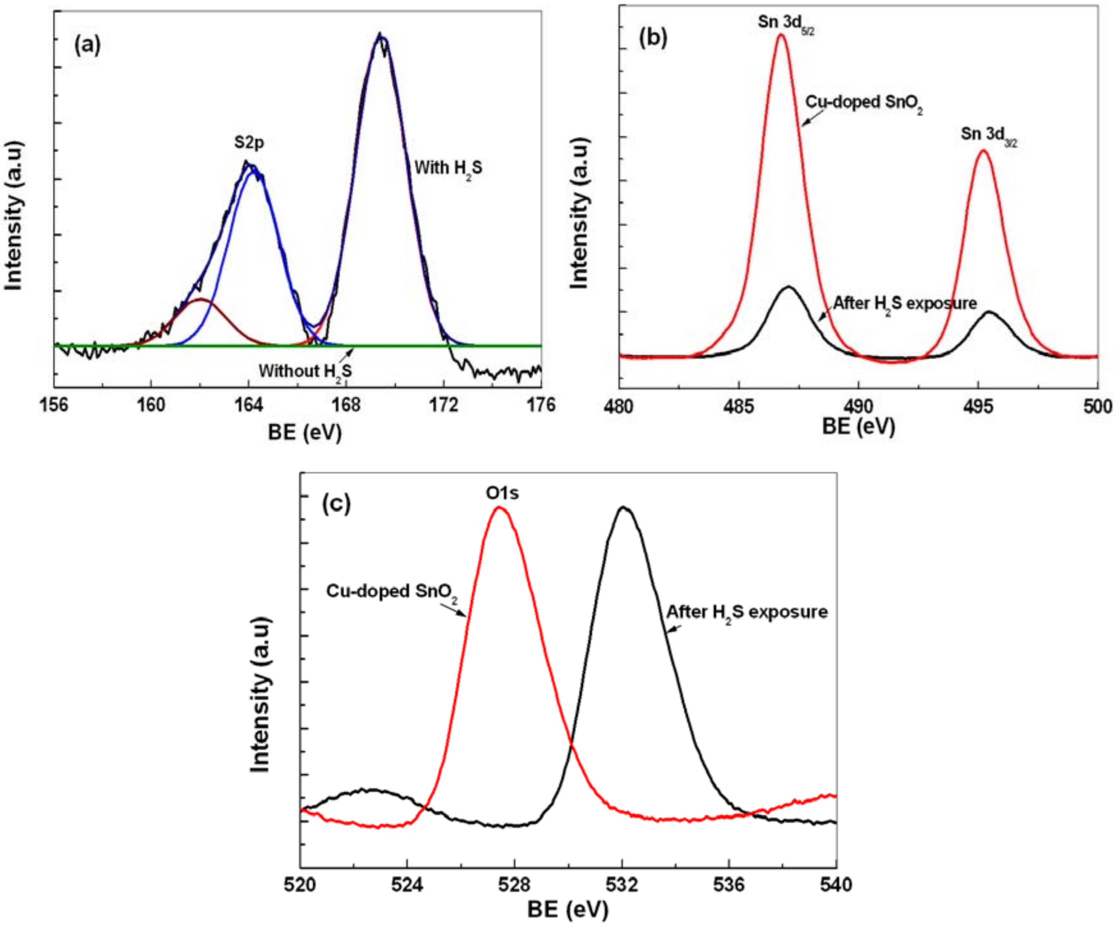

Figure 3.25. XP spectra of a Cu-doped SnO_2 thin film before and after the exposure to H_2S gas (a) S, (b) Sn, (c) O.

Figure 3.26 shows the XP spectra of thorium-doped SnO_2 before and after the exposure to TMA gas. The spectra of Th-doped SnO_2 (Figure 3.26a) show two separate signals at 486.7 and 495.1 eV, respectively, corresponding to Sn $3d_{5/2}$ and Sn $3d_{3/2}$ with a peak separation of 8.40 eV. The asymmetry in oxygen peaks (Figure 3.26b) implies that it can be resolved into three components corresponding to O1s of 530.5 eV belonging to lattice while 531.9 and 533.3 eV corresponding to adsorbed oxygen and free oxygen, respectively. The peak position of the hydroxyl ion (OH^-) was reported as 531.8 eV on a SnO_x surface. The peak at 533.3 eV can be attributed to the weakly bound surface oxygen. However, it is observed that as compared to pure SnO_2, the BE of Sn shifts towards higher values (1.5 eV) indicating an increase in the oxide moieties, i.e., more number of oxygen are absorbed, resulting in the higher resistance value. It is also possible that the shift may be due to an intrinsic size confinement effects. More sophisticated XPS measurements with better resolution are needed to confirm this. Compared to pure SnO_2 the BE values of oxygen for thorium-doped SnO_2 shifts towards lower side (0.5 eV) probably due to the shared oxygen by both Sn and Th. After the exposure to trimethylamine gas, an apparent shift of 0.2 eV is observed in oxygen and 0.04 eV for Sn. The thorium spectra (Figure 3.28c) show two prominent peaks at 335.7, and 343.2 eV corresponding to Th $4f_{7/2}$ and Th $4f_{5/2}$ respectively[61]. Interestingly, two satellite peaks at BE of 331.3 and 348.4 eV are also observed. The peak at 349.8 eV could be the result of an electronic excitation from the thorium–oxygen valence band to a conduction band minimum. After the exposure to trimethylamine there is an apparent shift in all the peaks to lower BE side. Incorporation of thorium in the SnO_2 matrix not only enhances the sensitivity towards TMA but also improves its selectivity. After the exposure to trimethylamine gas, the appearance of the nitrogen peak (Figure 3.28d) at 400.9 eV suggests a strong interaction of TMA with thorium-incorporated SnO_2.

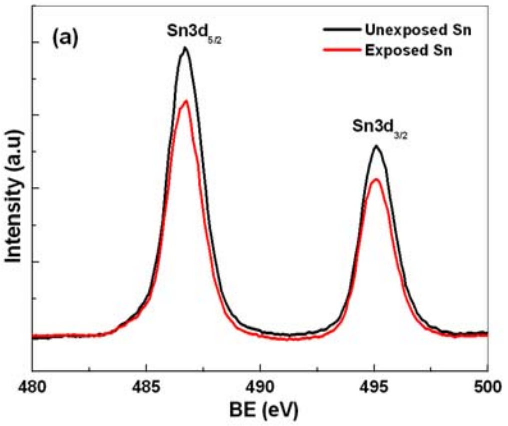

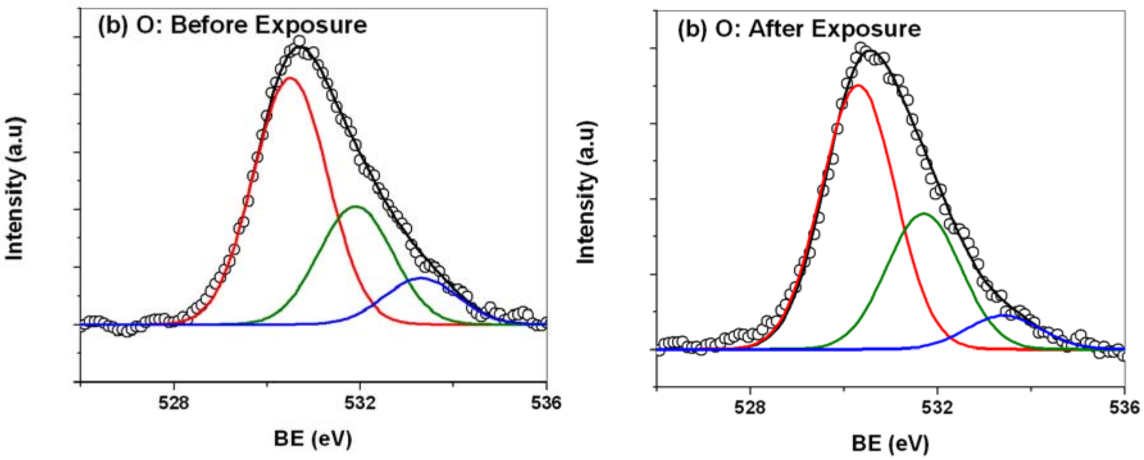

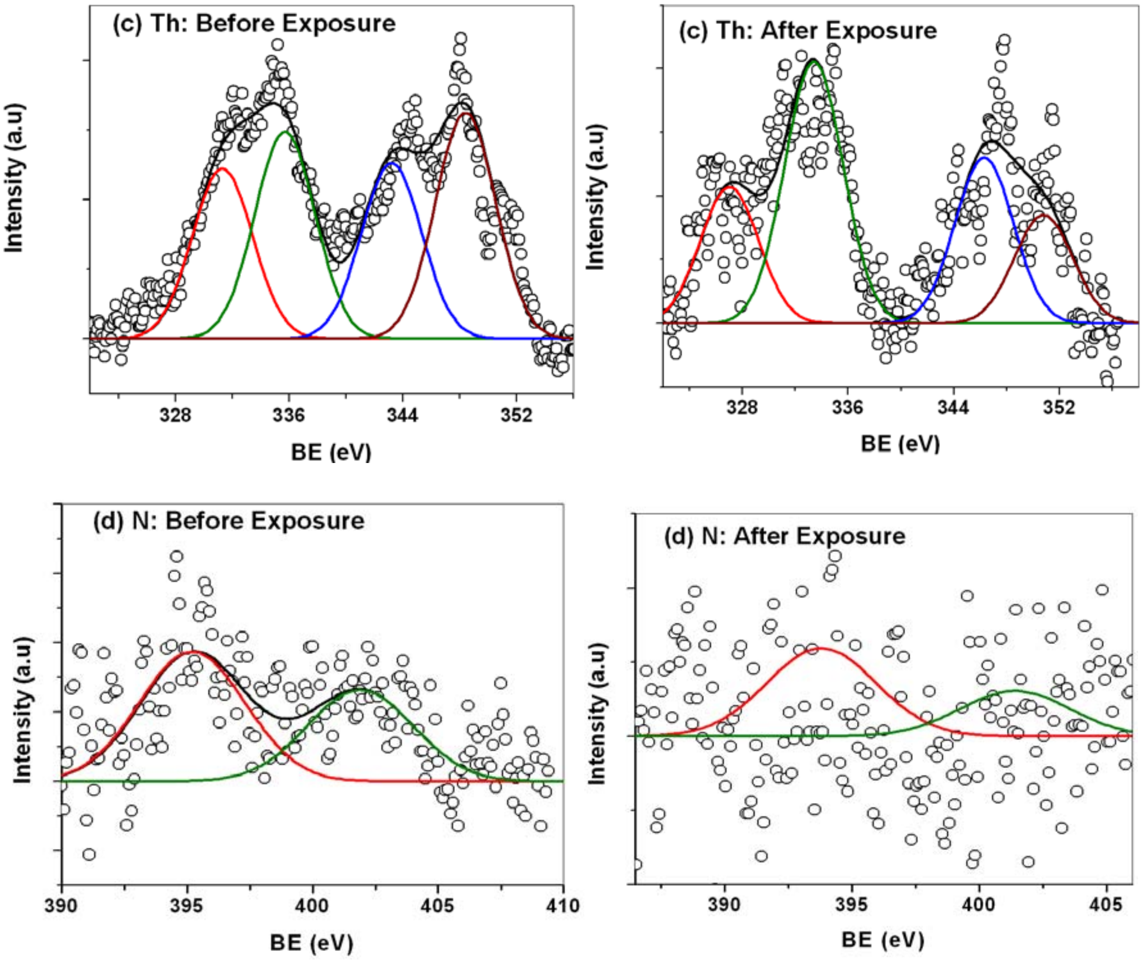

Figure 3.26. XP spectra of Th-doped SnO_2 films before and after the exposure to TMA gas: (a) Sn, (b) O, (c) Th and (d) N.

3.4.5. Gas Sensing Properties of SnO_2 Nanowires, Nanobipyramids and Cubes

In chapter 2, various aspects of low temperature of crystallization have been discussed in details, which controls the formation of nanostructures of SnO_2. A high surface to volume ratio along with inherent quantum size effects of these structures is promising in their utilization for sensor applications. Accordingly, Figure 3.27 shows the temperature dependent sensing behavior towards NO_2 in air for SnO_2 nanowires with different Ru content. With reference to Figure 3.29, R_a is the resistance in the presence of air and R_g is the resistance in the presence of the test gas. The (0.48 wt%) Ru-doped SnO_2 exhibits highest sensitivity towards NO_2 at the room temperature while SnO_2 with

0.23 wt% Ru shows different behavior, where the sensitivity initially increases with temperature, attains a maximum at 100 °C followed by a decrease in sensitivity with a further increase in temperature. Figure 3.28 reports the sensitivity results, averaged over the three sensors prepared under identical conditions (with similar Ru content) towards NO_2. All the sensors with 20 wt% RuO_2 in the starting mixture (Batch 1a–1c) show the highest sensitivity at room temperature. The marginal variation in the sensitivity values can be attributed to the nanowires distribution (i.e., diameter distribution) on the substrate. Sensors with 10 wt% RuO_2 in the starting mixture (Batch 2a–2c) always reveal higher sensitivity to NO_2 at the operating temperature of 100 °C. These result shows that sensors within a given Ru content behave similarly, thus also ensuring fairly good reproducibility, which is anyway important for nanostructured materials.

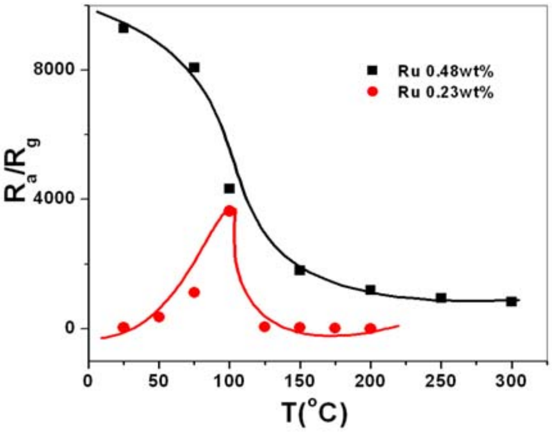

Figure 3.27. NO_2 sensitivity as a function of temperature for SnO_2 wires (1000 ppm) with different Ru concentrations.

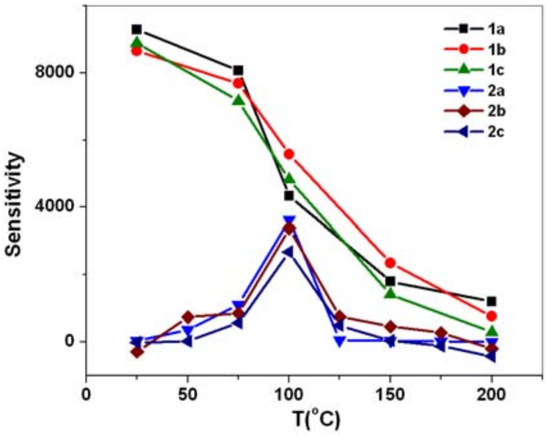

Figure 3.28. The sensitivity results averaged over the three sensors prepared under identical conditions with similar Ru content in the reaction mixture towards 1000 ppm of NO_2.

These wires also exhibit sensitivity towards LPG in air as shown in Figure 3.29, with a maximum at 250 °C in accordance to our earlier results. Interestingly, SnO_2 nanowires with 0.23 wt% Ru (as measured by EDX) show higher sensitivity towards NO_2 at room temperature. Further, a maximum sensitivity towards LPG is observed at 250^{o}C. These sensors also respond for test gases like CO, C_2H_5OH and H_2, although, no appreciable variation in sensitivity value is observed implying selectivity towards NO_2 and LPG.

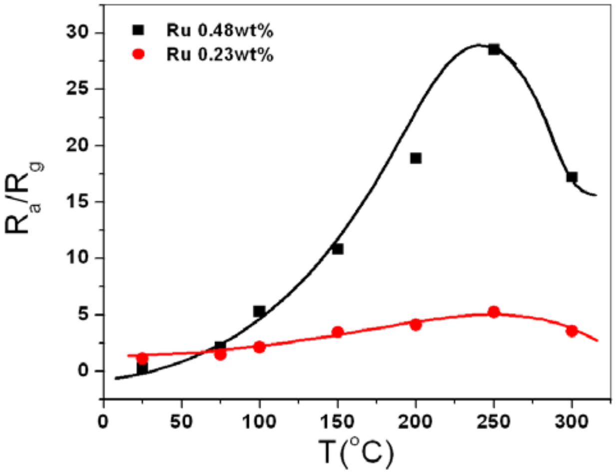

Figure 3.29. Response of SnO_2 nanowires with different Ru doping towards 1000 ppm of LPG; both samples exhibit a maximum in sensitivity at 250^{o}C.

One of the important parameters governing the sensor performance and reliability is the electrode contact. The nature of the electrical contacts between the SnO_2 and Ag electrode is thus important to understand the behavior of these devices, and accordingly, figure 3.30 shows a typical *I–V* measurement for nanowires at an operating temperature of 100 °C. The sample with 0.48 wt% Ru exhibits a linear behavior passing through the origin implying an ohmic contact. Since these high aspect ratio structures can act like a quasi-1D structure with interesting transport behavior, their electrical transport properties at low temperature can be more interesting especially single wires are investigated. Figure 3.31 depicts the low temperature conductance measurement of these samples (nanowire films) with 0.48 wt% Ru, wherein, a power law dependence on temperature is observed suggesting the material to behave as a Luttinger liquid[62]. Tomonaga-Luttinger liquid, more often referred to as simply Luttinger liquid, is a theoretical model describing interacting electrons (or other fermions) in a 1D conductor (e.g. quantum wires such as carbon nanotubes). Such a model is necessary since the commonly used Fermi liquid model breaks down for explaining many interesting aspects of 1D structures. The important features of Luttinger liquid are that it contains spin density waves (whose velocity, to lowest approximation, is equal to the unperturbed Fermi velocity), propagating independently from the charge density waves (commonly referred to as spin-charge separation). Further, the charge and the spin waves can be considered as the elementary excitations of the Luttinger liquid, unlike the quasiparticles of the Fermi liquid. The tunneling rate into a Luttinger liquid is suppressed to zero at low voltages and temperatures, as a power law. Accordingly, the low temperature conductance measurement of these nanostructures (having 0.48 wt% Ru) exhibits power law dependence with temperature as

$$G \propto T^{\alpha} \qquad -(1)$$

where, G is the conductance (μS), T the temperature and α is the luttinger liquid parameter having value 0.46. The observed behavior suggests that the Ru-doped SnO_2 nanowires behave as a Luttinger-liquid, i.e. a system with correlated electrons upto room temperature.

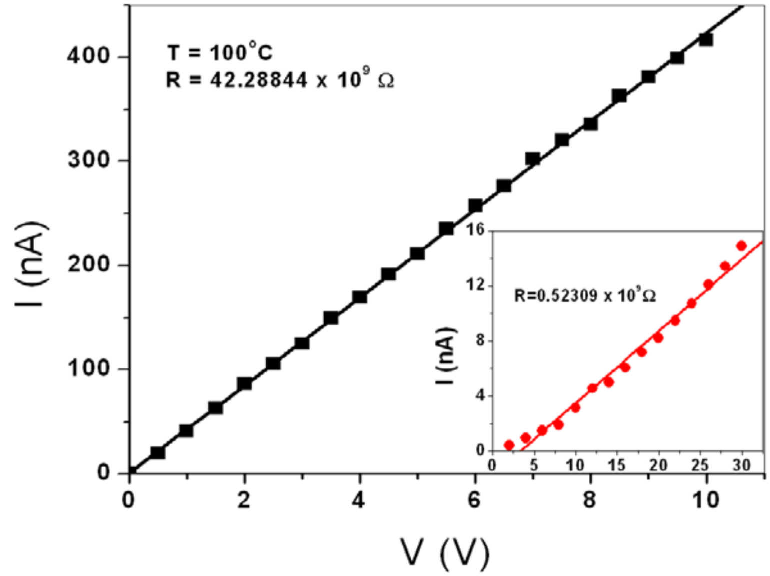

Figure 3.30. The *I–V* data of nanowires at the operating temperature of 100 °C, indicating a linear behavior passing through the origin.

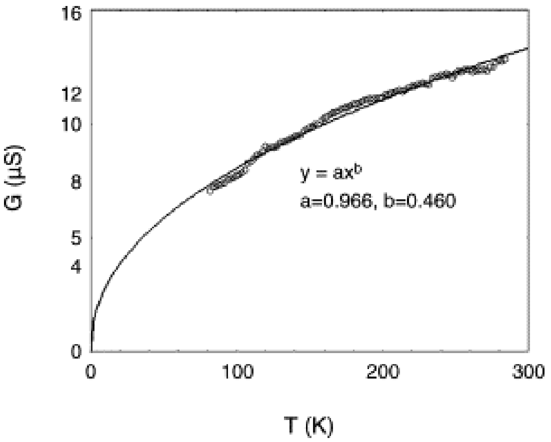

Figure 3.31. The low temperature conductance measurement of the sample with 0.48 wt% Ru in SnO_2, wherein a power law dependence on temperature is observed which suggests that the material behaves as a system with strongly correlated electron, i.e. a Luttinger liquid.

Figure 3.32 indicates the difference in sensitivity of 0.48 wt% Ru-doped SnO_2 sample at room temperature when NO_2 concentration is cycled from 0 to 200 ppm in discrete steps of 50 ppm. It is clear from the figure that the nanowires respond without much hysteresis suggesting a drift free operation. The response times of all the sensors are in the range of 30–90 s, although higher concentrations of the gases cannot be measured, due to their high resistance ($>10^{14}\ \Omega$). Figure 3. 33 reveal the change in electrical resistance as a function of temperature for 0.48 wt% Ru, as the sensor is switched repeatedly from air to 200 ppm NO_2 to demonstrate its stability. The magnitude of the resistance variation increases with temperature, starting from a marginal variation at room temperature to a remarkable variation of three orders at 100 °C.

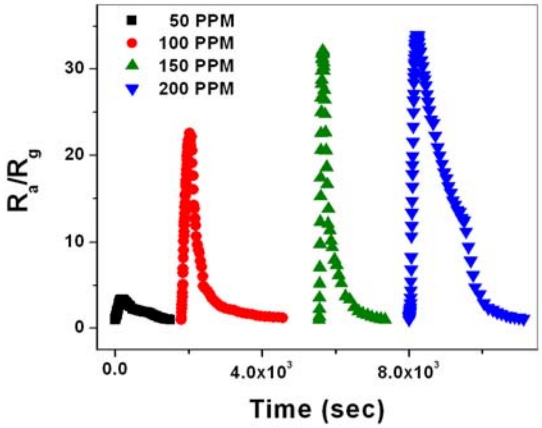

Figure 3.32. Response of Ru-doped SnO_2 nanowires upon cycling the concentration of NO_2 at room temperature; these measurements are carried out in the dry air at a constant voltage.

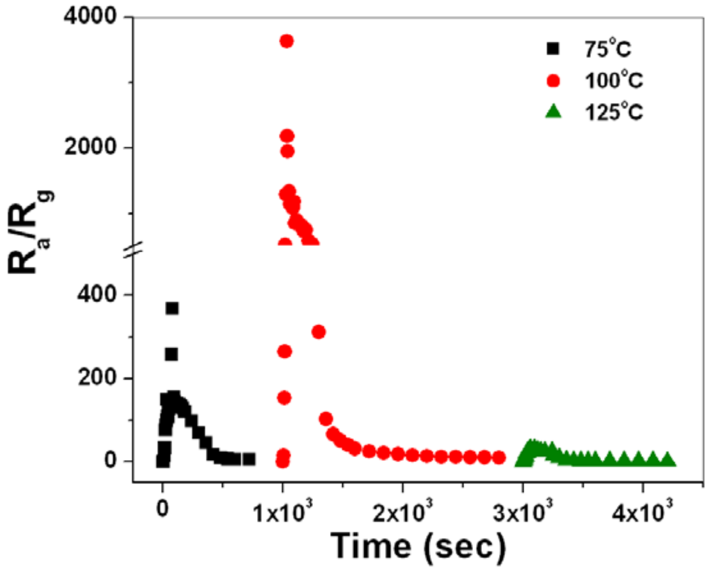

Figure 3.33. Change in electrical resistance as a function of temperature for 0.48 wt% Ru-doped SnO_2, as the sensor is switched repeatedly from the dry air to 200 ppm NO_2. The sensor responds with a maximum sensitivity at 100 °C. The sensors are initially kept at the operating temperature for 2 h and the test gas is introduced when the resistance becomes stable. Response behavior is shown as a function of time for simplicity.

3.5. Plausible Gas Sensing Mechanism

SnO_2 is an n-type semiconductor and the adsorption/desorption of gas molecules on its surface causes a significant change in the resistance. It is well known that the Ru^{4+} species gets converted to Ru^{3+} species by the adsorbed reducing gas. The test gas preferentially adsorbs on the Ru sites donating an electron in the process where Ru sites act as catalysts thereby increasing the adsorption of the gas molecules. The oxygen species O^{2-}, O^- and O_2^- are present on the surface and such adsorbed oxygen species abstract electrons from SnO_2 causing an increase in the potential barrier. When the test gas adsorbs on the surface, electron transfers from the ruthenium to the surface states near the conduction band edge of SnO_2 generating adequate Ru^{3+} species. The energy released during the decomposition of the adsorbed gas is sufficient for the electrons to jump into the conduction band of SnO_2 causing an increase in the conductivity. As the species of the decomposed test gas desorbs from the surface, oxygen is again adsorbed forming O^{2-} or O^- species by abstraction of electrons from the conduction band, thus causing a decrease in conductance.

In case of Cu-doped SnO_2 also, the adsorbed oxygen reacts with the H_2S gas releasing electrons into the conduction band by which the conductivity increases. In particular, at these operating temperature (<200 °C), when H_2S is chemisorbed on the surface, the metal oxide is chemically transformed at least partially into sulfides, i.e.

$$2H_2S+SnO_2 \leftrightarrow SnS_2+2H_2O \qquad -(2)$$

$$4H_2S_{(ads)}+6CuO_{(s)} \rightarrow 3Cu_2S_{(s)}+2H_2O+SO_{2(g)} \qquad -(3)$$

The formation of conducting CuS results in the removal of the electrical barrier between n-SnO_2 and p-CuO. Moreover, H_2S also interacts with chemisorbed oxygen resulting in the release of a large number of free electrons.

$$H_2S_{(ads)}+3O^{2-}{}_{(s)} \rightarrow SO_{2(g)}+2H_2O+6e^- \qquad -(4)$$

These electrons are responsible for the higher sensitivity values. On subsequent exposure to O_2 the sulfide is brought back to CuO as

$$CuS + 3/2O_2 \rightarrow CuO + SO_2 \qquad -(5)$$

Thorium species in the Th-doped SnO_2 thin films also helps in increasing the adsorb oxygen species on SnO_2. The adsorbed oxygen extracts the conduction electrons from the surface region of SnO_2 grains, leaving positively charged donor ions behind. Consequently, an electric field develops between the positively charged donor ions and the negatively charged oxygen ions such as O^{2-}, O^- on the surface[63]. The more the oxygen ions are on the surface, the higher the potential barrier and, therefore, the higher is the resistance[64]. As the concentration of trimethylamine gas increases, the amount of O^{2-} and O^- decrease due to the reaction with trimethylamine molecules, resulting in a lowering of resistance and hence thorium seems to help in speeding up the adsorption/desorption rate.

The nanostructures, interestingly, are also characterized by the presence of surface oxygen vacancies. Oxygen perhaps interacts strongly with a vacancy, forming a peroxide-bridge structure followed by a charge transfer leading to a large change in the resistance. Moreover, NO_2 (a combustion product that plays a key role in tropospheric ozone, and smog formation) acts as an electron-trapping adsorbate on SnO_2 crystal faces. It can bind strongly at an O vacancy as one of the NO_2 oxygen effectively fills the vacancy[29]. Direct adsorption is also proposed for strongly electronegative NO_2—whose effect is to decrease sensor conductance[10, 11]:

$$NO_{2,}\,(gas) \leftrightarrow NO_{2,\,ads} \qquad -(6)$$

$$e^{-} + NO_{2,\,ads} \leftrightarrow NO_{2}^{-}{}_{,\,ads} \qquad -(7)$$

The occupation of surface states, which are much deeper in the band-gap than oxygen's, increases the surface potential and reduces the overall sensor conductance. The presence of a porous structure, further, helps in improving the surface to volume ratio thereby increasing the sensitivity. Oxygen vacancies present on the surface of SnO_2 acts as active sites for water dissociation, and hence SnO_2 nanowires can also be used as humidity sensors[65]. Heating the nanowires at 400 °C ensures the removal of adsorbed hydroxyl groups present on the surface of nanowires. Further, the resistance remains stable as long as the environment around the sensor does not change.

3.6. Conclusions

In the present chapter we have elucidated a systematic improvement in the sensing properties of SnO_2 using two significant strategies, namely surface modification and doping with elements like Ru/Cu and Th. More importantly, novel nanostructures of SnO_2 in the form of nanowires, nanobipyramids and cubes exhibit encouraging sensing results. In particular, SnO_2 surface and matrix have been effectively modified to get sensors with improved performance. For example, the surface ruthenated SnO_2 thin films show enhanced sensitivity (45) and selectivity as compared to that of pure SnO_2 films (3). The surface of SnO_2 films can, however, be tailored to obtain sensors with very high selectivity for many gases. The response and recovery of these sensors are very fast as compared to that of pristine SnO_2 films and it is possible to obtain sensors with high sensitivity and selectivity by controlling the morphology of the films.

This chapter has also demonstrated that surface functionalized SnO_2 film with Cu MPCs shows a high sensitivity towards H_2S (400 ppm) at room temperature. The functional groups present in the capping agents of CuMPCs play an important role in determining the sensitivity under the existing relative humidity onditions. The number of -OH groups can enhance this property by acting as an intermediate for attachment of the thiol chains to the SnO_2 surface. In addition, increasing chain lengths also improves the sensitivity since the interaction of H_2S with shorter chain length forms a liquid like state while that with the long chain gives a disordered state. These preliminary studies give some insight regarding how the sensing takes place although a more thorough understanding of how the nanoclusters contribute in imparting these excellent sensing characteristics to SnO_2 needs more detailed investigations.

In addition, we have developed many Ru/Cu/Th –doped SnO_2 thin film sensors for the selective detection of gases like LPG, H_2S and TMA. These dopants in the SnO_2 matrix act as oxidative catalysts to achieve a considerable degree of sensitivity and selectivity although in many cases, the low temperature of preparation by the dual use of dopants as a sensitizer and a sintering aid remarkably enhances the sensing performance remarkably. Moreover, the electronic interaction between metallic additives and semiconducting oxide based gas sensors is shown in this chapter as one of the probable reasons for the enhancement of sensitivity towards hydrocarbon. The large change in conductance observed is attributed to the availability of free electrons during the oxidation of reducing gases on the surface of the gas sensitive layer. This effect is particularly significant for Ru-doped SnO_2 in the form of nanowires as they exhibit a highly selective sensing behavior towards NO_2 even at room temperature. The amount of Ru is the deciding factor here also governing the operating temperature and sensor response. Using thinner nanowires or utilizing a single nanowire with proper SnO_2-metal ohmic contacts probably would achieve additional increase in sensitivity. The study thus opens up the possibility of tailoring the SnO_2 nanowires for gas sensing applications by choosing proper doping element and its concentration.

3.7. References

1. Imawan, C.; Solzbacher, F.; Steffes, H.; Obermeier, E.; *Sens. Actuators B* **2000**, 68(1), 184.
2. Stankova, M.; Vilanova, X.; Calderer, J.; Llobet, E.; Brezmes, J.; Gràcia, I.; Cané, C.; Correig, X. *Sens. Actuators B* **2006**, 113, 241.
3. Wang, C.; Chu, X.; Wu, M. *Sens. Actuators B* **2006**, 113, 320.
4. Ménini, P.; Parret, F.; Guerrero, M.; Soulantica, K.; Erades, L.; Maisonnat, A.; Chaudret, B. *Sens. Actuators B* **2004**,103, 111.
5. Göpel, W.; Schierbaum, K. D. *Sens. Actuators B* **1995**, *26, 1.*
6. Heilig, A., Barsan, N., Weimar, U.; Göpel, W. *Sens. Actuators B* **1999**,58, 302.
7. (a) Zhang, G.; Liu, M. *Sens. Actuators B* **2000**, 69, 144. (b) Šetkus, A.; Baratto, C.; Comini, E.; Faglia, G.; Galdikas, A.; Kancleris, Ž.; Sberveglieri, G.; Senulienė, D. *Sens. Actuators B* **2004**, 103, 448. (c) Chen, Y.; Cui, X.; Zhang, K.; Pan, D.; Zhang, S.; Wang, B.; Hou, J. G. *Chem. Phys. Lett.* **2003,** 369, 16.
8. Zakrzewska**,** K. *Thin Solid Films,* **2001**, 391, 229.
9. G. Sberveglieri**,** *Sens. Actuators B* **1992**, 6, 239.
10. Comini, E.; Faglia, G.; Sberveglieri, G.; Contalini, C.; Paesacantando, M.; Santucci, S.; Li, Y.; Wlodarski, W.; Qu, W. *Sens. Actuators B* **2000**, 68, 168.
11. Garzella, C.; Comini, E.; Tempesti, E.; Frigeri, C.; Sberveglieri, G. *Sens. Actuators* B **2000**, 68, 189.
12. Steffes, H.; Imawan, C.; Solzbacher, F.; Obermeier, E. *Sens. Actuators B* **2000**, 68, 249.
13. Mukhopadhay, A.K.; Mitra, P.; Chaterjee, A.P.; Maiti, H. S. *Ceram. Int.* **2000**, 26, 123.
14. Shishiyanu, S. T.; Shishiyanu, T. S.; Lupan, O. I. *Sens. Actuators B* **2005**, 107, 379.
15. Schwebel, T.; Fleischer, M.; Meixner, H. *Sens. Actuators B* **2000**, 65, 176.
16. Zhu, W.; Tan, O.K.; Yan, Q.; Oh, J.T. *Sens. Actuators B* **2000**, 65, 366.
17. Liu, C.J.; Wang, S.Y.; Hsieh, J.C.; Ju, Y.H. *Sens. Actuators B* **2000**, 65, 371.
18. Yamazoe**,** N. *Sens. Actuators B* **1991**, 5, 7.
19. (a) Leite, E.R.; Weber, I.T.; Longo, E.; Varela, J.A. *Adv. Mater.* **2000**, 12, 965. (b) Vuong, D. D.; Sakai, G.; Shimanoe, K.; Yamazoe, N. *Sens. Actuators B* **2004**, 103, 386. (c) Yamazoe, N. *Sens. Actuators B* **2005**, 108, 2.

20. Ma, Y.-J.; Zhou, F.; Lu, L.; Zhang, Z. *Solid State Comm.* **2004***,* 130, 313.
21. Meng, X.Q.; Zhao, D.X.; Zhang, J.Y.; Shen, D.Z.; Lu, Y.M.; Liu, Y.C.; Fan, X.W. *Chem. Phys. Lett.* **2005**, 407, 91.
22. Templeton, A.C.; Wuelfing, W.P.; Murray, R.W. *Acc. Chem. Res.* **2000**, 33, 27.
23. Shantha Shankar, K.; Raychaudhuri, A.K. *Mater. Sci. Engin. C* **2005**, 25, 738.
24. Wang, Z.L. *Adv. Mater.* **2003,** 15**,** 432.
25. Dai, Z.R.; Gole, J.L.; Stout, J.D.; Wang, Z.L. *J. Phys. Chem. B* **2002,** 106, 1274.
26. Sun, S.H.; Meng, G.W.; Zhang, M.G.; An, X.H.; Wu, G.S.; Zhang, L.D. *J. Phys. D: Appl. Phys.* **2004,** 37, 409.
27. Wang, Y.; Jiang, X.; Xia, Y.*J. Am. Chem. Soc.* **2003,** 125**,** 16176.
28. Dai, Z.R.; Pan, Z.W.; Wang, Z.L. *J. Am. Chem. Soc.* **2002,** 124, 8673.
29. Law, M.; Kind, H.; Messer, B.; Kim, F.; Yang, P. *Angew. Chem. Int. Ed.* **2002**, 41, 2405.
30. Wang, Y.; Jiang, X.; Xia, Y. *J. Am. Chem. Soc.* **2003**,125, 16176.
31. Kolkamov, A.; Zhang, Y.; Cheng, G.; Moskovits, M. *Adv. Mater.* **2003**,15, 997.
32. Brust, M.; Walker, M.; Bethell, D.; Schffirin, J.D.; Whyman, R. *J. Chem. Soc., Chem. Commun.* **1994**, 7, 801.
33. Chaudhary, V.A.; Mulla, I.S.; Vijayamohanan, K. *J. Mater. Res.* **1999**, 14, 185.
34. Chaudhary, V.A.; Mulla, I.S.; Sainkar, S.R.; Belhekar, A.A.; Vijayamohanan, K. *Sens. Actuators A* **1998,** 65, 72.
35. Shirane, D.; Cox, D.E.; Ruby, S.L. *Phys. Rev. B* **1962,** 125, 1158.
36. Tao, Y.T.; Pandian K.; W.C. Lee, *J. Am. Chem. Soc.* **2001**, 122, 7072.
37. Malinsky, M.D.; Selly, K.L.; Schatz, G.C.; Duyne, R.P.V. *J. Am. Chem. Soc.* **2001**, 123, 1471.
38. (a). Lisieki, I.; Pileni, M. P.; *J. Am. Chem. Soc.* **1993,** 115, 3887. (b) Lisieki, I.; Billoudet, F.; Pileni, M.P. *J. Phy. Chem.* **1996,** 100, 4160.
39. Ayyappan, S.; Srinivasa, R.; Gopalan, G.; Subbanna, N.; Rao, C.N.R. *J. Mater. Res.* **1997**, 12, 398.
40. Patil, V.; Sastry, M. *Langmuir* 1998, 14, 2707.
41. Denkov, N.; Velev, O.; Kralchevski, P.; Ivanov, I.; Yoshimura, H.; Nagayama, K. *Langmuir*1992, 8, 3183.

42. Hicks, J.F.; Zamborini, F.P.; Osisek, A.J.; Murray, R.W. *J. Am. Chem.* Soc. **2001**, 123, 7048.
43. Freeman, T.L.; Evans, S.D.; Ulman, A. *Langmuir* **1995**, 11, 4411.
44. Chen, T.; Friedman, K.A.; Lei, I.; Heller, A. *Anal. Chem.* **2000,** 72, 3757.
45. Zhang, J.; Wang, B.; Xu, B.; Cheng, C.; Dong, S. Anal. Chem. **2000,** 72, 3455.
46. Sarala Devi, G.; Manorama, S.; Rao, V.J.; *Sens. Actuators B* **1995**, 28, 31.
47. Hicks, J.F., Zamborini, F.P., Osisek, A.J.; Murray, R.W. *J. Am. Chem.* Soc. **2001**, 123, 7048.
48. Freeman, T.L.; Evans, S.D. Ulman, A. *Langmuir* **1995**, 11, 4411.
49. Zhong, C.J.; Brush, R.C.; Anderegg, J.; Porter, M. D. *Langmuir* **1999**, 15, 518.
50. Hutt, D.A.; Cooper, E.; Leggett, G.J. *J. Phys. Chem. B* **1998**, 102, 174.
51. Valiokas, R.; Ostblom, M.; Svedhem, S.; Svensson, S.C.T.; Liedberg, B. *J. Phys. Chem. B* **2000**,104, 7565.
52. Dawar, A.L., Joshi, J.C. *J. Mater. Sci.* **1984**, 19, 1.
53. Klug, H.P.; Alexander, L.E. X-ray Diffraction Procedures for Polycrystalline and Amorphous Materials, 2nd Edition, Wiley, New York, **1974**, 687–690.
54. Vlachos, D.S.; Papadopoulous, C.A.; Avaritsiotis, J.N. *Appl. Phys. Lett.* **1996**, 69, 650.
55. Zhang, C.; Hu, P.; Alavi, A. *J. Chem. Phys.* **2000**, 112, 10564.
56. Schwalke, U.; Parmeter, J.E.; Weinberg, W.H. *Surf. Sci.* **1986**, 178, 625.
57. Egashira, M.; Shimizu, Y.; Takao, Y. *Chem. Lett.* **1988**,195, 389.
58. Takao, Y.; Nakanishi, M.; Kawaguchi, T.; Shimizu, Y.; Egashira, M. *Sens. Actuators B:* **1995**, 25, 375.
59. Wei, P.H.; Li, G.B.; Zhao, S.Y.; Chen, L.R. *J. Electrochem. Soc.* **1999**, 146, 3536.
60. Laibinis, P.E.; Whitesides, G.M.; *J. Am. Chem. Soc.* **1991**, 114, 9022.
61. Dash, S.; Singh, A.; Ajikumar, P.K.; Subramanian, H.; Rajalakshmi, M.; Tyagi, A.K.; Arora, K.; Narasimhan, S.V.; Raj, B. *J. Nucl. Mater.* **2002,** 303, 156.
62. Egger, R.; Gogolin, A. *Phys. Rev. Lett.* **1997**, 79, 5086.
63. Sze, S.M. Semiconductor Sensitivity, Chemical Sensors, Wiley, New York, **1995,** pp. 383–409.
64. Roy Morrison, S. *Sens. Actuators B* **1987**, 12, 425.
65. Jiang, X., Wang, Y., Herricks, T., Xia, Y., *J. Mater. Chem.* **2004**, 14, 695.

Chapter 4

Synthesis and Characterization of ZnO Nanostructures*

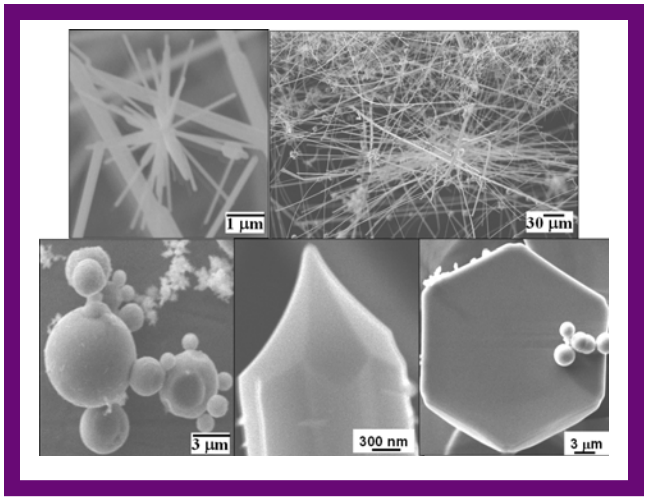

This chapter primarily deals with the shape selective synthesis of novel nanostructures of ZnO namely multipods, microwires, tetrahedra, micropencils and microhexagonal cones using a modified vapor deposition method. XRD studies indicate that the microwires are $(10\bar{1}0)$ oriented while the multipods show prominent peaks for both $(10\bar{1}0)$ and $(10\bar{1}1)$ miller indices. In comparison, tetrahedra structures show a biphasic mixture of Zinc and zinc oxide. The amount of oxygen in the reactant gas mixture is found to govern the final structure of ZnO. These studies reveal that multipod growth takes place via a screw dislocation mechanism while the tetrahedral and microwires grow possibly via a vapor-liquid-solid progression. Moreover, the geometry and the location of substrate are found to govern the morphology. The Si species present in the form of SiO and SiO_2 act as catalysts providing the nucleating sites, whereon the ZnO nanostructures grow. Further, it has been demonstrated that the micropencils grow via a vapor-liquid-solid (VLS) progression while the microhexagonal cones grow in two steps following vapor-solid (VS) and vapor-liquid-solid (VLS) mechanisms respectively.

---

*A part of the work has been published in ***J. Phys. Chem.*** **B 2006**,

4.1. Introduction

Semiconducting oxide nanostructures, with a well-defined geometry and perfect crystallinity are likely to be the model materials for a systematic experimental and theoretical correlation of the fundamental electrical, thermal, optical, and ionic transport processes with dimentionality[1-5]. Accordingly, ZnO nanostructures have been synthesized in various forms namely tetrapods[6], nanowires[7], nanotubes[8], nanosprings[9], prisms[10] etc using several methods, such as pyrolysis, chemical treatment, templated growth, thermal evaporation and so on. Of the various methods adopted, thermal vapor method is the widely exploited one as it offers the advantage of low reaction time below 1h with ease of controlling key parameters, namely size, shape and morphology as also illustrated previously in chapter 2 particularly for the synthesis of SnO_2 nanostructures. Moreover, it was demonstrated that the precise control over the geometry of the materials can be achieved by a simple modulation of the preparation parameters namely heating temperature and duration, nature of the substrate, type of carrier gas and oxygen flow rate. Usually, the nanostructure growth takes place via a self-catalytic process in which the precision, prediction and reproducibility, all emerge from the nature of interaction between the constituent elements.

ZnO crystallizes into the Wurtzite structure, and the polar (0001)-Zn and $(000\bar{1})$-O surfaces and the nonpolar $(10\bar{1}0)$ surface have been objects of experimental and theoretical studies. Of these surfaces, the nonpolar $(10\bar{1}0)$ surface is of particular interest from the viewpoint of surface chemistry, because the surface is terminated with the same number of O and Zn atoms, i.e., the surface is covered with both Lewis acid and base sites.[11] Structurally, ZnO, an ionic Wurtzite crystal with a non-centro symmetry, is described schematically as number of alternating planes composed of fourfold tetrahedral-coordinated O^{2-} and Zn^{2+} ions, stacked alternatively along the c-axis. The oppositely charged ions produce positively charged $(000\bar{1})$-Zn and negatively charged (0001)-O polar surfaces. Recently, Wang et al. have found that the (0001)-Zn surface is chemically active in growing nanostructures, while the $(000\bar{1})$-O surface is smooth and inert[12]. In an attempt to take part in the exciting nanoworld of ZnO, and to contribute to its striving challenges in particular for making field emission devices, the synthesis and characterization of ZnO have been explored in the present chapter. More specifically, we demonstrate the successful synthesis of novel ZnO structures namely multipods, microwires, tetrahedra, micropencil and microhexagonal cones using a modified vapor deposition method. The synthesis of these low dimensional building blocks is governed by simple self-assembly processes. Thus, in order to understand the growth kinetics and to explore intellectual terra incognita further, we had carried out SEM, XRD, TEM and XPS studies of these low dimensional materials. The results of these investigations are presented below with the help of a plausible growth mechanism. Our studies indicate that the growth of multipod structure is governed by the screw dislocation propagation. In comparison, submicron wires, tetrahedra and micropencils follow VLS mechanism while microhexagonal cones grow in two steps following VS and VLS mechanism, respectively.

4.2. Experimental Aspects

4.2.1. Synthesis of multipod and tetrahedral structures

The experimental setup used for the synthesis of multipods, microwires and tetrahedral structure is shown in scheme 4.1, which is essentially similar to the one used for the synthesis of SnO_2 structures. However, shape selectivity was achieved by precise control over process parameters. In brief, it consisted of a tubular furnace open at one end, in which the starting material, a pure Zn metal (Latent heat of fusion, $\Delta H_f \approx 5 \times 10^8$ J m^{-3}) was kept in the middle. Ar was passed continuously at a flow rate of 100 ± 5 sccm with different oxygen flow rate (20%v/v for multipods and 5% v/v for tetrahedral structure) through the furnace up to 950 °C. The material was heated for 2 h, and the furnace was allowed to cool naturally with uninterrupted Ar + O_2 flow. The microwires were collected adjacent to the alumina boat containing the source material whereas the multipod and tetrahedral structures were collected on the alumina substrates kept near the end of tube where the temperature was between 200 and 500 °C.

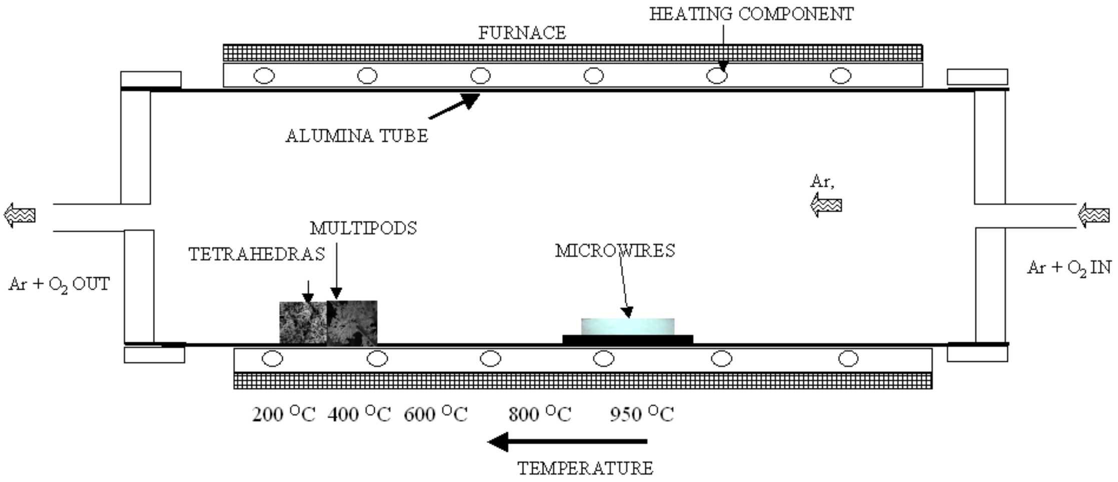

Scheme 4.1. The experimental set-up used for the synthesis of ZnO nanostructures. Pure Zn metal as the starting material was heated at a temperature of 950^{0}C. The microwires were collected adjacent to the alumina boat containing the source material whereas the multipods and tetrahedral structures were collected on the alumina substrates kept near the end of tube where the temperature was between 200 and 500 °C.

4.2.2. Synthesis of micropencils and microhexagonal cones

Scheme 4.2 shows the experimental set-up used for the synthesis of ZnO structures. Pure Zn metal, (melting point = 420 ^{0}C, boiling point = 907 ^{0}C) was heated at a temperature of 950^{o}C for 2 h in a mixed environment of argon and oxygen flowing at a rate of 100 ± 5 sccm and 20 sccm (20% v/v) respectively, on an alumina substrate kept on a commercially available aluminosilicate refractory brick substrates. The pencils were found to grow on the aluminosilicate substrate, while hexagonal cones were formed on the opposite side of the substrate kept downstream, where the temperature was between 200 and 500 ^{0}C.

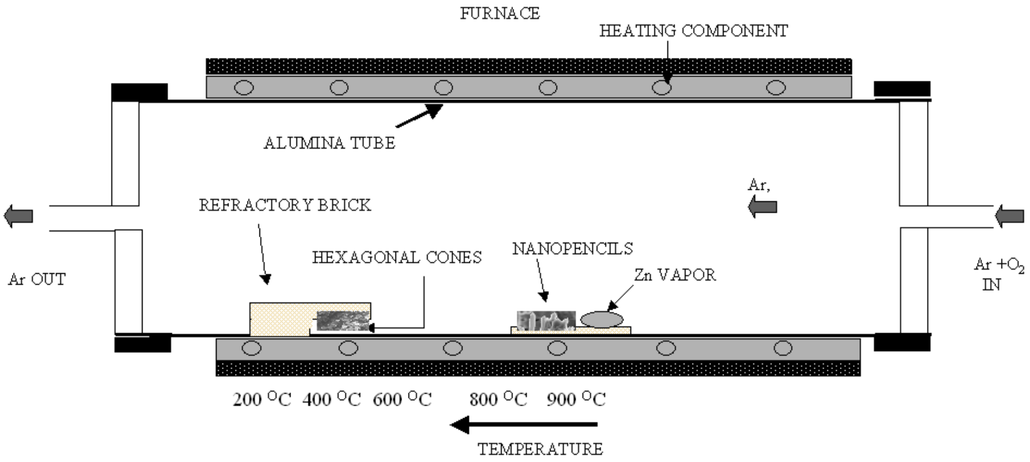

Scheme 4.2. The experimental set-up used for the synthesis of ZnO micropencils and microhexagonal cones. The micropencils were collected on an aluminosilicate refractory brick substrate, while hexagonal cones were collected on the opposite side of the substrate kept downward where the temperature was between 200 and 500 ^{0}C.

4.2.3. Material characterization

FT- Raman spectra were measured with Bruker FRA106 FT-Raman instrument with Nd:YAG (1064 nm) excitation. The other characterization details like XRD, SEM, HR-TEM, XPS and TG-DTS have been already described in Chapter 2, section 2.2 and chapter 3, section 3.2.5.1.

4.3. Results and Discussion

4.3.1. Structural and morphological variation

Figure 4.1 shows the SEM and TEM images of the as-synthesized multipods. It is obvious from these images [figure 4.1(b) and (c)] that the number of arms of the multipods is between 4 and 16 and all have a common origin with varying length from 10 to 80 μm. Most of the arms have uniform width, whereas some of them end like a cone (tip apex of ~ 24 nm). In few other arms, the width suddenly narrows down in the middle to a sharp protrusion. Figure 4.1 (d) shows the TEM image of a tetrapod exhibiting an arm length between 120 and 200 nm with the fourth arm standing perpendicular. These tetrapods are smaller in dimensions as compared to those reported earlier by Surya et al.[13] and others. They have elucidated that the oxidation of Zn in air resulted in the formation of tetrapod nanorods only, with no nanowires. Further, a Zn self-catalytic VLS process is involved for the growth of tetrapod-like structures. Interestingly, in the present case some of the tetrapods end with a hexagonal tip suggesting that the relative growth rate of various crystal faces bounding the crystal plays a crucial role in deciding the growth mechanism.

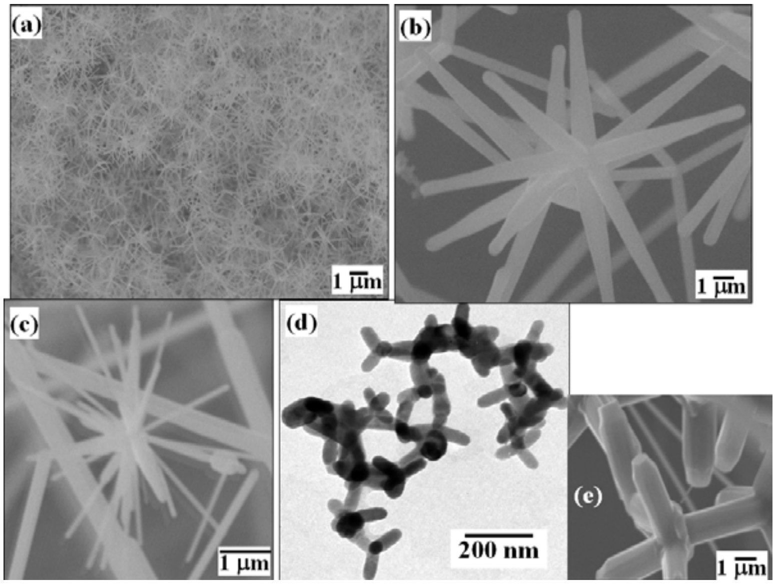

Figure 4.1. SEM images of multipod structure collected downstream (200 - 500^{0}C) (a) as-synthesized multipod structure, (b) an individual multipod structures with 8 arms with the tip ending into a hemispherical geometry, (c) another multipod structure wherein the sudden change in the width of the arm with narrowing tip apex is observed, (d) TEM image of tetrapod structure with smaller arm length between 100 and 180 nm; in some the fourth arm is observed perpendicular to the plane of the paper and (e) SEM image of the tetrapod with hexagonal tip apex.

Figure 4.2 shows the SEM image of the white fluffy microwires that are collected on the substrate containing Zn vapor source where the temperature is between 850 and 950^{0}C. The wires are polydispersed in nature with width varying from 200 nm to 3 μm and the length from 50 to 200 μm. Most of the wires observed, end with a hexagonal tip as shown in figure 4.2 (c). A tetrahedral like structure is also observed along with the wires as shown in figure 4.2 (d) suggesting the initialization of multipods to be taking place at the beginning according to a vapor-liquid-solid growth model.

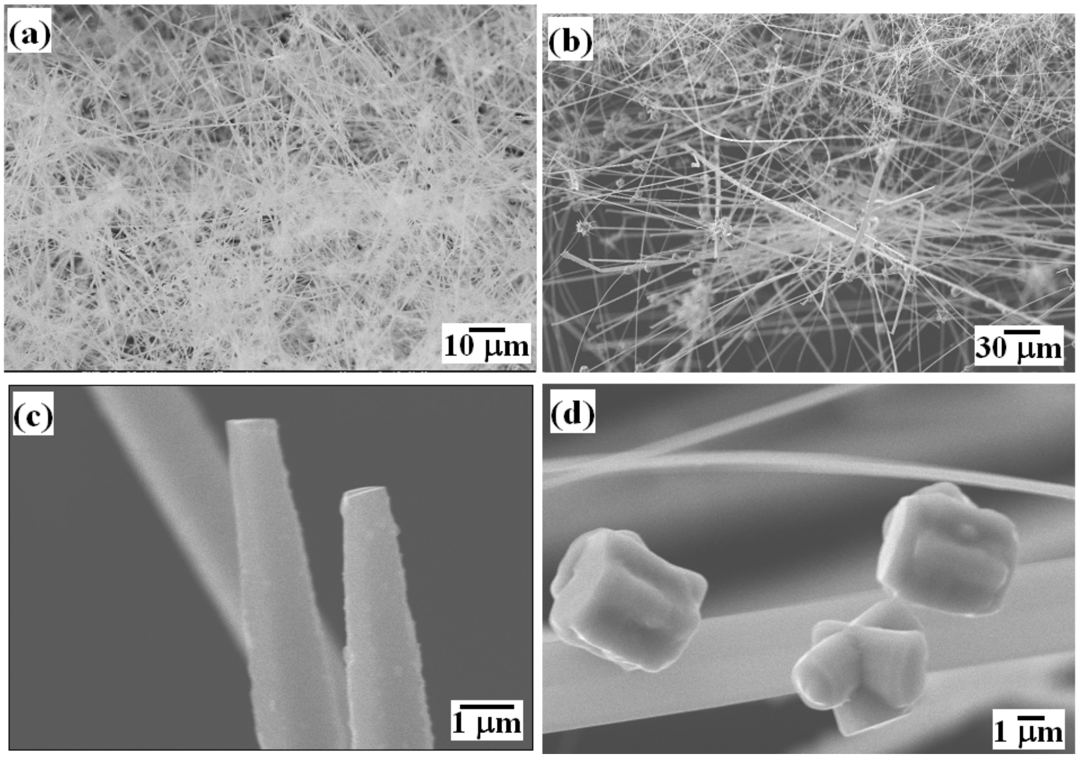

Figure 4.2. SEM images of the white fluffy microwires collected adjacent to source material where the temperature was between 850 and 950^{0}C (a) as-synthesized microwires with width varying from 200 nm to 3 μm and length from 50 to 200 μm. The wires closer to the source material are bigger in the dimensions (b) and end with a hexagonal tip as can be seen in figure 2 (c). A tetrahedral like structures was also observed (figure 2 (d)) suggesting the initialization of multipods to be taking place as per the vapor-liquid-solid progression.

At a typical low O_2 flow rate of 5 sccm, the gray colored powder was collected at a temperature of 200 - 500 ^oC and it mainly comprises the sphere-like with diffused tetrahedral geometry structures (Figure 4.3 (a) and (b)). These structures are polydispersed in nature with size varying between 200 nm and 5 μm. Some of these are found to form a wire like geometry (Figure 4.3(c)) suggesting them to be the probable nucleating sites for the growth of wires. The gray color of the sample indicates incomplete oxidation, which is also supported by the lower oxygen content as can be seen in the EDX (Figure 4.3(d)).

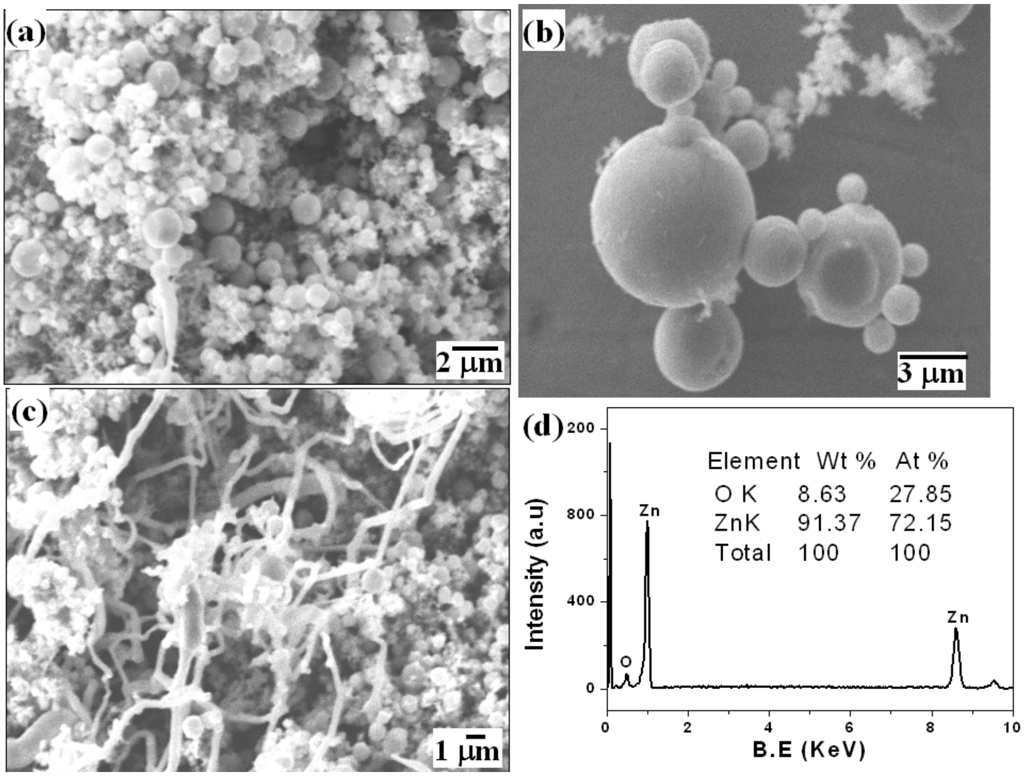

Element	Wt %	At %
O K	8.63	27.85
ZnK	91.37	72.15
Total	100	100

Figure 4.3. (a) SEM images of tetrahedral ZnO with diffused edges collected downstream where the temperature is between 200 and 500^{0}C, (b) isolated tetrahedra with size from 200 nm to 5 μm, (c) tetrahedra joined together to form a wire like geometry and (d) EDX of the gray colored tetrahedra emphasizing lower oxidation of Zn.

Figure 4.4 shows the SEM images of the micropencil structures. As can be seen (figure 4.4(a)) the substrate is uniformly coated with ZnO micropencils throughout its surface suggesting the high density of the freshly grown micropencils. Figure 4.4(b) shows the EDX of the micropencil exhibiting a strong signal corresponding to Zn and O. The intensity ratios among the Zn, O and Si peaks suggest that the Si content in the micropencils is approximately 0.61 atom%. Figures 4.4 (c) and (d) show slightly enlarged images of the micropencils revealing its clear features. It is observed that the micropencils have a hexagonal shank, with width varying between 0.8 and 1.2 μm and the shank terminates with a tapering end whose diameter is less than 100 nm. The tapering tip interestingly extends to a length of 300 to 600 nm, with a tip apex of less than 100 nm.

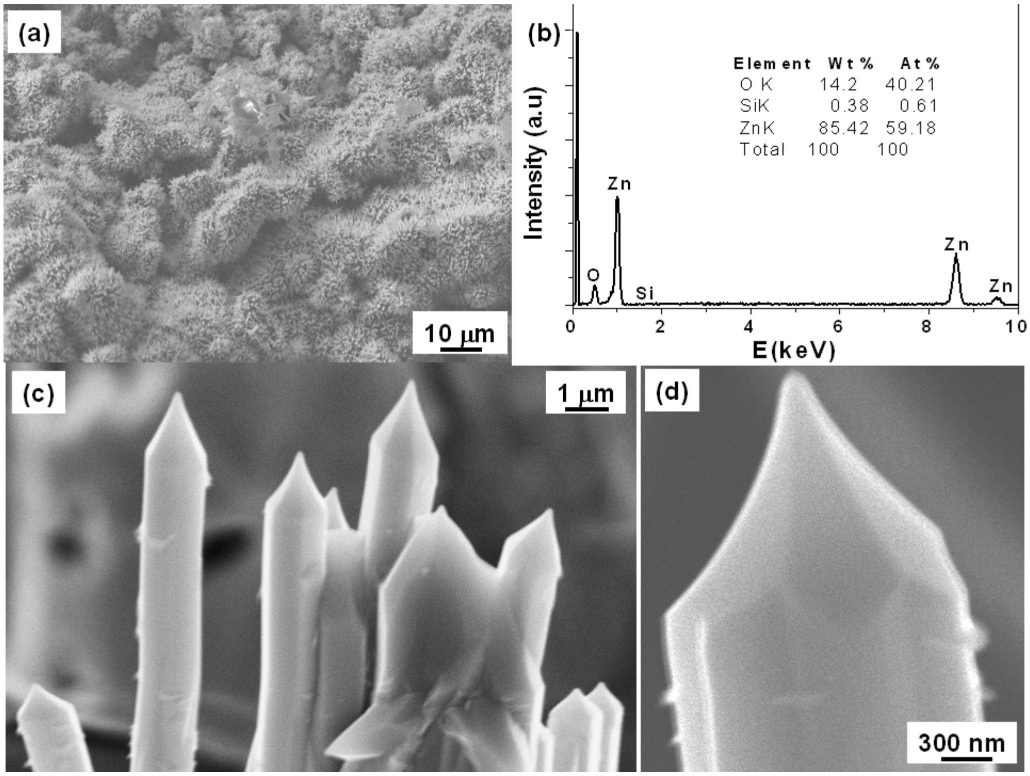

Figure 4.4. (a) SEM images of the micropencil structure grown on the aluminosilicate refractory brick substrate, (b) EDX of the micropencils exhibiting a strong signal corresponding to Zn and O, (c) and (d) shows the enlarged SEM of the micropencils.

Figure 4.5 shows the SEM images of the '*as grown*' ZnO microhexagonal cones; the hexagonal structures emerge from the surface of the substrate. Indeed, the structure resembles an upside down cone ending into a hexagonal disc. The hexagonal cones are poly dispersed in nature with a size varying from 1 to 80 μm (figure 4.5(b)); the number of edge to all structures is fixed to six. Moreover, the edge length varies randomly from 3 to 20 μm. The six side surfaces and the base of the hexagonal cones appear smooth with a small depression at the center. Figure 4.5(d) shows the EDX recorded for hexagonal cones. The intensity ratio among the Zn, O and Si peaks suggests that the Si content in the microhexagonal cones is approximately 9.11 atom%.

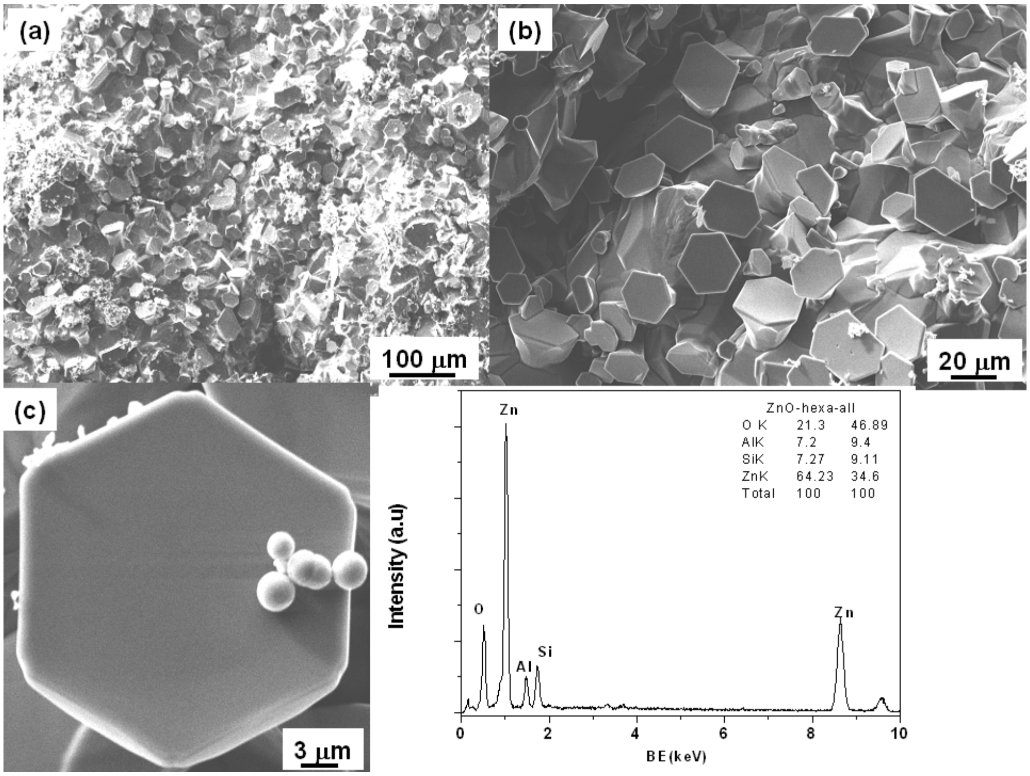

Figure 4.5. SEM images of the as grown ZnO microhexagonal cones; with different magnifications (a), (b) and (c) and the elemental composition as obtained from EDX recorded for hexagonal cones (d).

Wurtzite zinc oxide has a hexagonal structure (space-group *C6mc*) with lattice parameters, *a* = 3.2496 and *c* = 5.2065 Å (JCPDS Card No. 36-1451). The XRD patterns of the (a) microwires, (b) commercial ZnO (Aldrich 99.99% pure), (c) multipod, and (d) tetrahedra structures are shown in figure 4.6. The peaks of multipods and microwires match well with those of commercial ZnO; however, intensity of the peaks differs from the bulk, due to the larger number of planes along the long axis of the pods and the wires as compared to that across the diameter.[14] On the other hand tetrahedral structure show additional peaks, which could be attributed to signals from sub-oxides (ZnO_x, $x<1$) due to the incomplete oxidation. Interestingly, the microwire is found to be $(10\bar{1}0)$ oriented with lattice parameters a = 3.242(3) Å and c = 5.201(2) Å, matching well with similar structural data for commercial sample, while, multipod shows a prominent signal for both $(10\bar{1}0)$ and $(10\bar{1}1)$ miller indices with lattice parameters a = 3.239 (3) and c = 5.199 (3) Å.

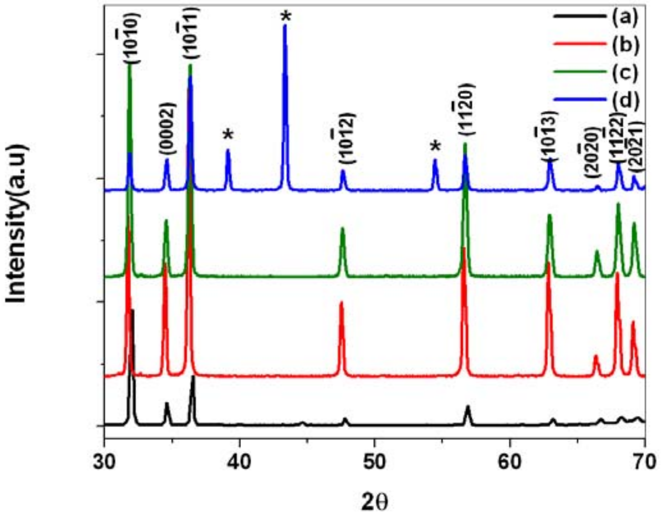

Figure 4.6 The XRD patterns of the (a) microwires, (b) commercial ZnO, (c) multipod and (d) tetrahedra structure. The * in the plot corresponds to the signal arising from Zn metal.

The XRD patterns of (a) commercial ZnO (Aldrich 99.99% pure), (b) micropencils and (c) microhexagonal cone structures are shown in figure 4.7. The peaks match well with those of commercial ZnO; however, the peak position are shifted towards higher 2θ values attributed to the incorporation of Si species into the ZnO matrix. The intensity of the peaks also differs from that for the bulk due to the larger number of planes along the long axis of the structures as compared to that across the diameter.[14]

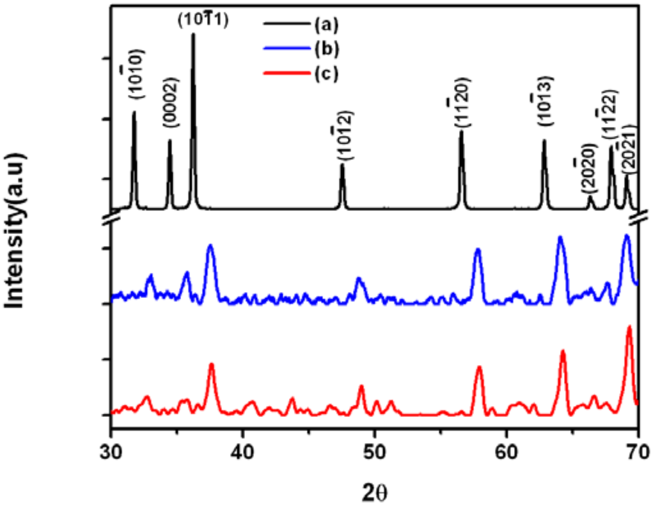

Figure 4.7. XRD patterns of (a) commercial ZnO (Aldrich 99.99%), (b) micropencils and (c) microhexagonal cones.

For ZnO nanostructures, the quantum confinement effect is expected below 20 nm, and the absorption edge will be shifted to a higher energy when the particle size decreases. In the present case the tips of multipod structures observed is less than 20 nm and hence it is expected to have an increase in the band gap. Accordingly, the band gaps of the ZnO samples are studied by Uv-vis diffuse reflectance spectroscopy (DRS). The Kubelka-Munk function, $F(R) = (1-R)^2/2R$, is used to determine the band gap by analyzing the DRS results. Figure 4.8 shows the plots of $F(R)$ vs. wavelength of ZnO structures. Band gap is defined by the extrapolation of the rising part of the plot to the *X*-axis (dotted line in Figure 4.8). The band gaps of commercial ZnO, microwires, and multipods are, 3.10(3) eV (400 nm), 3.15(3) eV (394 nm) and 3.13(3) eV (396 nm), respectively. These values suggest that band gap does not change significantly with the formation of multipods or microwires of ZnO.

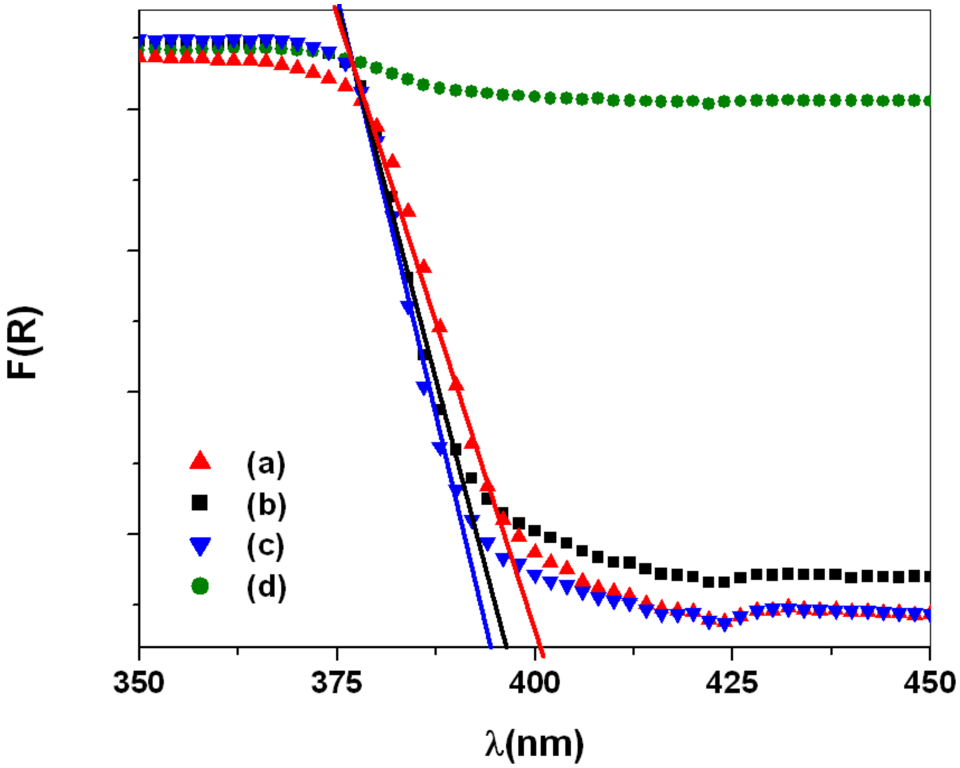

Figure 4.8. Plot of $F(R)$ vs. wavelength of (a) commercial ZnO, (b) multipod, (c) microwires and (d) tetrahedral structure, calculated from diffused reflectance spectra of these structures. The Kubelka-Munk function was calculated using $F(R) = (1-R)^2/2R$, where R is reflectance (a.u).

The band gap variation with size is more prominent with structures having dimension less that 20 nm. For example, Kanaev et al. have observed the variation in the band gap of ZnO as a function of size of ZnO particles. They observed a shift in band gap from 3.48 eV to 3.75 eV for ZnO nanoparticles having dimensions between 3 and 5 nm.[15]

Coupling between electronic and vibrational excitations plays an important role in semiconductor materials because of its significant influence on the optoelectronic properties of semiconductors, e.g. the transport processes, the energy relaxation rates of excited carriers and linear or nonlinear optical absorption. Moreover, the electric field within materials correlates to Coulomb interaction with the exciton and the strength of electron-phonon coupling will be enhanced if the wavelength of the phonon vibration is close to the spatial extent of the exciton. Accordingly, Raman scattering was performed (Figure 4.9) at room temperature to investigate the vibrational properties of the multipod ZnO. Since the wurtzite structure of ZnO belongs to the space group $C_{6v}^4(P6_3mc)$, one primitive cell includes two formula units, with all of the atoms occupying 2*b* sites of symmetry C_{3v}. Group theory predicts the existence of the following optic modes: (A_1 + $2B_1$ + E_1 + $2E_2$) at the Γ point of the Brillouin zone; B_1(low) and B_1(high) modes are normally silent; A_1, E_1, and E_2 modes are Raman-active; and A_1 and E_1 are both Raman and infrared-active[10]. Thus, A_1 and E_1 are split into longitudinal (LO) and transverse (TO) optical components. The peak at 330 cm^{-1} can be assigned to the second order Raman scattering arising from zone-boundary phonons 2-E_2(M) of ZnO, while the peak at 436 cm^{-1} corresponds to E_2(high). Another broadened peak around 585 cm^{-1} is contributed to the superimposition of A_1(LO) and E_1(LO), which are associated with the existence of some nonstoichiometric defects, such as oxygen vacancy, interstitial zinc or their complexes.

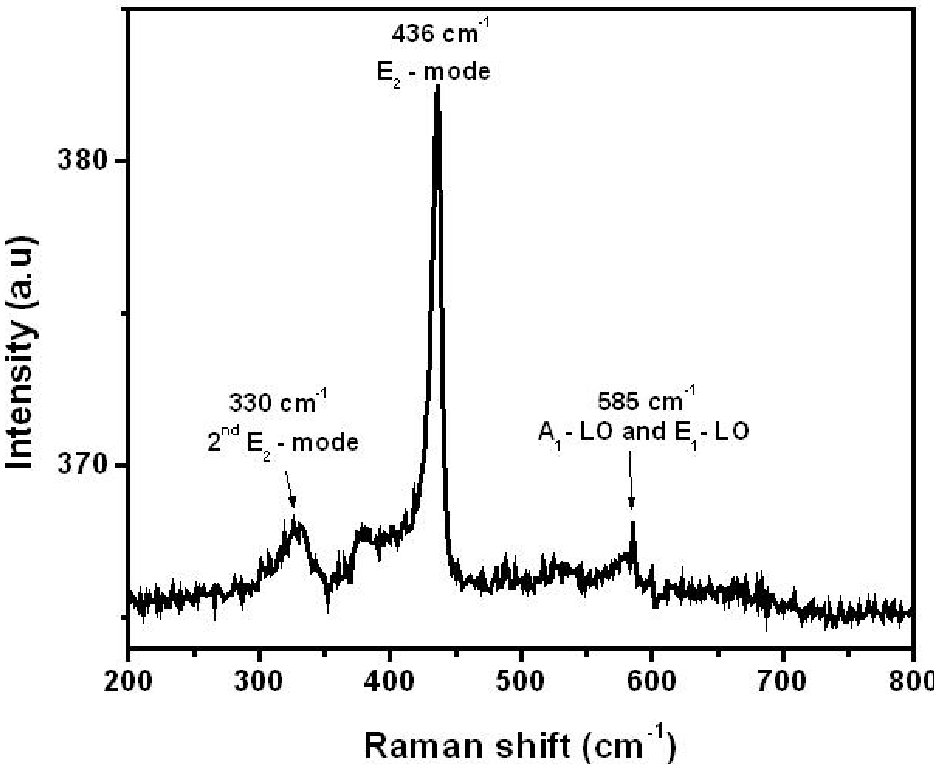

Figure 4.9. Raman spectrum recorded for ZnO multipod at room temperature. The peaks at 330, 436 and 585 cm^{-1} could be assigned to the second order Raman scattering arising from zone-boundary phonons 2-E_2(M) of ZnO, E_2(high) and to the superimposition of A_1(LO) and E_1(LO) respectively.

An analysis of the electronic state of the material is also of particular importance to understand the growth kinetics and hence XPS studies were carried out on all these structures. Consequently, Figure 4.10 shows the deconvulated C1s peak for commercial ZnO, multipod and tetrahedral structures. In all the cases representing XP spectra, the hollow circles denote the original data and solid lines represent the fitted curves and the deconvoluted individual peaks of different species present in the sample. All the binding energy positions of the elements are listed in Table 4.1. Figure 4.11 shows the deconvulated O1s peak for all the structures. For commercial ZnO, tetrahedral and multipod structures, the peaks at BEs of 530.2, 530.6 and 530.3 eV can be attributed to the O1s, while the peaks at binding energies of 531.8, 532.7 and 532.1 eV are attributed to the adsorbed oxygen species and Zn suboxides.

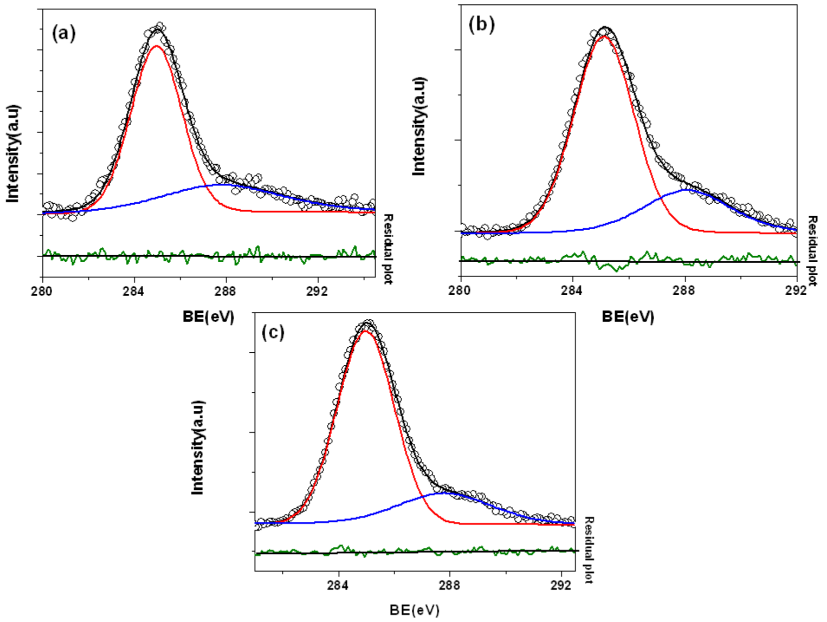

Figure 4.10. The core level spectra for C1s for different forms of ZnO (a) commercial ZnO (Aldrich 99.99%) powder, (b) tetrahedral and (c) multipods structure. The spectra were fitted using a combined polynomial and Shirley type background function.

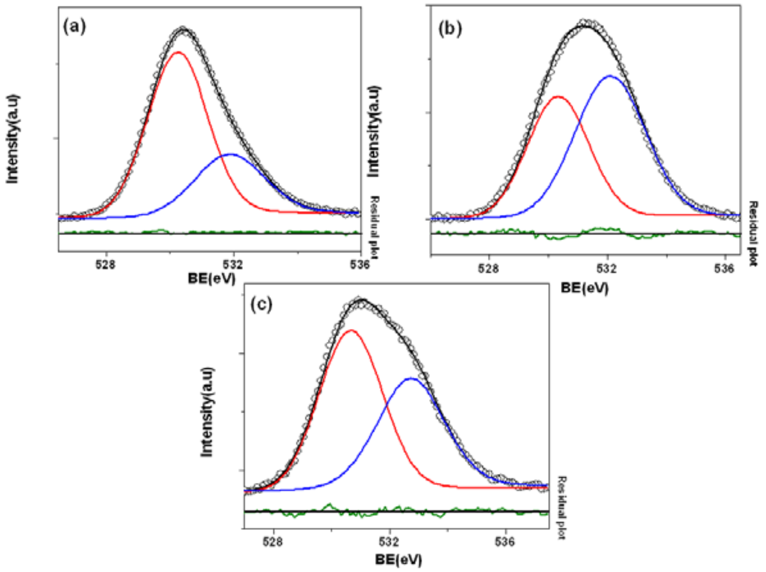

Figure 4.11. The spectra for O1s for different forms of ZnO (a) commercial ZnO (Aldrich 99.99%) powder, (b) tetrahedral and (c) multipod structure. The spectra were fitted using a combined polynomial and Shirley type background function.

Table 4.1. A comparison of relevant binding energy positions of Zn, C and O present in different structures of ZnO.

Species	**Chemical Species**	**B.E. (eV)**		
		ZnO- aldrich	**Multipods**	**Tetrahedra**
C	1s	285	285	285
	adsorbed	287.8	287.8	288
Zn	$2P_{1/2}$	1044.7	1044.8	1044.8
	$2P_{3/2}$	1021.7	1021.7	1021.8
O	1s	530.2	530.6	530.3
	adsorbed	531.8	532.7	532.1

Figure 4.12 shows the spectra for Zn signals for all the samples. Interestingly, both the multipod and the tetrahedral structures show two peaks at B.E. of 1044.8 and 1021.7 eV that can be attributed to the Zn $2p_{1/2}$ and Zn $2p_{3/2}$ signals, respectively. Using the atomic sensitivity factors the ratio of Zn:O is calculated using the relation

$$\text{Zn}\ (2p_{3/2})/\text{O1s} = I_{Zn}/I_O \times \sigma_o/\sigma_{Zn} \times (K.E_{Sn}/K.E_O)^{1/2} \qquad \text{-(1)}$$

where, I_{Zn} is the area under the curve of deconvulated Zn$2p_{3/2}$, I_O is the area under the curve of deconvulated Zn$2p_{1/2}$, σ_o and σ_{Zn} are the atomic sensitivity factors for O(2.85) and Zn(9.29) respectively and $K.E_{Zn}$ and $K.E_O$ are the kinetic energies of the electron of Zn and O respectively. The ratio of Zn:O varies from 1:1.01 for commercial ZnO, 1: 0.74 for multipods to 1:0.4 for tetrahedra. The gray color of the tetrahedral structures suggests the presence of Zn suboxides.

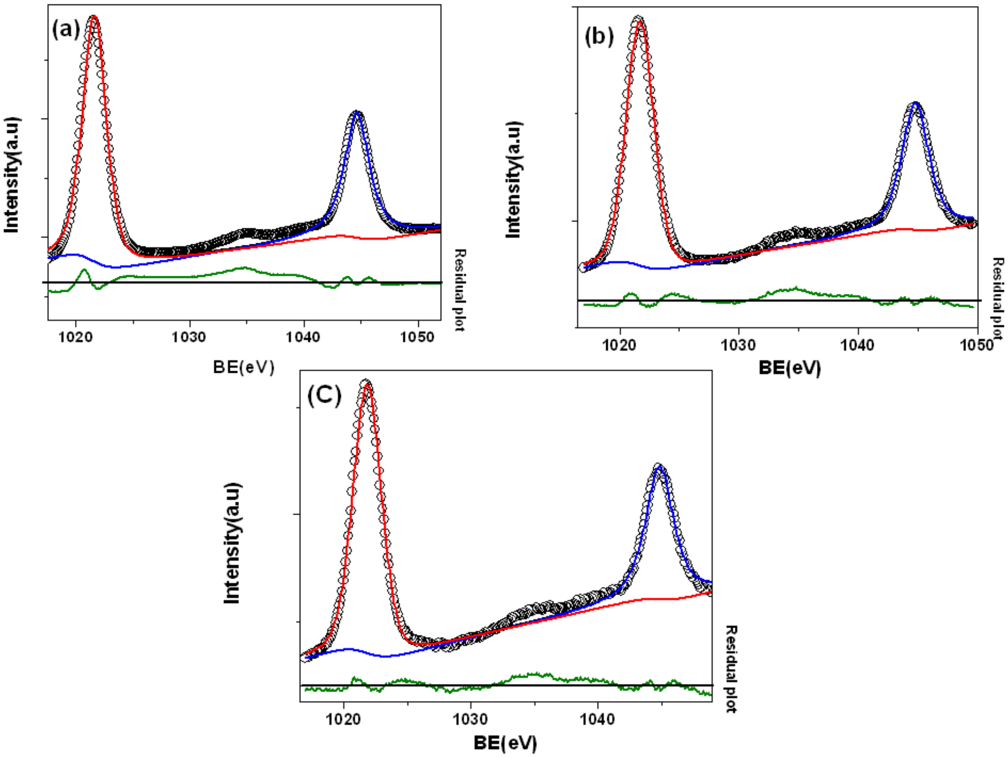

Figure 4.12. The separate Zn $2p_{3/2}$ and Zn $2p_{1/2}$ signals for Zn in (a) commercial ZnO (Aldrich 99.99%) powder, (b) tetrahedral and (c) multipods structure. The spectra were fitted using a combined polynomial and Shirley type background function.

Figure 4.13 shows the deconvulated C1s peak for commercial ZnO and freshly prepared micropencils and microhexagonal structures. All the binding energy positions of the elements are listed in Table 4.2. For commercial ZnO, micropencil and hexagonal structures, the peaks at binding energy of 285 eV can be attributed to the C1s, while the peaks at binding energies of 288.6, 287.6 and 287.1 eV could be attributed to the adsorbed carbon species.

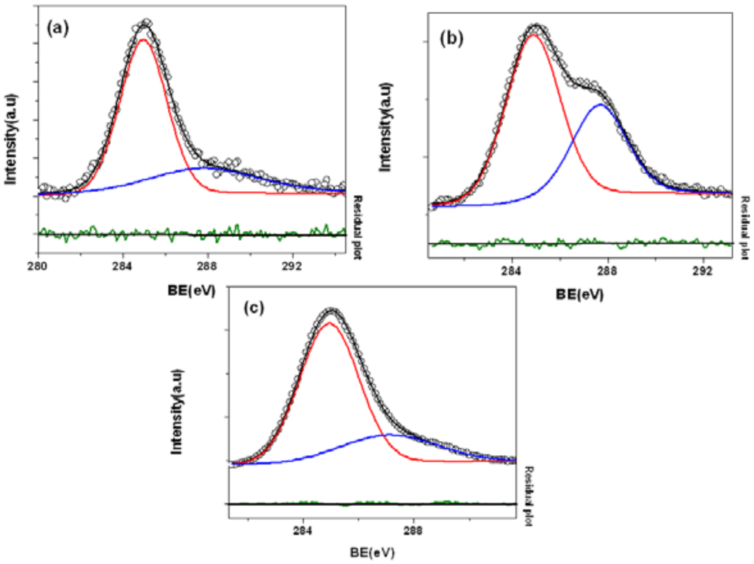

Figure 4.13. The deconvoluted C1s peak for (a) commercial ZnO, (b) micropencils and (c) hexagonal structures. The spectra were fitted using a combined polynomial and Shirley type background function.

Table 4.2. All the binding energy positions of the element present in different ZnO structures

Species	**Chemical Species**	**B.E. (eV)**		
		ZnO- aldrich	**Microhexagonal Cones**	**Micropencils**
C	1s	285	285	285
	adsorbed	287.8	287.6	287.1
Zn	$2P_{1/2}$	1044.7	1047.5	1045.4
	$2P_{3/2}$	1021.7	1024.5	1022.3
O	1s	530.2	530.2	530.6
	adsorbed	531.8	533.1.7	532.3
	lattice oxygen of ZnO_x/SiO_x	-	535.1	533.9
Si	$2P_{3/2}$	-	-	102.8
	$2P_{1/2}$	-	105.1	-

Figure 4.14 shows the deconvulated O1s peak for all the ZnO structures under investigations. For commercial ZnO the peak at binding energy of 530.2 eV can be attributed to the O1s, while the peak at binding energy of 531.8 eV is attributed to the adsorbed oxygen species. In case of micropencil and hexagonal cones, the oxygen peak can be deconvulated in three different signals corresponding to the O1s, adsorbed oxygen and lattice oxygen of ZnO/SiO$_x$.

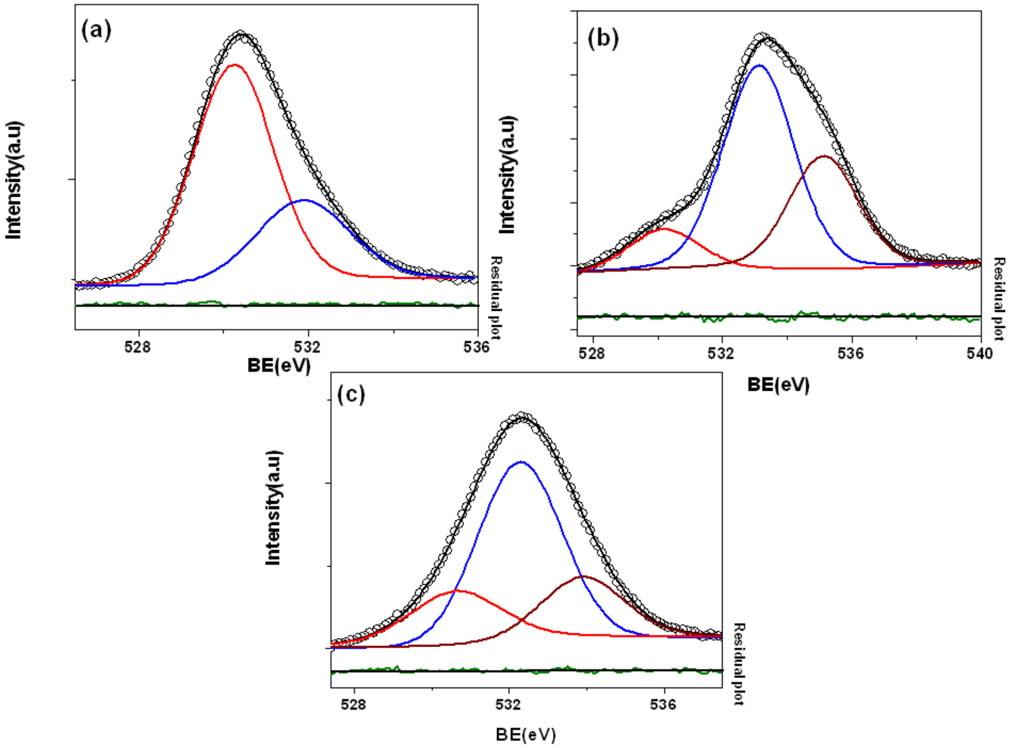

Figure 4.14. The deconvoluted O1s XPS peak for (a) commercial ZnO, (b) micropencils and (c) hexagonal structures. The spectra were fitted using a combined polynomial and Shirley type background function.

Figure 4.15 shows the spectra for Zn signals for all the samples. Interestingly, for both the micropencils and the hexagonal structures the two peaks corresponding to Zn 2p$_{1/2}$ and Zn 2p$_{3/2}$ levels, respectively are found to be shifted towards higher binding energy side and could be attributed to the incorporation of Si into the ZnO matrix. The ratio of Zn:O calculated using the atomic sensitivity factors and relation (1), varies from 1:1.01 for commercial ZnO, 1: 0.3 for micropencils to 1: 1.1 for hexagonal cones.

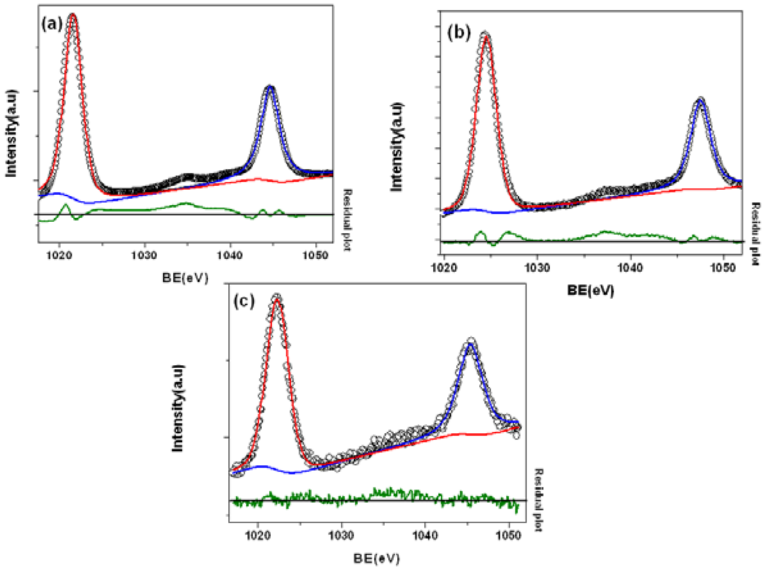

Figure 4.15. The deconvoluted Zn 2P XPS peaks for (a) commercial ZnO, (b) micropencils and (c) hexagonal structures. The spectra were fitted using a combined polynomial and Shirley type background function.

Figure 4.16 shows the spectra for the Si signals for both the micropencil and microhexagonal structures. Interestingly, for ZnO pencils, peak at binding energy of 102.8 eV is observed that could be attributed to the signal from Si^{2+} ($2P_{3/2}$, SiO). However, in the case of microhexagonal cones, signal at the BE of 105.1 eV could be attributed to the Si^{4+} ($2P_{1/2}$, SiO_2)[16]. The appearance of Si peaks further suggests that Si acts as a nucleating aid and probably gets incorporated into the ZnO matrix.

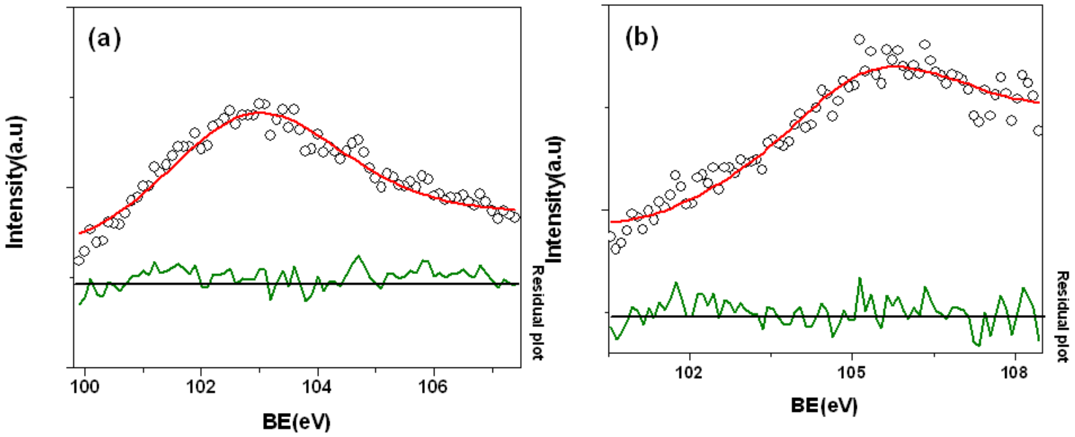

Figure 4.16. The deconvoluted Si XPS peak for (a) micropencils, (b) microhexagonal structures.

4.4. Plausible Growth Mechanism

4.4.1. Thermogravimetric and Differential Thermal Analysis (TG-DTA)

In order to understand the growth kinetics, Thermogravimetric and differential thermal (TG-DT) analysis of the Zn metal was performed under similar environment for the synthesis of these remarkable ZnO microstructures (Figure 4.17). Upto 300 ^{o}C, a weight loss of 1.08 wt% attributed to the evaporation of impurities like adsorbed moisture is observed. With a further increase in temperature upto 650 ^{o}C, the observed weight loss of 1.4 % could be attributed to the slow evaporation of Zn. However, from 650 ^{o}C to 730 ^{o}C, a small weight gain (0.94 wt%) due to the conversion of Zn to ZnO species is seen. On the contrary, above 730 ^{o}C, a sharp loss of about 10.3 wt % is seen, which could be assigned to the evaporation of Zn species. At this temperature, Zn metal gets transformed into a liquid droplet and with a further increase in temperature, a weight gain of about 2 wt% observed subsequently could be attributed to the conversion of Zn species to ZnO. Thus, with increase in the temperature, Zn metal transforms into liquid droplets with a small loss of Zn species, as per the equation

$$Zn(l) \rightarrow Zn(g), \qquad \Delta G_o = +114{,}200 - 96.99T \text{ J mol}^{-1} \qquad -(1)$$

$$Zn(l) + 1/2O_2 = ZnO(s), \qquad \Delta G_o(ZnO) = -355{,}970 + 107.53T \text{ J mol}^{-1} \qquad -(2)$$

A negative value for ΔG in equation (2) indicates that the reaction can proceed spontaneously without external inputs, while a positive value in equation (1) indicates that it will not proceed spontaneously and will require higher energy (temperature).

This liquid droplet subsequently grows into a ZnO layer consisting of large grains on which several nucleating sites are generated. On this site several ZnO nuclei selectively grow along the crystallographic orientation of ZnO grain due to the strong epitaxial relation between them[17]. Continuous feeding of Zn vapor and oxygen into the favorable nucleating sites will lead to vertical growth of ZnO structures possessing the same direction of c-plane to the ZnO grain as per the VLS progression.

$$Zn(g) + 1/2O_2(g) \rightarrow ZnO(s) \qquad -(3)$$

The process can be understood by looking at the Ellingham diagram of ZnO.

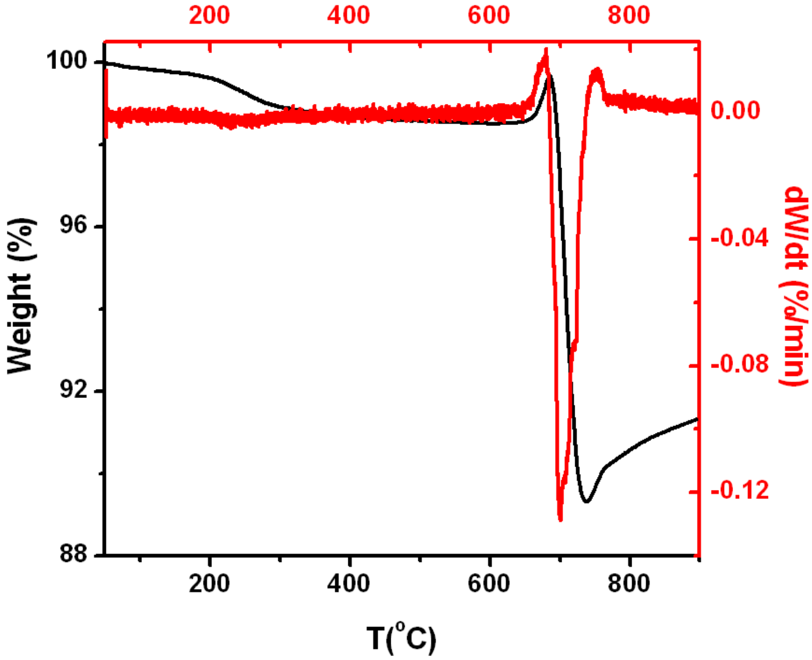

Figure 4.17. TGA-DTA curve of the source material i.e., Zn metal used for the synthesis

4.4.2. Ellingham Diagram of ZnO

The stability of materials at high temperature has been traditionally introduced through plots of the standard free energy of reaction (ΔG_0) as a function of temperature, commonly called Ellingham diagrams. Such diagrams can help to visualize the relative stability of metals and their oxidized products. The values of ΔG_0 on an Ellingham diagram are expressed as kJ/mole to normalize the scale and be able to compare the stability of these oxides directly, i.e. the lower the position of the line on the diagram, the more stable is the oxide.

For a given reaction ($2Zn + O_2 = 2ZnO$) assuming that the activities of Zn and ZnO are taken as unity, the following equations can be used to express the oxygen partial pressure at which the Zn metal and oxide coexist, i.e. the dissociation pressure of the oxide:

$$P_{O_2}^{M/MO_2} = e^{-\Delta G^o/RT} \qquad -(4)$$

Zn metal and volatile oxide species are important in the kinetics of high temperature and six types of oxidation phenomena were identified:

(a) At low temperature, diffusion of oxygen and metal species

(b) At moderate and high temperatures, a combination of oxide film formation and oxide volatility

(c) At moderate and high temperatures, the formation of volatile metal and oxide species at the metal-oxide interface and transport through the oxide lattice and mechanically formed cracks in the oxide layer

(d) At moderate and high temperatures, the direct formation of volatile oxide gases

(e) At high temperature, the gaseous diffusion of oxygen through a barrier layer of volatilized oxides

(f) At high temperature, spalling of metal and oxide particles

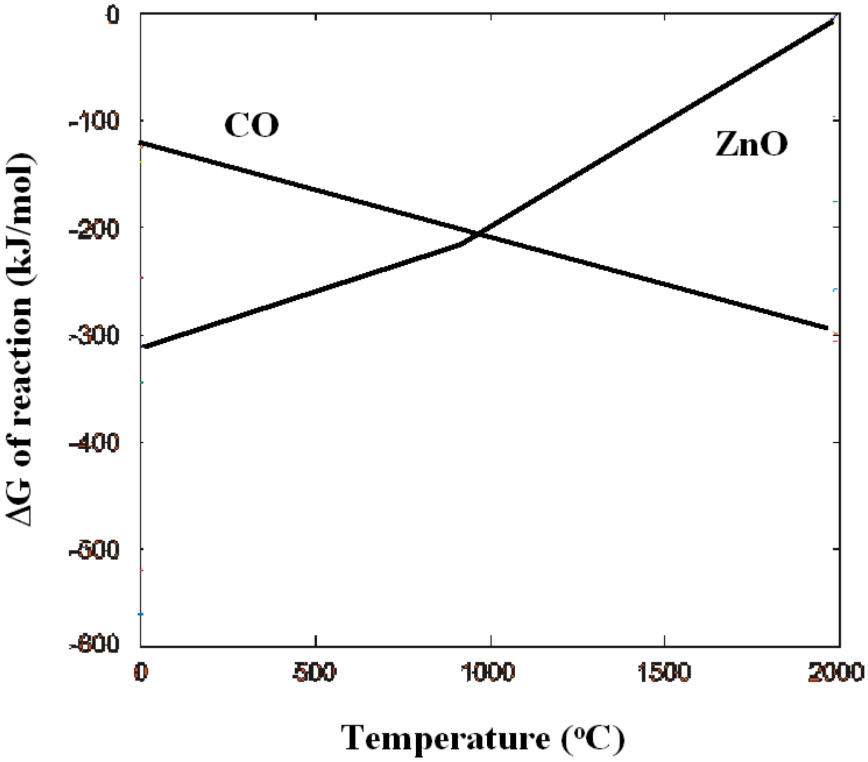

Figure 4.18. Plot of the free energy of formation of ZnO vs. temperature. This can be used to predict the temperatures at which a metal is stable and the temperatures at which it will spontaneously oxidize. For temperatures at which the free energy of formation (ΔG_0) of the oxide is positive, the reverse reaction is favored and the oxide will spontaneously decompose to the metal.[18]

From the plot (Figure 4.18) it is clear that between 423 ^{0}C and 911 ^{0}C, Zn and O species coexists with standard free energy change of ΔG_0 (J) = -355,890 + 107.5 T (K).

4.4.3. Growth Mechanism

The structure of ZnO can be simply described as a number of alternating planes composed of tetrahedrally coordinated O^{2-} and Zn^{2+} ions, stacked alternatively along the c-axis. The important characteristic of ZnO is the polar surfaces, the most common being the basal plane. The oppositely charged ions produce positively charged Zn-(0001) and negatively charged O-($000\bar{1}$) surfaces, resulting in a normal dipole moment and spontaneous polarization along the c-axis[9]. In ZnO, a VLS process is presumed to control the formation of various nanostructures. The nanostructure formation takes place via a self-catalyzed process. The growth habit of a crystal is related to the relative growth rate of various crystal faces bounding the crystal, which is mainly determined by the internal structure of a given crystal as well as is affected by the growth conditions. The appearance of porous hemispherical tetrahedra condensed on the inner wall close to the open end of the tube suggests the formation of liquid droplets in the initial stages, which are carried away by the carrier gas to the substrates kept downstream. This further emphasizes, that the tetrahedra follows the VLS progression.

To understand the growth kinetics further, the reaction was quenched after 15 and 30 min, respectively and the SEM studies were carried out. A sphere like tetrahedral are observed on the inner wall (figure 4.19(a)) of the thin layer like droplet, while on the upper side of the thin wafer (figure 4.19(b)) large number of needle like features with protruding tip ending into cones similar to multipod arms are observed. Figure 4.17(c) reveals the enlarged image of the area showing the needle like protrusion on the surface of the droplet wafer. A large number of wires [figure 4.19 (a)] are also formed at the edge of the solidified liquid droplet by the self-catalyzed growth mechanism on the ZnO nuclei. These wires have a uniform diameter although; the aspect ratio is small (<30) suggesting incomplete growth. For the reaction quenched after 30 m, a large number of nanowire (figure 4.20) is found protruding out of the thin vapor. At the substrate, along with the microwires, a structure resembling the tetrahedral morphology appears although the arm lengths are not sufficiently grown. Upon increasing the time duration or the oxygen flow rate (10 sccm) due to further oxidation, the concentration of oxygen in the droplets increases. The tetrahedral planes formed at the initial stage acts as nucleating sites where ZnO then deposits resulting in the growth of oriented ZnO structures. The tetrahedra formed at the substrate fuse together to form wires further confirming the process to follow the vapor-liquid-solid progression. Further, the sharp conic tip and the abrupt change in the width of the arms of multipod suggest the screw dislocation mechanism governing the tip morphology[19]. The spiral plane perpendicular to the screw dislocation line possesses a step as a low-energy site for growth. The growth rate along the dislocation line is then much faster than that of radial direction, which results in the 1-D morphology. Thus the multipod growth is initiated by the VLS mechanism and the screw dislocation governs the final structure/tip morphology.

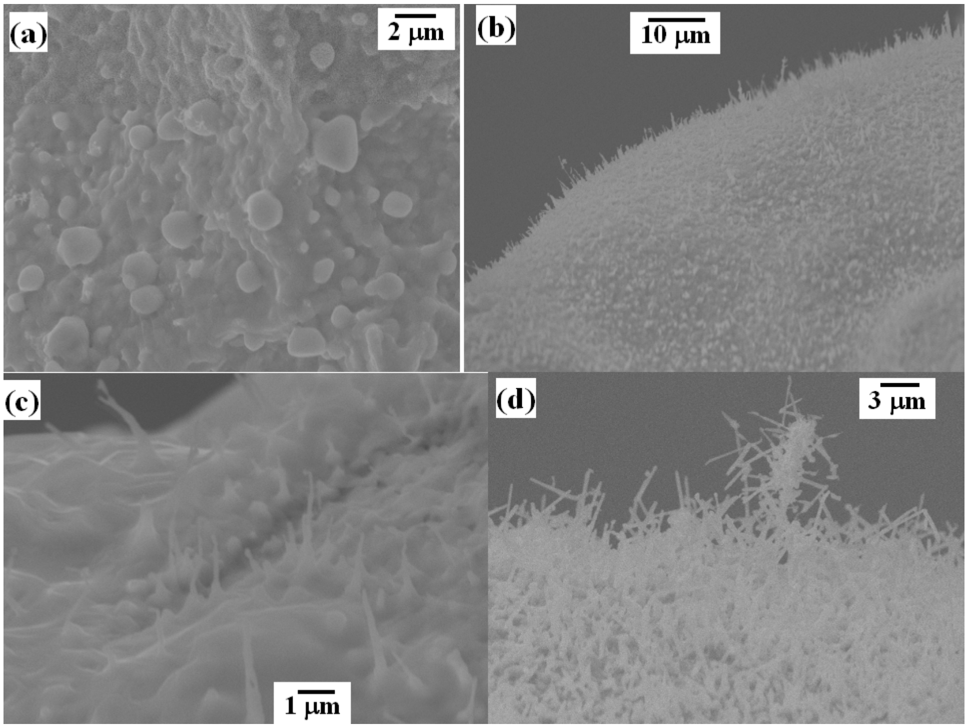

Figure 4.19. SEM images of the Zn droplets (globular thin wafer slightly yellowish in color) formed after quenching the process after 15 min, (a) globular or spherical Zn droplets seen on the inside wall of the droplet, (b) large number of conical tips protruded out of the surface of the molten droplet, spherical drops is also observed detached from the sharp needles, suggesting the growth via a VLS progression. Large number of wires is also observed protruding out of the surface of the thin wafer.

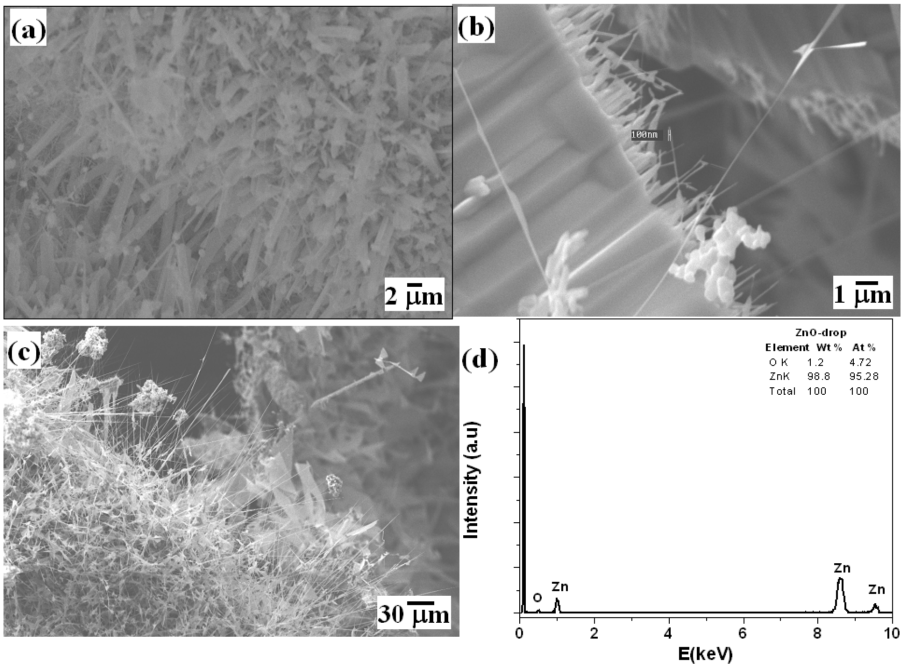

ZnO-drop

Element	Wt %	At %
O K	1.2	4.72
ZnK	98.8	95.28
Total	100	100

Figure 4.20. SEM images of the Zn droplet formed after quenching the process after 30 m, (a), (b) and (c) large number of wire/belt like features protruding outwards are seen and (d) EDX of the droplet suggesting that the droplet mainly comprises of Zn with traces of O_2.

4.4.4. Effect of Substrate and Temperature

Further, EDX carried out on the substrate used (refractory brick) (Figure 4.21(a)) implies that it mainly comprises of Si and Al. Among these, Si in the form of SiO_2 is expected to contribute for the microstructural growth. Surprisingly, when the experiments were carried out under similar conditions with Si-(100) wafer instead of aluminosilicate substrate, large number of hexagonal cones are seen originating from the substrate (figure 4.21(b)). Recently, Ajayan et al have reported the selective growth of oriented CNT's on patterned SiO_2 on Si (100) substrates[20]. They have observed that although there is no nanotube growth on silicon, aligned nanotubes grow readily on SiO_2 in a direction that is normal to the substrate surface. Similarly, in the present case, the shanks of the hexagonal cones originate from the substrate, (Figure 4.21(c)) probably from the sites containing the Si species. Moreover, the hexagonal cones resemble the micro-pyramids synthesized via strong electrostatic interactions between the ions in the melt (solvent) and the polar surfaces of ZnO[21]. During the crystal growth, the polar surfaces usually appear as growing surfaces because of their higher surface energy, exhibiting small facets even disappearing during the crystal growth. For example, in ZnO growth, the highest growth rate is usually along the c-axis and the large facets are usually $\{01\bar{1}0\}$ and $\{2\bar{1}\bar{1}0\}$ non-polar surfaces, rather than the polar {0001} surfaces. In contrast to the non-polar surfaces, the polar $\{10\bar{1}1\}$ planes have a higher surface energy and usually grow too fast to be seen in the final shape of the crystal[22]. Further, some of the pencil structures also exhibit a narrow pen tips on the top (Figure 4.21 (d)). Such structures have also been reported during cooling, owing to continuously decreasing zinc vapor pressure with decreasing temperature.[23] Moreover, the nucleation size of the pen tips is determined by the size of the platform area of the micropencil structures. Interestingly, when additional experiments were performed using alumina substrates instead of Si-wafer, multipod structures were observed. This further signifies that the presence of Si species is crucial in governing the morphology of ZnO structures.

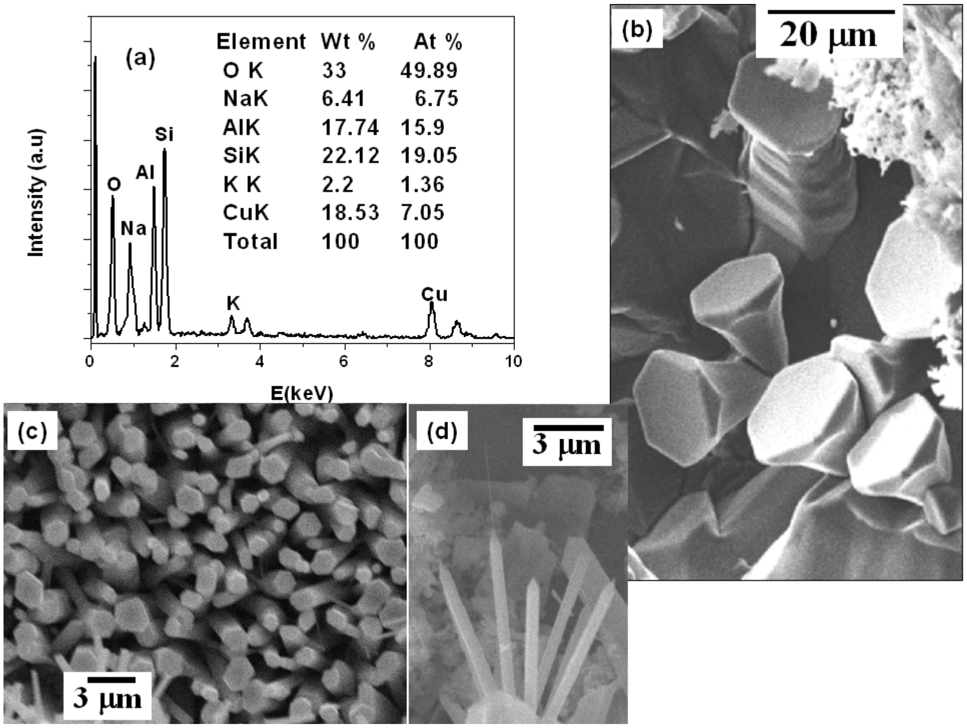

Element	Wt %	At %
O K	33	49.89
NaK	6.41	6.75
AlK	17.74	15.9
SiK	22.12	19.05
K K	2.2	1.36
CuK	18.53	7.05
Total	100	100

Figure 4.21. (a) EDX of the aluminosilicate refractory brick substrate used, (b) SEM image suggesting that the shank of the hexagonal cones originates from the substrates, (c) hexagonal cones emerging out of the Si-wafer, when the experiments were carried out in similar conditions and (d) narrow pen tips on micropencils.

Remarkably, a unique flower-like geometry is also observed on aluminosilicate substrates at lower temperature between 200 and 500 ^{o}C, as shown in figure 4.22. These structures are found to grow on a central microwire, like a tree with flowers. The flower consists of large number of nanowires originating from a single point with tapering end possessing a hexagonal structure on the tip. Some of the hexagonal structures are observed to be separate from the flower suggesting the growth of nanowires to be one of the prominent phenomena. The different length of the nanowires implies various stages of incomplete growth. Indeed, the structure resembles to the needles reported by Wang et al.[24] with bigger dimensions. In our case, we speculate that the metallic Zn droplets are carried away to the substrate wherein the Si species present on the substrate acts as a nucleating site to grow ZnO microstructures. Moreover, during the growth process the polar planes possessing the high surface energy grow faster to give the final morphology. However, when the arms of the wires grow sufficiently long, due to the strain induced in them, the hexagonal cones detach (figure 4.22) from the central wire leading to the formation of sharp-needle like structures. For substrates kept at the middle of the furnace (950^{0}C), the growth process is faster because of the high temperature following a VLS progression, while for the substrates kept at the lower temperature zone, the growth process is in the initial stages and hence only the hexagonal cones are observed. Further, some of the Zn vapor, evaporated from the starting material at a high temperature zone, flows and directly gets deposited on substrates at a low temperature region. At low temperature region the Zn vapors would be oxidized forming suboxides that could probably be assigned to the geometry of the substrate, which limits the amount of oxygen contributing to the reaction. Subsequently, suboxide forms liquid droplets, which in turn enhance the absorption and diffusion of Zn oxides during growth. Thus, the growth of hexagonal cones takes place via a two-step, first as per the VS mechanism where the Zn vapor at high temperature flows to low temperature and reacts with oxygen to form suboxide. Secondly, these suboxides form liquid droplets providing further nucleating sites along with SiO_2 for the formation of hexagonal cones and could be assigned to a VLS mechanism.

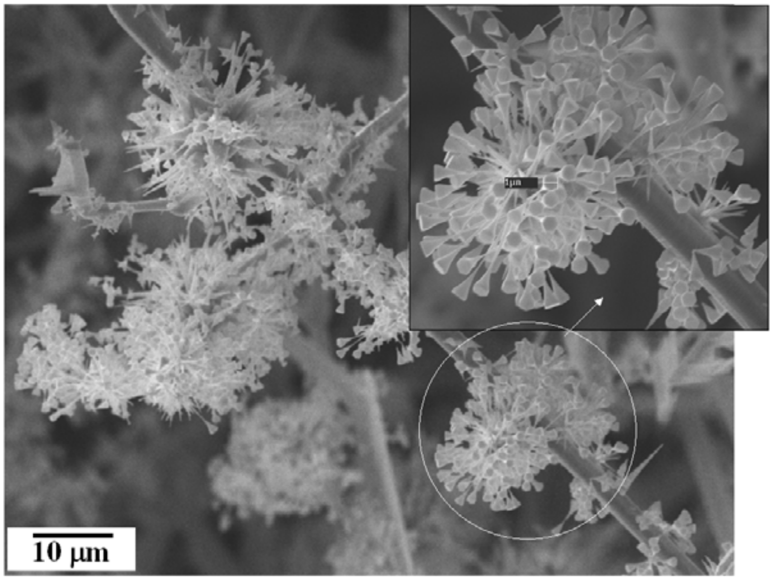

Figure 4.22. SEM image of a novel flower like geometry was also observed on the substrate kept at lower temperature between 200 and 500 °C.

4.5. Conclusions

In conclusion, this chapter deals with the synthesis of ZnO in different morphology, namely multipods, wires, tetrahedra, micropencils and microhexagonal cones by using a simple approach of vapor deposition. XRD studies indicate that the microwires are $(10\bar{1}0)$ oriented while the multipods show prominent peaks for both $(10\bar{1}0)$ and $(10\bar{1}1)$ miller indices. Tetrahedral structures show a biphasic mixture of Zn along with the oxide formation. Zn:O ratio calculated using XPS studies indicate that for the multipod structure there is complete oxidation. These studies reveal that the multipod growth takes place via a screw dislocation mechanism while the tetrahedral and microwires grow via a VLS progression. In case of micropencils and microhexagonal cones, XPS studies indicate that the BE of Zn species shifts to higher BE side attributed to the Si present in the matrix. Si species gets incorporated into the ZnO matrix in Si^{2+} (SiO) and Si^{4+}(SiO_2) forms which play crucial role in deciding the morphology. The Si species present in the form of SiO and SiO_2 acts as a catalyst providing additional nucleating sites, where ZnO nanostructures grow. It has been demonstrated that the micropencil grows via a VLS progression while the microhexagonal cones grow in two steps following VS and VLS mechanisms respectively. These results are believed to be important for controlling the growth of ZnO structures realizing their simultaneous, multidirectional growth on templates of SiO_2 for various device applications.

4.6. References

1. (a) Trindade, T.; O'Brien, P.; Pickett, N. L.; *Chem. Mater.* **2001,** *13*(11), 3843. (b) Fernandez-Garcia, M.; Martinez-Arias, A.; Hanson, J. C.; Rodriguez, J. A.; *Chem. Rev.* **2004,** *104*(9), 4063.
2. (a) Kong, X. Y.; Ding, Y.; Yang, R. S.; Wang, Z. L. Science **2004,** *303*, 1348. (b) Wang, Z. L.; Kong, X. Y.; Zuo, J. M. Phys. Rev. Lett. **2003,** *91*, 185502. (c) Bai, X.; Wang, E. G.; Gao, P. & Wang, Z. L. *Nano Lett.* **2003,** *3*(8), 1147. (d) Dai, Z. R.; Pan, Z. W.; Wang, Z. L. *Adv. Funct. Mater.* **2003**, *13*, 9.
3. (a) Kim, T. S.; Stiehl, J. D.; Reeves, C. T.; Meyer, R. J.; Mullins, C. B.; *J. Am. Chem. Soc.* **2003,** *125*(8), 2018. (b) Chu, S.-Z.; Inoue, S.; Wada, K.; Li, D.; Haneda, H.; Awatsu, S.; *J. Phys. Chem. B.* **2003,** *107*(27), 6586.
4. (a) Rumyantseva, M. N.; Gaskov, A. M.; Rosman, N.; Pagnier, T.; Morante, J. R.; *Chem. Mater.***2005**, *17*(4), 893. (b) Kim, C.; Noh, M.; Choi, M.; Cho, J.; Park, B.; *Chem. Mater.* **2005**, *17*(12), 3297. (c) Maiti, A.; Rodriguez, J. A.; Law, M.; Kung, P.; McKinney, J. R.; Yang, P.; *Nano Lett.* **2003**, *3*(8), 1025. (d) Baranauskas, V.; Fontana, M.; Guo, Z. J.; Ceragioli, H. J.; Peterlevitz, A. C. *Sensors and Actuators B* **2005,** *107***,** 474.
5. Shan, W.; Walukiewicz, W.; Ager, J. W.; Yu, K. M.; Zhang, Y.; Mao, S. S.; Kling, R.; Kirchner, C.; Waag, A. *Appl. Phys. Lett.* **2005***, 86*, 153117.
6. (a) Zhu, Z.; Chen, T.-L.; Gu, Y.; Warren, J.; Osgood, R. M., Jr. *Chem. Mater.* **2005,** *17*(16), 4227. (b) Lyu, S. C.; Zhang, Y.; Lee, C. J.; Ruh, H.; Lee, H. J.; *Chem. Mater.* **2003**, *15*(17), 3294. (c) Xing, Y. J.; Xi, Z. H.; Xue, Z. Q.; Zhang, X. D.; Song, J. H.; Wang, R. M.; Xu, J.; Song, Y.; Zhang, S. L.; Yu, D. P. *Appl. Phys. Lett.* **2003**, 83, 1689.
7. (a) Johnson, J. C.; Yan, H.; Yang, P.; Saykally, R. J.; *J. Phys. Chem. B.* **2003**, *107*(34), 8816. (b) Johnson, J. C.; Knutsen, K. P.; Yan, H.; Law, M.; Zhang, Y.; Yang, P.; Saykally, R. J.; *Nano Lett.* **2004**, *4*(2), 197.
8. (a) Goldberger, J.; Sirbuly, D. J.; Law, M.; Yang, P.; *J. Phys. Chem. B.* **2005**, *109*(1), 9. (b) Fan, Z.; Wang, D.; Chang, P.-C.; Tseng, W.-Y.; Lu, J. G. *Appl. Phys. Lett.* , **2004***, 85*, 5923.

9. (a) Batista P. D.; Mulato, M. *Appl. Phys. Lett.* **2005,** *87*, 143508. (b) Wang, H. T.; Kang, B. S.; Ren, F.; Tien, L. C.; Sadik, P. W.; Norton, D. P.; Pearton, S. J.; Lin, J. *Appl. Phys. Lett.* **2005**, *86*, 243503.
10. (a) Zhang, J.; Sun, L. D.; Yin, J. L.; Su, H. L.; Liao, C. S.; Yan, C. H.; *Chem. Mater.* **2002**, *14*(10), 4172. (b) Li, Z.; Xiong, Y.; Xie, Y. *Inorg. Chem.* **2003,** *42*(24), 8105.
11. Heo, Y.W.; Norton, D.P.; Tien, L.C.; Kwon, Y.; Kang, B.S.; Ren, F.; Pearton, S.J.; LaRoche, J. R. *Matr. Sci. Eng. R* **2004**, *47*, 1.
12. Pan, Z. W.; Dai, Z. R.; Wang, Z. L. *Science* **2001**, *291*, 1947.
13. (a) Roy, V. A. L.; Djurišić, A. B.; Chan, W. K.; Gao, J.; Lui, H. F.; Surya C. *Appl. Phys. Lett.* **2003,** *83*, 141. (b) Li, Q. H.; Wan, Q.; Chen, Y. J.; Wang, T. H.; Jia, H. B.; Yu, D. P. *Appl. Phys. Lett.* **2004**, *85*, 636. (c) Wan, Q.; Yu, K.; Wang, T. H.; Lin, C. L. *Appl. Phys. Lett.* **2003**, 83, 2253**.**
14. Yin, M.; Gu, Y.; Kuskovsky, I.; Andelman, T.; Zhu, Y.; Neumark, G. F.; O'Brien, S. *J. Am. Chem. Soc.* **2004**, *126*, 6206.
15. Monticone, S.; Tufeu, R.; Kanaev, A. V. *J. Phys. Chem. B.;* **1998**; *102*(16); 2854.
16. Chen, T. P.; Liu, Y.; Sun, C. Q.; Tse, M. S.; Hsieh, J. H.; Fu, Y. Q.; Liu, Y. C.; Fung, S.; *J. Phys. Chem. B.* **2004,** *108*(43), 16609.
17. Jeong, J. S.; Lee, J. Y.; Cho, J. H.; Suh, H. J.; Lee, C. J. *Chem. Mater.* **2005**, *17*, 2752.
18. Handbook of Corrosion Engineering Pierre R. Roberge**,** McGraw-Hill; Publication Date: 2000; ISBN 007-076516-2; 1140 pages**.**
19. Wang, R. C.; Liu, C. P.; Huang, J. L.; Chen, S.-J.; Tseng, Y.-K.; Kung, S.-C. *Appl. Phys. Lett.* **2005,** *87*, 013110.
20. Wei, B. Q.; Vajtai, R.; Jung, Y.; Ward, J.; Zhang, R. Ramanath, G.; Ajayan, P. M. *Nature* **2002**, *416*, 495.
21. Zhou, X.; Xie, Z.-X.; Jiang, Z.-Y.; Kuang, Q.; Zhang, S.-H.; Xu, T.; Huang, R.-B.; Zheng, L.-S. *Chem. Commun.* **2005**, (44), 5572.
22. Li- W.-J.; Shi, E.-W.; Zhong, W.-Z.; Yin, Z.-W. *J. Crys. Growth* **1999**, *203*, 186.
23. Wang, R. C.; Liu, C. P.; Huang, J. L.; Chen, S.-J.; Tseng, Y.-K.; Kung, S.-C. *Appl. Phys. Lett.* **2005,** *87*, 013110.
24. Yao, B. D.; Chan, Y. F.; Wang, N. *Appl. Phys. Lett.* **2002,** *81*, 757.

Chapter 5

Enhanced Field Emission Properties of ZnO Nanostructures[*,†]

This chapter primarily deals with the field emission characteristics of novel multipod, marigold, microbelt and tetrahedra nanostructures of ZnO. The studies have been carried out both in the close proximity (C-P) configuration and the conventional field emission microscope (FEM) especially because the use of FEM configuration overcomes the drawback of arc formation at high field values. Interestingly, a current of 1 nA with an ultralow onset voltage of 40 V (for 1nA) and the current density of 2.8 x 10^4 A/cm^2 achieved with a field of 1.26 x 10^5 V/μm are observed for the single multipod as well as for the arm. The nonlinearity observed in the F-N plots for all the morphologies have been interpreted on the basis of the theory of electron emission from semiconductors. A scheme explaining the field emission behavior in both the high and the low field regions owing to the very high geometrical factor has been picturized in this chapter. The current stability exhibited by these structures is also promising for sustained emission behavior facilitating their application in next generation field emission devices.

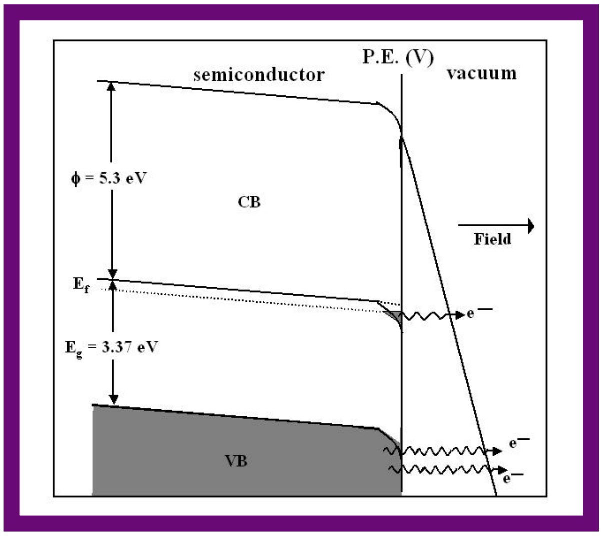

---

[*] A part of the work has been published in "**Appl. *Phys. Lett.* 2006,** 88(3), 042107 and another part has been communicated to ***Nanotech.* 2005** ".

[†] The field emission was carried out in the Department of Physics, University of Pune.

5.1. Introduction

Application of a sufficiently high electric field (10^6-10^7 V/cm) normal to the surface of a metal or a semiconductor leads to the emission of electrons by quantum mechanical tunneling through the surface barrier[1]. It has diverse technological applications in flat panel displays, microwave-generation devices and vacuum micro/nano-electronic devices.[1, 2] With the advent of various anisotropic nanostructured materials like CNTs[3], AlN[4], GaN[5], SiC[6], TiO_2[7], SnO_2[8] and ZnO[9-12], there has been an upsurge in the interest considering their promising potential as efficient field emission cathodes. This is mainly because it is easier to generate nearly monoenergetic electron beams by accurately controlling the density and the geometry of the emitter. Consequently, field emission from novel nanostructures of ZnO supported on various substrates has been investigated owing to the excellent mechanical, chemical and thermal properties. Besides this, ZnO nanostructures have negative electron affinity and the ease with which the morphology (sharp nanotips) can be controlled makes them an appropriate alternative to carbon nanotubes and other solid-state devices for field-emission microelectronic devices. The effects of geometrical factors, areal density and morphological features have been reported for arrays of multiple needle-like ZnO nanostructures, primarily with the objective of attaining higher values of emission current density and lower onset voltage, compared to various other materials. The minimum emission current density of 1 mA/cm^2 is required to produce the luminance of 300 cd/m^2 from video graphics array-field emissive displays (VGA-FED) with typical high-voltage phosphor screen efficacy of 9 lm/W.[13] Among the reported field emission results of ZnO nanowires, Lin et al. reported the lowest electric field of 4.5 V/μm.

The field emission studies of these nanostructures have been carried out in the close proximity (C-P) configuration wherein the field emitter arrays in the form of thin film are mounted in proximity with an anode screen separated by an insulating spacer (~50 μm to a few mm) as shown in figure 5.1. Electron tunneling in this configuration is generally referred to as ‘thin-film tunneling’. However, such a configuration poses a serious limitation on the strength of the applied electric field as relatively high field may lead to the arc formation. The emission properties can be analyzed by the classic

Fowler–Nordheim (F–N) law,[14] discussed in detail in chapter 1 (section 1.10.5), which was derived on the basis of the electron-emission properties from a semi-infinite flat metallic surface, used to describe the relationship between the current density (J) and the local field nearby the emitter E_{local}, which is usually related to the average applied field E as follows:

$$E_{local} = \beta E = \beta\ V/d \qquad \text{-(1)}$$

where d is the interelectrode spacing, V is the applied voltage and β quantifies the ability of the emitter to amplify the E and is defined as the field enhancement factor. Considering the screening effect between adjacent emitters, E_{local} can be expressed by Filip model[15],

$$E_{local} = s\ V/r + (1\text{-}s)\ V/d \qquad \text{-(2)}$$

where, r, is the radius of the emitter and s is a parameter describing the degree of the screening effect, which ranges from 0 for densely arranged emitters to 1 for a single one. Combining equation (1) and (2) gives the field enhancement factor i.e. the ability of the emitter to amplify the applied field, from the emitter array

$$\beta = 1+s(d/r-1) \cong 1+ sd/r \qquad \text{-(3)}$$

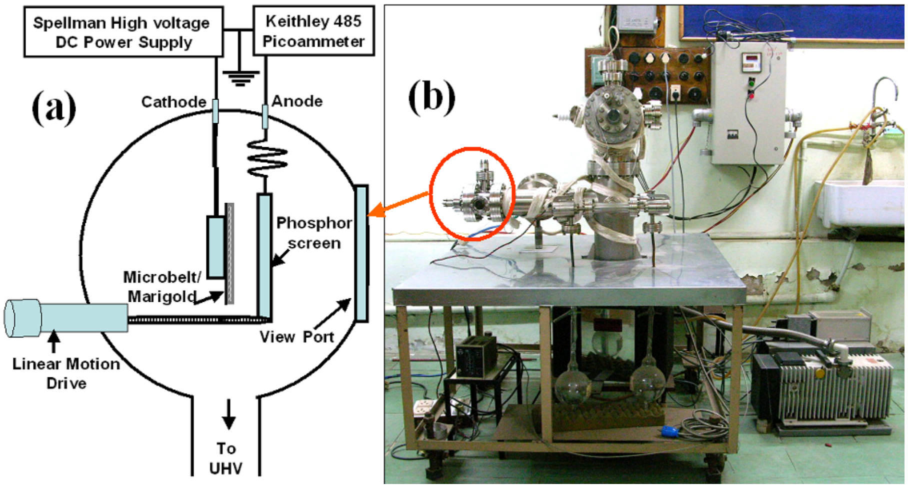

Figure 5.1. (a) Schematic of the emitter tip assembly in close-proximity (C-P) configuration; (b) actual Instrument used for studying field emission of nanostructures deposited/coated on Si-wafer in C-P configuration. (Courtesy: Prof. D. S. Joag, Department of Physics, University of Pune)

In order to understand the physics of field emission from such a novel nanostructured ZnO, it is an essential prerequisite to study the field emission characteristics in a conventional field emission microscope (FEM) configuration, along with the C-P configuration. In the conventional FEM configuration, the emitter (cathode), in the form of a fine needle with a tip radius of about 10^{-4} cm or less, is placed inside an evacuated chamber, in front of an anode screen, typically 5 to 7 cm apart. (Figure 5.2) In such a configuration, it is possible to enhance the range of applied electric field overcoming the drawback of arc formation observed in C-P configuration.

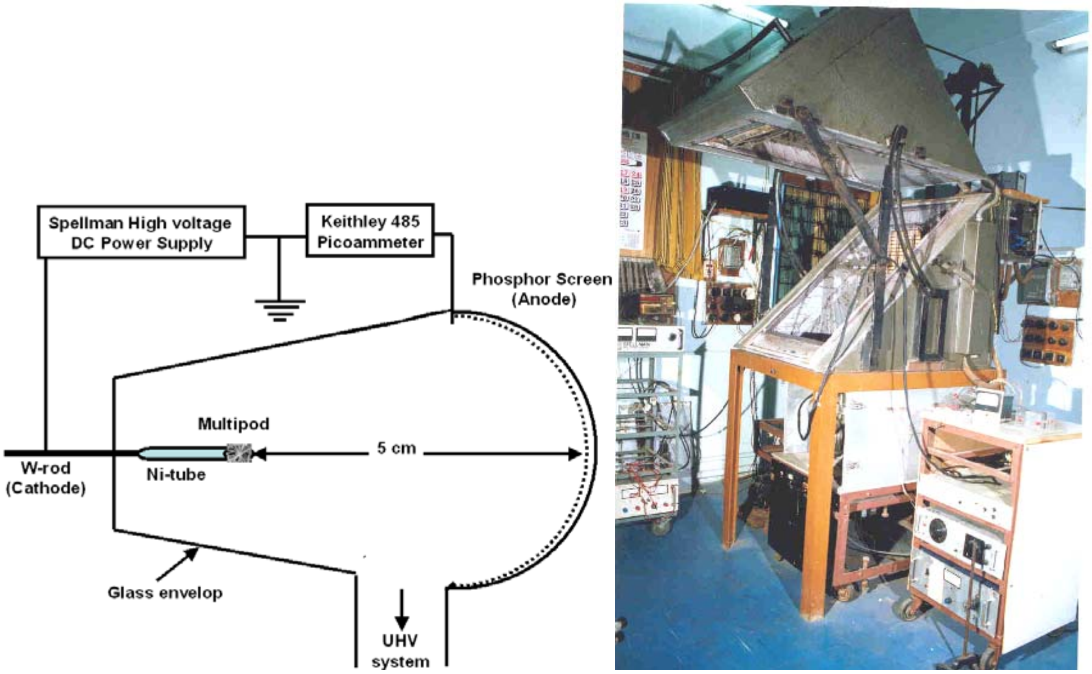

Figure 5.2. (a) Schematic of the conventional FEM configuration, the emitter (cathode), in the form of a fine needle with a tip radius of about 10^{-4} cm or less, is placed inside an evacuated chamber, in front of an anode screen, typically 5 to 7 cm apart; (b) Photograph of field emission instrument used in the present study. (Courtesy: Prof. D. S. Joag, Department of Physics, University of Pune)

In this chapter we demonstrate the field emission studies carried out in both the configurations for various novel ZnO nanostructures namely multipod, marigold, microbelt and tetrahedra synthesized by a modified vapor phase deposition as explained in chapter 4. For a single arm of a multipod structure an ultra-low onset voltage of 40 V to extract a current of 1 nA has been observed. The F-N theory of electron emission from the metal has already been discussed in detail in chapter 1, section 1.10.5.[14] The emergence of ultra-low onset voltage has been explained on the basis of theory of electron emission from semiconductors. Further, our results emphasize that the electrons from both the valence and the conduction bands contribute to the field emission current. Interestingly, all the structures exhibit an improved stability implying them to be some of the promising materials for next generation field emission devices.

5.2. Experimental Aspects

5.2.1. Specimen preparation

The experimental details regarding the synthesis of ZnO structures have already been described in chapter 4, section 4.3. In brief, Zn–metal as a starting material was heated at 950^{0}C for 2 h with Ar and O_2 flow rates of 100 sccm and 20 sccm (20% v/v), respectively. The multipod structures were collected at the substrate kept downstream where the temperature was between 300 and 500 ^{0}C. The ZnO microbelts and marigold structures were grown on the Si - (100) substrates kept adjacent to the source material where the temperature is 800 ^{0}C.

5.2.2. Morphological and structural characterization

The morphology and the structure were characterized using techniques such as XRD, SEM, TEM, XPS in a way similar to that described in chapter 2, section 2.3.

5.2.3. Field Emission studies

5.2.3.1. Construction of conventional FEM tube

The delicate nature of the components and the stringent conditions required for FEM experiments makes its construction intricate and a schematic of an all-glass FEM tube is shown in Figure 3. Basically it comprises of four parts, viz. (a) an emitter tip assembly, (b) an optically transparent conducting coating from inside to serve as an anode, (c) a phosphor screen on top of the conducting coating to display the field emission pattern, and (d) a getter bulb to serve as an appendage pump to improve vacuum conditions in the sealed-off tube. A getter bulb contains a heating filament of a getter material (0.267 mm diameter titanium wire closely over wound on a tungsten wire of 0.25 mm diameter) that can be evaporated onto a surface at room temperature or below. Chemically active gases are pumped at the evaporated film by chemisorption forming stable chemical compounds with low vapor pressure.

5.2.3.2. Specimen mounting: the emitter tip assembly

5.2.3.2.1. ZnO microbelts and needles grown on Si-wafer

Field emission measurements for ZnO microbelts and marigold structures grown on Si-wafer were carried out in a close proximity configuration in a vacuum chamber with a pressure less than 1 x 10^{-9} mbar at room temperature. The sample was mounted on a stainless-steel stub ($\phi \approx$ 6mm) using Ag paste as conducting glue, which is known to give a proper ohmic contact. A phosphor screen, used as an anode, was mounted on a linear motion drive parallel to the cathode and held at a distance of 1mm.

5.2.3.2.2. Multipod structure

The multipods were mounted skillfully, with several attempts, on a tungsten (W)-needle using silver paste (vacuum compatible) under an optical microscope. As seen from the SEM, the silver paste does not have any sharp protrusions that may be expected to contribute to the field emission, which is a surface sensitive technique. Further, the scanning electron microscopy was carried out to confirm proper mounting of a single multipod and a single arm on the tungsten-needles. Two such needles containing a single multipod and a single isolated arm of a multipod were selected for the field emission measurements, carried out in all glass conventional field emission microscope (FEM) tube assembly consisting of an emitter cathode and a transparent anode with SnO_2 and phosphor coating. The emission sites could be seen directly on the anode screen, kept at a distance of 5 cm from the needle.

Also, a nickel tube (1 mm in diameter and 5 mm in length) was crimped at one end keeping the other end filled with silver paste. The multipod structures were inserted into the paste end and dried at ambient temperature. In order to study the effect of areal density, the loading of the multipods was carried out carefully to yield different densities: higher density sample is referred to as multipod-1 and the lower density sample is referred to as multipod-2.

5.2.3.2.3. Tetrahedral structures on W-tip

The tetrahedral structures were grown directly on the tungsten-needle for field emission studies. The field emission measurements were carried out in all glass conventional field emission microscope tube assembly consisting of an emitter cathode (tetrahedral on tungsten needle) and a transparent anode with conducting screen.

5.2.3.3. Vacuum processing and Instrumentation

The emitter-tip assembly either of C-P configuration or conventional FEM configuration were then mounted on an all-metal ultrahigh vacuum system equipped with a diffusion pump and a liquid nitrogen cooled chevron trap, a sputter ion pump, and a titanium sublimation pump. After baking the tube at 250 °C for 8 h, pressure of 1×10^{-9} mbar was obtained. The measurements of the current–voltage (I–V) characteristic and the current-stability (I-t) were carried out at this pressure using a Keithley 485 picoammeter and a Spellman high voltage DC power supply with a proper grounding. Before starting the I-V measurement, the picoammeter was stabilized (as per the instructions in operating manual) for 30 min and zero reading on display was ensured. Also, a special care was taken to avoid any leakage current by using shielded cables with proper grounding. The emission current measurements were carried out at the base pressure $\sim 1 \times 10^{-9}$ mbar.

5.3. Results and discussion

5.3.1. Field emission studies of isolated multipods on W-tips

Among various structures of ZnO, the isolated multipod and one of the pods were tested for field emission properties. Interestingly, a current of 1 nA with an ultra-low onset voltage of 40 V is observed repeatedly for the single multipod as well as for the arm (pod) as depicted in figure 5.4, which is highlighted in the inset. The corresponding onset current density and applied field generated at the emitter tip apex are 2.76×10^{7} μA/cm^2 and 3700 V/μm, respectively. For ZnO nanostructures, the lowest ‘threshold field’ in parallel plate geometry corresponding to the current density of 0.1 μA/cm^2 is 0.8 V/μm.[16] Further, de Jonge et al. have extracted a current in the range of 0.4 – 80 nA by applying the voltage in the range of 300 – 420 V from a single carbon nanotube attached to a tungsten wire in a geometry similar to that used in the present one. An explicit comparison of our results with the reported ones will be more useful, if done for similar current density.[8] The onset current density in our case is very high (2.76×10^7 μA/cm^2) and none of the previous researchers have achieved such a high value for ZnO. Therefore, the unique observation of 40 V to draw a current of 1 nA is considered to be ultralow. Remarkably, this voltage is unaffected even after operating the emitter at much higher voltages (10 kV and above) for recording the current-voltage (I-V) characteristics and a total emission current of 1 μA at 10 kV is observed in all the cases.

Figure 5.5 shows the F-N plot, In(I/V^2) versus 10^4/V plot derived from the above I-V characteristics of these multipod structures. A very interesting nonlinear behavior is observed in the F-N plot which could be clearly understood for two distinct ranges of applied fields as depicted in figure 6 (a) and (b). In these two ranges, the F-N plots are fairly linear with distinct slopes. For semiconductors, in low current approximation, the F-N plot should be a straight line for electrons emitted from conduction band as well as from valence band. Moreover, we believe that the F-N plot is not sensitive to contributions from surface states and band bending.

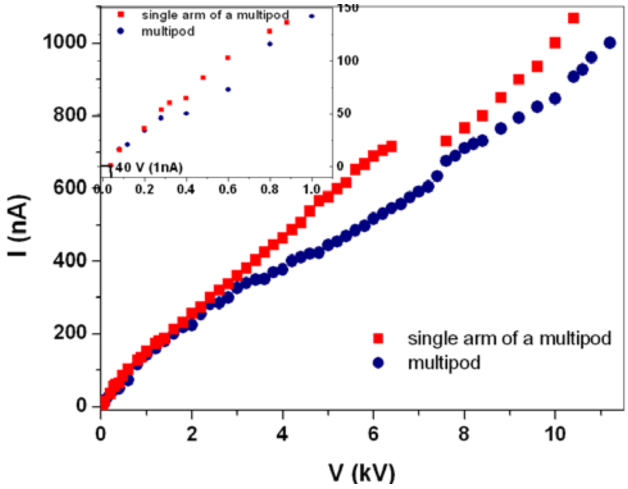

Figure 5.4. (a) Current-voltage (I-V) characteristics of isolated multipod and an individual arm with the inset highlighting the low onset voltage for these samples.

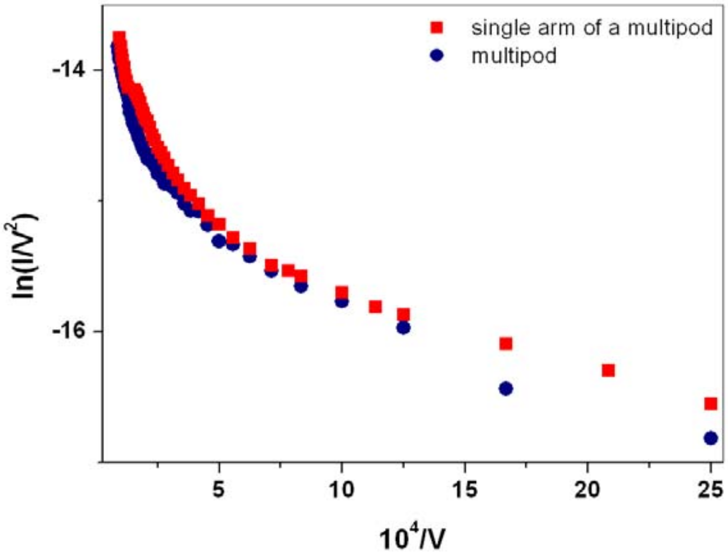

Figure 5.5. An F-N plots of isolated multipod and an individual arm over the large potential range of 40 V to 10 kV.

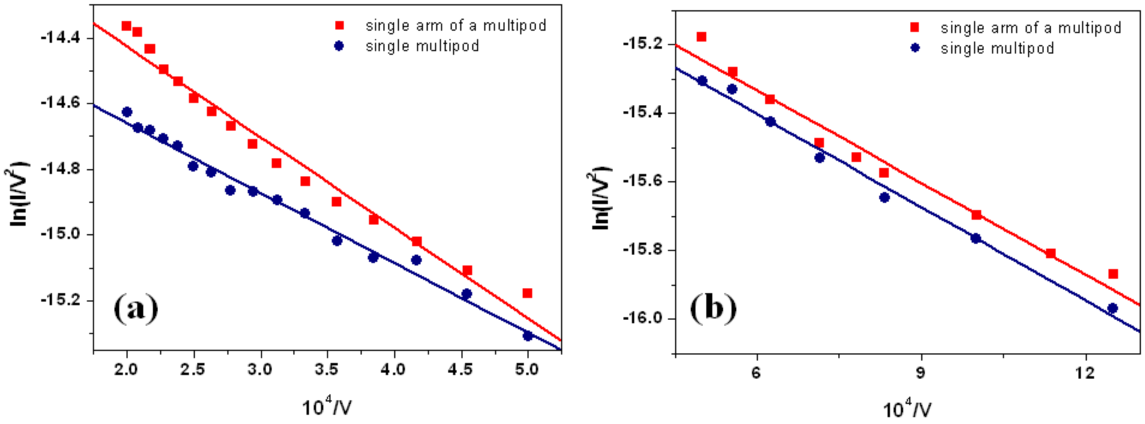

Figure 5.6. The F-N plot of isolated multipod and an individual arm in the two linear ranges (a) a higher region from 5 kV to 10 kV and (b) a lower region between 40 V and 5 kV.

The field enhancement factor β is related to the slope of the F–N plot, m, by the following equation[17]

$$\beta = (-6.83 \times 10^3 \, \phi^{3/2})/m \qquad -(4)$$

where, ϕ is the work function of the emitter material in eV. In the present case, the work function of ZnO (ϕ) is assumed to be 5.3 eV and is reported to be independent of the size and aspect ratio of the nanostructure[18]. In the low field region, the field enhancement factor (β) is calculated to be 9.25×10^5 cm^{-1}, which is identified to be directly dependent on the aspect ratio (ratio of length to tip radius) of the nanostructure[19].

In the context of F-N theory, for conventional FEM configuration used in the present case, the applied field is defined as $F = \beta V$, where, V is the applied voltage (V) and β is the field enhancement factor (cm^{-1}). Further $\beta = 1/kr$, where k is a constant known as the geometrical factor and has the value 5 for hemispherical emitter, and r is the tip radius.[20] If the same factor β is assumed in the two regions, the low field region corresponds to emission from the conduction band of ZnO and the high field region corresponds to an additional emission from the valence band, 3.37 eV below the conduction band. The value of ϕ calculated from the slope of the F-N plot in the high field region is 11.24 eV and is in general agreement with the proposed scheme-5.1, wherein the effective work function is assumed to be 8.67 eV ($\phi_o = \phi + E_g$). This difference may be attributed to the contributions from the field penetration-induced band bending. It was demonstrated by Zheng et al.[21] that for metallic CNT the field penetration at the tip lowers the potential barrier leading to a deep potential well in the region where a large number of excess electrons reside. Moreover, the lowering of barrier height is a non-linear function of the applied field, which is system independent. Indeed, the theory of field emission from semiconductors is not so simple as in the case of metallic emitters [22, 23]. Moreover, the F-N theory cannot resolve the fine structure in the energy distribution of electrons although it describes fairly well, the relationship between the emitted current and the applied field. However, the non-linearity in the F-N plot (Figure 5.5) can be understood upon considering the theory of electron emission from semiconductors as represented in scheme-I, which explains the behavior in both the high and the low field regions owing to a high field enhancement factor and contributions from the valence band states. It is likely that the modification of tip may lead to a drastic alteration of emission current or threshold voltage.

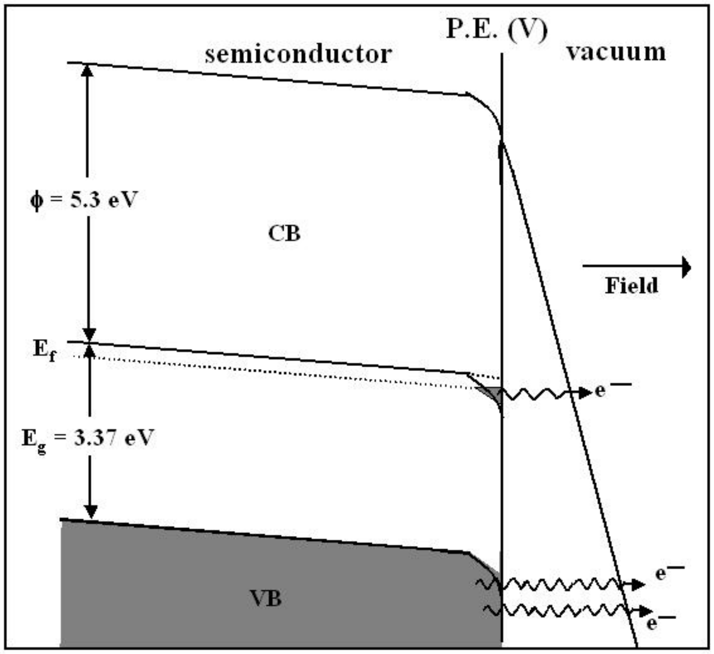

Scheme 5.1. The schematic of the band diagram of bulk ZnO based on the calculation using field emission energy distribution[27]; VB is the valence band, CB is the conduction band, E_g is the energy gap of ZnO (3.37 eV) and ϕ is the work function (5.3 eV). In the absence of the electric field there exists a semi-infinite barrier to the emission of electrons present near the Fermi level. However, after the application of the field, this barrier reduces to a triangular barrier as shown. While at the lower fields, electrons in the conduction band are responsible for the emission current, at the higher fields, electrons in the conduction band and those from the valence band with the effective work function of $\phi_o = \phi + E_g = 5.3 + 3.37 = 8.67$ eV, tunnel to generate the emission current.

Further, assuming hemispherical geometry of the emitter surface, the current density (J) generated at the emitter tip is calculated using

$$J = I/2\pi r^2 \qquad \text{-(5)}$$

where, I is the total current and r is the radius of the emitter tip as estimated from the scanning electron micrograph. The current density from a single multipod and a single arm are 1.48×10^{10} μA/cm^2 and 2.76×10^{10} μA/cm^2 respectively, measured at an applied field of 1.26×10^5 V/μm and 1.64×10^5 V/μm.

5.3.1.2. Tip radius determination using Iterative Approach

If the work function ϕ is assumed to be known and uniform, the radius of the tip, correct to within 20%, can be determined from the slope of F-N plot given by equation 1.34. An accurate method of evaluating r is as follows: (a) evaluate $d(\ln(I/V^2)/d(10^4/V)$ for clean tip, (b) assume S(y) = 1, ϕ is known and assumed to be uniform, (c) from β from the slope, (d) find r knowing α for the standard tip geometry from β, (e) then evaluate $y = 3.79 \times 10^{-4} F^{1/2}/\phi$ by substituting $F = \beta V$, (f) from tables, find S(y), (g) using this S(y), iterate to no further change in r.

The emitter tip radius of the field emitter is calculated using this method wherein the work function of ZnO is assumed to be 5.3 eV. The final value of the radius obtained is 17.4 nm, which is in good agreement with the SEM results (24 nm). A post operation SEM study indicates no significant change in the geometry of the emitter, emphasizing that ZnO is highly resistant to ion bombardment and has excellent structural stability against high electric fields (12 kV and above).[20] This is especially important for fabricating field emission devices with stable, high current density field emission, as these multipods have remarkable functional stability for repeated performance without any obvious signs of degradation.

In order to harness the advantages of lower threshold voltage and high current density offered by these individual arms of ZnO multipod, a precise control over the spacing is desired. For practical applications of field emission electron sources, along with the emission capability, the current stability is also crucial. Accordingly, figure 5.7 shows the current-time (I-t) plot for the two structures measured with a base pressure of 1×10^{-9} mbar. For the single multipod and a single arm, the stability at current levels of 400 nA and 200 nA respectively, is appreciable, as the fluctuations in the field emission current lie within 10% of the average value of the current, which however decays to ~50% of the initial value. Perhaps, the current fluctuations might have been resulted from the dangling bonds on the surface or from the diffusion of adsorbates, on the surface of the multipods[24]. Moreover, the self-diffusion process of the atoms at the tip of the multipod in the presence of high electric field is also expected to contribute.

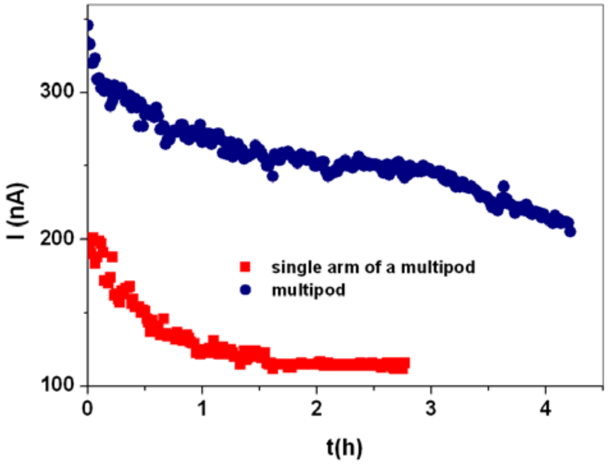

Figure 5.7. Current-time transients for both the samples suggesting reasonable stability.

Figure 5.8 shows the field emission micrographs of single multipod and a single arm of a multipod recorded at an applied potential of 10 kV. For single multipod four bright spots on the screen attributed to the emission from the four arms are observed while for a single arm of a multipod only a single bright spot in the middle of the screen is observed.

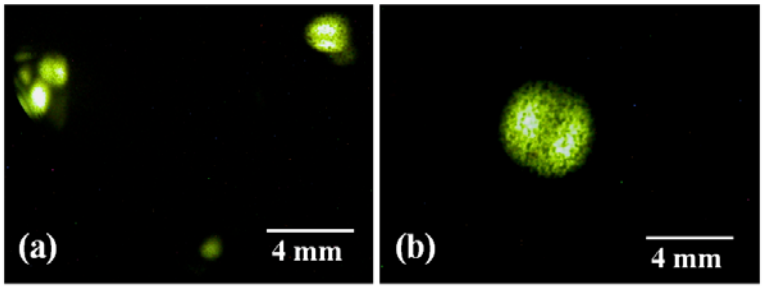

Figure 5.8. (a) Field emission micrographs of single multipod showing four bright spots on the screen attributed to the emission from the four arms and (b) a single arm of a multipod showing a single bright spot in the middle of the screen. Both the micrographs are recorded at an applied potential of 10 kV. The bar indicates the scale on the screen.

5.3.2. Field emission studies of microbelts and marigold structures deposited on Si wafer, and multipods crimped in Ni tube: A comparison

5.3.2.1. Morphological and structural characterization

Figure 5.9 (a) shows the SEM image of marigold structure deposited on a Si wafer. It consists of a number of nanotips randomly oriented and mostly protruding outwards. The nanotips are conical in shape with shank ~ 1μm in width and the tip apex <100 nm in diameter. The oxides with the belt-like morphology cover cations with different valence states and materials with different crystallographic structures, and it is a common structural characteristic for the family of semiconducting oxides. Figure 5.9(b) shows the SEM image of the microbelts deposited on the Si wafer. These have width between 500 and 5000 nm, and a length of 50 –150 μm. The inset of figure 5.9 (b) shows the SAED pattern, which clearly reveals the hexagonal type ZnO. Figure 5.9(c) and (d) shows the SEM images of the multipod-1 and multipod-2 structures. It is obvious from these images that the number of arms of the multipods is between 4 and 16 and all have a common origin with varying length from 10 to 80 μm. Most of the arms have uniform width, whereas some of them end like a cone (tip apex of ~ 24 nm). In a few other arms, the width suddenly narrows down in the middle to a sharp protrusion.

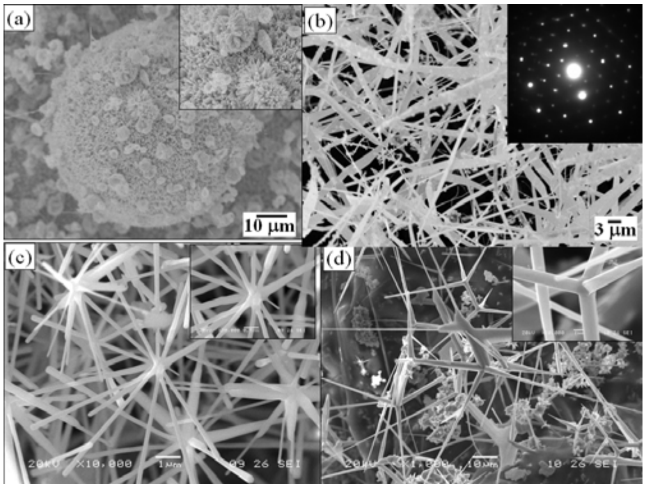

Figure 5.9. SEM images of ZnO structures mounted for field emission studies (a) marigold, (b) microbelts, which are collected on a Si substrate kept adjacent to the substrate containing the starting material where temperature is 800^{0}C, (c) multipod-1 and (d) multipod-2, mounted with different density on W-tip and are collected downstream where the temperature is between 300 and 500^{0}C.

5.3.2.2. Field emission studies

In case of C-P configuration the applied field is usually calculated as E = V/d, where V is the applied voltage and d is the separation. This gives an average electric field and not the field at the apex of an individual emitter tip, due to the complexity posed by large number of emitters on the cathode substrate. On the other hand, in the conventional FEM configuration, the corresponding field generated at the emitter apex is calculated using $F = \beta V$, and the theoretical field enhancement factor $\beta = 1/kr$, where k is a constant called as the geometrical factor and has the value 5 for hemispherical emitter, and r is the tip radius. This field is referred to as local field at the emitter. As a result, comparison of field emitters is pertinent only if the field emission measurements have been performed under the same experimental configurations. I–V characteristics for all the ZnO morphologies are shown in figure 5.10. The overall field emission characteristics exhibited by ZnO structures are observed to obey the F-N theory, except multipod-2 sample. In case of multpod-2, the current seems to be linearly dependent on applied voltage, which may be attributed to the randomness in number of pods, their lengths, sizes and distributions. The onset voltage, required to draw a current of 1nA, for marigold and microbelts is observed to be 3.3 kV and 2 kV, respectively. In case of marigold structures, when the applied voltage is increased beyond 4 kV an arc formation is observed in the C-P configuration. Hence the emission characteristics for these structures could not be investigated at high electric fields. On the other hand for microbelts, no arc formation is observed, suggesting them to be one of the robust materials that can withstand sufficiently high voltages. This could be attributed to the random distribution of microbelts lying parallel to the Si-wafer substrate. Above 2 kV the microbelts exhibit an increase in the current upto 80 μA.

In the case of multipod-1 and multipod-2 structures, the onset voltage is observed to be 5.1 kV and 0.32 kV, respectively. The difference in the onset voltages for the two multipod structures may be due to the variation in areal density. As seen in the SEM images, the areal density of multipod-2 is lower than that of multipod-1. It is expected that the field screening effect will be less in multipod-2 and consequently it exhibits lower onset voltage. This clearly signifies the importance of tuning the density of nanostructures, in order to exploit the advantage of low onset voltage offered by an individual nanostructure.

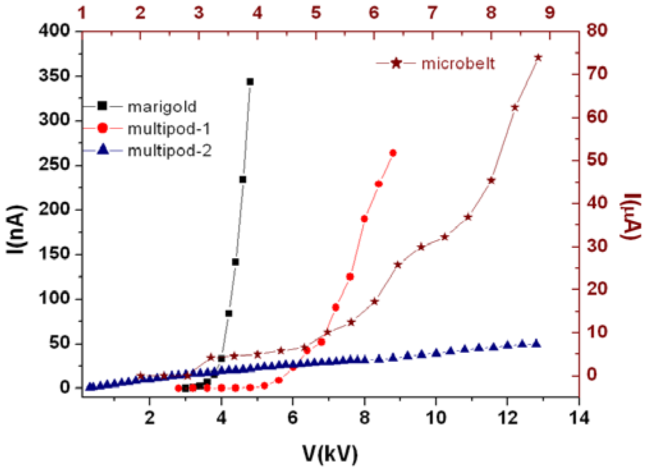

Figure 5.10. I-V characteristics for different ZnO structures; the onset voltage required to draw a current of 1nA, for marigold and microbelts is observed to be 3.3 kV and 2 kV, respectively while in the case of multipod-1 and multipod-2 structure; the onset voltage is 5.1 kV and 0.32 kV, respectively.

The F–N plot for all the ZnO structures investigated is shown in figure 5.11. Interestingly, all the F–N plots are seen to be nonlinear reflecting the semiconducting nature of ZnO. It is surprising to note that such nonlinear characteristic has not been highlighted for ZnO nanostructures investigated by various researchers. However, a careful observation of reported F-N plots clearly shows a signature of nonlinearity towards relatively high field region.[8] Most of these studies have been carried out in C-P configuration wherein, the emission behavior in high field region could not be carried out. However, in the present case, the conventional configuration mentioned earlier offers the advantage of application of high electric fields. In order to compare the observed F-N plots with the reported ones, we have analyzed the F-N plot in the two electric field regions, namely normal operating region (2 – 4 x 10^4/V) and the high field region (<2 x 10^4/V) respectively. The analyzed F-N plots show two distinct linear natures in the two field regions. It is interesting to note that all the F-N plots show a sudden change in the linearity at a specific knee field value, corresponding to 2 x 10^4 V^{-1} in the F-N plot, irrespective of different morphologies. This implies that the knee field is the characteristics of the emitter material. The F–N plot suggests that the field emission is a barrier tunneling process and in the two field regions obeys the equation 1. In these two regions, the F-N plots are fairly linear with distinct slopes.

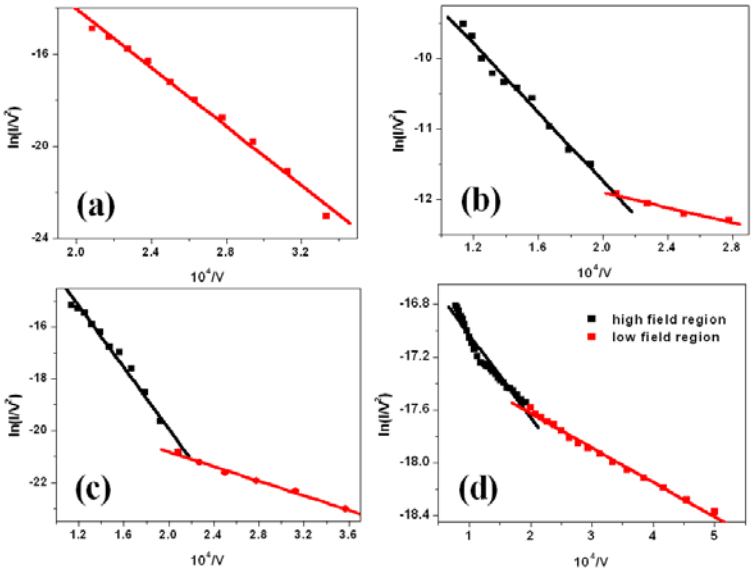

Figure 5.11. The F–N plot for (a) marigold, (b) microbelts, (c) multipod-1 and (d) multipod-2 ZnO structures.

Although the F–N theory and the formulae used in the field emission microscopy are strictly valid for hemispherical emitter tips which assume a free electron model, a rough estimate of the field enhancement factor β could be obtained from the F–N plot [15]. For semiconductors, in low current approximation, the F-N plot is a straight line for electrons emitted from both the conduction and the valence bands. Moreover, we believe that the F-N plot is not sensitive to contributions from surface states and band bending. Further, the deviation from the linearity could also be attributed to the strong dependence of Fermi energy on the applied field.

Taking the work function of ZnO (ϕ) to be 5.3 eV (as reported to be independent of the size and aspect ratio of the nanostructure)[17], the field enhancement factor is calculated for different structures as shown in Table 5.1 along with the onset voltage. If the same β is assumed in the two regions, the normal operating range could be attributed to the electron emission from the conduction band. However, when the applied field is further increased, additional emission from the valence band i.e., 3.37 eV below the conduction band also starts contributing to the emission current along with the emission from the conduction band. This phenomenon is reflected as a linear behavior of F-N plot in the high field region. The β values, thus calculated using the increased work function of 8.67 eV ($\phi_o = \phi + E_g$) agrees well with the low field region values. However, the difference may be attributed to the contributions from the field penetration-induced band bending. Moreover, the field penetration at the tip lowers the potential barrier leading to a deep potential well in the region where a large number of excess electrons reside[19]. This lowering of barrier height is a nonlinear function of the applied field and is system independent. A post operation SEM study indicates no significant change in the geometry of the emitter, emphasizing that ZnO is highly resistant to ion bombardment and has excellent structural stability against high electric fields.[21] It also supports our assumption of the same β in the two field ranges. This is especially important for fabricating field emission devices with stable, high current density field emission, as these structures have remarkable functional stability for repeated performance without obvious signs of any degradation.

Table 5.1. The onset voltage and the field enhancement factor (β) calculated for different structures of ZnO. In low field region, β is calculated by taking the work function (ϕ) of ZnO to be 5.3 eV while at high field region, β is calculated with effective work function to be ($\phi_0 = \phi + Eg = 3.37 + 5.3 = 8.67$ eV) where E_g is the band gap of ZnO.

Structure	Field Enhancement Factor β (x 10^5 cm^{-1}) Low field (1-2 kV) (ϕ = 5.3 eV)	Field Enhancement Factor β (x 10^5 cm^{-1}) High field (2-5 kV) (ϕ = 8.67 eV)	Onset Voltage (V)
Marigold	1.23	-	3300
Microbelt	14.5	6.72	2000
Multipod-1	5.59	2.76	5100
Multipod-2	30.06	26.24	320

The emission stability over a definite period of time for these structures is shown in figure 5.12. Marigold structures exhibit a reasonably good stability as compared to that for the microbelts. However, the emission current is found to fluctuate within 20% of the average value in both the cases, which could be attributed to the poor contact between the ZnO structures and the Si-substrate. However, in case of multipods, good stability with current fluctuations within about 15% of the average value is observed. The current fluctuations may also result from the dangling bonds on the surface and/or from the diffusion of adsorbates, on the surface of the emitters. Moreover, the self-diffusion process of the atoms at the tip of the structures in the presence of high electric field is also expected to contribute to the fluctuations.

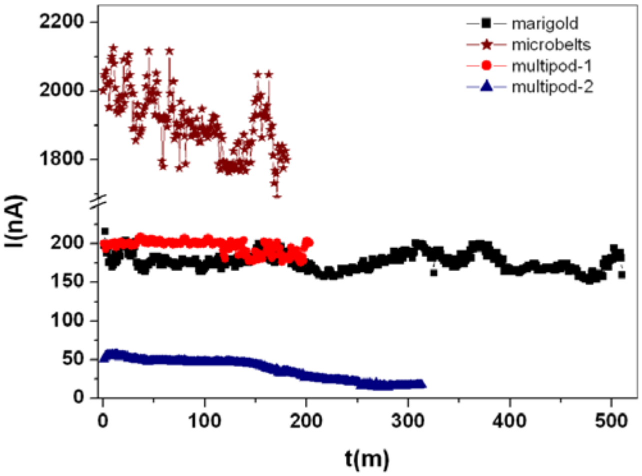

Figure 5.12. Variation of the emission current stability over time for different ZnO structures; marigold structure exhibits a better stability in comparison with both the microbelt and the multipod structures.

The field emission images are found to display a number of spots and lobes, which flickers in intensity in accordance with the emission current fluctuations. Figure 5.13 shows field emission micrographs for all the ZnO structures. The microbelts (figure 5.13a) exhibit a stable lobe pattern, while marigold structures exhibit a pattern with large number of uniform dots. This can be attributed to the larger density of the needle like emitter on the marigold structures as can be seen in the SEM images. Further, the emission from these structures depends on size of individual sharp structures. The FE micrograph for multipod-1 shows two lobes that are due to the two long pods in proximity with each other. At low field a large number of dots are seen on the screen, which can be attributed to the large number of smaller pods. However, with increase in the field bright lobe pattern is observed due to the two larger pods (as seen in SEM images). In case of multipod-2, a spot pattern as expected is observed and is attributed to the larger pods. While recording the current stability, (at the set current values) the ZnO structures have not shown any noticeable temporal changes in the emission micrographs. This indicates that the emission sites for all the ZnO structures are sustained without the generation of newer sites. The overall features of the emission micrographs remain in variant with time; however, the slight variation in the brightness of the emission pattern could be attributed to the reasons mentioned above.

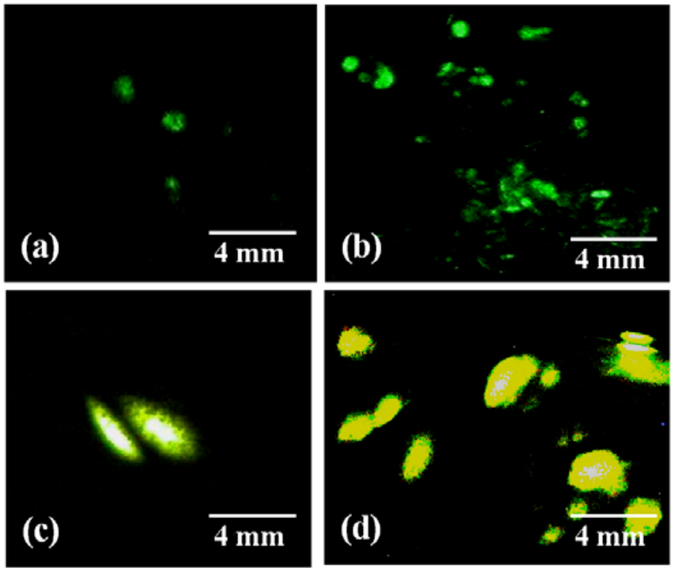

Figure 5.13. The field emission micrographs for (a) marigold, (b) microbelts, (c) multipod-1 and (d) multipod-2; each pod of the multipod and the number of sharp tips present on the surface act as active sites from where emission occurs. The bar indicates the scale on the screen.

5.3.3. Field emission from tetrahedral structures

The tetrahedral structures were grown directly on the W-tips for field emission measurements. Accordingly, Figure 5.14 shows the SEM images of the tetrahedral structures during the very early stages of growth. The size of each individual ZnO particle is approximately 1-1.5 μm with well-developed facets/edges as can be seen in figure 5.14 (b). Figure 5.15 shows the I-V characteristics for a typical tetrahedral structure. Interestingly, an onset voltage of 120 V has been observed corresponding to a current of 1nA and the value seems to be stable even during the operation at higher voltages (>10 kV). The corresponding F-N plot [ln (I/V^2) vs $1/V \times 10^4$] in figure 5.16 over a wide range of applied voltage, is seen to be nonlinear and could be attributed to the semiconducting nature of the emitter. This nonlinearity of F-N plot observed stands distinct from the behavior reported in literature[12, 19]. This is mainly due to the extended range of voltage applied in the present experiments. Although the F–N theory and the formulae used in the field emission microscopy are strictly valid for hemispherical emitter tips based on the free electron model, a rough estimate of the field enhancement factor β could be obtained from equation (1).

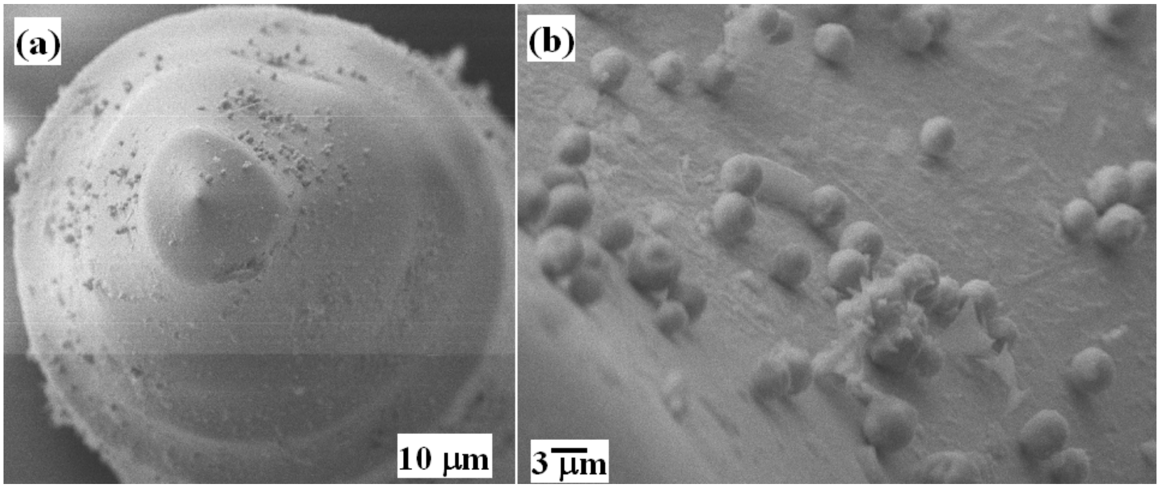

Figure 5.14. SEM of tetrahedral structure grown on tungsten-needle with an inset showing the enlarged image.

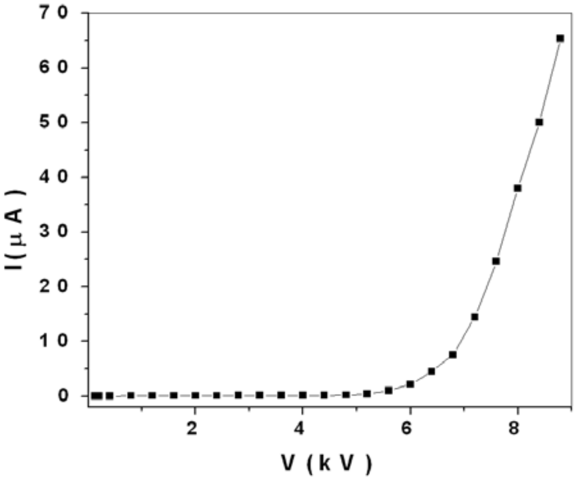

Figure 5.15. I-V characteristics of tetrahedral structure of ZnO; an onset voltage of 120 V corresponding to a current of 1nA seems to be stable even during the operation at higher voltages (>10 kV).

The observed plots are found to obey the F-N equation (2) in two distinct ranges of applied voltage. In these two ranges, the F-N plot is linear with distinct slopes. Taking the work function of ZnO (ϕ) to be 5.3 eV, the field enhancement factor is calculated to be 5.1 x 10^5 cm^{-1}. The low field region could be attributed to emission from the conduction band of ZnO and the high field region to the emission from the valence band, i.e., 3.37 eV below the conduction band, as well as the conduction band. Moreover, the un-oxidized Zn species present are also expected to contribute by creating the surface states in the mid gap region of ZnO.

The emission stability recorded over a certain period of time for these structures is shown in figure 5.17. A good current stability with fluctuations within about 15% of the average value is observed over a period of 3 h. The current fluctuations could be attributed to the dangling bonds on the surface or from the diffusion of adsorbates on the surface of the emitters. Moreover, the self-diffusion process of the atoms at the tip in the presence of high electric field is also expected to contribute to the fluctuations. Indeed, the field emission micrograph shows a slightly deformed spherical patterns corresponding to the individual ZnO particle on the tip as depicted in figure 5.17. Each individual particle serves as an emitter supported on the tungsten tip.

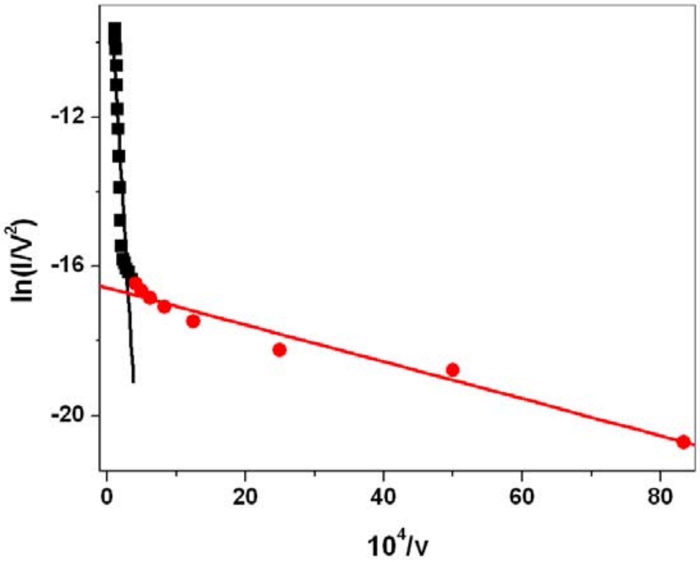

Figure 5.16. The F-N plot of tetrahedral structure showing a nonlinear behavior a characteristic of semiconductor.

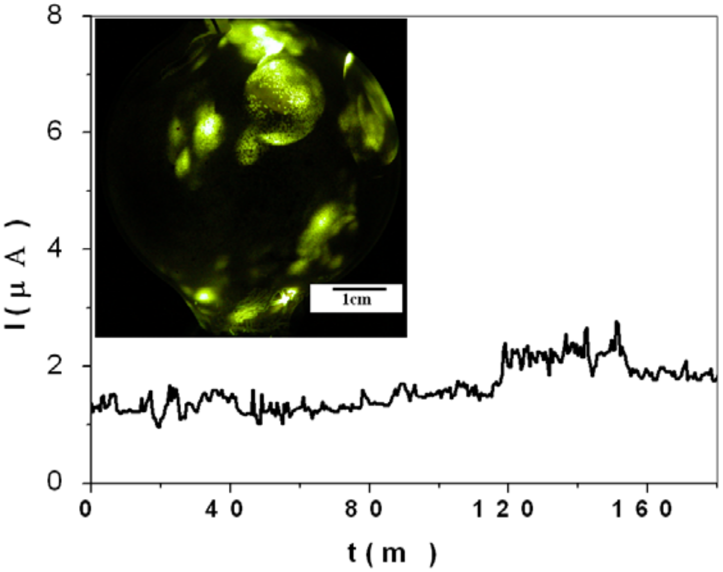

Figure 5.17. Current stability (I-t) plot of tetrahedral structure recorded over a certain period of time (3 h) with an inset showing a field emission micrograph. The bar indicates the scale on the screen.

A unique feature of non-linearity in the F-N plot, a characteristic of the semiconductor, is observed for all mulitpods, marigold, microbelts and tetrahedra ZnO structures. Further, the onset voltage is observed to be dependent on the sharpness of the emitter tip. Moreover, the density and the distribution of the individual emitter tip on the surface govern the field emission properties. The results show that electrons are more easily emitted from ZnO nanostructures with sharp tips, or surface perturbations than from microbelts with uniform diameter implying a strong dependence on the morphology. Therefore, improvement of the emission efficiency further requires continued shrinkage of the tip size.

5.4. Four-probe conductivity measurements

Figure 5.18 shows the temperature dependent I-V measurements of pellet of tetrahedral structure (a), marigold (b) and microbelt (c) grown on Si-wafer. The measurements were carried out in the presence of Ar. Interestingly, tetrahedra structures show ohmic relation attributed to the metallic Zn species present due to incomplete oxidation, while both marigold and microbelt forms exhibit a rectifying feature attributed to the semiconducting nature of the ZnO.

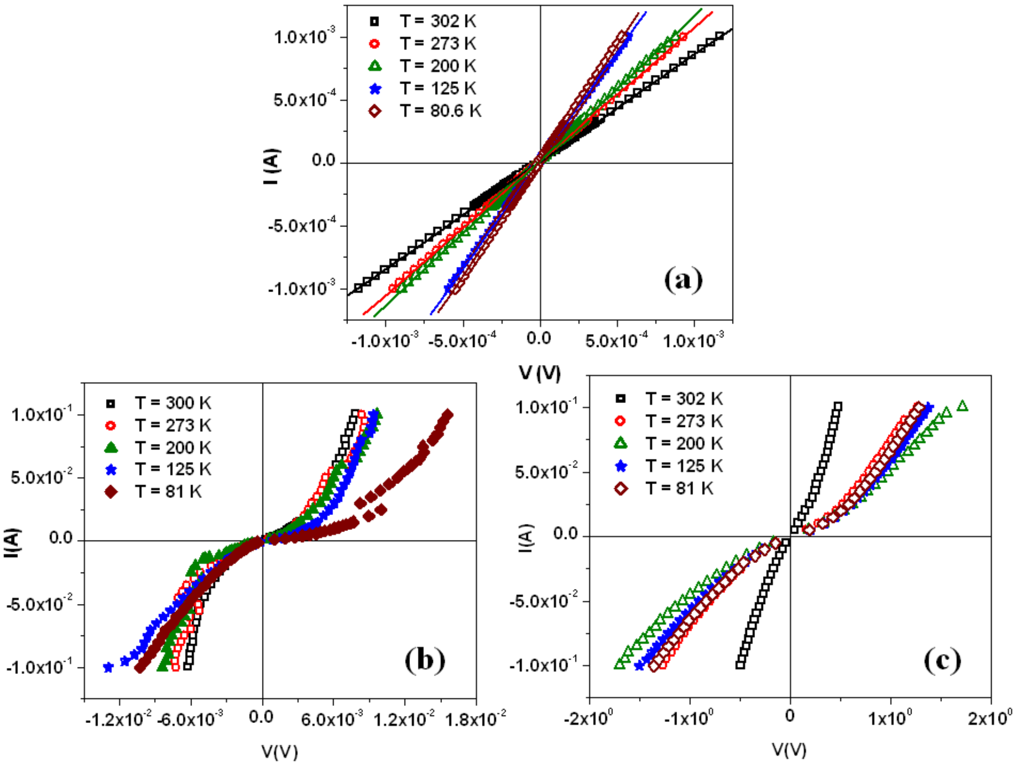

Figure 5.18. Temperature dependent I-V measurements carried out in the presence of Ar for pellet of tetrahedral structure (a), marigold (b) and microbelt (c) grown on Si-wafer.

Table 5.2 depicts the dependence of resistivity of all these structures as a function of temperature and morphology. From the Table 5.2, it is clear that there is no systematic trend in resistivity with temperature. Interestingly, tetrahedra exhibit a metallic behavior; resistivity increases with temperature. However, marigolds exhibit an overall semiconductor feature; resistivity decreases with temperature being the dominant phenomena. It also show a maximum at 200 K, attributed to the presence of zinc suboxides, which governs the resistivity at temperatures between 125 and 200 K, as per Matthiessen’s rule. Matthiessen's rule is an empirical rule which states that the total resistivity of a crystalline metallic specimen is the sum of the resistivity due to thermal agitation of the metal ions of the lattice and the resistivity due to the presence of imperfections in the crystal. Further, the electrical resistivity at room temperature (300 K) for metals is dominated by collisions of the conduction electrons with lattice phonons and at low temperature, by collisions with impurity atoms and mechanical imperfections in the solid[25]. In tetrahedral structures, the suboxides are assumed to be present as an impurity in metallic zinc, while in marigold and microbelt reverse is the case. Thus, a similar feature for microbelt is observed, although, impurities in the form of metallic Zn species dominate between 80 and 200 K.

Table 5.2. Resistivity values calculated for different morphologies of ZnO as a function of temperature. In case of tetrahedra the resistivity shows a metallic behavior and for marigold and microbelts a semiconducting behavior is observed.

Sr. No	**Temp (K)**	**ρ (Ω-cm)**		
		Tetrahedra	**Marigold**	**Microbelt**
1	80	3.33	97.83	8019.56
2	125	3.57	58.84	8622.44
3	200	5.47	60.60	10770.2
4	273	5.83	52.44	7944.2
5	300	7.33	49.84	3026.96

These results along with the field emission results indicate the possibility of controlling the electrical properties of ZnO by virtue of its morphology. Moreover, temperature plays a crucial role in deciding the material performance.

5.5. Limitations of ZnO nanostructures

Although these ZnO nanostructures exhibit encouraging properties, they however suffer from various limitations. The physical processes that take place at the very tip of an emitter play a critical role in the electron emission from the surface. There are various emitter parameters (defects) that influence field emission and more often than not, individual parameter contributions are difficult to identify and characterize. The field screening effect is a commonly observed phenomenon and can be alleviated by synthesizing/assembling vertically aligned nanostructures (having uniform emission) with ideal separation in device configuration on large-area substrates. Accurate current measurements from these structures and the correlation of findings with material properties are vital for making the appropriate links and for the future development of ‘designed electronic properties’.

5.5. Conclusions

This chapter summarizes, the unique field emission behavior of the isolated multipod and a single arm of a multipod ZnO structures, exhibiting an ultra-low turn-on voltage of 40 V (for 1nA) and the current density of 2.8 x 10^4 A/cm^2 achieved with a field of 1.26 x 10^5 V/μm. The F-N plots have been interpreted on the basis of the theory of electron emission from semiconductors and a scheme, explaining the field emission behavior in both high and low field regions. Moreover, the formation of sharp tips with nanometer-scale radius of curvature and high mechanical stiffness offers unprecedented advantages, thus providing robust materials for electron sources. In addition, our results also emphasize that tuning of the spacing between the individual field emitters in an array could yield better devices with low threshold voltage and high current density. Further, we believe that the ease with which these multipod nanostructures can be picked up and mounted to facilitate smaller size of emitting area, higher beam current and importantly, longer lifetime promise several new opportunities for making compact and more efficient field emission devices in the near future.

Further, the field emission behavior of different morphologies of ZnO has been studied in both C-P and conventional FEM configuration. F-N plots for these morphologies are found to be nonlinear and linear in the two distinct field regions respectively. Based on the theory of field emission from semiconductors, the low field region corresponds to the emission from conduction band, while the high field region corresponds to the emission from conduction and valence bands of ZnO respectively. The current stability exhibited by the multipod, marigold, and tetrahedral structures is promising for sustained emission behavior facilitating their applications as electron sources. Thus, in order to get excellent field emission, both the small emitter radius and appropriate growth coverage are necessary.

5.6. References

1. Stratton, R. *Phys. Rev. Lett.* **1962**,125 61-82.
2. Wildoer, J. W. G.; Venema, L. C.; Rinzler, A. G.; Smalley, R. E.; Dekker, C. *Nature* **1998,** 391, 59.
3. De Jonge, N.; Iamy, Y.; Schoots, K.; Oosterkamp, T, H. *Nature* **2002**, 420 393.
4. Tondare, V. N.; Balasubramanian, C.; Shende, S. V.; Joag, D. S.; Godbole, V. P.; Bhoraskar, S. V.; Bhadbhade, M. *Appl. Phys. Lett.* **2002,** 80, 4813.
5. Joag, D. S.; Late, D. J.; Lanke, U. D. *Solid State Comm*. **2004**, 130, 305.
6. Pan, Z. W.; Lai, H. L.; Au, F. C. K.; Duan, X. F.; Zhou, W. Y.; Shi, W. S.; Wang, N.; Lee, C. S.; Wong, N. B.; Lee, S. T.; Xie, S. S. *Adv. Mater.* **2000**, 12, 1186.
7. Wu, J.-M.; Shih, H. C. Wu, W.-T. *Chem. Phys. Lett.* **2003**, 413, 490.
8. Xu, N. S.; Huq, S. E. *Mater. Sci. and Eng.* R **2005**, 48, 47.
9. Baranauskas, V.; Fontana, M.; Guo, Z. J.; Ceragioli, H. J.; Peterlevitz, A. C. *Sens. Actuators B* **2005**, 107, 474.
10. Xu, C. X.; Sun, X. W. *Appl. Phys. Lett.* **2003**, 83, 3806.
11. Li, Y. B.; Bando, Y.; Golberg, D. *Appl. Phys. Lett.* **2004**, 84, 3603.
12. Li, Q. H.; Wan, Q.; Chen, Y. J.; Wang, T. H.; Jia, H. B.; Yu, D. P. *Appl. Phys. Lett.* **2004**, 85, 636.
13. Wan, Q.; Yu, K.; Wang, T. H.; Lin, C. L. *Appl. Phys. Lett.* **2003**, 83, 2253.
14. Fowler, R. H.; Nordheim, L. W.*Proc. R. Soc. London, Ser. A,* **1928**, 119, 173.
15. Filip, V.; Nicolaescu, D.; Tanemura, M.; Okuyama, F. *Ultramicroscopy* **2001**, 89, 39.
16. Jo, S. H.; Banerjee, D.; Ren, Z. F. *Appl. Phys. Lett.* **2004**, 85, 1407.
17. Gomer, R. Field emission and field ionization, American Vacuum Society Classics, AIP, Woodbury, New York, **1993**.
18. Tseng, Y. K.; Huang, C. J.; Cheng, H. M. ; Lin, I. N.; Liu, K. S.; Chen, I. C. *Adv. Func. Mater.* **2003,** 13, 811.
19. Bai, X.; Wang, E. G.; Gao, P.; Wang, Z. L. *Nano Lett.* **2003**, 3(8), 1147.
20. de jonge, N.; Allioux, M.; Oostveen, J. T.; Teo, K. B. K.; Milne, W. I. *Phys. Rev. Lett.* **2005,** 94, 186807.
21. Zheng, X.; Chen, G.; Li, Z.; Deng, S.; Xu, N. *Phys. Rev. Lett.* **2004**, 92, 1068031.

22. Modinos, A. Field emission, thermionic and secondary electron emission spectroscopy, Plenum Press, New York, **1984**.
23. Rhion, N. *Surf. Sci.* **1978,** 70, 92.
24. Sachtler, W. M. H. *Angew. Chem. Intern. Ed.* **1968,** 7, 668.
25. C. Kittle, Introduction to Solid State Physics, 7th Ed., John Wiley and Sons, Inc., New York, **2000**.

Chapter 6

Conclusions and Future Prospects

This last chapter deals with the significant conclusions of the present study. It also outlines several limitations of such nanostructures along with few suggestions for their improvement. Related promising developments and daunting challenges are also discussed to stretch the applications of these fascinating nanomaterials in view of the fundamental and technological interests of the interdisciplinary terms of physicists, chemists, biologists and engineers. Finally, some of the future prospects and precautions for processing nanostructured materials are also explained within the broad perspective of general applications and societal impacts.

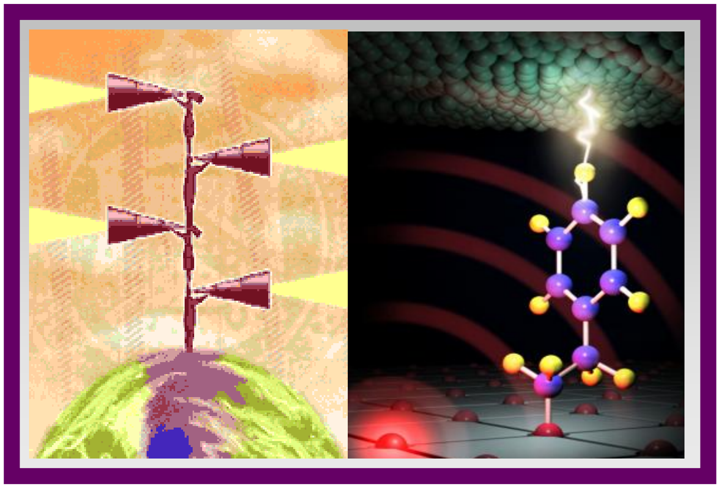

Technological and scientific potentials of high aspect ratio structures of semiconducting oxides are immense and the future of these nanostructured materials is certainly bright as revealed in the present study on SnO_2 and ZnO. Moreover, the ultimate use of these nanostructures is strongly dependent upon the ability to precisely control their dimension, composition, surface property, phase purity and crystal structure. Judged against these matrices, the methods demonstrated need to be still greatly improved before their widespread commercial use. A thorough understanding of the growth mechanism is a key towards achieving a controlled growth (size, distribution, shape, crystal structure, defect distribution, morphology), which is of particular significance both for the creation of new materials as well as for the fabrication of devices using these structures.[1, 2] Additionally, these unique structures represent promising candidates for fundamental studies of low dimensional physics and applications in various fields like nanoelectronics, nanosensors etc.

Accordingly, we have successfully demonstrated the ability to exert a simple control over the shape of the SnO_2 nanostructures, namely bipyramids, cubes and wires using RuO_2 as a unique catalyst during chemical vapor deposition. In addition, the key role of RuO_2 as an important nucleating agent in promoting the growth of low dimensional structures of SnO_2 is also revealed. The presence of a carrier gas and the amount of RuO_2 in the initial reaction mixture help in gaining control over interactions between the nuclei of the building blocks (RuO_2 and SnO liquid droplets). Such interactions are extremely helpful in understanding a correlation between specific types of reactions and specific target structures. For example, by modulating the precise location of doping element (catalyst), pressure and temperature gradients it is possible to get control over growth position and morphology. Additionally, the fabrication process is simple and cost effective and can be widely applied for the synthesis of other doped semiconducting oxides. Oxygen vacancy defects are hard to avoid during the synthesis of such oxide nanostructures, resulting in the formation of non-stoichiometric phases. On the other hand, the existence of the oxygen vacancies makes their properties tunable. Hence, the fundamental issues to be investigated are (i) the understanding of the relationship between the oxygen vacancies and stability of nanostructures, (ii) correlation of the properties with oxygen defects and (iii) effect of annealing/heat treatment on the morphology. This is especially significant in ensuring the stability of these structures since oxygen non-stoichiometry is intricably related also to the stability under ambient conditions. Development of techniques in this direction is therefore, desirable before extending the preparation to large-scale manufacturing.

Tin oxide is looked upon as a promising material for the fabrication of miniaturized, ultrasensitive chemical sensors. The unique conductance property, low cost and ease of fabrication into desired form (thin film and nanostructures) are exploited further, to make sensors possessing high sensitivity, selectivity and compatibility with the electronic circuitry. It is possible to enhance the sensing performance either by surface functionalisation or by controlling the film morphology. For example, the surface ruthenated SnO_2 thin films show enhanced sensitivity (45) and selectivity as compared to that of pure SnO_2 films for hydrocarbons (3). Moreover, surface functionalisation with CuMPCs makes it possible to detect H_2S at room temperature. The nature of functional group and the number of -OH groups present have been demonstrated to have a substantial effect on the sensing behavior. However, more understanding of nanocluster's contribution in imparting these excellent sensing characteristics to SnO_2 is needed prior to their commercialization.

The results of the present studies clearly illustrate that SnO_2 matrix can be effectively tailored by doping with elements like Ru, Cu and Th for the selective detection of LPG, H_2S and trimethylamine gases, respectively. Dopants were found to play a dual role, as a sensitizer leading to the enhancement in the sensing performance, and as a sintering aid resulting in low temperature crystallization. Further, electronic interactions between metallic additives and SnO_2 during the oxidation/reduction reactions occurring on the surface of the gas sensitive layer are crucial in determining the sensitivity and selectivity.

Moreover, because of the shape selective synthesis of different nanostructures, it is interesting to establish a relation between the morphology and the sensing properties. Sensing being surface dependent phenomena, the morphology implicitly affects the interaction occurring on the surface and consequently SnO_2 wires show enhanced sensitivity and selectivity towards NO_2 as compared to that of bipyramids and cubes.

Once again the amount of Ru determines the operating temperature and sensor response. The use of thinner nanowires or utilizing a single nanowire with proper SnO_2-metal ohmic contacts probably would achieve additional increase in sensitivity. However, in order to tailor the operating temperature, sensitivity and above all selectivity towards other test gases, it is important to choose proper doping element and its concentration. Hence more experiments are needed to optimize the doping process and concentration. Further, our method has demonstrated the possibility of synthesizing heterostructures, junctions and barriers, exploring also the possibility of preparing mixed oxides involving two or more type of cations, often needed to impart multifunctionality. Surface functionalisation of these structures is also an important, emerging direction where interesting results are likely to offer many advantages.

The simple method of vapor deposition used for SnO_2 is successfully extended and applied for the synthesis of various ZnO morphologies namely multipods, wires, belts, tetrahedral, micropencils and microhexagonal cones. Proper tuning of the process parameters viz. heating duration, temperature, type of substrate and the nature of carrier gas govern the final morphology. One of the important outcomes of the present work is the role of Si-species in governing the ZnO morphology. Si species get incorporated as Si^{2+} (SiO) and Si^{4+}(SiO_2) forms into the ZnO matrix, which act as catalysts providing the additional nucleating sites, where ZnO nanostructures grow. This result is of particular significance for development of techniques for integration of these structures with other nano-microstructures, such as microelectromechanical systems (MEMS) and Si based technology realizing their simultaneous, multidirectional growth on templates of SiO_2 for next generation devices. For example, it is possible to fabricate large arrays of crossbar junction with relatively high density by patterning the SiO_2 layer on the substrate by nanolithography or e-beam lithography.

The use of conventional field emission microscope configuration has made it possible to study the field emission over the wide potential range (upto 12kV), which is otherwise not possible in the close-proximity configuration. Interestingly, an ultra-low onset voltage of meager 40 V to draw a current of 1 nA is obtained for isolated single multipod and one of its arm. The sharp tips of ZnO structures resulted in the onset current density of 2.76×10^7 $\mu A/cm^2$, which is much greater than the minimum emission current density (1mA/cm^2) required to produce the luminance of 300 cd/m^2 from VGA-FED with typical high-voltage phosphor screen efficacy of 9 lm/W. Additionally, the non-linearity in the F-N plot over the wide potential range (linear in the two distinct field regions selected) emphasizes the contribution of electrons from both the valence and the conduction band. Additionally, field emission measurement with different level of loading reveals the importance of appropriate growth coverage in exploiting the advantage of low threshold voltage and high current density using a single emitter. Further, the ease with which these structures can be picked up and mounted facilitates their efficacy for designing the robust and reliable electron source to be used in a variety of future applications.

Besides the applications in sensors and field emission as discussed in the thesis, these nanostructures have other uses. Examples may include, near field probing, nonlinear optical conversion and information storage[3,4]. These applications, together with a fundamental interest in nanoscience will continuously provide compelling motivation for research into synthesizing novel nanostructures with precise control of dimensions. It is also a challenge to demonstrate radically new applications for these structures in an effort to greatly expand the scope of areas that these materials will impact on. Further, as the utilization of such nanostructures grows in importance the demand for new and more effective methods for their preparation will certainly increase. However, one should also realize that some potential environmental and health issues might arise when more and more nanostructures are produced in Laboratories[5]. Hence it is of utmost importance to take greater precaution while handling these structures as their long-term impact on environmental and health is still unclear[6].

References

1. (a) Yang, P. et al., *Adv. Mat.* **2003**, 15, 353. (b) Ross, C. *Annu. Rev. Mater. Sci.* **2001**, 31, 203. (c) Jie, J. S.; Wang, G. Z.; Han, X. H.; Hou, J. G. *J. Phys. Chem. B.* **2004**, *108*(44), 17027. (d) Vayssieres, L.; Keis, K.; Hagfeldt, A.; Lindquist, S.-E. *Chem. Mater.* **2001**, *13*(12), 4395.
2. (a) Zhang, Y.; Wang, L.; Liu, X.; Yan, Y.; Chen, C.; Zhu, J. *J. Phys. Chem. B.* **2005**, *109*(27), 13091. (b) Lin, Y.-R.; Tseng, Y.-K.; Yang, S.-S.; Wu, S.-T.; Hsu, C.-L.; Chang, S.-J. *Cryst. Growth Des.* **2005**, *5*(2), 579. (c) Jeong, J. S.; Lee, J. Y.; Cho, J. H.; Suh, H. J.; Lee, C. J. *Chem. Mater.* **2005**, *17*(10), 2752.
3. (a) Yun, W. S.; Urban, J. J.; Gu, Q.; Park, H. *Nano Lett.* **2002**, 2, 447. (b) Thelander, C.; Nilsson, H. A.; Jensen, L. E.; Samuelson, L. *Nano Lett.* **2005**, *5*(4), 635. (c) Star, A.; Lu, Y.; Bradley, K.; Gruner, G. *Nano Lett.* **2004**, *4*(9), 1587.
4. (a) *Societal Implications of Nanoscience and Nanotechnology*; Roco, M. C., Bainbridge, W. S. Eds. National Science Foundation Report: Arlington, VA; Kluwer Academic Publishers: Boston, MA, 2001. Near field probing, nonlinear optical conversion and information storage
5. (a) http://www.hazards.org/nanotech/safety.htm (b) Roco, M. C., Karn, B. *Environ. Sci. Technol. A - Pages* **2005**, *39*, 106A and reference there in.
6. (a) Goho, A. 2005. Buckyballs at bat: Toxic nanomaterials get a tune-up. *Science News* 166(Oct. 2): 211. (b) http://www.nano.gov/html/facts/home_facts.html. (c) James, J.T., and C. Lam. 2005. Pulmonary toxicity of carbon nanotubes in mice and implications for human risk assessment. Society of Toxicology 44th Annual Meeting and ToxExpo. March 6-10. New Orleans.

List of Publications

1. *"Surface Ruthenated Tin Oxide Thin Film as a Hydrocarbon Sensor"* **R. S. Niranjan**, V.A. Chaudhary, S.R. Sainkar, K.R. Patil, K. Vijayamohanan and I.S. Mulla, ***Sens. Actuators B***, 2001**,** 79, 132.
2. *"Bilayered Tin Oxide: Zirconia Thin Film as a Humidity Sensor"* **R. S. Niranjan**, S. D. Sathaye, I.S. Mulla, ***Sens. Actuators B*****,** 2001, 81, 64.
3. *"Ruthenium: Tin Oxide Thin Film as a highly selective Hydrocarbon Sensor"* **R. S. Niranjan**, S.R. Sainkar, K. Vijayamohanan and, I.S. Mulla[*], ***Sens. Actuators B***, 2002, 82, 82.
4. *"A Novel Room Temperature Sensor for Hydrogen Sulfide based on Copper Nanoclusters fictionalized Tin Oxide Thin Films"* **R. S. Niranjan,** V. A. Chaudhary, I. S. Mulla and K. Vijayamohanan, ***Sens. Actuators B***, 2002, 85, 26.
5. *"Trimethylamine sensing properties of thorium-incorporated tin oxide"* **R. S. Niranjan**, M. S. Londhe, A. B. Mandale, S. R. Sainkar, L. S. Prabhumirashi, K. Vijayamohanan and I. S. Mulla, ***Sens. Actuators B*** 2002, 87, 406.
6. *"Spin coated tin oxide: a highly sensitive hydrocarbon sensor"* **R. S. Niranjan** and I. S. Mulla, ***Mater. Sci. Eng. B****,* 2003*,*103, 103.
7. *"High H_2S-sensitive copper-doped tin oxide thin film"* **R. S. Niranjan**, K. R. Patil, S. R. Sainkar and I. S. Mulla, ***Mater. Chem. Phys.*** 2003, 80, 250*.*
8. *"Comparative studies of doped and Surface Tin oxide as a hydrocarbon Sensor"* **R. S. Niranjan** and I. S. Mulla, ***Asian Journal of Physics***, 2003, 12, 311.
9. *"Effect of Copper on the Hydrogen Sulfide Gas Sensing Properties of the Tin Oxide Thin Film"* **R. S. Niranjan**, K. Vijayamohanan and I. S. Mulla, ***Proceedings of the IEEE Sensors***, 2003, 2, 412.
10. *"Morphological and sensing properties of spray pyrolysed Th: SnO2 thin films"* **R. S. Niranjan**, K. R. Patil, K. Vijayamohanan and I. S. Mulla, ***Mater. Chem. Phys.*** 2004, 84, 137.
11. *"Shape Selective Synthesis of Unusual Nanobipyramids, Cubes and Nanowires of RuO_2: SnO_2"* **N. S. Ramgir,** I. S. Mulla and K. P. Vijayamohanan, SnO_2, ***J. Phys. Chem. B*****,** 2004*,* 108, 14815.
12. *"Semiconducting tin oxide gas sensors: bulk to thin films"* I. S. Mulla, **R. S. Niranjan,** Y. K. Hwang and J. S. Chang, ***J. Indus. Eng. Chem.*****,** 2004, 10, 1242.
13. *"A Room Temperature Nitric Oxide Sensor Actualized from Ru-doped SnO_2 nanowires"* **N. S. Ramgir,** I. S. Mulla and K. P. Vijayamohanan, ***Sens. Actuators B***, 2005, 107, 708.
14. *"Nanostructured tin oxide: Synthesis and gas sensing properties"* **R. S. Niranjan,** Y. K. Hwang, D. K. Kim, J. S. Chang and I. S. Mulla, ***Mater. Chem. Phys.*** 2005**,** 92, 384.
15. *"Effect of RuO_2 in the Shape Selectivity of Submicron –Sized SnO_2 Structures"*

N. S. Ramgir, I. S. Mulla and K. P. Vijayamohanan, ***J. Phys. Chem. B***, 2005, 109, 12297.

16. *"Effect of Pt concentration on the physicochemical properties and CO sensing activity of mesostructured SnO_2"*
N. S. Ramgir, Y. K. Hwang, S. H. Jhung, I. S. Mulla and J.- S. Chang, ***Sen. Actuators B*,** 2005, in press.
17. *"CO Sensor Actualized from Mesostructured Au-doped SnO2 Thin Film"*
N. S. Ramgir, Y.-K. Hwang, S. H. Jhung, H.-K. Kim, I. S. Mulla and J.-S. Chang, ***Appl. Surf. Sci.,*** 2005, accepted.
18. *"Liquid phase oxidation of alkanes using Cu/Co-perchlorophthalocyanine immobilized MCM-41 under mild reaction conditions"*
P. Karandikar, A.J. Chandwadkar, M. Agashe, **N. S. Ramgir** and S. Sivasanker, ***Applied Catalysis A: General***, 2006, 297, 220.
19. *"Ultra-Low Threshold Field Emission from a Single Multipod Structure of ZnO'*
N. S. Ramgir, D. J. Late, A. B. Bhise, I. S. Mulla, M. A. More, D. S. Joag and K. P. Vijayamohanan, ***Appl. Phys. Lett.*** 2006, *88,* 042107.
20. *"Micropencils and Microhexagonal Cones of ZnO"*
R.S. Niranjan, I. S. Mulla, K. P. Vijayamohanan, ***J. Phys. Chem. B,*** **2006** in press.
21. *"Field emission studies of novel ZnO nanostructures in high and low field regions*"
N. S. Ramgir, D. J. Late, A. B. Bhise, I. S. Mulla, M. A. More, D. S. Joag and K. P. Vijayamohanan, ***Nanotech.***, 2005, under revision.
22. *"Evidence of Doping Concentration Induced Particle Size and Strain Effects in Nanocrystalline SnO_2"*
N. S. Ramgir, Y. K. Hwang,; S. H. Jhung, I. S. Mulla and J.- S. Chang, (submitted to Solid State Science)
23. *"Shape Selective Synthesis of ZnO Multipods, Submicron Wires and Tetrahedral Structures, and their Unique Field Emission Behavior",* **N. S. Ramgir,** D. J. Late, A. B. Bhise, I. S. Mulla, M. A. More, D. S. Joag and K. P. Vijayamohanan. (submitted to Cryst. Grow. Des.)

List of Patents

1. "An improved hydrocarbon gas sensing instrument"
N. S. Ramgir, V. A. Chaudhary, K. P. Vijaymohanan, I. S. Mulla, 135/DEL/2002, **Indian.**
2. "A process for the preparation of impregnated thin film hydrocarbon sensor materials using spray pyrolysis technique"
N. S. Ramgir, V. A. Chaudhary, K. P. Vijaymohanan, I. S. Mulla, 136/DEL/2002, **Indian**.
3. "Proton transport at polymer surface"
S. P. Vernekar, S. S. Kothawade, K. Vijayamohanan, **N.S. Ramgir,** M. P. Kulkarni, R. A. Potrekar, NF-196/2004, **Indian**.
4. A method for the preparation of metal substituted mesoporous metal oxide thin films as a gas sensor by spray pyrolysis,
N. S. Ramgir, J. S. Yoo, S. H. Jhung, Y. K. Hwang, J. S. Chang and I. S. Mulla, **Korea**.

List of Abbreviations

Abbreviation	Expansion
1D	One-Dimensional
2D	Two-Dimensional
3D	Three-Dimensional
AC	Alternating Current
AFM	Atomic Force Microscope
BE	Binding Energy
bcc	Body Centered Cubic
CB	Conduction Band
CMOS	Complementary Metal Oxide Semiconductor
CNLS	Complex Nonlinear Least Square
DSC	Differential Scanning Calorimetry
DMS	Diluted Magnetic Semiconductors
DMSO	Dimethyl Sulfoxide
DMS-QDs	Diluted Magnetic Semiconductor Quantum Dots
DOS	Density of States
ECL	Electrochemiluminescence
EDX or EDS	Energy Dispersive X-Ray Spectroscopy
EELS	Electron Energy Loss Spectroscopy
EGA-MS	Evolved Gas Analysis - Mass Spectrometry
ET	Electron Transfer
fcc	Faced Centered Cubic
FET	Field-Effect Transistors
F-N	Fowler-Nordheim
FTIR	Fourier Transform Infrared
FWHM	Full Width at Half Maximum
GMR	Giant Magnetoresistance
hcp	Hexagonal Closed Packed

HOMO	Highest Occupied Molecular Orbital
HREELS	High-Resolution Electron Energy Loss Spectroscopy
HRTEM	High-Resolution Transmission Electron Microscopy
K	Kelvin
KKR	Korringa-Kohn-Rostoker
LB	Langmuir Blodgett
LED	Light Emitting Diodes
LFM	Lateral Force Microscope
LPG	Liquefied Petroleum Gas
LUMO	Lowest Unoccupied Molecular Orbital
MCD	Magnetic Circular Dichroism
MEMS/NEMS	Micro/Nano-Electromechanical Systems
MFM	Magnetic Force Microscope
MFP	Mean Free Path
MIM	Metal-Insulator-Metal
MINIM	Metal–Insulator–Nanocluster–Insulator–Bulk Metal
MIS	Metal-Insulator-Semiconductor
MIT	Metal-to-Insulator Transition
MOCVD	Metal-Organic Chemical Vapor Deposition
MOSFET	Metal Oxide Semiconductor Field-Effect Transistor
MPCs	Monolayer Protected Nanoclusters
NB	Nanobelts
NC-AFM	Non-Contact Atomic Force Microscope
NLO	Nonlinear Optical
NMR	Nuclear Magnetic Resonance
NSOM	Near-field Scanning Optical Microscope
NW	Nanowires
OAG	Oxide Assisted Growth
PL	Photoluminescence
ppm	Parts Per Million
QDL	Quantized Double Layer Charging
Q-dots	Quantum Dots
SAED	Selected Area Electron Diffraction

SAM	Self-assembled Monolayer
SAXS	Small Angle X-ray Scattering
sccm	Standard Cubic Centimeter
SECM	Scanning Electrochemical Microscopy
SET	Single-Electron Transistors
SIMS	Secondary Ion Mass Spectroscopy
SLS	Solid-Liquid-Solid
SPM	Scanning Probe Microscope
SPR	Surface Plasmon Resonance
SPS	Surface Plasmon Spectroscopy
STM	Scanning Tunnelling Microscope
STS	Scanning Tunnelling Spectroscopy
TDA	Tridecylamine
TEA	Triethylamine
TEM	Transmission Electron Microscopy
TG	Thermogravimetry
TMA	Trimethylamine
TPD	Temperature Programmed Desorption
UV	Ultra-Violet
UV-Vis	Ultra-Violet-Visible
VB	Valence Band
VS	Vapor-Solid
VLS	Vapor-Liquid-Solid
WKB	Wentzel Kramers Brillouin
XANES	X-ray Absorption Near-Edge Structure
XPS	X-ray Photoelectron Spectroscopy
XRD	X-ray Diffraction